FACULTÉ
DES SCIENCES

Autumn to spring inorganic carbon processes in pack and landfast sea ice in the Ross Sea, Antarctica

Thesis submitted by Fanny VAN der LINDEN
in fulfilment of the requirements of the PhD Degree in sciences ("Docteur en sciences")
Academic year 2020-2021

Supervisors : Doctor Bruno DELILLE (Université de Liège)

and Professor Jean-Louis TISON (Université Libre de Bruxelles)

LA LIBERTÉ DE CHERCHER

A mon Papa

Table of contents

Abstract

The Ross Sea, the southernmost sea on Earth, presents several iconic features of polar seas: sites of deep water formation, high summer primary production, floating ice shelves, the annual cycle of advance and retreat of sea ice, polynyas and katabatic winds. Furthermore, sea ice in McMurdo sound (western Ross Sea) is one of the most productive marine environments. However, sea ice inorganic carbon dynamics and related air-ice CO_2 fluxes have never been documented in the Ross Sea.

Two surveys were carried out in the western Ross Sea to bridge over a critical gap in the current understanding of sea ice: autumn and winter processes. The land-based YROSIAE project was a temporal survey from late winter to summer within landfast sea ice. The ship-based PIPERS project was an unique opportunity to study the early stages of sea ice formation (in polynyas) and more common consolidated pack ice in autumn. Based on these two consistent surveys, this work aims to (i) examine the bulk ice pCO_2 dynamics in landfast sea ice from late winter to summer (ii) investigate the seasonal pattern (net source vs net sink) and diurnal pattern of air-ice CO_2 fluxes (iii) analyse the depth-dependent physical and biogeochemical processes involved in inorganic carbon dynamics (iv) assess the precipitation of calcium carbonate in autumn and during a full bloom season.

CO_2 fluxes were measured using the chamber technique in autumn, late winter and spring, over open surface water, frazil ice patch, grey unconsolidated ice and consolidated first-year ice. These new autumn and winter data provide a first step to set up the budget of air-ice CO_2 fluxes over the year and evaluate the large-scale influence of these fluxes on the annual uptake of CO_2 by ice-covered oceans. Our results confirm that sea ice acts as a CO_2 source for the atmosphere during ice growth, with enhanced fluxes reported at the early stages of sea ice formation, and shifts to a sink in spring. In late spring, diel pattern superimposed upon this seasonal pattern and was potentially assigned to either ice skin freeze-thaw cycles or diel changes in net community production. The snowpack plays a complex role in CO_2 exchanges and can no longer be considered as an inert reservoir lying at the sea ice surface.

The main features of the normalized DIC distribution (DIC_{35}) through the ice column were: (i) a marked depletion at the surface from autumn to spring induced by the CO_2 releases to the atmosphere (ii) bubble-driven gas enrichment below or within impermeable layers and (iii) an initial DIC_{35} enrichment in the bottom layer disappearing in spring when the seasonal peak in biomass occurs.

At the bottom of landfast ice, in spring, a particular assemblage of microorganisms, the biofilm, led to a massive biomass build-up counterintuitively associated with nutrients accumulation. This biofilm formation may also promote calcium carbonate precipitation. However, in young pack ice or in cold landfast ice in early spring, limited calcium carbonate precipitation was reported. This suggests that calcium carbonate precipitation is not an ubiquitous process, especially in winter and autumn Antarctic sea ice. Comparison of calcium carbonate precipitation and pCO_2 measurements advocates that the calcium carbonate precipitation is rather controlled by pCO_2 than temperature.

Résumé

La Mer de Ross, la mer la plus méridionale du globe, présente de nombreuses caractéristiques emblématiques des mers polaires: zones de formation d'eaux profondes, un niveau élevé de production primaire en été, des plateformes de glace flottante, un cycle annuel de croissance et décroissance de la banquise, des polynies et des vents catabatiques. La glace de mer dans le détroit de McMurdo (en Mer de Ross occidentale) est par ailleurs l'un des environnements marins les plus productifs. Pourtant, à ce jour, ni la dynamiques du carbone inorganique au sein de la glace de mer, ni les flux de CO_2 qui en découlent n'y ont été documentés.

Deux suivis ont été menés en Mer de Ross occidentale afin de combler un déficit critique dans notre compréhension actuelle de la glace de mer: les processus automnaux et hivernaux. Le projet YROSIAE visait à étudier la glace de mer côtière de la fin de l'hiver à l'été. Le projet PIPERS, mené en mer en automne, était une occasion unique d'étudier les premiers stades de la formation de la glace de mer (dans les polynies) et la glace dérivante consolidée.

À la croisée de ces deux suivis, ce travail vise à (i) examiner la dynamique de la pCO_2 au sein de la glace de mer côtière de la fin de l'hiver à l'été, (ii) étudier les variations saisonnières (source vs puits) et diurnes des flux de CO_2 à la surface de la glace, (iii) évaluer l'impact des processus physiques et biogéochimiques sur la dynamique du carbone inorganique en fonction de la profondeur, et (iv) évaluer la précipitation de carbonate de calcium en automne et au printemps.

Les flux de CO_2 ont été mesurés à l'aide de cloches automatiques en automne, à la fin de l'hiver et au printemps, dans les eaux de surface, au-dessus de la glace de frasil, de la glace non consolidée et de la glace consolidée de première année. Ces nouvelles données automnales et hivernales sont cruciales pour établir un bilan annuel des flux air-glace de CO_2 et évaluer l'influence à grande échelle de ces flux sur l'absorption annuelle de CO_2 par les océans polaires. Nos résultats confirment que la glace de mer agit comme une source de CO_2 pour l'atmosphère pendant la croissance de la glace, avec des flux plus importants durant les premiers stades de la formation de la glace, et qu'elle devient progressivement un puits de CO_2 au printemps. À la fin du printemps, des variations journalières dans les flux de CO_2 ont été observées et potentiellement attribuées aux cycles de gel-dégel des couches de glace superficielles ou aux changements journaliers de la production communautaire nette. Le manteau neigeux joue également un rôle complexe dans les échanges de CO_2 et ne peut plus être considéré comme un réservoir inerte situé à la surface de la glace de mer.

Les principales caractéristiques de la distribution verticale du DIC normalisé (DIC_{35}) au sein de la glace sont: (i) une diminution marquée en surface de l'automne au printemps liée au rejet de CO_2 vers l'atmosphère, (ii) un enrichissement en gaz par formation de bulles en dessous ou au sein des couches imperméables et (iii) un enrichissement initial en DIC_{35} à la base de la glace qui disparaît au printemps lorsque survient le pic saisonnier de biomasse.

À la base de la glace de mer côtière, au printemps, un assemblage particulier de micro-organismes, le biofilm, a conduit à une accumulation importante de biomasse associée, contre toute attente, à une accumulation de nutriments. La formation d'un tel biofilm pourrait également favoriser la précipitation du carbonate de calcium. Cependant, autant dans la jeune glace dérivante que dans la glace côtière froide au début du printemps, des précipitations limitées de carbonate de calcium ont été observées. Cela suggère que la précipitation de carbonate de calcium n'est pas un phénomène omniprésent dans la glace de mer antarctique en hiver et en automne. La comparaison des mesures de précipitation de carbonate de calcium et de pCO_2 suggère que la précipitation de carbonate de calcium est plutôt contrôlée par le pCO_2 que par la température.

Acknowledgments

Ce long chemin escarpé qu'a été cette thèse a heureusement été égaillé et pimpé par de nombreuses petites et grandes mains tendues.

En premier lieu, je voudrais remercier Bruno et Jean-Louis, mes deux promoteurs, qui m'ont accompagné durant toute cette aventure.

Bruno, je te dois un immense merci pour tout le chemin parcouru en ta compagnie pendant ces 6 ans. Merci pour la confiance que tu m'as accordée tout au long de cette thèse. Le but était qu'on travaille ensemble et on a su le faire en se marrant beaucoup, c'était une très bonne option à mon sens. Tu t'es rendu disponible pour nous superviser d'assez près, Marie et moi, et je crois que ce fut une des clés de la réussite. J'ai eu beaucoup de chance de participer à 4 missions et je te remercie particulièrement de m'avoir entraînée dans ces aventures et de privilégier l'apprentissage sur le terrain. Sans compter tout ce que tu m'as appris avec beaucoup de rigueur, patience et créativité surtout quand je ne comprenais pas et que je voulais comprendre à tout prix. Lors de la mission Pipers, on s'est parfois un peu pris la tête mais c'était inévitable en 3 mois de huis clos?! Je retiendrai d'ailleurs plutôt nos câlins groupés avec Gauthier sur la banquise, nos sorties risquées en zodiac au milieu de l'Océan Austral, ton déguisement (comment dire... inattendu ?) lors du baptême à 66° Sud ou ce road trip en Nouvelle Zélande. Dans les moments plus difficiles, j'ai apprécié ton côté humain et ta bienveillance. Enfin, je retiendrai que, de manière générale, tu n'aimes pas les remarques pertinentes et le "n'émets pas des ondes négatives" répété à tout-va. Il y a peu, tu m'as dit "je me fannyétise" et ça c'est pas peu dire en fin de thèse!

Jean-Louis, c'est grâce à toi que je me suis retrouvée au laboratoire de glaciologie, grâce au temps que tu m'as consacré en rhéto pour mon TFE portant sur les régions polaires, c'était il y a un petit temps déjà. Merci de laisser ta porte toujours ouverte aux jeunes et étudiant·e·s (dont j'ai fait partie) et de nous transmettre si bien ta passion. Chaque réunion avec toi durant ma thèse était un coup de pouce énorme grâce à ton expertise ainsi que tes conseils et idées avisés. Il valait d'ailleurs mieux t'enregistrer pour être sûr de tout comprendre et ne rien louper. Tu m'as parfois attendue au tournant, le mémorable "work first, then penguins" est un bon exemple gravé dans ma mémoire ;) Ca m'a beaucoup touché quand tu prenais la plume pour les cartes de vœux à chacun·e ou ce petit mail lors du décès de mon Papa. J'espère que tu profiteras de ta pension pour relâcher la pression en prenant plus ta guitare à la main.

Je voudrais aussi remercier chaleureusement les membres de mon comité, Pierre Coheur et Emmanuel Mahieu, pour avoir suivi de près ce travail et m'avoir parfois redonner espoir.

I want to thank the members of my jury, Steve Ackley, Daïki Nomura, Alberto Borges and François Fripiat for your time and implication in the reading and defenses. I would like to thank the F.R.S.-FNRS and the funding David and Alice Van Buuren with the foundation Jaumotte-Demoulin for all the financial supports.

Marie, mama, ma fidèle collègue de bureau, heureusement que tu as été là pendant tout ce temps ! On en a passé des heures à discuter dans ce bureau de tout et de rien mais pas toujours de science en tout cas ! J'ai bien en mémoire nos 2 missions au Spitzberg, nos rires quand on était crevée, notre look avec ces magnifiques vestes vertes pomme, les heures de filtrations sur la table à manger de Stefano, les bons repas sur cette même table avec les 3 cocos, la piscine de Longyearbyen, ce caca qui a volé sur la banquise, ces nuits dans la cabane et j'en passe. Et quand je partais sans toi, je trouvais toujours des petits mots et dessins glissés dans mon sac d'expédition, hihi merci pour tout et vivement nos prochains moments sans parler de thèse :)!

Caro, trop chouette de t'avoir rencontrée pendant cette thèse et de s'être épaulées mutuellement pour arriver au bout de l'aventure. Je ne suis pas prête d'oublier notre petite escapade à Nassogne, au milieu des têtes de sangliers. Vivement la prochaine escapade à la campagne pour discuter des autres sens de la vie!

Gauthier, sans relâche tu me demandais : "c'est pour quand cette thèse ?" Et bien la voilà ! Merci pour ces nombreuses discussions scientifiques sur Yrosiae, déjà pendant mon mémoire où tu m'as bien aidée et puis pour rédiger ce foutu papier. J'ai toujours admiré chez toi cet esprit d'ouverture en sciences, cette capacité à rebondir même quand on te pose des questions qui dépassent ton domaine d'expertise. Et à côté de cela, j'ai apprécié nos échanges sur la vie et ses épreuves qui nous ont chacun.e marquées ces dernières années. La mission Pipers n'aurait pas été pareille sans toi. Les nombreuses heures dans ce labo du Palmer m'évoquent plutôt filtrations, rires, pleurs, découragements, sourires, fatigue, casse, nuits, jours, couture, Lonely Planet de la NZ... Alors que sur la glace, c'était plutôt bonhommes Michelin, câlins groupés, photos de manchots ou du sac Ortlieb, à choisir. Au plaisir de rejouer des parties de babyfoot comme sur ce bateau et de trinquer au coca avec toi !

Fred et Tonio, un tout grand merci de m'avoir embarquée sur 3 de vos missions au Spitzberg. J'aimerais retourner un jour sur cette magnifique île, rencontrer à nouveau des ours s'ils sont toujours là, conduire un motoneige mais éviter de faire un accident si Fred n'est pas là pour me sauver de justesse et manger des pizzas à pas d'heure de retour à

Longyearbyen. Merci aussi à Tonio pour ton accueil chaleureux à chaque fois que nous venions à Paris avec Marie.

Le labo des Belges sur l'Atalante n'aurait jamais existé sans toi Martin, merci pour ton précieux coup de main sur cette mission et aussi pour ces nombreux fous rires et la bonne ambiance dans nos autres missions au Spitzberg ou en conférence.

Seb, merci pour l'attention particulière que tu m'as accordée même depuis l'autre bout de la Terre! Elle s'est traduite à maintes reprises par les coups de pouce, échanges scientifiques, aide pour le talk à Davos, relectures en tout genre ou juste des petits verres à discuter de tout et de rien lors de tes passages en Belgique.

Un tout grand merci à Odile pour ce dernier coup de boost dans la dernière ligne droite de rédaction. Merci pour tes relectures, tes remarques directes et efficaces qui ont bien fait avancer le schmilblick.

Merci à mes collègues de l'ULB, Frank, Lio, Sophie, Morgane, Célia, Heiko, Saïnan, Kons, P-H, Elise, Sarah, Vio et François pour cette chouette ambiance qui anime le laboratoire. Un merci special à Saïda pour les heures de manip pCO_2 ou les bons plans réparations de tout style. Merci à toi, Claire, pour ton efficacité remarquable pour la paperasse de l'ULB, ta gentillesse et ton écoute dans les moments difficiles.

Merci aussi à mes collègues de Liège, Alberto, Gersande, Fleur, Marc et Willy. Même si je n'ai pas été très présente à Liège, je n'oublie pas les heures devant le GC en compagnie de certain·e·s d'entre vous, votre aide pour préparer mon FRIA ou des missions.

Thanks to the scientific team of the PIPERS cruise to welcome and receive 6 belgian scientists on board during 65 days in a closed area that was the Palmer icebreaker. It was the first experience of quarantine for me but not the last one apparently :o

Merci à mes colocs qui m'ont soutenue et tellement apporté durant ces 4 dernières années. Merci à Ana et son Papa pour la relecture de l'introduction de cette thèse et les conseils linguistiques.

Merci à ma famille de m'avoir accompagnée sur le chemin de ces folles aventures que sont les expéditions ou la réalisation d'une thèse. Merci pour votre intérêt, votre confiance et vos efforts lors de mes expéditions quand Papa était si gravement malade.

Un merci particulier à François pour toute ta patience et ta bienveillance pendant ces longs mois d'absence ou d'écriture, vivement nos futurs projets à 2 :)

Mon dernier merci mais de loin le plus grand ira à mon Papa, parti trop tôt durant cette thèse. Merci d'avoir suivi de près toutes mes aventures en Arctique et en Antarctique et pour la force que tu m'as transmise les derniers mois de ta vie, celle-là même qui m'a poussée à aller au bout de ce projet. Ce refrain, que tu aimais bien et fredonnait à mon départ, restera gravé dans ma mémoire:

"Des chercheurs qui cherchent
On en trouve
Des chercheurs qui trouvent
On en cherche
Inventrices et vous inventeurs
De tous les pays unissez-vous
L'homme n'a pas été au bout
De tous ses possibles
L'homme n'a pas été au bout
De tous ses possibles"

Julos Baucarne, L'imagination Au Pouvoir

Chapter I. Introduction

I.1. Motivation and objectives

One of the first paper describing the sea ice carbon pump (i.e. the transport of CO_2 across the sea ice-ocean interface) was published in the eighties by Jones and Coote (1981). Today, 40 years later, the role of sea ice in the global carbon cycle remains a challenging subject, of particular importance in the context of climate change.

Beyond the question of the large-scale influence of sea ice on the annual uptake of CO_2 by ice-covered oceans, the regional cycle of CO_2 (source vs sink) and the seasonality of the CO_2 dynamics within sea ice itself still remain open questions. Among the invokable reason for these remaining open-questions is the lack of measurements during the cold season in these remote ice-covered regions.

This research aims to refine our understanding of the sea ice CO_2 dynamics with fieldwork results from Antarctica. Both landfast ice and pack ice in the Ross Sea are investigated. The first survey (YROSIAE, Chapter III.) was land-base, offering, therefore, the possibility of long-term deployment, but restricted to landfast ice. To complete this, a ship-based survey (PIPERS, Chapter IV.) allowed us to explore both the early stages of sea ice formation (in polynyas) and common consolidated pack ice.

In the frame of this PhD thesis, I focused on the following objectives:

- Examine the bulk ice pCO_2 dynamics in landfast sea ice from late winter to summer

  The pCO_2 gradient between the ice and the atmosphere controls the direction and magnitude of CO_2 exchanges. Direct brines pCO_2 measurements were performed in several surveys (Delille (2006) and Delille et al. (2007)). However, these measurements were applied only to brines, bypassing gas bubbles trapped in the ice matrix. These measurements have a poor vertical resolution, and the original location of sampled brines is unknown. To avoid these biases and accurately estimate the pCO_2 at the interface, we measured the bulk pCO_2 using the method developed by Verbeke (2005) and Geilfus et al. (2012b) and adapted by Crabeck et al. (2014a). The survey YROSIAE presented here differs from the previous ones using the same method (summarised in Table 5) by presenting the first temporal series of bulk ice pCO_2 measurements through several months and seasons and with a high vertical resolution within the entire ice column.

- Investigate the seasonal pattern (net source vs net sink) and diurnal pattern of air-ice CO_2 fluxes

  Over the last decade, ice-air CO_2 fluxes measurements have been intensified in both the Arctic and Antarctica (Table 2). While sea ice CO_2 fluxes in spring and summer received increased attention (Brown et al., 2015; Delille et al., 2014; Geilfus et al., 2013, 2012a, 2015, 2014; Nomura et al., 2013a, 2010b), winter and autumnal observations are scarce due to harsh and variable weather conditions at these seasons. It has repeatedly been suggested that ice-air CO_2 fluxes are impeded when the ice is impermeable, mainly during ice growth (e.g. Delille et al. (2014), Tison et al. (2016)). Observations of CO_2 releases over the Arctic sea ice in winter (Else et al., 2011; Miller et al., 2011; Nomura et al., 2018) presently challenge this concept. However, we face a lack of data in Antarctica.

  This work provides measurements of air-ice CO_2 fluxes in autumn and winter in the Ross Sea using automated chambers (LICOR). The YROSIAE survey started in late winter and lasted until late spring, allowing us to catch the transition from net source to net sink. Thanks to a buoy recording both the air temperature and the ice temperature at different depths, we examinated the effect of diurnal temperature changes at the sea ice surface on CO_2 fluxes. The PIPERS survey took place in autumn. Measurements of CO_2 fluxes were performed over common consolidated pack ice and over the youngest sea ice stages (frazil ice, unconsolidated grey ice, pancakes...) using a floating chamber developed at the University of Liege during this thesis.

- Analyse the depth-dependent physical and biogeochemical processes involved in inorganic carbon dynamics

  Today, the role of the trophic status (autotrophy vs heterotrophy) and biogeochemical processes on CO_2 dynamics in Antarctic sea ice is still poorly understood. Only few studies reported DIC data and, in parallel, took into account the biogeochemical state of Antarctic sea ice. Delille et al. (2007) and Geilfus et al. (2014) provided DIC values in brines or platelet ice layer in late spring at maximum two discrete depths per station.

  The two surveys in this work present full-depth DIC profiles and at high vertical resolution. In order to highlight biogeochemical processes implicated in DIC changes, we completed those profiles by measurements of $CaCO_3$ content, nutrients, chl-a and POC concentrations, O_2/Ar ratios, and associated CO_2 fluxes. By comparing the DIC results with the biogeochemical dataset, we were able to discuss the impact of CO_2 fluxes at the surface, the role of the trophic status (autotrophy vs heterotrophy) in interior and bottom ice and the implications of the biofilm formation at the sea ice bottom, particularly in the precipitation of calcium carbonate.

- Assess the impact of the calcium carbonate precipitation in autumn and during a full bloom season

  Despite several dedicated studies, there are still critical gaps in the current understanding of calcium carbonate precipitation in sea ice. For instance, the conditions, timing and amount of calcium carbonate precipitation are still poorly constrained. The presence of calcium carbonate was well addressed in Arctic sea ice where direct (observations with naked eye) or indirect measurements of calcium carbonate concentration were reported (Table 1). In Antarctica, the first detection of calcium carbonate precipitation as ikaite crystals was performed by Dieckmann et al. (2008). Since then, few studies investigated this process in Antarctica. We addressed calcium carbonate precipitation in sea ice by systematically carrying out two indirect measurements on each ice sample and suggested a mechanism for calcium carbonate precipitation within the biofilm at the bottom of landfast sea ice.

I.2. Thesis outlines

This work consists of three main chapters. The Chapter II. is an exhaustive state of the art to settle essential prerequisite and processes covered within the main body of the thesis. The Chapter III. consists of a peer-reviewed article about CO_2 dynamics within landfast sea ice during the transition from winter to summer. The Chapter IV. focus on the autumnal CO_2 dynamics within unconsolidated sea ice and common pack ice (PIPERS study). To conclude, the researches and findings achieved during this six years PhD thesis are synthetised.

Chapter II. State of the art

II.1. Atmospheric CO_2 and the crucial role of the Southern Ocean in the global carbon cycle

The rapid accumulation of CO_2 in the atmosphere is currently one of the major environmental concerns because of its involvement in the current global warming. CO_2 is the second most important greenhouse gas, after water vapor, in the atmosphere (Zeebe and Wolf-Gladrow, 2001) but is recognized as the largest contributor to positive radiative forcing over the period 1750–2011 (IPCC, 2014). Over this period, atmospheric CO_2 concentrations increased by 40%, from 278 ppm to 390.5 ppm (IPCC, 2014) as other greenhouse gases did such as methane (CH_4) and nitrous oxide (N_2O) (Figure 1). In the decade 2002-2011, CO_2 concentrations increased at the fastest decadal rate of change (2.0 ± 0.1 ppm per year) since direct atmospheric concentration measurements began in 1958 (IPCC, 2014). Current atmospheric CO_2 concentrations reached up to 410 ppm in January 2020 (NOAA/ESRL, 2020).

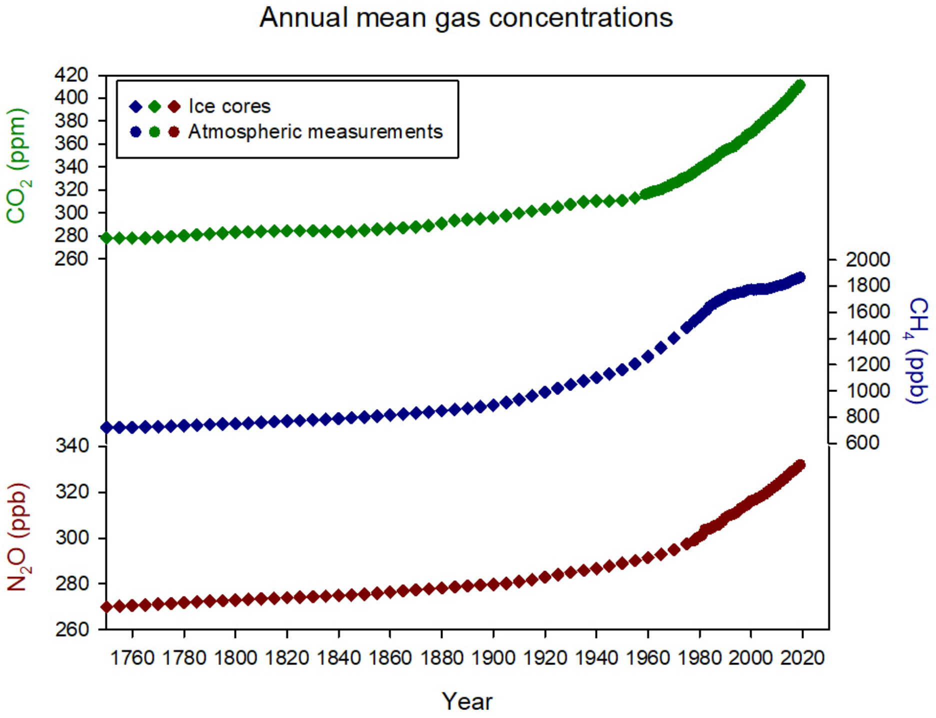

Figure 1: Observed changes in atmospheric concentrations of carbon dioxide (CO_2, green), methane (CH_4, blue), and nitrous oxide (N_2O, red). Diamonds indicate ice cores data, dots indicate recent atmospheric data. CO_2 concentrations are provided by NOAA/ESRL and CH_4 and N_2O concentrations are provided by AGAGE (Advanced Global Atmospheric Gases Experiment, MIT).

Atmospheric CO_2 represents only a tiny fraction of the carbon in the Earth System, the rest of which is tied up in other reservoirs (land ecosystems and oceans) (IPCC, 2013).

The global ocean plays a crucial role in storing 98% of the carbon of the atmosphere-ocean system (Zeebe and Wolf-Gladrow, 2001). Considering only the "natural" CO_2, i.e. the quantity of carbon in the atmosphere-ocean system existing already in preindustrial times, Gruber et al. (2019a) estimated that the ocean was a net CO_2 source, releasing about 5 ± 3 Pg C over the period 1994 to 2007. However, the ocean also buffers the effects of anthropogenic CO_2 emissions (Zeebe and Wolf-Gladrow, 2001) and acts as a sink of anthropogenic CO_2. Over the period 1994 to 2007, this ocean sink removed nearly 31 ± 4% of the global anthropogenic CO_2 emitted in the atmosphere over the same period (Gruber et al., 2019a). The resulting net (natural and anthropogenic CO_2) ocean uptake is estimated at 29 ± 5 Pg C for the 1994 - 2007 period and is comparable to the net terrestrial biosphere sink over the same period estimated at 31 ± 9 Pg, regardless of the CO_2 emissions from land use change (Gruber et al., 2019a). Although this $\sim$ 30% increase in the oceanic storage of anthropogenic CO_2 between 1994 and 2007 allows to slow down the accumulation of CO_2 in the atmosphere, Gruber et al. (2019a) observed substantial regional differences in storage rate. Considering these regional differences, there is uncertainty about the robustness of the oceanic CO_2 uptake over time (Gruber et al., 2019a).

Over the global oceans, polar oceans act as a major sink for atmospheric CO_2 (Gruber et al., 2019b; Takahashi et al., 2002). Since the early 90's, carbon fluxes in the Southern Ocean (SO) constitute a long-lived critical question for the ocean science community. The primary role of the SO in the global carbon cycle is directly related to its unique circulation, initiating both the deep water masses of the world's ocean and the primary return pathway for this deep water to the surface (e.g., Marshall and Speer (2012), Morrison et al. (2015)). The SO is therefore one of the main window between the atmosphere and the deep ocean. Even though covering only around 20% of the world's ocean's surface, the SO stores roughly 75% of the excess heat generated on Earth (Frölicher et al., 2015) and is responsible itself for approximately 40% of the global oceanic uptake of anthropogenic CO_2 (Caldeira and Duffy, 2000; DeVries, 2014; Mikaloff Fletcher et al., 2006). The majority of this uptake of anthropogenic CO_2 takes place between the Antarctic Polar Front and the Subpolar Front (between 45°S and 55°S) where recently upwelled waters with a very low initial anthropogenic CO_2 concentration flow northward and are exposed to the atmosphere in a region of high wind speeds, leading to high-uptake fluxes (Gruber et al., 2019b). The waters enriched in anthropogenic CO_2 are then transported to depth through the subduction of mode and intermediate waters (Mikaloff Fletcher et al., 2006; Sabine, 2004).

The SO plays a crucial role in storage of heat and carbon dioxide for the planet. As a result, change in the SO CO_2 sequestration capacity appears to be a major control on glacial-interglacial succession (Ai et al., 2020). Hence, a robust assessment of air-sea CO_2 fluxes in the SO is crucial for the understanding of past, current and future global carbon budget and eventually the Earth's climate.

II.2. Sea ice overview

II.2.1. Sea ice formation

Sea ice results from the freezing of seawater. Sea ice is a mixture of pure ice, brine inclusions (pockets or channels) and gas bubbles. In autumn or winter, when the ocean surface cools down to temperatures close to -1.86°C (the freezing point of seawater with a salinity of 34), frazil ice starts to form. Frazil ice crystals have isometric and rounded sides or can exhibit some specific shapes such as needles, spicules or platelet (Petrich and Eicken, 2016). Crystal sizes are typically small: from less than 1 mm thick up to a few tens of millimeters in side length (Petrich and Eicken, 2016).

Under turbulent conditions due to waves and current shear, frazil ice crystals accumulate to form a grease ice layer (thin slush layer) on the ocean surface (Figure 2). The grease ice layer consolidates, gets thicker and thicker and freezes into pancakes that will grow from a surface area covering a squared centimeters (proto pancakes) to several squared meters. Pancakes bump against each other and raft on top of each other under the action of winds and waves, resulting in raised edges and thicker cakes ($>$ 10 cm thick) (Petrich and Eicken, 2016). With ongoing freezing, the pancakes congeal into larger units and finally form a continuous ice sheet by bottom freezing at the ice-water interface.

Under calm conditions, the frazil ice crystals freeze up together resulting in uniform sheets of new ice ($\leq$ 10 cm in thickness) called nilas. As the sheets get thicker and thicker, bottom vertical ice growth takes place to form columnar ice. Once the sea ice thickness reaches more than 10 cm, the ice sheet is classified as young ice. First-year sea ice is generally thicker than 30 cm (Petrich and Eicken, 2016).

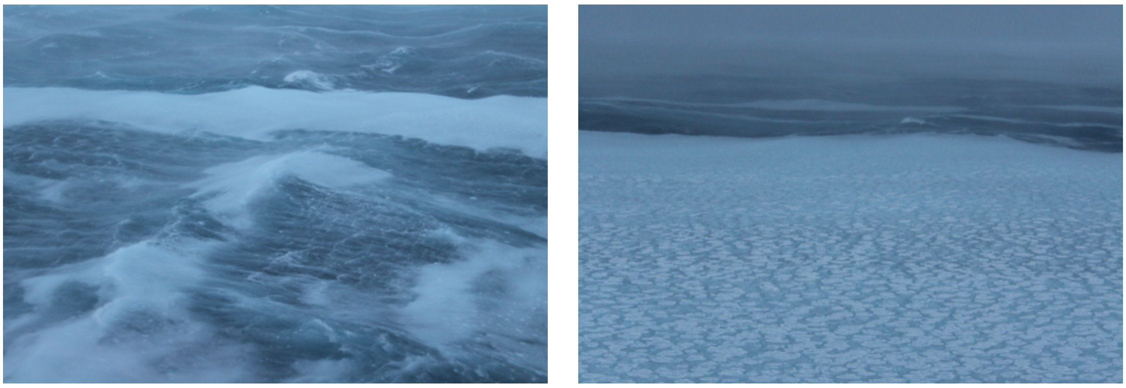

Grease ice Proto pancakes

Pancakes Consolidated pancakes

Figure 2: Ice growth forms in turbulent conditions. Pictures from the Ross Sea, winter 2017, during the Pipers cruise. Pictures by F. Van der Linden

These growth conditions lead to different ice textures. Granular ice results from the consolidation of individual frazil ice crystals and is therefore frequently observed at the top of the sea ice with randomly oriented, isomeric or prismatic crystals (Weeks, 2010). Granular texture is also associated with superimposed ice formation and snow ice. Superimposed ice forms when snowmelt water draining to the ice surface refreezes as a solid ice layer and snow ice results from the freezing of the snowpack after flooding (Massom et al., 2001).

The ice texture evolves step by step towards columnar ice under the granular layers (Figure 3). Columnar ice is characterized by vertically elongated crystals exhibiting a diameter of several centimeters in size and a length in tens of centimeters (Petrich and Eicken, 2016). During growth, brines are incorporated as intra-crystalline brine layers, i.e. parallel alignments of brine inclusions in individual crystals (Petrich and Eicken, 2016; Weeks and Ackley, 1986). At the bottom columnar ice, the skeletal layer, consisting of intra-crystalline layers and an interconnected brine network crossing it, is highly porous, with brine volume fraction of about 30%, which allows convective brine exchanges (Petrich and Eicken, 2016).

Granular ice Columnar ice Platelet ice

Figure 3: Ice textures, examples from ice cores collected in McMurdo Sound, Antarctica, during the YROSIAE field campaign.

In the vicinity of Antarctic ice shelves or under Arctic sea ice within a meltwater lens (Notz, 2003) or a melt pond (Jeffries et al., 1995), platelet ice formation is readily observed underlying columnar ice. Platelet ice is characterized by large crystals (centimeter-sized) randomly oriented. Crystals are classified as draped crystals with curved grain boundaries as observed by Jeffries et al. (1993) and Tison et al. (2013) or bladed crystals as observed in McMurdo Sound by Jeffries et al. (1993). Platelet ice layer is known to host large concentrations of sea ice algae (Arrigo et al., 1995). The process of its formation is discussed in section II.6.4..

II.2.2. Landfast sea ice vs pack ice

Landfast sea ice refers to immobile sea ice, anchored either to coasts, continental ice formations (ice shelves or glacier-tongues) or grounded over shoals (Meiners et al., 2018). Pack ice refers to drifting ice floes in open ocean under the action of winds or currents.

In both the Arctic and Antarctica, pack ice tends to be much thinner than landfast ice (Arrigo, 2017), with a mean thickness of less than 1 m. Landfast ice can typically reach 1 to 2 m in thickness, and its appearance is relatively smooth and flat (at least in the inner part of the ice floe) compared to pack ice that can be highly deformed. Surface flooding by seawater, a widespread phenomenon over pack ice in Antarctica (Massom et al. (2001) and references therein), strongly affects sea ice ecology and the development of surface algal communities as described in section II.5.4.. The composition of pack ice is generally a mixture of columnar and frazil ice whereas landfast ice is predominantly columnar ice as shown in Figure 4. Platelet ice, reaching between few centimeters to several meters in thickness, can form beneath the columnar landfast sea ice and harbor some of the highest concentrations of algae and intense primary production as discussed in sections II.5.4. and II.5.5.

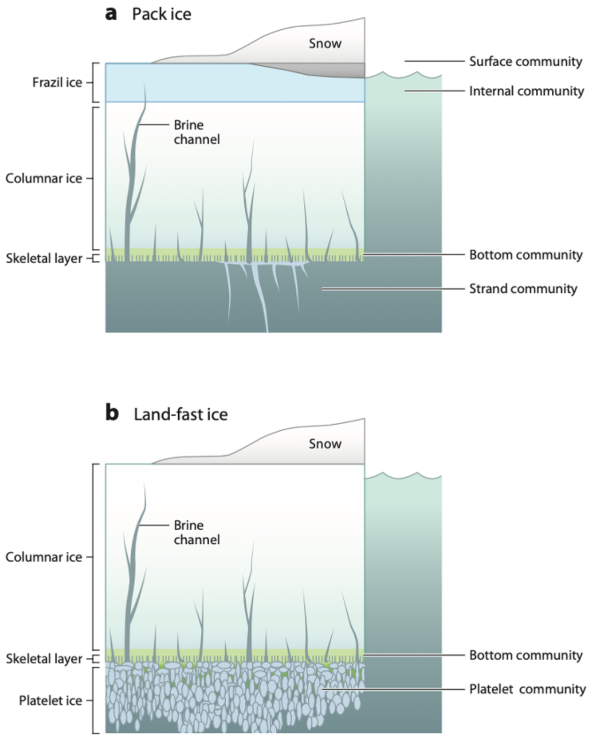

Figure 4: Typical positions of different ice types and algae communities in (a) pack ice and (b) landfast ice from Arrigo (2014).

In this work, we will discuss the biogeochemistry of both landfast sea ice and pack ice in the Ross Sea sampled during the Year-Round survey of Ocean-Sea Ice-Atmosphere Exchanges (YROSIAE) in 2011-2012 and during the PIPERS (Polynyas, ice production and seasonal evolution in the Ross Sea) cruise in 2017, respectively.

II.2.3. Sea ice extent

The sea ice extent is defined as the area of ocean covered with at least 15% of sea ice (NSIDC, 2019). In the Arctic, the maximum sea ice extent is observed around the end of March when sea ice covers an area of about 15.64 million km^2 (average for 1981-2010, NSIDC (2020a)) while the minimum sea ice extent in summer is about 5 million km^2 although an extreme low extent of 3.4 million km^2 was recorded in 2012 (Parkinson and Comiso, 2013). In September 2019, the minimum sea ice extent averaged 4.15 million km^2 (Figure 5a), this was the third lowest sea ice extent after 2012 and 2007 over the 41-year continuous satellite record (NSIDC, 2020a). The maximum extent for the winter 2019-2020 was 15.05 million km^2 reached on 5th of March, which is below the average of 1981-2010 and above the minimum recorded in 2017 (NSIDC, 2020a). All Arctic regions also showed a substantial decrease in ice thickness, estimated in average at 40%, from an ice thickness of 3 m to less than 2 m (Perovich, 2011). Hence, since the 1980's, there has been a reduction in ice extent, a decrease in ice thickness, and a shift from multiyear ice to first-year ice (Perovich, 2011).

In Antarctica, sea ice extent reaches typically a maximum of about 19 million km^2 in September–October and a minimum of about 3-4 million km^2 in February. Since 1979, Antarctic sea ice extents followed a slight and uneven increase but this trend reversed after the maximum record of 2014 (Parkinson, 2019). The decline observed afterwards reached a minimum record in 2017 over the last 40-y 1979–2018 satellite data considered (Parkinson, 2019). The National Snow & Ice Data Center (2020b) observed the same trend from 2016 onwards with a sea ice extent below their reference period 1981-2010 (Figure 5b).

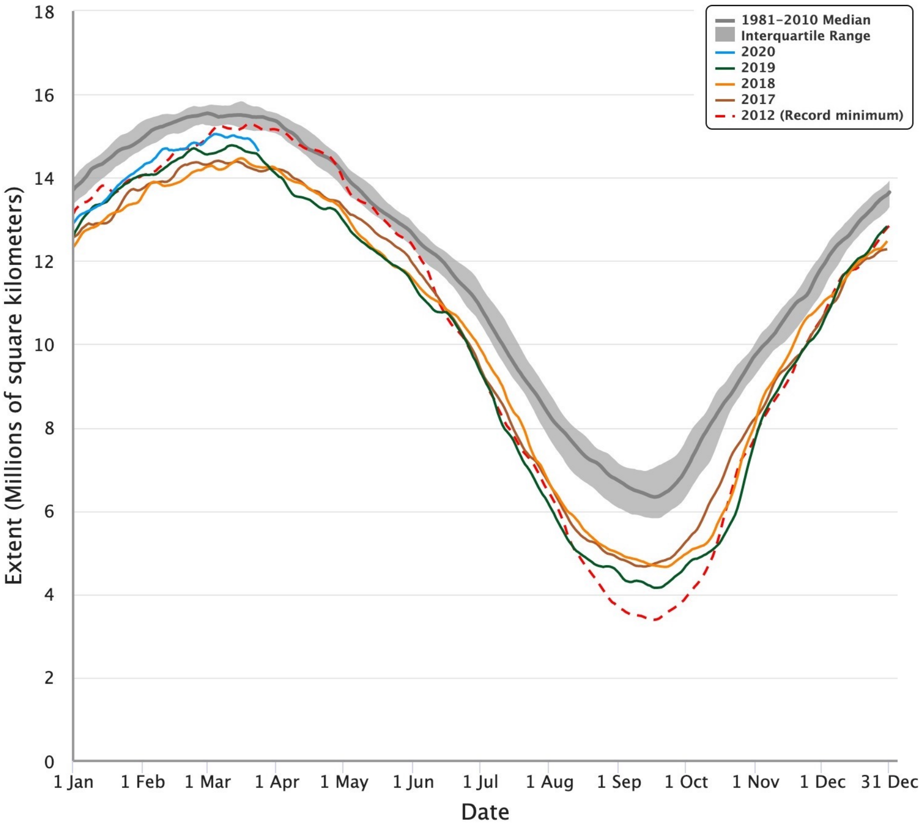

(a) Arctic

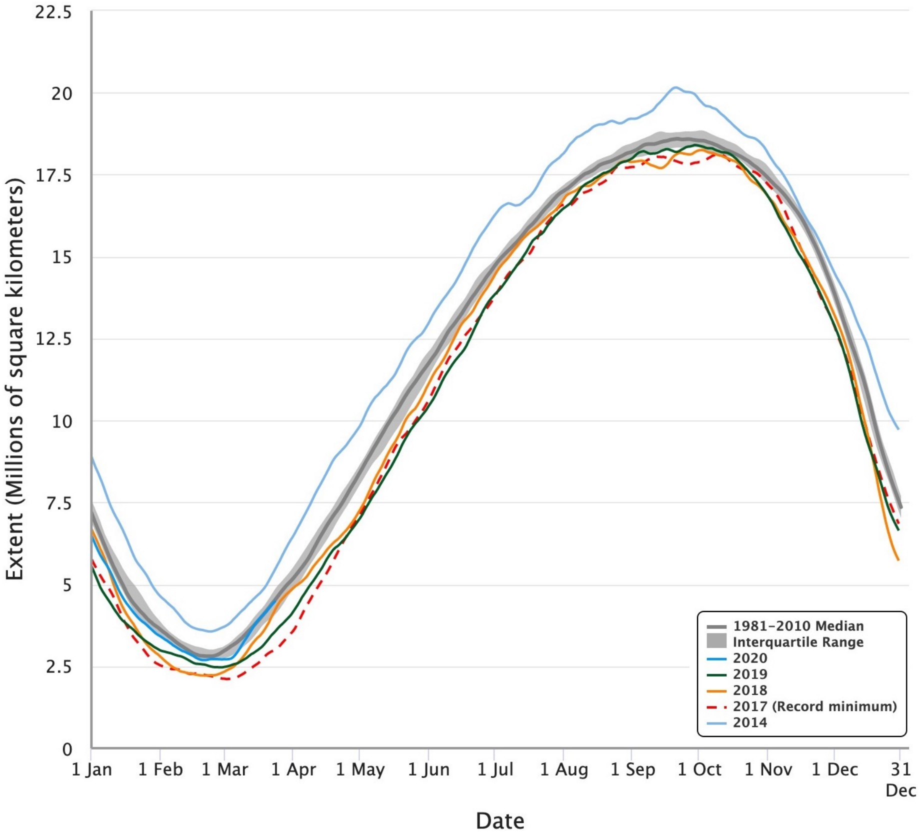

(b) Antarctic

Figure 5: Sea ice extent in both poles for the last 4 years and the minimum/maximum records. Plots are from NSIDC (2019).

II.2.4. Polynyas

Polynyas are recurrent zones of open water and/or thin ice cover or low ice concentration (Barber and Massom, 2007), surrounded by a more consolidated and thicker ice cover. They result from complex interactions at the sea-ice-atmosphere-ocean interfaces. Polynyas differ from leads that are short-lived linear openings of meters to hundreds of meters wide and kilometers to tens of kilometers long and most of the time not recurrent at the same location (Barber and Massom, 2007; Smith et al., 1990). Polynyas are usually categorized into two types based on their formation mechanism:

- Sensible-heat polynyas which are thermally driven and form where sufficient oceanic heat arrives to the surface by upwelling of warm water, vertical mixing or deep-ocean convection that locally prevents ice formation or enhances melting (Barber and Massom, 2007).
- Latent-heat polynyas which are mechanically driven by winds and/or ocean currents causing ice divergence. Intense heat loss allows frazil ice formation and ice is removed as quickly as it forms by ice divergence. The open-water area is maintained thanks to the latent heat provided by the formation of newly forming ice (Barber and Massom, 2007). This heat source counterbalances the surface heat loss to the atmosphere. Mechanically driven polynya can be divided in two regions: an inner region of open water where frazil ice forms continuously and an outer region where new and young ice floes accumulate by accretion of frazil ice (Morales Maqueda et al., 2004).

A different classification than latent or sensible heat polynyas can be used based on the location of their occurrence: deep water and shelf water polynyas (Figure 6).

Deep water polynyas are formed at or beyond the continental shelf and often by a sensible heat mechanism in areas where a weak pycnocline separates the cold and fresh surface waters from underlying warmer, saltier waters (Morales Maqueda et al., 2004). Warm waters can reach the surface through enhanced mixing or convection and either trigger sea ice melting or prevent sea ice formation.

Shelf water polynyas occur over the shelf and most of them are maintained by a latent-heat mechanism. Shelf water polynyas are referred to as “ice factories”, where the constant removal of frazil ice triggers intense ice formation (Morales Maqueda et al., 2004). Resulting brine-rich, cold water will accumulate over the shelf and flow down the shelf break slope to eventually contribute to deep and bottom water formation (Morales Maqueda et al., 2004). During spring and summer, those polynyas remain open and absorb large amounts of solar radiation leading to ice melt, becoming in this way "ice melt factories" (Ohshima et al., 1998).

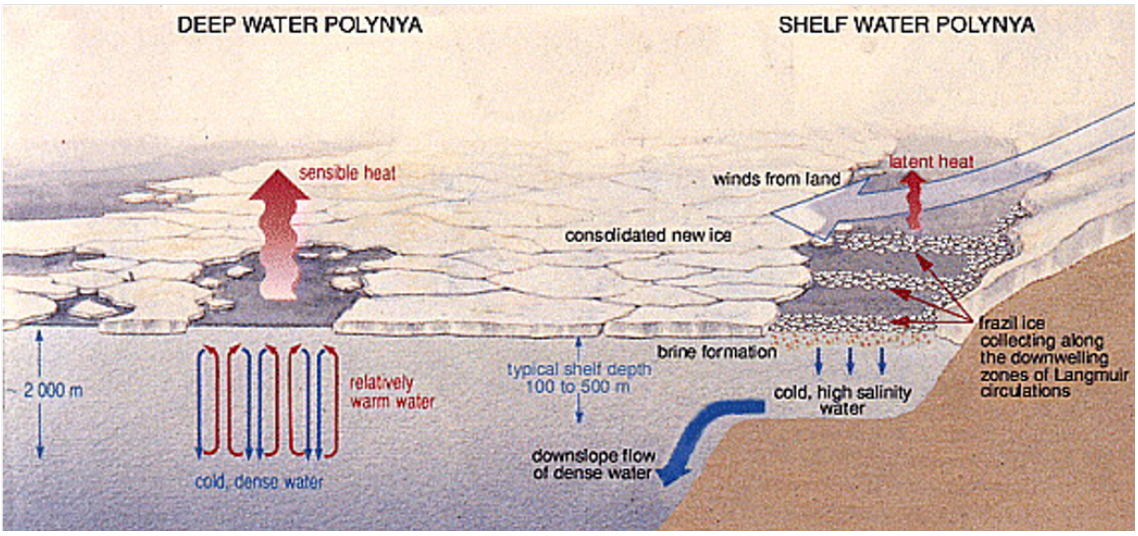

Figure 6: Location of deep water and shelf water polynyas and processes implicated. Figure from Morales Maqueda et al. (2004).

As pointed out by Massom and Stammerjohn (2010), polynyas play important roles:

- Zones of high sea ice production, contributing in some cases to deep water formation (Antarctic Bottom Water formation) (Bindoff et al., 2000; Rintoul, 2013)
- Ventilation "windows" between the deep ocean and the atmosphere. Polynyas dominate the regional heat budget in winter through intense heat exchanges (Smith et al., 1990)
- Sites of early melt of the pack ice in spring/early summer (Martin et al., 2007), allowing high biological primary productivity (Arrigo, 2002)

In the Arctic, most of the polynyas are shelf water polynyas except the Kashevarov Bank polynya in the Okhotsk Sea with (Figure 7(A)) which is the only purely deep water polynya from the northern hemisphere (Martin, 2001). While ice-bridge, land-bridge or strait can play important role in the formation of polynyas in the northern hemisphere, other "icescape" features are implicated in Antarctic polynyas formation such as coastal promontories, icebergs and glacier tongues (Barber and Massom, 2007).

The total average wintertime circum-Antarctic polynya area estimated by Kern et al. (2009) represents about 1.5% of the mean Antarctic sea ice area (Parkinson and Cavalieri, 2012). The contribution of the East Antarctic coastal polynyas to this total area is about 40% and together the Weddell and Ross Seas contribute to another 30% (Parkinson and Cavalieri, 2012). Only three deep-water polynyas occur(ed) in Antarctica (Figure 7(B)) - the eastern Weddell Sea polynya (originally centered on the Greenwich meridian and 66°S) and the Maud Rise polynya (at approximately 65°S, 2°E) observed during the winters of 1974–1976 and the Cosmonaut Sea polynya that forms annually at approximately 65°S and 45°E (Barber and Massom, 2007). Most of Antarctic polynyas are coastal or shelf water polynyas and mechanically driven, therefore falling in the latent-heat type (Massom et al., 1998). Their formation is currently associated to katabatic winds as at least 18 of the 28 East Antarctic polynyas are located at outlet confluence zones of these winds (Barber and Massom, 2007). Katabatic winds are observed when cold denser air generated by intense radiative cooling of air masses above the inland ice-sheet plateau descends the slopes of the Antarctic continent (Ball, 1956; Tauber, 1960). Katabatic winds are channeled by local topography (glacier valleys, ice shelves), attain high wind speeds exceeding 50 m s^{-1} (Parish and Bromwich, 1989) and blow the newly-formed ice offshore.

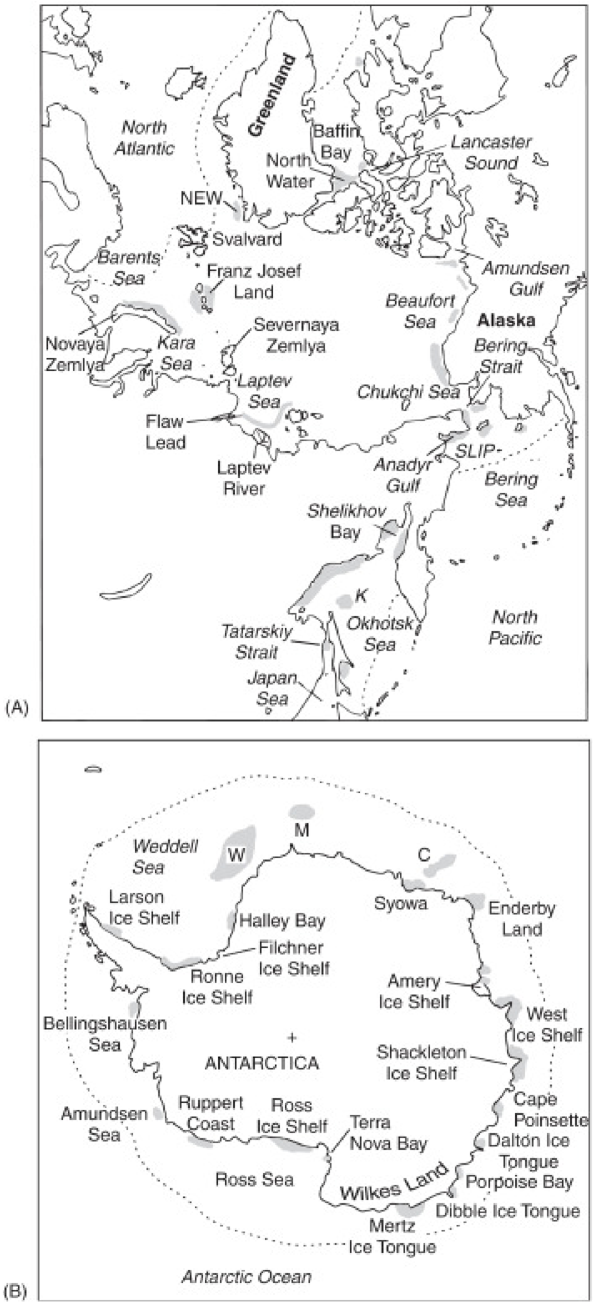

Figure 7: Location of (A) the Arctic polynyas (SLIP is the St. Lawrence Island Polynya, NEW is the North-east Water, and K is the Kashevarov Bank polynya) and (B) the Antarctic polynyas (W is the Weddell polynya, M is the Maud Rise polynya and C is the Cosmonaut Sea polynya). Dashed lines indicate the maximum ice edge. Figure from Martin (2001).

In this work, we will mainly focus on two Antarctic shelf water polynyas located in the Ross Sea: the Terra Nova Bay and Ross Sea polynyas. The Terra Nova Bay Polynya in the western Ross Sea, which extends for 3000 km^2, is maintained by strong offshore winds removing ice more rapidly than it forms (Smith et al., 1990; Smith et al., 2012). Katabatic winds principally drain into Terra Nova Bay through the Reeves Glacier valley (Figure 8) (Bromwich and Kurtz, 1984). Furthermore, the Drygalski Ice Tongue blocks the westward currents preventing ice advection into the polynya (Smith et al., 1990) and maintaining this ice free area. The Ross Sea Polynya, adjacent to the Ross Ice Shelf, is giant ($\sim$20,000 km^2 in winter) and the most active around Antarctica, producing 390 km^3 of ice per year (Smith et al., 2012). In comparison, Terra Nova Bay Polynya generates 59.2 km^3 of ice per year (Martin et al., 2007). The formation of the Ross Sea polynya is influenced both by katabatic and synoptic winds (Bromwich et al., 1998; Jacobs and Comiso, 1989) and by upwelling of warm Circumpolar Deep Water onto the continental shelf which induces sea ice melt (Jacobs and Comiso, 1989). Both of these polynyas in the Ross Sea are important sites of High Salinity Shelf Water (HSSW) formation due to brine plumes rejected during ice formation in winter (Budillon and Spezie, 2000). HSSW eventually evolves into other water masses, e.g. Ice Shelf Water (ISW) and Antarctic Bottom Water (AABW) (Morales Maqueda et al., 2004).

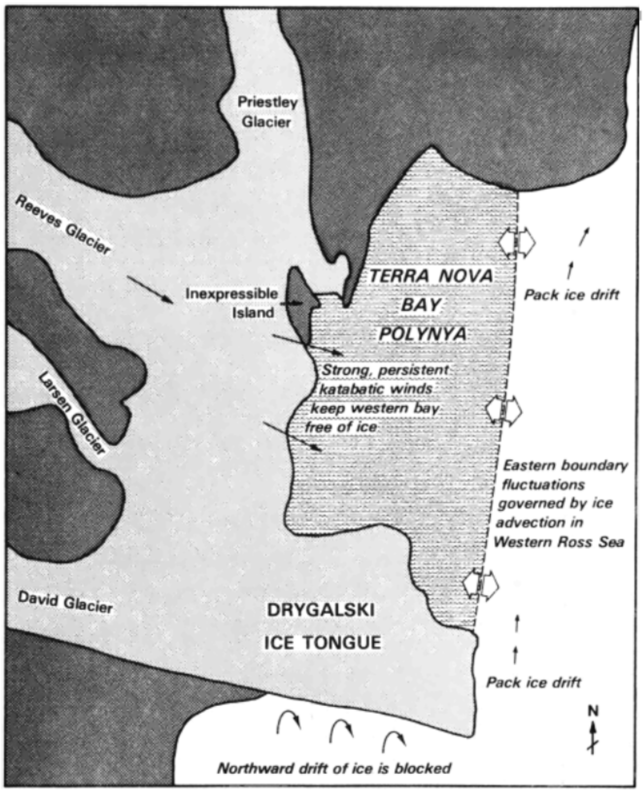

Figure 8: Schematic illustration from Bromwich & Kurtz (1998) showing the mechanisms maintaining the ice free area in Terra Nova Bay.

II.3. Carbon marine cycle

II.3.1. Inorganic carbon chemistry

The concentration of CO_2 in surface seawater is given by Henry's law. It states that the concentration of dissolved CO_2 in solution ($[CO_2(aq)]$) is proportional to the partial pressure of CO_2 (pCO_2) above the solution:

$$[CO_2(aq)] = K_0 \cdot pCO_2 \tag{1}$$

Where K_0 is the CO_2 solubility ($mol\,kg^{-1}\,atm^{-1}$) which depends on temperature, pressure and salinity in seawater. CO_2 not only dissolves in seawater but it also reacts with water to form free protons and the conjugate bases bicarbonate and carbonate. In details, gaseous carbon dioxide entering the surface ocean gets first hydrated to form aqueous CO_2 ($CO_2(aq)$) which reacts with water to form carbonic acid (H_2CO_3). These two species are difficult to separate and are usually combined under the hypothetical species, CO_2* or H_2CO_3* (Dickson and Goyet, 1994). To simplify, we will term it H_2CO_3 from now onwards. The latter dissociates into bicarbonate (HCO_3^-) and carbonate (CO_3^{2-}) ions. These reactions are really fast and the thermodynamic equilibrium is established between all species as described in the following reactions:

$$CO_2(aq) + H_2O \longleftrightarrow H_2CO_3 \tag{2}$$

$$H_2CO_3 \xleftrightarrow{K_1} H^+ + HCO_3^- \tag{3}$$

$$HCO_3^- \xleftrightarrow{K_2} H^+ + CO_3^{2-} \tag{4}$$

Where K_1 and K_2 are the thermodynamic equilibrium constants of the carbonate system and are related to the ions concentrations, so that:

$$K_1 = \frac{[H^+][HCO_3^-]}{[H_2CO_3]} \tag{5}$$

$$K_2 = \frac{[H^+][CO_3^{2-}]}{[HCO_3^-]} \tag{6}$$

The relative concentrations of each species is governed by the pH ($-\log_{10}[H^+]$) of the solution as depicted by the Bjerrum plot (Figure 9). Since the mean surface pH of the ocean is slightly above 8, the dominant dissolved species is HCO_3^-, the second dominant species is CO_3^{2-} and dissolved CO_2 is only present in small concentrations.

In Antarctic surface waters in equilibrium with today's atmosphere (S = 34, T = 5°C, DIC = 2100 μmol kg^{-1}, pCO$_2$ = 410 ppm), concentrations of CO$_2$, HCO$_3^-$ and CO$_3^{2-}$ account for 1.02%, 94.2% and 4.8%, respectively.

The sum of the dissolved forms is known as dissolved inorganic carbon (DIC):

$$DIC = [H_2CO_3] + [HCO_3^-] + [CO_3^{2-}] \tag{7}$$

DIC is usually expressed in μmol kg^{-1} of seawater. The total alkalinity (TA), formally defined by Dickson (1981), is a measure of the excess of bases (proton acceptors) over acids (proton donors) and is defined as:

$$TA = [HCO_3^-] + 2[CO_3^{2-}] + [OH^-] - [H^+] + [B(OH)_4^-] + minorbases \tag{8}$$

TA in marine waters is dominated by the carbonate species, usually accounting for >95% of the alkalinity, with borate contributing another ~3-4% (Middelburg, 2019).

Many processes affect the carbonate system and the concentration of DIC and TA. While DIC is affected by both air-sea CO$_2$ exchanges and by biological processes, TA is only affected by biological processes (Figure 10).
Air-sea CO$_2$ exchanges. Any uptake of atmospheric CO$_2$ by seawater causes an increase in DIC and pCO$_2$, a decrease in pH but does not change TA. On the contrary, an efflux of CO$_2$ from seawater to the atmosphere, results in a decrease of both DIC and pCO$_2$ and an increase in pH. These CO$_2$ exchanges may be initiated either by changing atmospheric mixing ratios of CO$_2$ or by cooling or warming of seawater.
CaCO$_3$ precipitation leads to both DIC and TA decrease. The chemical reaction of CaCO$_3$ formation-dissolution is:

$$Ca^{2+} + 2HCO_3^- \longleftrightarrow CaCO_3(s) + H_2O + CO_2(aq) \tag{9}$$

So that, the precipitation of one mole of CaCO$_3$ lowers DIC by one mole and TA by two moles, with the result that pCO$_2$ increases and pH declines. Dissolution of calcium carbonate results in the increase of DIC by one mole and TA by two moles and a decrease in pCO$_2$ and an increase in pH.
Primary production involves the fixation of inorganic carbon and the assimilation of inorganic nutrients (nitrate and phosphorous) to produce organic matter. Primary production based on nitrate is described by the following stoichiometric formula from Redfield et al.

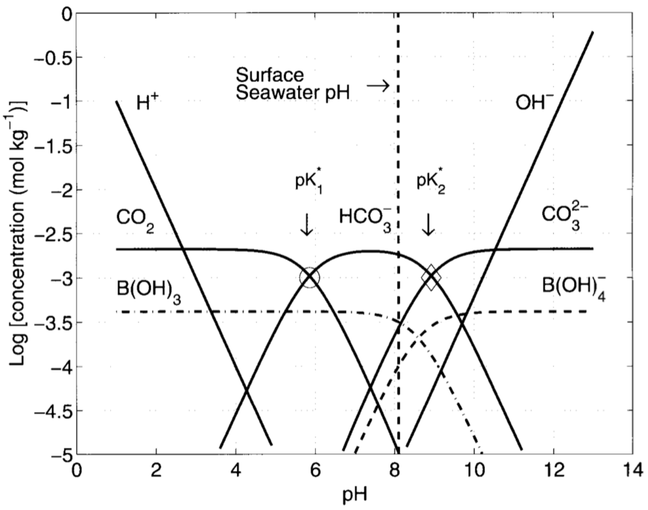

Figure 9: Bjerrum plot from Zeebe and Wolf (2001) showing the concentrations of CO_2, HCO_3^-, and CO_3^{2-} as functions of pH=-$\log_{10}[H^+]$. The concentrations are plotted for a DIC concentration of 2100 μmol kg^{-1}, S = 35 and T = 25°C.

(1963):

$$106CO_2 + 16NO_3^- + H_2PO_4^- + 17H^+ + 122H_2O \longrightarrow (CH_2O)_{106}(NH_3)_{16}(H_3PO_4) + 138O_2 \quad (10)$$

The stoichiometric ratios C:N:P of 106:16:1 are termed Redfield ratios. Photosynthesis lowers DIC due to the consumption of inorganic carbon and slightly increases TA. Indeed, for each mol of inorganic nutrient consumed (NO_3^- or $H_2PO_4^-$), one mol of H^+ is consumed to maintain electroneutrality, decreasing the concentrations of free protons and therefore increasing TA. The reverse process of aerobic respiration/remineralization leads to an increase in DIC and a decrease in TA.

II.3.2. Ocean carbon pumps

DIC is removed or exported from the ocean surface layers through the solubility pump, the biological pump and the carbonate pump presented in Figure 11. As mentioned by Legendre et al. (2015), the three pumps include both

- the downward export of carbon from the surface ocean (i.e. to the deepest part of either the euphotic zone or the seasonal surface mixed layer), indicated as carbon export in Figure 11
- the downward transfer of this exported carbon below the maximum depth of the pycnocline ($\sim$ 1000 m)

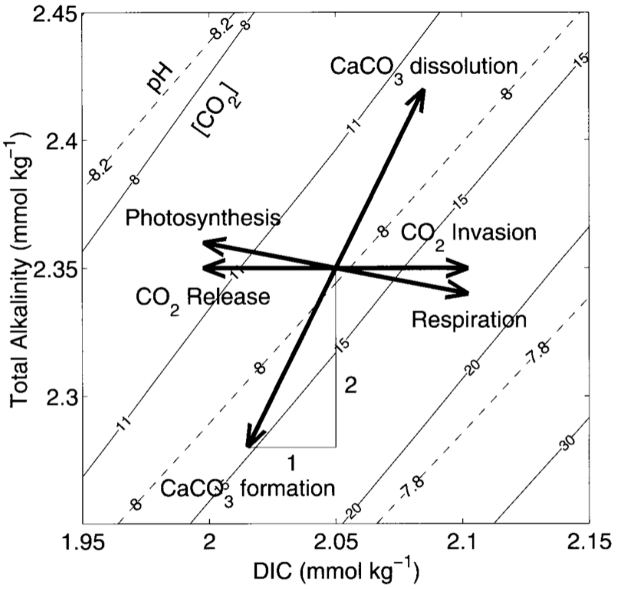

Figure 10: Processes affecting DIC and TA according to Zeebe and Wolf (2001).

The solubility pump refers the dissolution of atmospheric CO_2 in surface waters followed by the sinking of CO_2 (as DIC) enriched surface layer to depth.

In the literature, the so-called "biological carbon pump" (BCP) refers to either the organic component of the ocean carbon pump only, or both the organic and $CaCO_3$ components. In this work, BCP refers only to the organic component, consistent with the definition of IPCC (2013). The BCP is driven by the fixation of inorganic carbon into organic matter through photosynthesis by biota and the export of this organic carbon (POC plus DOC) to depth by sinking plankton material (as dead organisms and particles) (Vancoppenolle et al., 2013b).

The carbonate pump refers to the formation of calcium carbonate ($CaCO_3$) by shell- and skeleton-building marine microorganisms (Heinze et al., 2015) and subsequent release of CO_2 (Sigman et al., 2010) as shown in (Eq. 9).

As pointed out in Figure 11, most of the carbon sinking particles is respired by bacteria in the surface and intermediate layers (within the upper 1500 m, Heinze et al. (2015)) and is eventually recirculated to the surface as DIC. Only around 25% of the Particulate Organic Carbon (POC) produced in the ocean surface layer sinks through the water column (Schlitzer, 2000). The carbonate pump counteracts the organic carbon pump but more carbon is bound to POC and DOC during biological production than released during $CaCO_3$ formation (Heinze et al., 2015). Thus, the carbonate pump compensates only partially the organic carbon pump (Heinze et al., 2015).

Thanks to these three carbon pumps, a vertical gradient in CO_2 (as DIC) between the surface and the deeper layers of the ocean is maintained (IPCC, 2007). These pumps regulate as well the air-sea CO_2 exchanges (IPCC, 2007). The strength of the solubility pump depends globally on the strength of the Meridional Overturning Circulation[1], surface ocean temperature, salinity, stratification and ice cover (IPCC, 2007). The efficiency of the biological pump depends on the export of organic matter from the ocean surface, the nutrient supply, light availability, changes in ocean circulation and plankton community composition and physiology (IPCC, 2007; Sarmiento and Gruber, 2006).

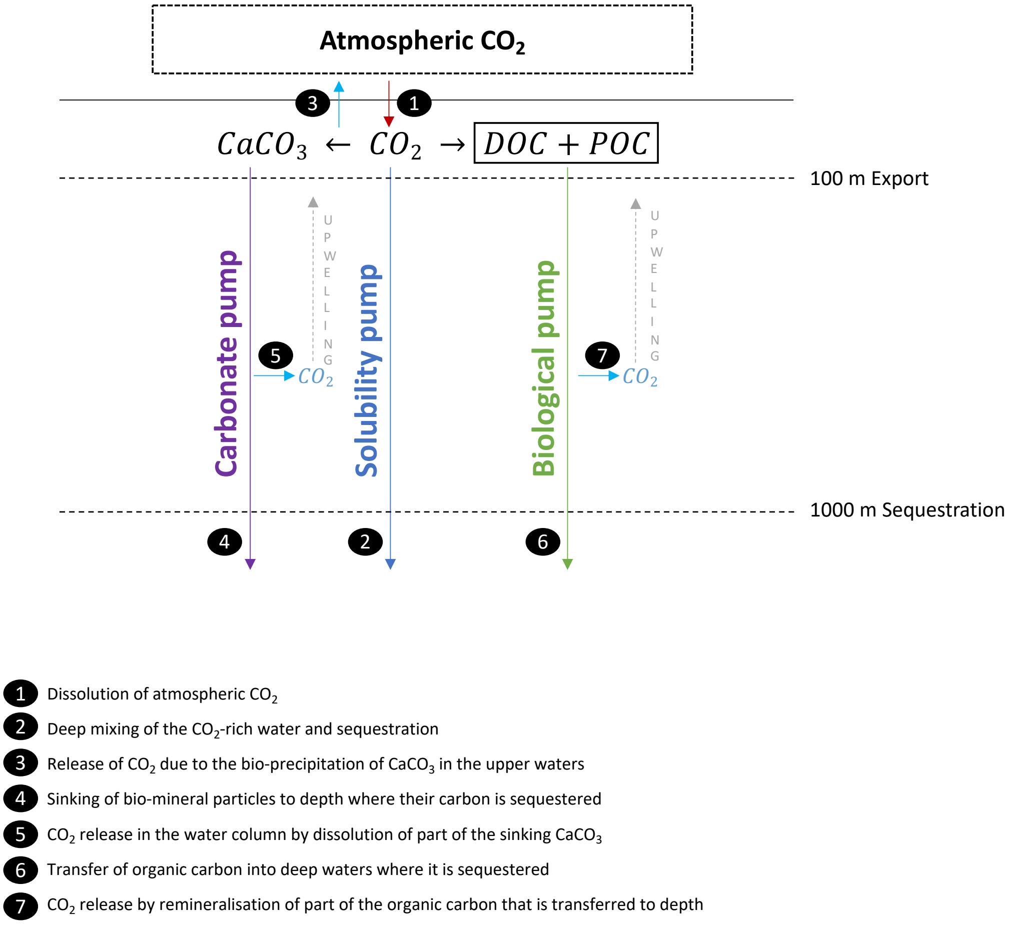

Figure 11: Three main ocean carbon pumps: the solubility pump, the biological carbon pump and the carbonate pump. Figure adapted from Legendre et al. (2015).

---

[1] The global Meridional Overturning Circulation consists primarily of dense waters sinking to the abyssal ocean at high latitudes in the North Atlantic Ocean and near Antarctica (IPCC, 2007).

II.4. Role of sea ice in the marine carbon cycle

II.4.1. Sea ice carbon processes

Three different sea ice carbon pumps can be distinguished. The first one is related to the physical–chemical dynamics of brines (a), the second to the the primary production (b) and the third one to carbonate precipitation within sea ice (c).

(a) During sea ice growth, dissolved salts, DIC, CO_2 as well as other gases are expelled from the ice matrix and concentrated in brines. Along with the sea ice formation, brine rejection occurs through brine drainage and DIC is rejected in the underlying water. When surface waters enriched in DIC and TA are exported downward and sink to depth, it provides a pathway for carbon sequestration.

(b) Primary production within sea ice by sympagic algae communities contributes to CO_2 drawdown. Primary production lowers DIC due to the consumption of inorganic carbon and slightly increases TA.

(c) Precipitation of calcium carbonate as ikaite, a metastable hydrated $CaCO_3$ mineral ($CaCO_3 \cdot 6H_2O$), has been observed both in Antarctic and Arctic sea ice (Dieckmann et al., 2010; Dieckmann et al., 2008; Geilfus et al., 2013; Rysgaard et al., 2007; Rysgaard et al., 2013). Carbonate precipitation produced CO_2. If the precipitation occurs at the bottom of sea ice, the ikaite crystals can be trapped within the skeletal layer while CO_2 is expelled to underlying waters and entrained to depth. The dissolution of the ikaite crystals in sea ice in spring and summer will drive CO_2 uptake. Sea ice is in that specific case a CO_2 sink for the atmosphere as suggested by Rysgaard et al. (2007; 2013). Most of the studies published so far derived a relative atmospheric CO_2 uptake based on that scenario. However, several other scenarios are possible as discussed in Delille et al. (2014).

II.4.2. Estimates of the sea ice carbon processes

Delille et al. (2014) estimated that the contribution of primary production to spring and summer sea ice pCO_2 changes and CO_2 uptake was lower than the contribution of other processes (brine dilution and ikaite dissolution). The authors reported that primary production represents only 45% of the contribution of each other process but still contributes to 18% of the total atmospheric CO_2 uptake. Delille et al. (2007) observed similar trends. Søgaard et al. (2013) estimated that only 4% of the sea-ice-driven CO_2

uptake could be explained by the net biological production and that the DIC depletion in sea ice was mainly controlled by brine drainage and $CaCO_3$ precipitation. A recent 1D modeling study in the Arctic of Mortenson et al. (2018) suggested that sympagic biological activity accounts for 1% of the net ocean carbon uptake.

Rysgaard et al. (2011) used a box model to discuss the importance of sea ice as a carbonate pump. Taking into account the sea ice DIC and TA, they derived the changes of pCO_2 in ocean surface waters during ice melting and the related uptake of atmospheric CO_2 over the Southern Ocean estimated at -0.019 and -0.052 $\mathrm{Pg\,C\,yr^{-1}}$, considering respectively the absence of $CaCO_3$ formation or occurrence of $CaCO_3$ formation in sea ice. Since no TA and DIC data for Antarctic sea ice were available at that time, the authors estimated the Antarctic sea ice DIC and TA based on the values observed in Arctic sea ice, following a conservative behaviour to salinity. They hypothesized that:

- Carbonate precipitation occurs at the bottom, in the skeletal layer
- CO_2 is released to the underlying waters and entrained to deeper layers
- $CaCO_3$ crystals are trapped within sea ice
- All DIC-rich brine would sink to depth

Delille et al. (2014) focused on the dependency of sea ice temperature on brines pCO_2, measuring brines pCO_2 in Antarctic pack ice and related CO_2 fluxes. They used the temperature field from the model NEMO-LIM3 large-scale sea ice-ocean to upscale their observations to the whole Antarctic sea ice cover and estimated that the Southern Ocean was a net sink of 0.029 Pg C over the spring and summer. This result falls within the estimates of Rysgaard et al.(2011) but considered only the warming/melting season. Delille et al. (2014) based also their estimation on DIC depletion in sea ice.

In a model study, Moreau et al. (2016) estimated that several hundred $\mathrm{Tg\,C\,yr^{-1}}$ (266/204 $\mathrm{Tg\,C\,yr^{-1}}$ in the surface Arctic/Southern Oceans) were released to the surface ocean due to DIC rejection during sea ice growth but suggested that only 1.4% of the DIC rejected during sea ice growth is exported to the deep Arctic Ocean, and only about 2% to the deep Southern Ocean. This leads to a notable but weak redistribution of DIC towards deep polar basins. Moreau et al. (2016) explained this weak redistribution by:

- The growth of sea ice develops not only where deep water forms,
- The dilution of deep water properties on their way downwards

- The resupply of some of the deep carbon to the surface due to exchanges between the deep ocean and the surface

Furthermore, Moreau et al. (2016) suggested a weak impact of active carbon processes (mainly $CaCO_3$ precipitation) on the net ocean-atmosphere CO_2 exchanges, estimated at a few $\mathrm{Tg\,C\,yr^{-1}}$ in the sea ice zone. Similarly, the model study of Grimm et al. (2016) showed that the CO_2 uptake in sea ice covered areas ranges from 2 to 14 $\mathrm{Tg\,C\,yr^{-1}}$, which accounts for up to 7% of the simulated net CO_2 uptake in polar regions, but only 1% of the current global oceanic CO_2 uptake (Grimm et al., 2016). Both of these studies concluded that the sea ice carbon pump plays a minor role in the global carbon cycle but is important for the regional carbon cycle in polar regions.

In a recent modeling study, Mortenson et al. (2018) used a 1-D model including air-ice fluxes, ice algae growth, ikaite precipitation and dissolution and brine rejection/dilution of DIC and TA during ice growth/melt. The results indicate that ikaite precipitation within sea ice, and subsequent dissolution in the water column during ice melt, induces a small change in the net ocean carbon uptake estimated at $\sim$ 1% for ikaite concentrations of $\sim 54\ \mu\mathrm{mol\,kg^{-1}}$ based on Geilfus et al. (2016). However, the authors pointed out that the net ocean carbon uptake could become important for larger ikaite concentrations, as observed by Rysgaard et al. (2013) with a range of 900 $\mu\mathrm{mol\,kg^{-1}}$ in the upper ice to 100 $\mu\mathrm{mol\,kg^{-1}}$ at the sea ice bottom in Greenland or by Fischer et al. (2013) in Antarctic landfast ice (Table 1). Furthermore, in terms of gas exchanges, the parameterization includes the carbon release during ice growth and the uptake of atmospheric CO_2 during ice melt to match current observations. This results in a net air-to-ice uptake of 50 $\mathrm{mmol\,m^{-2}}$ over the length of the standard run, representing 5% of the net ocean carbon uptake during the open-water season (Mortenson et al., 2018). They acknowledged that the exchanges of carbon between the ice and the atmosphere during growth and melt were not well constrained, due to the lack of direct measurements of ice-air and ice-water CO_2 fluxes and the differences between measurements techniques (chamber vs eddy-covariance). However, the proportions of the carbon released to both the ocean and the atmosphere are essential to estimate the net uptake of atmospheric carbon by the ice-ocean system. Any increase in the CO_2 release during ice growth or in the uptake during ice melt will induce a change in the net uptake by the ice-ocean system.

II.4.3. Calcium carbonate precipitation in sea ice

For a long time, only indirect evidences of calcium carbonate precipitation were suggested, e.g to explain high pCO_2 observed in spring below sea ice in Young Sound and

Franklin Bay, Arctic (Rysgaard et al., 2007) or to explain the TA changes in Antarctic fast ice in spring (Delille et al., 2007). For the first time, Dieckmann et al. (2008) observed calcium carbonate precipitation as ikaite ($CaCO_3 \cdot 6H_2O$) crystals in Antarctic sea ice and a bit later in the Arctic (Dieckmann et al., 2010).

Since then, several others studies focused on ikaite crystals observation and distribution within Arctic sea ice. Rysgaard et al. (2012) performed microscopic examinations and x-ray diffraction analysis of single crystals and observed ikaite crystals throughout the sea ice during summer in Arctic (Fram Strait). They found larger crystals in the upper ice layers. Rysgaard et al. (2013) used a stereomicroscope and found that ikaite crystals concentrations decreased with depth in land fast ice and a polynya region from Young Sound (Greenland) in early spring (18-24 March). Accordingly, Rysgaard et al. (2014) observed that ikaite concentrations in artificial sea ice decreased with depth. In the same study, the modeled concentrations with FREZCHEM (Marion et al., 2010) suggested that ikaite concentration in the brines in general increases with decreasing temperatures. Another study performed during the same experiment reports ikaite concentration of up to 167 μmol kg^{-1} based on TA and DIC analyses (Geilfus et al., 2016), which is in the same range as the estimates of Rysgaard et al. (2014). In spring at Barrow, Geilfus et al (2013) found ikaite crystals in frost flowers (FF) and at all depths in young sea ice using Raman spectroscopy and X-ray analysis. The maximal amount of ikaite precipitated was observed in FF (around 25 μmol kg^{-1}) and at the surface, probably favoured by the expulsion of salty supersaturated brine. However, the authors concluded that the amount of CO_2 generated by precipitation was minor compared to the total flux estimated by DIC depletion.

Nomura et al. (2013a) observed ikaite crystals in Svalbard using a Raman microscope and quantified the ikaite content with a relationship between TA and salinity. Ikaite crystals were mainly observed in the bottom of the snowpack, in slush and the surface layers of the sea ice where the temperature was generally lower and salinity higher than in other layers.

In Antarctica, few studies reported ikaite precipitation. In addition to the observations of Dieckmann et al. (2008), Fischer et al. (2013), using micro X-ray diffraction to identify the mineral and spectrometry to quantify the calcium ions, observed the same pattern as in the Arctic, i.e. maximum ikaïte concentrations found mostly in the uppermost layers of sea ice.

All the studies reported in the Table 1 addressed ikaite precipitation during spring or summer with sea ice temperature above -14.2°C.

Table 1: Observations and quantification of calcium carbonate precipitation in the Arctic and Southern Oceans (FF is used for frost flowers, SI for sea ice, MY for multi-year).

Location	Season	Ice type	Ice depth (cm)	T (°C)	Snow depth (cm)	$CaCO_3$ concentration (μmol kg^{-1})	Method	Reference
Southern Ocean								
Weddell Sea	Spring	Nilas MY ice	25-225			0 to 103	Weighed mineral mass	Dieckmann et al. (2008)
Adélie Land, East Antacrtica	Spring	Top 5 cm of young landfast ice	~15	-5.5 to -2.6	~0	25-550	Ca^{2+} quantity by spectrometry	Fischer et al. (2013)
		Landfast ice	~60		~0	0-26		
East Antarctica	Late Winter - Early summer	Pack ice	49-133	-11.7 to -4 at the top	N/A	1-52	Ca^{2+} quantity by spectrometry	Fischer et al. (2013)
Arctic Ocean								
Fram Strait	Summer (June)	Pack ice	50–100	-1.7 to 0		162–241.5	From TA and DIC	Rysgaard et al. (2012)
Greenland	Early spring (18-24 March)	Landfast ice	110-115	-10 to -2	70	100–900	Microscopic images analyses	Rysgaard et al. (2013)
		Polynya	30	-5 to -2	17	200–700		
Barrow	Spring (April)	Landfast ice	20	-14.2 to -2		FF: 25 SI: 15-19	TAb - TAf	Geilfus et al. (2013)
Svalbard	Spring	Pack ice (1st year)	31–125	-4.2 to -0.8	1–39	30–60 at the surface	TA and salinity	Nomura et al. (2013a)
Canada	Growth and melt	Artificial sea ice	0–24	-7 to -2		1–167	From TA and DIC	Geilfus et al. (2016)
						<100 at the bottom	Microscopic obs.	Rysgaard et al. (2014)

II.4.4. Sea ice-atmosphere gas exchanges

II.4.4.1. pCO_2 dynamics

While observations of direct air-ice CO_2 fluxes have been repeatedly reported, most of the previous studies have not included those direct flux measurements. To estimate the CO_2 fluxes between two reservoirs, the partial pressure of CO_2 (pCO_2) is a useful parameter. The pCO_2 of a seawater sample refers to the partial pressure of gaseous CO_2 that is in equilibrium with that seawater. The pCO_2 is one of the the fourth carbonate system parameters (in addition to DIC, TA, pH) that can be determined analytically and once it is determined, the use of Henry's law (Eq. 1) allows to calculate the concentrations of dissolved CO_2. The difference in pCO_2 between two reservoirs, such as seawater (or sea ice) and the overlying air, can also be used to derive the air-sea (ice) CO_2 fluxes.

The brine pCO_2 at the top of sea ice is therefore a key parameter driving ice-atmosphere carbon exchanges (Moreau et al., 2015). Surface brine pCO_2 depends on several physical (brine concentration-dilution, permeability, bubbles formation), chemical (ikaite precipitation/dissolution), and biological processes (photosynthesis, respiration) as shown on the Figure 12. During the winter ice growth, brine contraction due to cooling results in the concentration of salts, CO_2 and other gases as well as brine rejection and upward transport. Higher CO_2 brine concentration can lead to CO_2 release to the atmosphere (Geilfus et al., 2016; Nomura et al., 2018), if the gas permeability allows it. The low temperatures and high brine salinities conditions in sea ice may further promote the precipitation of ikaite (Dieckmann et al., 2010; Dieckmann et al., 2008; Rysgaard et al., 2012; Rysgaard et al., 2013) which also induces an increase in CO_2 brine concentration. However, the timing, conditions and net efficiency of carbonate precipitation in natural sea ice are still debated.

During the warming period, the brine pCO_2 decreases below air saturation and atmospheric CO_2 uptake by sea ice takes place (Delille et al., 2014; Geilfus et al., 2013, 2012a; Nomura et al., 2010a) as a consequence of ice melting and subsequent brine dilution, increase in sea ice permeability, net inorganic carbon uptake by ice algae (Arrigo, 2017) and the dissolution of ikaite (Rysgaard et al., 2011).

II.4.4.2. Permeability

Permeability controls gas transport in sea ice, including gas fluxes at the ice-atmosphere interface. It has been suggested repeatedly that ice-air CO_2 fluxes are impeded when the

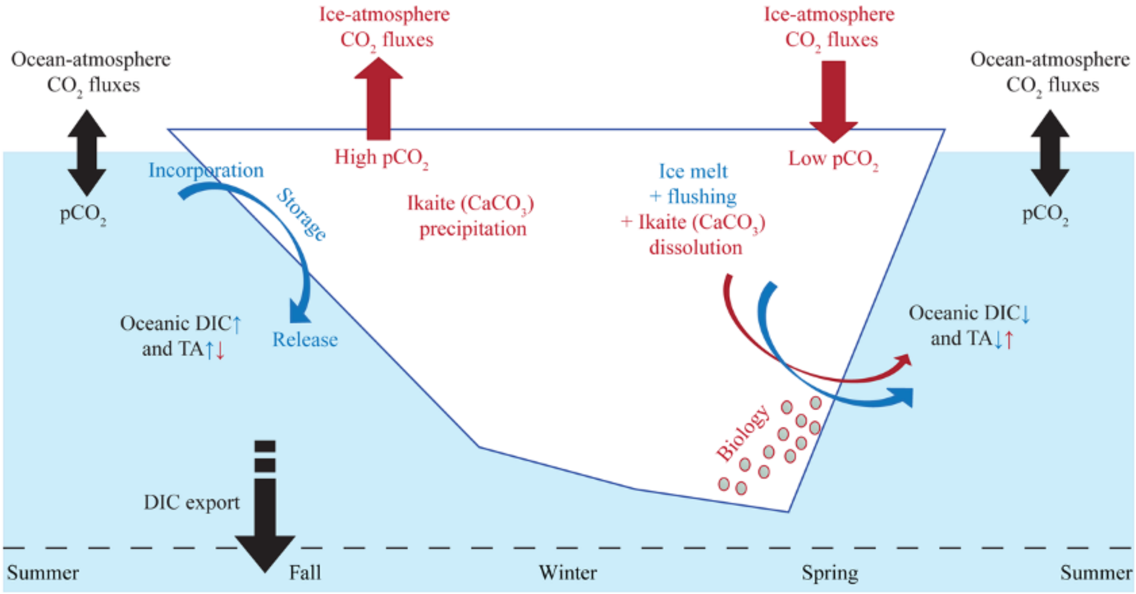

Figure 12: Scheme from Moreau et al. (2015) presenting the seasonal inorganic carbon dynamics in first year landfast sea ice. Physical processes (ice growth/decay, incorporation of DIC and TA) appear in blue and active carbon processes ($CaCO_3$ precipitation/dissolution, CO_2 exchanges and net community production) are presented in red.

ice is impermeable, mainly during ice growth (e.g. Delille et al. (2014), Tison et al. (2016)). When the sea ice starts to warm up, the permeability increases and allows larger CO_2 fluxes. The brine volume of sea ice controls its permeability. Sea ice is considered impermeable to fluid transport for brine volume fractions below 5% (Golden et al., 1998). The ∼5% of brine volume fraction corresponds to a bulk ice salinity of 5 and temperature of –5°C, the so-called rule of fives (Golden et al., 1998b). Above this threshold, brine pockets coalesce and brine channels are connected to each other and sea ice with a columnar structure becomes permeable for fluid transport. Until now, a first-order estimate of the gas permeability range was based on the one for liquids (i.e. BrV≥5%). However, it remains unclear whether this threshold for liquids should be transposed for gas exchanges. The gas permeability threshold has been assessed between 6.1% and 7.9% in young artificial sea ice (Loose et al., 2010), between 7.5% and 10% according to field observations (Zhou et al., 2013) and around 10% in the model study of Moreau et al. (2014).

In sea ice, gases are either dissolved in brines or exists as air bubbles in brine inclusions or trapped within the ice matrix. In the absence of brine convection, the main pathway to transport dissolved gas is the diffusion, which is driven by dissolved gas gradients (Delille et al., 2007; Miller et al., 2011). An alternative gas transport pathway is via gas bubbles. Bubbles nucleation takes place at the onset of sea ice growth when air inclusions are trapped within the ice matrix and further develop when gases are concentrated in brines during ice growth as suggested by Crabeck et al. (2014a; 2016) and Zhou et al. (2014). Gas bubbles can further reach the ice surface by buoyancy when the brine network is connected with a brine volume above a given threshold. Both model and experimental studies suggested gas bubbles nucleation and/or upward migration. Zhou et al. (2013) showed that during ice growth, a portion of the dissolved gas in the brines appeared to transfer to gas bubbles as indicated by the total Ar super-saturation levels observed. A model study of Moreau et al. (2014) suggested an intense and rapid release of Argon gas bubbles to the atmosphere in spring. Kotovitch et al. (2016) showed that the magnitude of the ice-air CO_2 fluxes observed in a controlled experiment with artificial ice can only be reproduced with their model by adding an intense gas bubbles formation and escape pathway to the atmosphere.

It appears that permeability is not the only factor controlling gas transport. Both diffusion processes and gas bubbles migration depend on the tortuosity of brine channels. As observed by Loose et al. (2010), bubble inclusions can be entirely sealed off from the brine network or present “dead-ends”. Gas bubbles can therefore get stuck within the porous microstructure of the ice and/or slow down on their way to the atmosphere as suggested by Moreau et al. (2014) and Kotovitch et al. (2016), still neglecting this effect of tortuosity on gas bubble rise in their models.

In line with the impact of tortuosity, it has also been suggested that the permeability threshold for fluid transport varies with ice texture. For example, the threshold for granular ice may be higher than the permeability of columnar ice at a given porosity (Golden et al., 1998). This could be explained by the less aligned structure and distribution of brine pockets and channels in granular ice (Meiners and Michel, 2016) which is formed by frazil accumulation and exhibits randomly oriented crystals. The permeability thresholds for gas transport potentially depend also on the ice texture.

II.4.4.3. Conditions at the air-ice interface

Ice-atmosphere CO_2 exchanges are moreover strongly affected by the conditions at the interface, i.e. the ice type (superimposed ice[2], snow ice[3], the presence or absence of snow cover and the ice and snow chemical and physical properties. CO_2 fluxes may be impeded due to deep snow, especially if superimposed ice is forming (Delille et al., 2014; Geilfus et al., 2012a; Nomura et al., 2010b; Zemmelink et al., 2006). Snow salinity, wetness, density, grain sizes among others are likely to affect the magnitude and direction of CO_2 fluxes (Delille et al., 2014; Nomura et al., 2018; Nomura et al., 2010b). Brine-wetted snow is a multiphase reactor hosting specific physical and chemical processes that may influence

---

[2] A fresh ice layer formed from snow meltwater.

[3] Snow ice is formed when seawater that floods the bottom of the snow pack freezes. Flooding occurs due to the depression of the ice surface below sea level under snow loading.

CO_2 fluxes: uptake and migration of trace gas, diffusion, and sources and sinks processes (Bartels-Rausch et al., 2014). While the impact of fresh snow cover on gas fluxes has been documented for terrestrial environments (Brooks et al., 2005; Takagi et al., 2005), the role of the snow on sea ice is still overlooked.

II.4.4.4. Measurements of air-ice CO_2 fluxes

Over the last several decades the two main field measurement techniques used to measure ice-air CO_2 exchanges were the chamber technique and the eddy-covariance (EC) technique. Within the chamber temporally closed over the sea ice or the snow, the change in gas concentration over time is measured. The EC technique is based on the measurement of vertical wind speed and gas concentration at high frequencies. The covariance between changes in vertical wind and changes in the gas concentration, averaged over a period of time, gives the flux (Butterworth and Else, 2018). As pointed out by Butterworth and Else (2018), the shortcoming of the chamber technique is the alteration of the surface enclosed in the chamber and the potential changes in temperature, radiation, pressure gradients, wind speed and turbulence. However, to deal with the pressure gradient, a mobile cap to vent the chamber is added and allow to maintain an ambient pressure inside the chamber. The chamber can also be moved between each measurement to limit the alteration of the surface. The fluxes measurements are spatially and temporally limited but allow to capture only the fluxes occurring above sea ice while the EC technique allows to cover a broad area but may include open water areas, ice cracks and flow originated from land.

The EC technique would allow long term measurements but other problems are encountered. A fixed tower with the EC system allows to avoid the motion contamination associated with ship-based EC. Two places are possible for the deployment of the tower:

- On sea ice, allowing to capture the autumn to spring fluxes but not summer fluxes if sea ice melts
- On the land, but then a large part of the flow originated from land and other flow distortion can occur with reliefs. Many corrections are required.

Until recently, these techniques gave large differences in the estimated fluxes. Ice-air CO_2 fluxes measured with the chamber technique over bare sea ice ranged from -5.4 (negative flux indicates CO_2 uptake by sea ice) to $+9.9\ \mathrm{mmol\,m^{-2}\,d^{-1}}$ (positive flux signifies gas release from the sea ice to the atmosphere; Table 2). Much higher CO_2 fluxes were derived from EC technique and estimated to range from -259 to 295 $\mathrm{mmol\,m^{-2}\,d^{-1}}$ (Butterworth and Else (2018) and references therein). Butterworth and Else (2018) addressed the shortcomings of these previous EC systems with water vapor issues associated with the use of open-path infrared gas analyzer (IRGAs). They used a closed-path IRGA with a dried sample airstream. This new EC system relies on techniques to dry the air samples such as a cold trap or a moisture exchanger (Nafion) and requires maintenance for the replacement of this desiccant. The authors showed that the dried, closed-path EC system greatly reduces the magnitude of measured CO_2 fluxes compared to the open-path EC system, therefore matching with chamber flux measurements over sea ice. The CO_2 fluxes measured with the dried, closed-path EC system during the spring season prior to ice breakup in Cambridge Bay, Nunavut, revealed a mean value of -0.25±1.75 $\mathrm{mmol\,m^{-2}\,d^{-1}}$. This falls within the range measured by the chamber technique (Table 2).

Table 2: Overview of CO_2 fluxes measurements using the chamber technique. Positive fluxes indicate gas release, negative fluxes indicate gas uptake.

Location	Ice type	Snow depth (cm)	Season	CO_2 fluxes ($\mathrm{mmol\,m^{-2}\,d^{-1}}$)	Reference
Saroma-ko, Japan	Landfast ice	0 – 19	Winter	Snow interface (<9 cm): -1.8 – -1.2 Snow interface (>9 cm): -0.4 – 0.0 Ice interface: -3.6 – -1.2	Nomura et al. (2010b)
Arctic Ocean					
North of Svalbard	Pack ice	2 – 60	Winter-Spring	Ice interface: -1.8 – +6.8 Snow interface: 0 – +0.4	Nomura et al. (2018)
North of Svalbard	Pack ice	1 – 30	Spring	Ice interface: -0.3 – +0.2 Snow interface: -0.8 – +0.3	Nomura et al. (2013a)
Winnipeg, Canada	Artificial sea ice	0 – 9	Growth Decay	+0.29 – +4.4 -2.8 – -1.3	Geilfus et al. (2016)
Resolute Passage, Nunavut	Landfast ice		Late spring	-5.4 – -0.04	Geilfus et al. (2015)
Barrow, Alaska	Landfast ice (young, ≤ 20 cm)		Spring	+4.2 – +9.9	Geilfus et al. (2013)
Beaufort Sea, Canada	Landfast and pack ice		Spring	Ice interface: -2.6 – +0.84 Snow interface: -1.49 – +2.1	Geilfus et al. (2012a)
Barrow, Alaska	Landfast ice	16 – 2	Spring	Snow interface: -1 – +0.7	Nomura et al. (2010a)
Resolute Passage, Canada	Landfast ice	11 – 15	Spring	All interfaces: -4.4 – +5.0	Brown et al. (2015)
Southwest Greenland	Landfast ice	3 – 8	Late winter	Ice interface: -1.5 – +9.5 Snow interface: -2.2 – +7.3	Fischer (2013)
Southern Ocean					
Bellingshausen Sea Weddell Sea Indian sector of the SO	Pack ice		Spring – summer	-2.9 – -0.4 -5.2 – -1.8 -1.1 – +1.9	Delille et al. (2014)
Lützow-Holm Bay	Landfast ice (MY)	9 – 68	Summer	Ice interface: -0.4 – +0.2 Snow interface: -0.5 – +0.2	Nomura et al. (2013a)
Bellingshausen Sea	Pack ice	28 – 106	Spring	Ice interface: -2.9 – +0.3	Geilfus et al. (2014)

II.5. Sympagic communities

The sea ice ecosystem is characterized by steep gradients in temperature, salinity, light and nutrient availability. Despite these challenging environmental conditions, sea ice provides a dynamic habitat for diverse communities of microorganisms. These sympagic communities include a wide variety of organisms from different taxonomic groups such as algae, bacteria, heterotrophic protists, fungi and viruses (Deming, 2010; Horner et al., 1992; Poulin et al., 2011). Sympagic communities are dominated by bacteria in terms of abundance, and by algae in terms of biomass (Meiners et al., 2004), particularly diatoms during the spring bloom (Vancoppenolle et al., 2013b).

II.5.1. Indicators of sea ice biomass

The organic matter content in sea ice is quantified using several indicators or quantities. The concentration of chl *a*, the dominant photosynthetic pigment in marine microalgae (Vancoppenolle et al., 2013b), is measured by fluorometry or HPLC (high performance liquid chromatography) and is an indicator of autotrophic biomass. It varies by geographic region, ice type and over seasons as reported by Meiners et al. (2012) for Antarctica. High chl *a* concentrations ($> 1000\,\mu\mathrm{g\,L^{-1}}$) were reported in both Antarctic pack and fast ice (Arrigo, 2017; Meiners et al., 2018), with maximum values ($> 6000\,\mu\mathrm{g\,L^{-1}}$) observed in platelet ice in the McMurdo Sound in the Ross Sea (Arrigo et al., 1995). Concentrations are generally highest in landfast ice, which is more productive due to the nutrient supply by coastal processes such as riverine influence (in the Arctic) or tidal currents promoting vertical mixing and forced convection in sea ice (Vancoppenolle et al., 2013b) or due to the occurence of platelet ice allowing biomass accumulation.

Chl *a* measurements specifically targets phototrophic biomass (excluding cyanobacteria) while POC includes all of the organic carbon regardless of its physiological role (e.g., healthy cells or detritus) or trophic functions (autotrophic or heterotrophic) (Vancoppenolle et al., 2013b). The distribution of chl *a* and POC in sea ice are usually correlated, implying that ice algae represent a large part of POC and partly produce it (Vancoppenolle et al., 2013b). A decoupling between sea ice POC and chl *a* concentrations can indicate a significant contribution of non-pigmented biomass (heterotrophs and detritus) in POC concentrations (Vancoppenolle et al. (2013b) and references therein).

Dissolved organic matter (DOM) is a diverse pool of complex organic compounds such as carbohydrates, proteins, amino acids as well as more complex substances (e.g. humic substances) (Meiners and Michel, 2016; Vancoppenolle et al., 2013b). DOM is defined as organic matter smaller than 0.2 μm but in practice, it is routinely measured after filtration through GF/F glass fiber filters with a pore size of $\sim$0.7 μm (Thomas et al., 2010). Sea ice DOM includes both material produced in situ by organisms through biological release and material trapped during sea ice formation (Meiners and Michel (2016) and references therein). Among the element making up DOM are found the dissolved organic carbon (DOC), dissolved organic nitrogen (DON) and dissolved organic phosphorus (DOP). Considerably less is known about DON and DOP than about DOC (Sarmiento and Gruber, 2006). Sea ice DOC concentrations are generally higher than the seawater values (Smith et al., 1997; Thomas et al., 2001) and the high concentrations are often associated with the highest standing stocks of organisms (Meiners and Michel, 2016). In Arctic sea ice, DOC concentrations up to $2.5 \times 10^3 \mu$M were reported (Riedel et al., 2008) while in Antarctic sea ice, large variability and lower values were reported, with concentrations higher than $1.8 \times 10^3 \mu$M in melted ice cores (e.g. Papadimitriou et al. (2007), Thomas et al. (2001, 2010)). DOC and DON concentrations are generally correlated, although DOC/DON ratios are highly variable, ranging from 3 to 50 (Krell et al., 2003; Norman et al., 2011; Papadimitriou et al., 2007; Thomas et al., 2001).

II.5.2. Seasonal evolution of biomass

In winter, sea ice algal biomass is usually limited (Krell et al., 2003; Ratkova et al., 2004; Werner et al., 2007) because of harsh sea ice conditions, i.e. low temperature, high brine salinity and insufficient light levels. In spring, algae concentrations increase in parallel with the increase of temperature and desalinisation processes (Delille et al., 2002; Mundy et al., 2005). The algal biomass taken by sea ice from seawater is minimal ($\sim$0.01 $\mu\mathrm{g\,L^{-1}}$) but increases by five to seven orders of magnitude during the bloom (Arrigo, 2014). The bloom often peaks in late spring or early summer as observed on the Figure 13 in October and November, before the ice melts and breaks up and when the ice column is nearly isothermal and highly permeable allowing enhanced nutrient exchanges with seawater (Arrigo and Sullivan, 1994; Garrison et al., 2005). Subsequent declines in ice algal abundance in summer may be related to losses from melting sea ice (Grossi et al., 1987), nutrient limitation (Fripiat et al., 2017) and/or increased grazing pressure (Hegseth and Von Quillfeldt, 2002). When the ice pack starts to form again in autumn, a secondary ice algal bloom may develop (Fritsen et al., 1994; Meiners et al., 2012) but is usually short lived owing to environmental conditions becoming too harsh to support algal growth (Garrison et al., 2005; Kennedy et al., 2002; Meiners et al., 2003).

It is important to keep in mind that algae both photosynthesize and respire, while heterotrophic bacteria and grazers (including protozoans and metazoans) only respire and their growth and cell maintenance depend on the photosynthetically produced biogenic matter (Thomas et al., 2010). Prior to the bloom period or during winter, the heterotrophic community can dominate (Niemi et al., 2011; Paterson and Laybourn-Parry, 2012; Riedel et al., 2008). During the ice algal bloom in the growing season, intense autotrophy generally superimposes on the heterotrophic activity (Thomas et al., 2010). But net heterotrophic phases associated with spring biomass build-up has also been reported in the Arctic (Campbell et al., 2017; Rysgaard et al., 2008; Rysgaard and Glud, 2004).

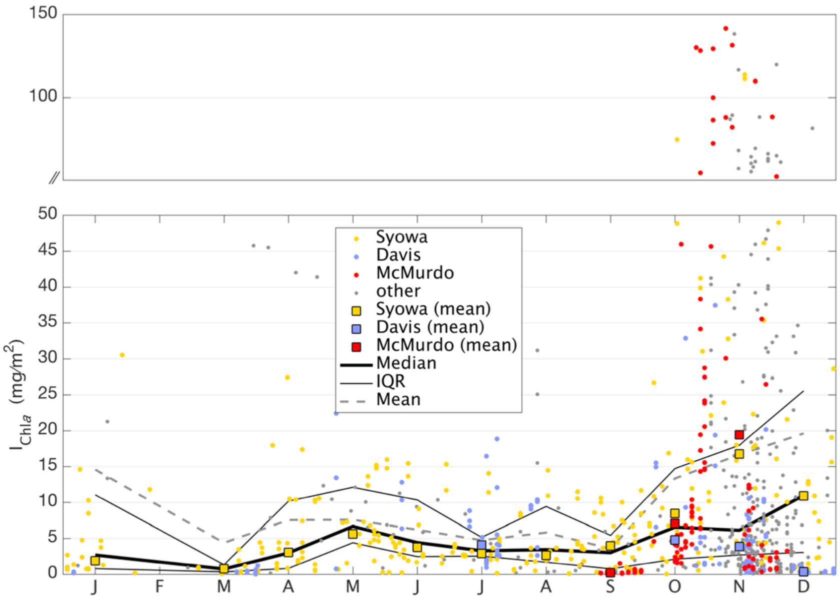

Figure 13: Seasonal evolution of integrated ice algal biomass in Antarctic landfast sea ice (mg m^{-2}) from Meiners et al. (2018). The main sampling locations are Syowa (yellow), Davis (blue), and McMurdo (red) stations. Grey symbols refer to other locations. The thick, thin and dashed lines indicate the monthly median, interquartile and mean biomass of full (≥3 ice sections for the entire ice thickness), complete (≤2 ice sections) and intermittent (sampling gaps) cores.

II.5.3. Net community production

Net community production (NCP) refers to the balance between gross primary production and respiration of all organisms. It described the net trophic status of the ice, net autotrophic or net heterotrophic. This trophic status subsequently affects gas fluxes at the interfaces ice-water (Brown et al., 2015) and ice-atmosphere. Positive NCP (autotrophy) leads to a consumption of DIC and a production of O_2, whose stoichiometry is tightened to photosynthetic and respiratory reactions (i.e., photosynthetic quotient) (Anderson, 1995; Glud et al., 2002). The measurement of NCP can be performed in different ways, via:

- Chl *a* or Particulate organic carbon (POC) measurements to estimate the accumulation of algal biomass and its temporal change. As mentioned by Zhou et al.

(2014), this method requires the extraction and the melting of sea ice which alters microenvironmental conditions (change of salinity, temperature, nutrients concentrations…) and the microorganisms growth. Furthermore, a conversion factor C:chl *a* is required to calculate the equivalent C uptake.

- ^{14}C incubation technique (Steemann-Nielsen, 1952). A similar incubation method based on ^{13}C-labelled carbon and two ^{15}N-labelled nitrogen substrates (NO_3^-, NH_4^+) was developed at ULB-VUB to measure C, N uptake in the sea-ice (Roukaerts et al., 2016). Incubation techniques are generally based on ice crushing and addition of filtered seawater or by thawing the sample prior to adding tracer. As mentioned by Glud et al. (2002), these procedures change the microenvironmental conditions and alter the photosynthetic activity (e.g. gradients of O_2, DIC and nutrient concentrations, salinity, temperature, microbial organization and light conditions). Samples incubation can be performed in glass bottles placed under the ice in order to mimic the in-situ light conditions. However, it's difficult to reproduce the exact light field conditions of the microalgae during incubations (Glud et al., 2002).

- O_2 exchanges between the ice and the underlaying water using pulse-amplitude-modulated (PAM) fluorometry (Glud et al., 2002), O_2 micro-electrodes (McMinn and Ashworth, 1998), O_2 micro-optodes (Mock et al., 2002) or ice–water interface O_2 eddy correlation (Long et al., 2012). These techniques allow to minimize the disturbance of the microenvironmental conditions (Glud et al., 2002) but depend on the structure and the physical properties of sea ice (i.e., permeability and brine dynamics). The PAM fluorometry is sensitive to the spatial variability of the algal biomass and the optical properties of the ice (Glud et al., 2002). The O_2 concentrations measured using microsensors will also differ if the sensors are set in brine, ice, gas bubbles or bacterial films (Mock et al., 2002) and measurements are only possible in permeable ice layers where O_2 diffuses to the microsensors (Glud et al., 2002). The eddy-correlation technique covers a large footprint and limits the disturbance of the environment (natural light conditions, no ice melting or crushing, hydrodynamic conditions) (Long et al., 2012). But, this technique assumes that the dominant form of vertical transport is turbulent mixing and can therefore produce inaccurate results in case of stratification and insufficient turbulence (Long et al., 2012).

- O_2/Ar ratios. O_2 and Ar measurements in ice are performed by ice crushing, which allows to include both O_2 dissolved in brines and gaseous O_2 in bubbles, in both permeable and impermeable sea ice layers. Furthermore, Ar measurements are used to remove the influence of physical impact on O_2 concentrations. Argon has indeed no biological sources or sinks and is therefore a tracer of physical processes.

The Table 3 presents the community production rates for landfast sea ice of the Arctic and Southern Oceans with different measurements method. Some studies documented the net community production across the Arctic using standard measurement methods such as incubation of melted ice cores (Campbell et al., 2017; Søgaard et al., 2010) and highlighted succession of distinct heterotrophic and autotrophic phases. A study of McMinn et al. (2012) estimated the NCP at Casey Station (East Antarctica) using O_2 microelectrode and reported a smaller range of values than the NCP reported in McMurdo Sound in the bottom platelet layer using standing crop of chl *a* (Arrigo et al., 1995).

II.5.4. Algal communities in Antarctic sea ice as a function of depth

Each sea ice layer hosts its own microalgae communities with different abundance, physiological characteristics and production rates.

The surface algal communities exhibit commonly lower chl *a* values than in the bottom layers, ranging between 270 and 730 $\mu\text{g}\,\text{L}^{-1}$ in spring in the McMurdo Sound (Lizotte and Sullivan, 1992). The presence of infiltration layers or gap layers[4] at the sea ice surface enhances the microalgae growth (Haas et al., 2001; Kattner et al., 2004; Kennedy et al., 2002), providing fresh nutrients and developing where no light limitation is encountered (Van Leeuwe et al., 2018). Production rates in these infiltrations layers can reach more than 2 $\text{g}\,\text{C}\,\text{m}^{-2}\,\text{day}^{-1}$ (Lizotte and Sullivan, 1991). In Antarctica, infiltration layers are quite common while melt ponds[5] occurs more frequently in the Arctic (Ackley et al., 2008; Andreas and Ackley, 1982; Massom et al., 2001).

---

[4] Partially melted layer filled with slush or seawater underneath a surface layer of snow and ice (Ackley et al., 2008; Ackley and Sullivan, 1994)

[5] Pools of melted snow and ice at the sea ice surface

Table 3: Community Production Rates for Landfast Sea Ice of the Arctic and Southern Oceans

Location	Layer	Method	NCP ($\mu\text{mol}\,\text{L}^{-1}\,\text{day}^{-1}$)	NCP ($\text{mg}\,\text{C}\,\text{m}^{-2}\,\text{day}^{-1}$)	Reference
Southern Ocean					
McMurdo Sound	Bottom, platelet	Standing crop of chl *a*		170 to 1200	Arrigo et al. (1995)
Casey Station	Bottom	O_2 microelectrode		103 to 163	McMinn et al. (2012)
Arctic Ocean					
Barrow, Alaska	Surface-internal	O_2/Ar	-6.6 to 3.6		Zhou et al. (2014)
Malene Bight, SW Greenland	Surface Bottom	Oxygen incubations	0.8 ± 3.5 6.3 ± 2.3		Søgaard et al. (2010)
Nunavut, Canada	Bottom	Oxygen optode incubations	1.6 to 2.8		Campbell et al. (2017)

Species of flagellates are the dominant taxonomic group in both surface and interior layers in landfast and pack ice (Van Leeuwe et al., 2018). In antarctic internal ice layers, during winter, the highest ice algal chl *a* concentration is found in the sea ice interior, likely as a result of autumnal ice accretion trapping bottom-ice communities (Meiners et al., 2018). Hence, internal and surface communities are particularly important during seasons with low overall biomass (Meiners et al., 2018). In the Weddell Sea, maximum ice algal biomass in internal layers ranged between 4 and 10 $\mu\mathrm{g\,L^{-1}}$ in summer and up to 440 $\mu\mathrm{g\,L^{-1}}$ in autumn (Arrigo (2017) and references therein).

Highest concentrations of sea ice microalgae are often found in the bottom 20 cm of the ice where environmental conditions are more stable and favorable for growth (Arrigo, 2017). Some of the most favorable habitats are found beneath landfast ice in Antarctica, where platelet ice develops (Arrigo, 2017). Platelet ice layer harbors some of the largest biomass concentrations on Earth (Arrigo et al., 1995). In spring, chl *a* concentrations in platelet layers may exceed 6000 $\mu\mathrm{g\,L^{-1}}$, which is 6 times higher than the concentrations in the columnar ice from the same study (Arrigo et al., 1995). Pennate diatoms (longer along one axis) dominate the bottom layers, accounting for 28% of the whole community in landfast ice and about 83% of the whole community in pack ice (Van Leeuwe et al., 2018). In some case, strand communities of colonial diatoms (e.g. *Berkeleya antarctica* in Antarctica) develop under the sea ice, attached to the bottom layers and suspended into the surface ocean layers (Arrigo, 2014) (Figure 4). These algae find their nutrient supply in the water column, allowing them to accumulate large amounts of biomass and grow up to a length of 1 m or more (Arrigo, 2014).

II.5.5. Large-scale contribution of sea ice to primary production

Annual production rates are similar in the Arctic and Antarctic sea ice, ranging from 0.001 to 23 $\mathrm{g\,C\,m^{-2}\,y^{-1}}$ and from 0.3 to 38 $\mathrm{g\,C\,m^{-2}\,y^{-1}}$, respectively (Arrigo (2017) and references therein). By far the maximum production rate in Antarctica, estimated at 38 $\mathrm{g\,C\,m^{-2}\,y^{-1}}$, was observed in platelet ice from the McMurdo Sound. Lizotte and Sullivan (1991) compared the production rates of pack ice and landfast ice communities and observed higher production rates in the pack ice. They related this to higher irradiance levels under the pack ice. Ugalde et al. (2016) concluded also that light availability was a determining factor in production rates, more than the more porous structure of pack ice with thick frazil layers.

In situ data (e.g observations of chl *a*) and modeling studies allow to evaluate the large-scale total phytoplankton primary production in sea ice (Vancoppenolle et al., 2013b). In the Southern Ocean south of 50°S, 1949 ± 70.1 $\mathrm{Tg\,C\,y^{-1}}$ are produced in the open ocean with a major contribution from the Ross Sea (Arrigo et al., 2008), 114 $\mathrm{Tg\,C\,y^{-1}}$ are produced in the marginal ice zones and the contribution from sea ice ranges from 40 to 70 $\mathrm{Tg\,C\,y^{-1}}$ based on models and field data, respectively (Arrigo et al., 1997; Legendre et al., 1992). Sea ice ecosystems account therefore for 2 to 4% of the total annual production in Antarctic waters. This contribution would increase substantially while only considering the sea ice zone of the Southern Ocean (Arrigo et al., 1997).

II.5.6. Macro-nutrients

Macro-nutrients, such as nitrate (NO_3^-), nitrite (NO_2^-), phosphate (PO_4^{3-}), silicic acid ($Si(OH)_4$) and ammonium (NH_4^+) are used by all organisms to synthetize structural and functional components (Gruber, 2008; Paytan and McLaughlin, 2007). Nutrient dynamics in sea ice depend on the brine transport, the biologically-mediated consumption and assimilation into biomass and the production via remineralization (Fripiat et al., 2017). Macro-nutrients are dissolved in brine inclusions, except NH_4^+ that can be trapped within ice crystals during freezing (Weeks, 2010). Hence, in the absence of biological uptake or remineralization, nutrient concentrations conservatively follow sea salt concentrations. Concentrations in interior ice are generally small and lower than seawater concentrations (Meiners and Michel, 2016; Vancoppenolle et al., 2013b) while concentrations higher than seawater values are commonly encountered in the sea ice bottom in spring and summer (Fripiat et al., 2017) as also observed by Roukaerts et al. (2018) at Cape Evans (McMurdo Sound, Antarctica). In the absence of an external supply, macro-nutrients are likely to be easily exhausted (Vancoppenolle et al., 2013b). As pointed out in several observations and modelling studies, key limiting nutrients for sea ice algal growth are nitrate and silicic acid (Gradinger, 2009; Lavoie et al., 2005; Saenz and Arrigo, 2014). Relative to nitrogen, silicic acid has a low rate of recycling within sea ice (Arrigo et al., 2002; Gleitz et al., 1995) and diatoms, often dominating the sea ice algal communities, are particularly affected by its limitation (Meiners and Michel, 2016). Algae reactions to nutrient stress can include the release of DOC from their cells by both passive (leakage) and active processes (exudation) (Meiners and Michel, 2016).

A compilation of macro-nutrient data in Antarctic pack ice performed by Fripiat et al. (2017) showed that the salinity-normalized concentrations of dissolved inorganic nitrogen and $Si(OH)_4$ follow the general trend expected for productive ecosystems by decreasing from spring to summer in parallel with the biomass build-up (Figure 14). In late summer (from March), both dissolved inorganic nitrogen and silicic acid concentrations increased, led by an imbalance in their production and consumption rates and faster remineralization. Intermediate nutrients (NH_4^+ and NO_2^-) showed relatively invariable concentrations indicating a balance between production and consumption rates. The phosphate concentrations had a different dynamic and were in excess from spring to summer. Several hypotheses were proposed by the authors to explain this excess: greater allocation to phosphorus-rich biomolecules during the bloom, convective loss of excess dissolved nitrogen, preferential remineralization of phosphorus, and/or phosphate adsorption onto metal-organic complexes (Fripiat et al., 2017).

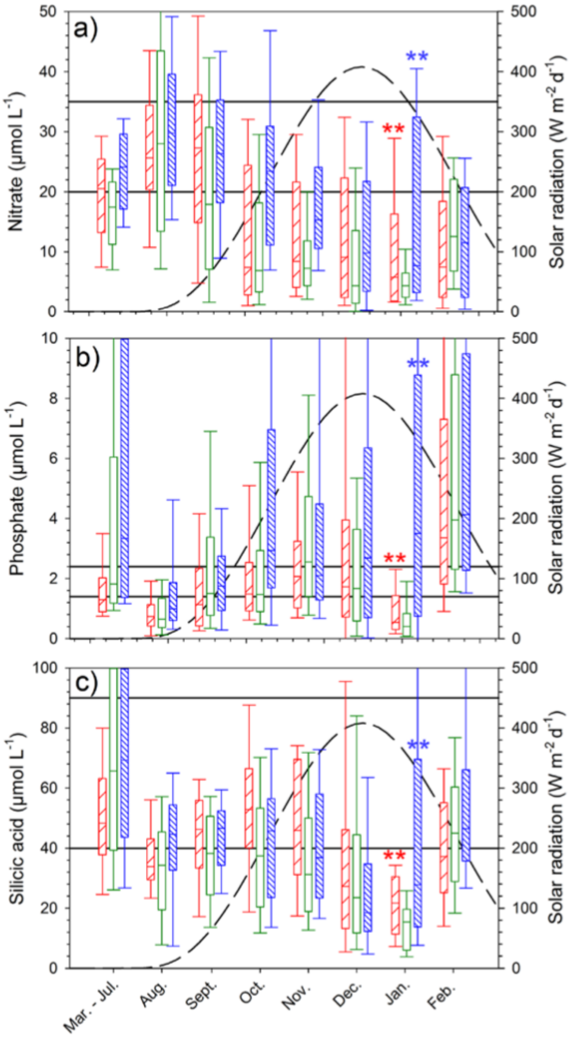

Figure 14: Annual cycle of salinity-normalized concentrations of nutrients in Antarctic pack ice, Fripiat et al. (2017). The red, green, and blue boxes indicate the concentration ranges in surface (0–0.2 m), interior, and bottom -most 0.1 m- layers in sea ice, respectively. The solid lines indicate the concentration range in seawater and the dashed line indicates the average solar radiation. The two stars indicate occasions with less than 15 data points in a depth interval.

II.5.7. EPS and biofilm formation

In both terrestrial and aquatic environments, algae and bacteria secrete extracellular polymeric substances (EPS) which are complex organic materials composed primarily of polysaccharides with carbon backbones of high molecular weight (1–3 × 10^5 Daltons) (Krembs and Deming, 2008). EPS can represent up to 70 % of the sea ice POC pool (Krembs et al., 2002; Meiners et al., 2004, 2003).

By forming a gelatinous matrix, EPS lies at the root of the biofilm formation (Stewart and Franklin, 2008). Ice-associated biofilms have been suggested in several studies (Boetius et al., 2015; Deming, 2010; Meiners et al., 2003, 2008). EPS can aggregate in the ice by coating the surface of brine channel walls (Meiners et al., 2003) as shown on Figure 15 and under the ice (see Boetius et al. (2015) and references therein). Diatoms cultured in subzero brine are known to produce high concentrations of EPS (Aletsee and Jahnke, 1992) and observations in sea ice revealed the prevalence of EPS coatings around diatom cells (Krembs et al., 2002). EPS concentrations are also correlated with the abundance of bacteria (Deming, 2010; Meiners et al., 2004, 2003).

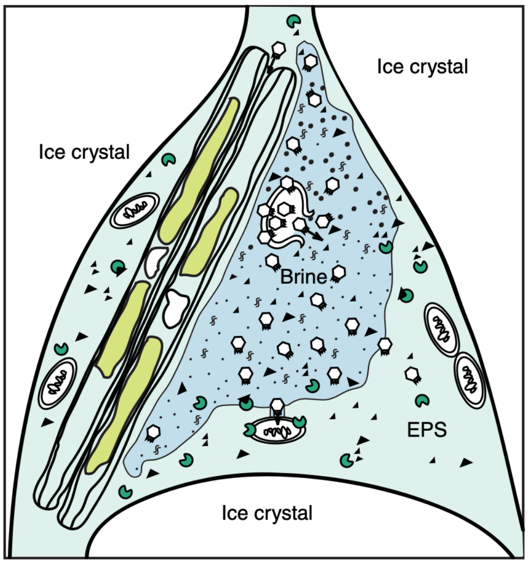

Figure 15: Scheme from Deming (2016) showing a brine inclusion with bacteria (white cells) and a pair of diatoms embedded in EPS lining the pore space. EPS provide a defense against viruses (hexagons). Also shown are organic substrates (black triangles) and extracellular enzymes (green) hydrolysing the substrates.

II.5.7.1. Why are EPS produced in sea ice?

Besides their contribution to the sea-ice particulate organic carbon pool (Riedel et al., 2006), EPS are sticky and may promote organisms attachment and adhesion to crystal surfaces (Hoagland1993, Meiners2008). It may also serve other functions such as cryoprotection maintaining a liquid environment around cells and buffering against ice-crystal damage (Aslam et al., 2012; Krembs and Deming, 2008; Krembs et al., 2002). Indeed, Krembs et al. (2002) suggested that polyhydroxyl compounds, able to depress the homogeneous nucleation temperature of water, is largely present in sea ice.

The production and release of EPS by microorganisms in their environment is known to increase in response to stress (Hoagland et al., 1993; Tamaru et al., 2005) and in case of shifts of environmental conditions, e.g. temperature, salinity or pH (Bowman, 2008; Krembs and Deming, 2008; Marx et al., 2009; Meiners et al., 2008; Steele et al., 2014). Sea ice is in particular an environment in which temperature changes and subsequent physical and chemical changes occur and affect the transport and availability of water, nutrients and gases concentrations as well as increase the concentration of various dissolved substances, sometimes to toxic level (Krembs and Deming, 2008).

II.5.7.2. Specificity and implications of a biofilm

The biofilm matrix is an aqueous solution but due to the locally high cell densities and the presence of EPS, diffusion processes and water flow are impeded in its direct vicinity (Stewart, 2003). For example, the diffusion rate in the matrix of solutes with the size of oxygen is approximately 60% of their diffusion rate in pure water (Stewart, 2003). Furthermore, the diffusion distance in a biofilm is increased and in the same order of magnitude as the dimension of multicellular clusters while the diffusion distance for a freely suspended microorganism is the dimension of an individual cell (Stewart, 2003). The slower exchanges of metabolic substrates and products lead to spatial heterogeneity and concentration gradients within the biofilm as shown on Figure 16 (Stewart and Franklin, 2008). In this way, accumulation of nutrient is possible via trapping within the biofilm (Stewart and Franklin, 2008) or production of inorganic nutrients (remineralization) faster than their diffusion out of the biofilm (Roukaerts, 2018). These gradients create different micro-niches within the biofilm with diverse species and growth rates of microorganisms (Costerton et al., 1994; Stewart, 2003).

EPS also alter the pore microstructure and desalination processes of growing sea ice (Krembs et al., 2011). The authors observed disordered ice crystals as well as greater pore density and more complex pore geometries in ice sections grown with added EPS. Together, the complex tortuosity, the pore clogging and the increase in viscosity can contribute the salt retention and higher bulk salinities (Krembs et al., 2011). Pore clogging will also enhance retention of organisms in ice layers with light levels sufficient to support substantial algal activity (Krembs et al., 2002).

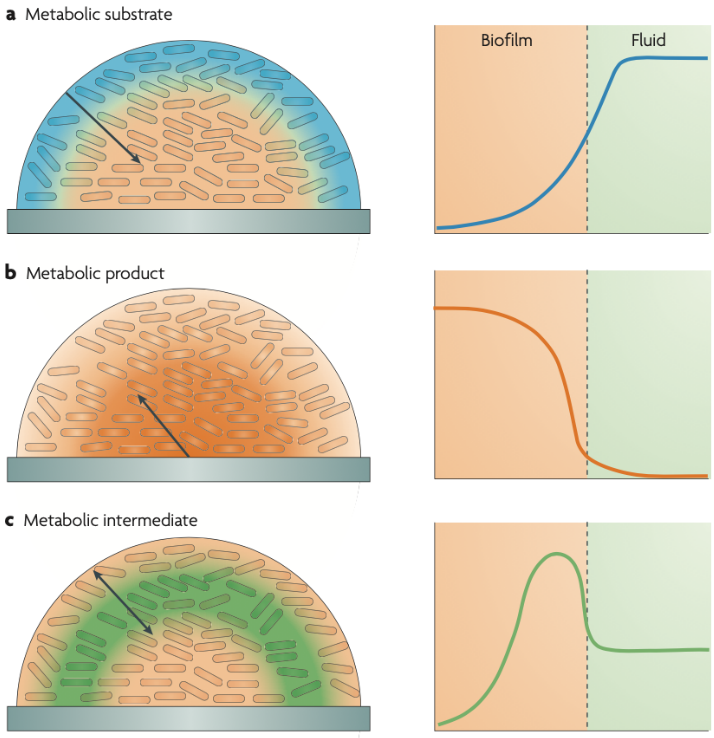

Figure 16: Scheme of chemical heterogeneity in biofilm due to reaction-diffusion interactions (Stewart and Franklin, 2008): a) metabolic substrate consumed in biofilm, its concentration decreases towards the biofilm's interior b) metabolic product produced and concentrated in the biofilm c) metabolic intermediate with solutes both produced and consumed in the biofilm.

II.6. General oceanography of the Ross Sea

Facing the Pacific sector of the Southern Ocean, the Ross Sea extends between Cape Adare (170°E) and Cape Colbeck (158°W). On the southern side of the Ross Sea lies the Ross Ice Shelf (RIS), one of the Earth's largest ice shelf covering an area of 520 000 km^2 and reaching an average thickness of 370 m (W. Smith et al., 2012). The continental shelf extending north of the RIS covers an area of 466 000 km^2, with an average depth of $\sim$ 530 m (W. Smith et al., 2012). The RIS limits the uppermost water layers circulation, while deep waters continue to circulate freely under the floating ice shelf (Budillon et al., 2002). The Antarctic Circumpolar Current (ACC), following the continental slope from east to west, acts as the northern oceanographic boundary of the Ross Sea. It carries the 2500 m mid-depth layer of Circumpolar Deep Water (CDW), a voluminous, relatively warm ($>$ 2°C), salty, oxygen-poor and nutrient-rich water mass. Some CDW is entrained poleward and enters the Ross Sea gyre, a wind-driven cyclonic feature which extends well north of the Ross Sea itself. Over most of the shelf areas east of 160 °W, the Antarctic Surface

Water (AASW) occupies the top half of the water column above the CDW. This fresh surface water mass (S < 34.3), with a thickness varying locally from 300 m at 162°W to less than 38 m around 170°E (Orsi and Wiederwohl, 2009), enters the Ross Sea around Cape Colbeck and continues westward as a narrow coastal flow along the RIS (Smith et al., 2012). It brings low-salinity surface waters to the Ross Sea Polynya. Near the shelf break, mixing of CDW with colder and low-salinity AASW produces what farther south is commonly known as Modified Circumpolar Deep Water (MCDW). MCDW can intrude well onto the shelf (Figure 17).

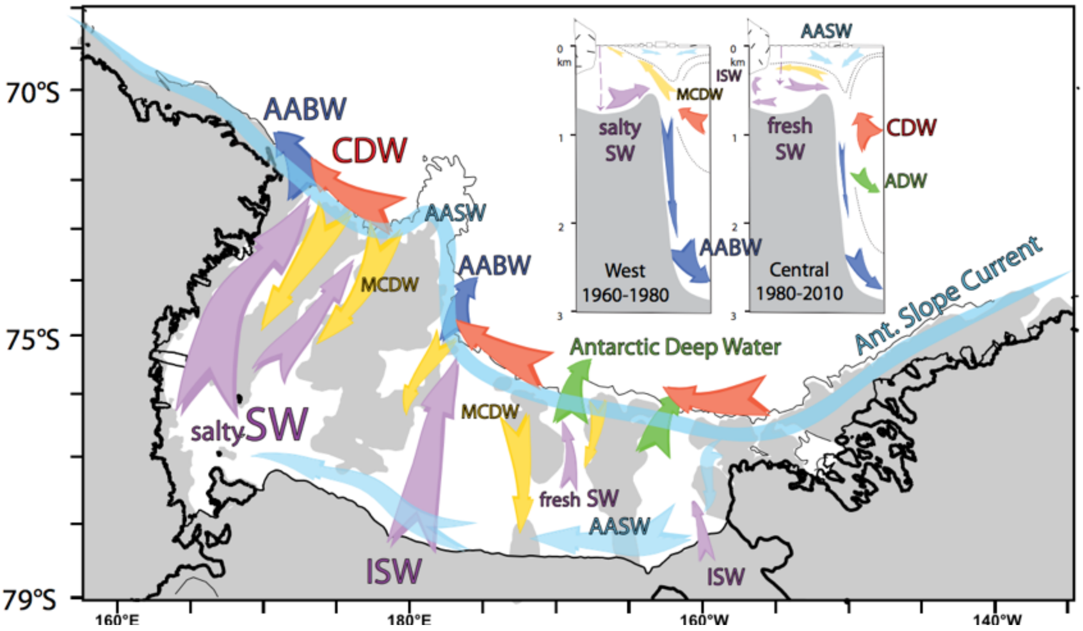

Figure 17: Ross Sea Circulation observed in the past 50 years from Smith et al. (2012) with CDW in red, AASW in light blue, SW in purple, MCDW in yellow and AABW in dark blue.

II.6.1. Antarctic Bottom Water origin

Sea-ice formation within the Ross Sea modifies local upper waters, AASW or the relatively warm MCDW into Shelf Water (SW) or High Salinity Shelf Water (HSSW), by inducing extensive brine rejection and hence increased sea surface salinities. The HSSW is the densest water mass found around Antarctica with the salinity increasing with depth (34.75 to 35) and temperatures close to or below the surface freezing point (between −1.95 and −1.75°C) (Budillon et al., 2002). It forms along the western sector of the Ross Sea, mostly within the Terra Nova Bay polynya during the winter (Budillon and Spezie, 2000). The saltiest HSSW (S > 34.82) masses are located within the western Ross Sea, most likely being the local production region (Orsi and Wiederwohl, 2009). Overlying the HSSW, the Low Salinity Shelf Water (LSSW) with salinities lower than 34.54 is found at intermediate depths in the eastern Ross Sea (Orsi and Wiederwohl, 2009). HSSW fills most of the continental shelf bottom layer and part of it flows southward under the Ross Ice Shelf, creating different water mass called Ice Shelf Water (ISW). Cooling and basal melting under ice shelves and glacier tongues forms this ISW which is characterized by an in situ temperature colder than the sea surface freezing point (Jacobs, 2004). ISW is primarily located on the central continental shelf and then moves and sinks northward, therefore contributing to the formation of the Antarctic Bottom Water (AABW).

II.6.2. McMurdo Sound dynamics and ice-shelf influence

McMurdo Sound is located in the south-western corner of the Ross Sea, bordered by the Ross Island to the east, Victoria Land to the west, and to the south by the McMurdo Ice Shelf, the northwest part of the much larger Ross Ice Shelf (Figure 18). The pattern of the currents is different in the eastern and the western McMurdo Sound. Net southerly flow, derived from the Ross Sea, is observed in the eastern Sound while net northward flow occurred in the western Sound (Barry and Dayton, 1988). The southerly flow either continues towards the sub shelf area before it turns west and exits the Sound or mixes with northerly flowing sub Ross Shelf waters and flows across the front of the McMurdo Ice Shelf (Robinson et al., 2010).

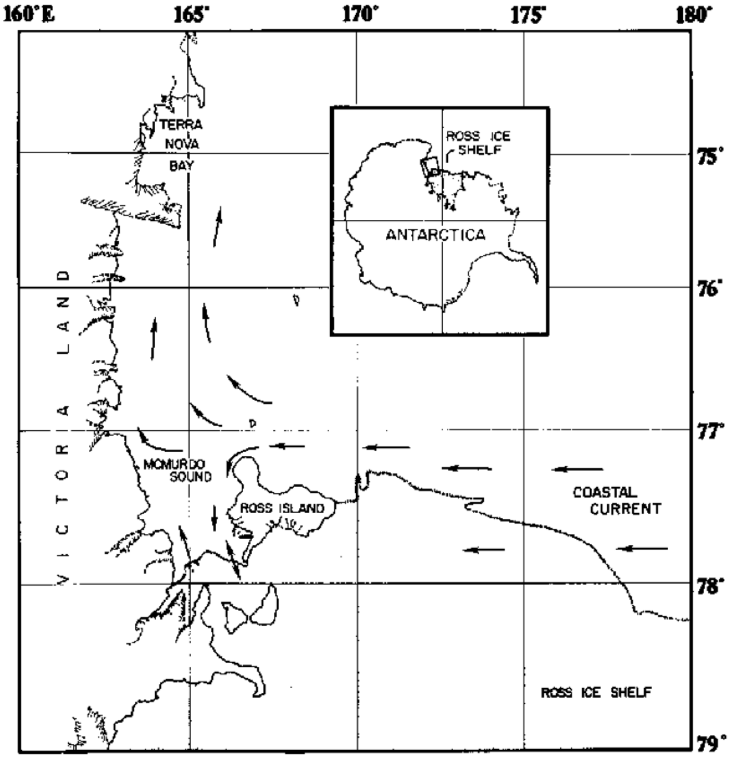

Figure 18: Map of McMurdo Sound from Barry (1988). Arrows represent the westward coastal current.

II.6.3. Ice Shelf Water plume

As High Salinity Shelf Water (HSSW) sinks under the Ross Ice Shelf, its freezing point is reduced with the increasing pressure. The water mass can therefore lose heat and melt ice at depth (Hughes et al., 2014). In this way, HSSW entering the ice-shelf cavity is modified at depth by mixing with the shelf water resulting in the formation of Ice Shelf Water (ISW). The resultant buoyant water can flow out in a plume towards the surface. This ISW plume becomes supercooled as it rises because its freezing point increases with the falling pressure (Foldvik and Kvinge, 1974). When the plume becomes supercooled, frazil ice crystals start to grow within the supercooled water mass to counterbalance this local supercooling (Dempsey et al., 2010). Crystals remain initially suspended in the water column, decreasing the plume density and hence increasing the local buoyancy and the plume speed (Smedsrud and Jenkins, 2004). This mechanism creates a positive feedback between plume speed and frazil ice concentration (Jenkins and Bombosch, 1995). The plume continues further towards the surface as long as it is buoyant. Larger crystals first deposit at the base of the ice shelf, forming solid marine ice.

II.6.4. Platelet ice formation

Platelet ice refers either to loose platelets crystals underlying sea ice or to the incorporated platelets into columnar ice (Jeffries et al., 1993; Smith et al., 2001). Platelet ice can develop underneath existing sea ice, such a sub-ice platelet layer has been observed many times in the McMurdo Sound (Dempsey et al., 2010; Gough et al., 2012; Jeffries et al., 1993; Smith et al., 2001). The origin of platelet crystals is still a matter of debate. One hypothesis is that platelet ice growth is linked to ISW plume emerging from beneath the ice shelf. As described by Smith et al. (2001), platelet ice can form either at depth and then float upwards, as observed in the vicinity of the Filchner Ice Shelf (Dieckmann et al., 1986), or they grow in supercooled water masses present at the sea ice-water interface. In the western McMurdo Sound, ISW plume exiting the cavity of the McMurdo-Ross Ice Shelf has been identified (Robinson et al., 2014). This plume continues northwards beneath the shelf and the contiguous sea ice and flows along Victoria Land Coast where high platelet concentration, known as the "platelet corridor", has been observed by Dempsey et al. (2010) and Hughes et al. (2014). In the eastern McMurdo Sound, Hughes et al. (2014) and Dempsey et al. (2010) observed thinner layers of platelet ice and the transition from columnar to platelet ice occurred lower in the core. On the other hand, Mahoney et al. (2011) observed a shallower layer of ISW and an ISW arrival later in the season at this location. A switch in surface flow direction indeed occurred around March-April: the net southward flow of relatively warm water derived from the Ross Sea observed in summer is replaced by a northward flow of fresher and supercooled water at the surface in winter (Leonard et al., 2006; Mahoney et al., 2011). As pointed out by Robinson et al. (2014), this suggests that the ISW plume extends eastward during ice growth, allowing platelet ice formation on the eastern side of the McMurdo Sound.

Chapter III. Sea Ice pCO_2 Dynamics Across Seasons: Impact of Processes at the Interfaces

F. Van der Linden, J.-L. Tison, W. Champenois , S. Moreau, G. Carnat, M. Kotovitch, F. Fripiat, S. Wauthy, A. Lourenço, F. Vivier, F. Deman, A. Roukaerts, T. Haskell, and B. Delille

Article published in JGR:Oceans, May 2020, DOI 10.1029/2019JC015807

Abstract

Winter to summer CO_2 dynamics within landfast sea ice in McMurdo Sound (Antarctica) were investigated using bulk ice pCO_2 measurements, air-snow-ice CO_2 fluxes, dissolved inorganic carbon (DIC), total alkalinity (TA), and ikaite saturation state. Our results suggest depth-dependent biotic and abiotic controls that led us to discriminate the ice column in three layers. At the surface, winter pCO_2 supersaturation drove CO_2 release to the atmosphere while spring-summer pCO_2 undersaturation led to CO_2 uptake most of the time. CO_2 fluxes showed a diel pattern superimposed upon this seasonal pattern which was potentially assigned to either ice skin freeze-thaw cycles or diel changes in net community production. In the ice interior, the pCO_2 decrease across the season was driven by physical processes, mainly independent of the autotrophic and heterotrophic phases. Bottom sea ice was characterized by a massive biomass build-up counterintuitively associated with transient heterotrophic activity and nitrate plus nitrite accumulation. This inconsistency is likely related to the formation of a biofilm. This biofilm hosts both autotrophic and heterotrophic activities at the bottom of the ice during spring and may promote calcium carbonate precipitation.

Plain Language Summary

Sea ice participates actively in the regional cycling of CO_2 both as a source and a sink at different times of the year depending on ice physics, ice chemistry, and ice trophic status (autotrophic vs. heterotrophic). We identified the key processes driving the CO_2 dynamics in each sea ice layer (surface, interior, and bottom) from McMurdo Sound (Antarctica) from late winter to summer. At the surface, CO_2 release from the ice to the atmosphere occurred in late winter while CO_2 uptake occurred in summer. Superimposed upon this

seasonal pattern, we observed a diurnal pattern with both release and uptake occurring over 24 hr period. This diurnal pattern can be related to physical processes (nocturnal freeze-up and diurnal melting) or biotic processes (autotrophy or heterotrophy). In the ice interior, a succession of autotrophic and heterotrophic phases took place. At the sea ice bottom, a particular assemblage of microbial cells and organic matter, called biofilm, enabled the accumulation of biomass and nitrate plus nitrite simultaneously leading to both autotrophic and heterotrophic activities. In addition, this biofilm is suggested to promote calcium carbonate precipitation.

III.1. Introduction

Over the global oceans, polar oceans act as a major sink for atmospheric CO_2 (Gruber et al., 2019b; Takahashi et al., 2002), with air-sea fluxes estimated at -199 $\mathrm{Tg\,C\,year^{-1}}$ (Rysgaard et al., 2011). At high latitudes, the CO_2 cycle is strongly affected by the presence of sea ice. More than just an interface affecting gas transfers, sea ice is also one of the most extensive and dynamic ecosystems that consumes and produces CO_2. Over the last decade, studies highlighted the complex role of sea ice in CO_2 exchanges and reported CO_2 fluxes over sea ice ranging from -5.4 to +9.9 $\mu\mathrm{mol\,m^{-2}\,day^{-1}}$, with a negative value indicating CO_2 uptake and a positive value indicating CO_2 release from the ice to the atmosphere (Table 2). Fluxes have been documented mainly in spring and summer (Brown et al., 2015; Delille et al., 2014; Geilfus et al., 2013, 2012a, 2015, 2014; Nomura et al., 2013a, 2010b). No studies have examined the winter CO_2 exchanges above sea ice in Antarctica - a prerequisite to budget air-ice CO_2 fluxes over the whole year.

The partial pressure of CO_2 (pCO_2) within sea ice is a highly relevant parameter to understand the carbonate system. Factors affecting the sea ice pCO_2 include biotic (e.g. primary production and respiration (Delille et al., 2007)) and abiotic (e.g. CO_2 transport and exchanges, freezing, melting, calcium carbonate precipitation and dissolution (Rysgaard et al., 2007)) processes. The strong seasonality of these biotic and abiotic processes in brine inclusions, coupled with the thermodynamically driven evolution of brine inclusions volume, salinity, and connectivity lead to strong temporal variability in the sea ice CO_2 dynamics (Geilfus et al., 2012a; Papadimitriou et al., 2012).

The gradient of pCO_2 between the ice and the atmosphere is driving CO_2 exchanges, controlling both the fluxes direction and magnitude. Ice-atmosphere CO_2 exchanges are moreover strongly affected by the conditions at the interface, including ice type (superimposed ice, snow ice, granular ice), presence or absence of snow cover and the ice and snow chemical and physical properties. Snow salinity, wetness, density, grain sizes among others are likely to affect the magnitude and direction of CO_2 fluxes (Delille et al., 2014; Nomura et al., 2018; Nomura et al., 2010b). The presence of brine within the snowpack is induced by four processes: flooding, brine wicking, frost flowers formation and aerosols deposition (Domine et al., 2004; Massom et al., 2001). Brine-wetted snow is a multiphase reactor hosting specific physical and chemical processes that may influence CO_2 fluxes: uptake and migration of trace gas, diffusion, and sources and sinks processes (Bartels-Rausch et al., 2014). While the impact of fresh snow cover on gas fluxes has been documented for terrestrial environments (Brooks et al., 2005; Takagi et al., 2005), the role of the snow on sea ice is still overlooked.

As a biome, sea ice provides a dynamic habitat for diverse communities of microorganisms including algae, bacteria, heterotrophic protists, fungi as well as viruses (Deming, 2010; Horner et al., 1992; Luhtanen et al., 2018; Poulin et al., 2011; Thomas and Dieckmann, 2010). In landfast sea ice, i.e. immobile sea ice anchored either to coasts or continental ice formations or grounded over shoals (Meiners et al., 2018), communities are mainly concentrated either at the bottom of the ice or within a loose and unconsolidated layer of ice crystals, known as platelet underneath the columnar ice (Arrigo et al., 1995). Platelet ice is formed in supercooled waters observed around Antarctic ice shelves (Jeffries et al., 1993; Leonard et al., 2006). Bacterial and algal production affect the CO_2 dynamics by releasing or consuming CO_2, impacting concentrations of dissolved inorganic carbon (DIC) and total alkalinity (TA) - key parameters that drive the ocean-sea ice-atmosphere CO_2 fluxes. In oxic conditions, apart from the calcification, the contribution of microbial processes to DIC changes is best described by the net community production (NCP). NCP corresponds to the balance between photosynthesis and respiration of all organisms and determines the net trophic status of the ice (autotrophic vs heterotrophic). Positive NCP (autotrophic) leads to a consumption of DIC and a production of O_2, whose stoichiometry is tightened to photosynthetic and respiratory reactions (i.e., photosynthetic quotient) (Anderson, 1995; Glud et al., 2002). Some studies documented the net community production across the Arctic using standard measurement methods such as incubation of melted ice cores (Campbell et al., 2017; Søgaard et al., 2010) and highlighted succession of distinct heterotrophic and autotrophic phases. However, the processes and conditions in which heterotrophy or autotrophy dominates remain unclear.

Considering the lack of long-term and diurnal surveys of sea ice CO_2 dynamics and the need to integrate the full development of a microalgae bloom, we present results from a year-round survey of landfast sea ice carbon dynamics in Cape Evans, McMurdo Sound (Antarctica). We report O_2 and pCO_2 profiles within bulk sea ice as well as seasonal and diel patterns of CO_2 fluxes at the air-snow-ice interface. The potential for calcium carbonate precipitation is also investigated. We further examine chlorophyll *a* (chl-*a*) abundance, particulate organic carbon (POC), nitrate plus nitrite concentrations, and DIC changes over the bloom. We also compare these parameters with estimates of NCP and related ice trophic status.

III.2. Materials and Methods

III.2.1. Study site and sampling scheme

Year Round survey of Ocean-Sea Ice-Atmosphere Exchanges (YROSIAE) was a temporal survey at one single ice location at Cape Evans (77°38'S, 166°23'E), on the eastern side of McMurdo Sound, Antarctica (Figure 19). Sampling was supported by Scott Base facilities and carried out in two phases, from November to December 2011 and from September to December 2012. The sampling area is characterized by the annual occurrence of smooth, thick first-year landfast ice. Ice retreat began in early February 2012 in Cape Evans and the area remained ice-free until the beginning of April 2012, approximatively 5 months before the second sampling phase (19 September 2012). Ice cores, snow and seawater samples were collected during twelve ice stations. For the sake of consistency with other reports of YROSIAE results (Carnat et al., 2018, 2014), each station number, referenced hereafter as YRS#, corresponds to a dedicated sampling date as indicated in Figure 20 and in Table 4. Each time the site was visited, a new sampling square area of 10 m^2 was delimitated next to the sampling site of the previous station in order to minimize the bias from spatial heterogeneity. The snow cover was first sampled using plastic scoops and LDPE bottles, then the ice coring started. Ice cores were collected using an electropolished stainless-steel ice corer (14 cm ID). Immediately after drilling, cores were sealed in polyethylene bags and stored in a box containing -30°C frozen bags. Attention was paid to prevent brine drainage by keeping ice cores horizontally. Seawater sampling through core holes was performed at three different depths (0, 1 and 30 m) using a peristaltic pump (Cole Palmer, MasterflexVR - Environmental sampler) with Tygon® tubing.

Table 4: Mean Snow Depths

Station	Sampling date	Mean snow depth (cm)
YRS1	28 November 2011	2.5
YRS2	3 December 2011	1.6
YRS3	8 December 2011	0.9
YRS4	19 September 2012	1.2
YRS5	5 October 2012	1.5
YRS6	18 October 2012	0.8
YRS7	25 October 2012	0.8
YRS8	1 November 2012	0.6
YRS9	7 November 2012	0.8
YRS10	13 November 2012	0.8
YRS11	22 November 2012	0.7
YRS12	30 November 2012	0

Outside the sampling site, one soil CO_2 flux system (LI-COR LI8100A) was deployed with two long term deployment automatic chambers (LI-COR 8100-104). Chambers for CO_2 fluxes measurements were deployed over the snow and ice surfaces and were continuously running until they were blocked by the snowdrift. Every four to seven days, maintenance and repositioning of the chambers on an unaltered surface were performed. From September to December 2012, an Ice-T ice mass balance buoy developed at LOCEAN (UPMC, Paris) provided continuous measurements of air temperature and ice temperature at different depths. The experimental setting and sampling scheme are also detailed in Carnat et al. (2014).

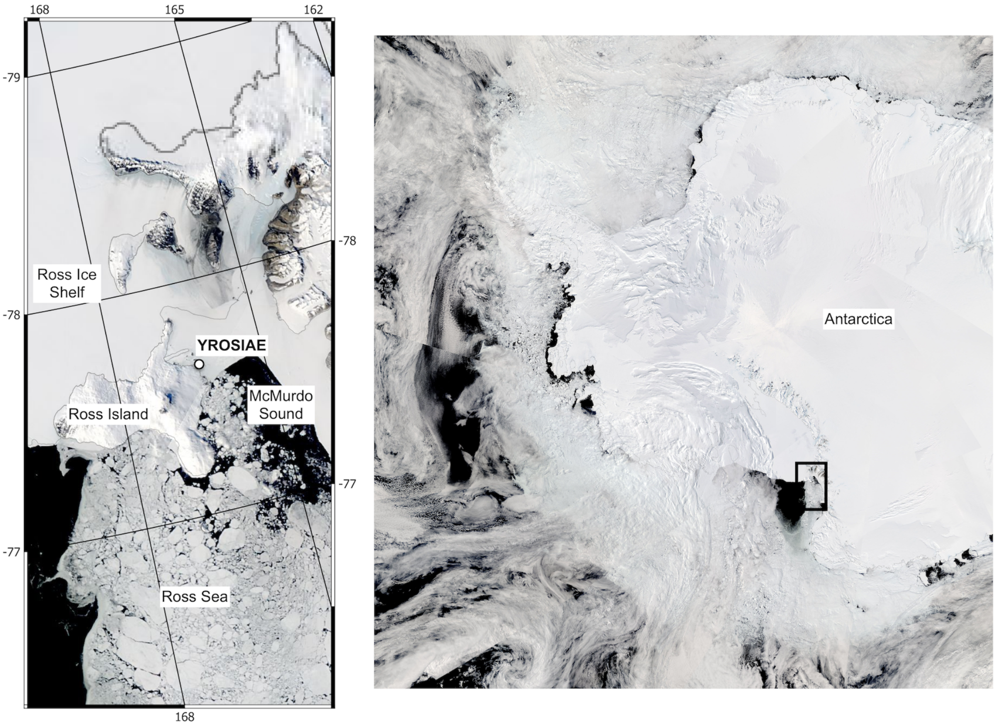

Figure 19: Location of the YROSIAE year-round sea ice biogeochemistry station, along Ross Island, Ross Sea, Antarctica. The satellite picture is a visible image from NASA's Moderate Resolution Imaging Spectroradiometer (MODIS) Terra on November 29, 2012.

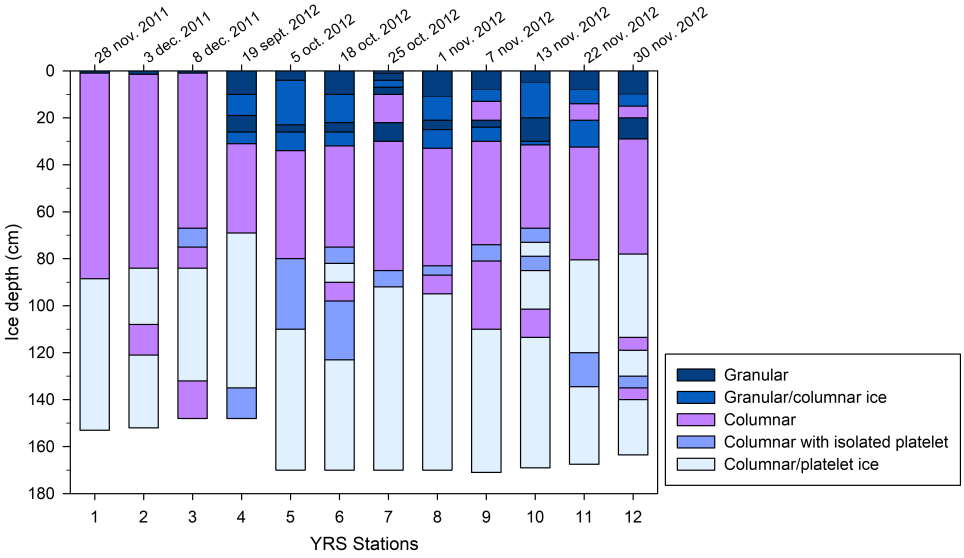

Figure 20: Ice texture of Yrosiae (YRS) stations from 2011 and 2012.

III.2.2. Measured parameters

III.2.2.1. Physical parameters

In situ ice temperature was measured on ice cores immediately after sampling with a vertical resolution of 5 cm using a calibrated probe TESTO® 720 (precision ±0.1°C, accuracy ±0.2°C). Bulk ice salinity measurements were performed using the same 5 cm vertical resolution as for temperature measurements using a Thermo Scientific Orion® 3 Star conductivity meter (accuracy of 0.1‰). The conductivity meter was calibrated at the beginning and at the end of the survey with standard solutions. The conversion from conductivity to salinity is performed via a built-in temperature-dependent conversion program (UNESCO, 1966). Further details about physical measurements are provided in Carnat et al. (2013, 2014).

III.2.2.2. Air-snow-ice CO_2 fluxes

CO_2 fluxes were measured using a LI-COR® LI-8100A soil CO_2 flux system. During the survey, two chambers were used and installed on the snow or on the ice after removing the initial snow cover. The chambers consist of a metal cylinder, with a diameter of 20 cm and a height of 9.7 cm, closed at the top by a mobile cap to vent the chamber and maintain an ambient pressure inside. A rubber seal surrounds the cylinder and ensures an airtight connection at the chamber-ice interface. For measurements over snow, a stainless-steel seal was mounted at the base of the chamber and pushed down to the ice to enclose snow and prevent lateral diffusion of air in the snowpack. The chambers (LI-COR® 8100-104) were temporarily closed above the snow or ice interface and were connected using a LI-COR® LI-8150 Multiplexer to an infrared gas analyzer a LI-COR® LI-8100A recording the pCO_2 during a designated time interval (30 min). The flux was determined by measuring the change of pCO_2 within the chamber. Flux calculations were performed routinely using the LI-COR® SoilFluxPro software, with volumes adjusted to include collar offsets (i.e. rim height above the surface) and applying water vapor corrections for dilution and band broadening. The fluxes were determined by the slope of the linear or exponential regression of pCO_2 over time, depending on the best fit. All fluxes were visually checked to discard measurements biased by contamination or poor sealing of the chamber. The detection limit was $\pm 0.004\ \mu\mathrm{mol\,m^{-2}\,s^{-1}}$. Fluxes below the detection limit were considered as null. The uncertainty of the flux computation due to the standard error of the regression slope was ±8%.

III.2.2.3. Thin sections of ice

Thin sections of thickness ranging from 600 μm to 700 μm were obtained using a Leica SM2400 microtome. These thin sections were then examined on a light table equipped with cross-polarized sheets (Langway, 1958). The textural types were visually identified based on the size, shape, and orientation of the ice crystals and compared to descriptions found in the literature (Eicken and Lange, 1991; Tison et al., 2013).

III.2.2.4. Biomass and nutrients

One core per station was dedicated to chl-*a*, nutrients and POC analyses. For chl-*a* analyses, ice sections of 10 cm were cut with a band saw, in the cold lab (at -25°C) on the day of extraction and subsequently melted at 4°C in the dark, in pre-filtered seawater. Melted ice was filtered using 10 μm then 0.8 μm Nuclepore® polycarbonate membranes. Filters were stored frozen in cryovials until measurements at the home laboratory. Extraction was performed in 10 mL acetone at 4°C for 16 h. Chl-*a* concentrations were determined using a Turner Design TD700 fluorometer.

Particulate organic carbon (POC) and nutrient analyses were performed at a 10 cm depth resolution for the bottom of the core, and at 30 cm resolution for the rest of the core. Samples were melted at room temperature in the dark and then filtered on 0.7 μm precombusted (5 h at 450°C) GF/F filters (Whatman®). The filtrate was collected and stored in 60 ml acid-washed, pre-rinsed HDPE bottles. Both filters and filtrate were stored at -25°C. For POC analysis, filters were acid fumed (HCl) to remove carbonates and packed in silver cups fitting the autosampler. POC concentrations were determined using an Elemental analyzer (Eurovector®) coupled with an isotope ratio mass spectrometer (Delta V, Thermo®).

Nitrate+nitrite ($[NO_3]^-$+$[NO_2^-]$), nitrite ($[NO_2^-]$) and phosphate ($[PO_4^{3-}]$) concentrations from filtered water samples were measured spectroscopically using a colorimetric method and a QuAAtro39 auto-analyzer (Seal Analytical Inc., Mequon, WI, USA).

The change over time of the nitrate plus nitrite concentrations was obtained from the following equation:

$$\triangle[NO_3^-] + \triangle[NO_2^-] = \frac{[NO_3^-](t_{n+1}) + [NO_2^-](t_{n+1}) - [NO_3^-](t_n) - [NO_2^-](t_n)}{\triangle t} \quad (\mu\mathrm{mol\,L^{-1}\,d^{-1}}) \quad (11)$$

$\triangle$t denotes the elapsed time between two stations, t_n and t_{n+1} correspond to one station *n* and the next station *(n+1)*, respectively. The change over time of the POC concentrations was computed in the same way.

III.2.2.5. Total alkalinity and pH

Ice cores were cut into 10 cm sections in a cold room (at -25°C). Each section was placed in a gas-tight Supelco® Tedlar® bag equipped with a push/pull lock valve. The bag was sealed with a clip, and the air was removed using a vacuum pump through the valve. The bagged sea ice samples were then melted at room temperature for less than 24 h. Attention was paid to mix the bags regularly in order to keep the meltwater at melting temperature and to treat meltwater as soon as possible after complete melting to avoid warming of the meltwater and subsequent carbonate dissolution as suggested by Dieckmann et al. (2008). Meltwater was shaken to resuspend the crystals and aliquots were collected for pH, bulk alkalinity (TAb) and filtered alkalinity (TAf) analyses. pH was measured using a Metrohm® combined electrode calibrated on the total hydrogen ion scale using TRIS (2-amino-2hydroxymethyl-1.3-propanediol) and AMP (2-aminopyridine) buffers prepared at salinities of 5, 35 and 75 according to the formulations proposed by DOE (1994). The pH measurements were carried out at low temperature (typically below +4°C). The accuracy of pH measurements was ±0.01 pH units. Samples for TAf were filtered on 0.2 μm polycarbonate filters. Filtration was carried out at 4°C in order to avoid any dissolution of calcium carbonate. TA was measured by open-cell titration with HCl 0.1 M on 50 ml of sea ice melt samples, following Gran (1952) endpoint determination. Titration was stopped for 10 minutes at pH 4.2 to ensure the dissolution of any calcium carbonate crystals, prior to perform the measurements between pH of 4.2 and 3 required for the Gran function. The accuracy of TA measurements was ±4 μmol kg^{-1}. Data were quality checked with certified reference material from Andrew Dickson (Scripps Institution of Oceanography, University of California, San Diego).

III.2.2.6. O_2 and Ar concentrations

The dry-crushing technique, developed for gas measurements in continental ice (Raynaud et al., 1982), was used to extract O_2 and Ar from the ice samples. This technique allows the extraction of both gas bubbles and gas dissolved in liquid brines. The ice core was cut into 5 cm sections, and each ice cube of about 60 g was placed into a vessel, with seven stainless steel balls. The latter was crushed in the vessel as described in Stefels et al. (2012), at a temperature of -25°C and under a vacuum of 10^{-3} torr. The vessel was then kept at -50°C in a cold ethanol bath and connected to the gas chromatograph equipped with a thermal conductivity detector for concentration analyses. We used He (Air Liquide® – Alphagaz 2) as the carrier gas and a 22 ml packed column (Mole Sieve 5A 80/100; 5 m × 1/8 in.). The repeatability of the analyses (i.e., the precision of the gas chromatograph) was 0.7% for O_2 and 2.3% for Ar (Zhou et al., 2014).

III.2.2.7. Bulk ice pCO_2 measurements

Bulk ice pCO_2 was measured using the method developed by Verbeke (2005) and Geilfus et al. (2012b) and adapted by Crabeck et al. (2014a). The general principle of the method is to equilibrate sea ice samples with a N_2/CO_2 gas mixture of known concentration (standard gas) as close as possible to the in situ temperature (i.e. the temperature of the ice upon ice collection). Once the ice sample is equilibrated, the gas phase is injected into a gas chromatograph (Varian 3300) to measure the CO_2 concentration (Geilfus et al., 2012b).

The ice core was first cut with a vertical resolution of 5 cm. Ice sections were then precisely cut into 4 x 4 x 4.5 cm cubes to tightly fit the equilibration container. Attention was paid to maximize the sea ice volume, to minimize the headspace volume and to keep it equivalent for each sample. Standard gas was injected at atmospheric pressure into the headspace of the container containing the ice sample. Tests were carried out with standard gas at 150 ppm, 300 ppm and 500 ppm. While the three standards gave consistent results below 200 ppm, as expected the 150 ppm standard provided underestimated measurements above 200 ppm. Standards at 300 ppm and 500 ppm provided consistent results below 350 ppm and above 500 ppm, overestimated values in between were observed with the standard at 500 ppm. As a consequence, we used a standard gas of 300 ppm for all samples. The container, kept at -50°C during the standard injection, was then placed in a thermostatic bath to bring the ice sample to the in situ temperature. After 20 h, the sample was assumed to be in equilibrium with the standard gas (Crabeck et al., 2014a; Geilfus et al., 2012b). The headspace was then injected in the gas chromatograph to measure the CO_2 concentration. Shortly afterward, the sample temperature was measured using a calibrated probe (TESTO® 720). The method is expected to be valid if the ice is permeable at the in situ conditions. Standard gas concentration should be as close as possible from the expected concentration of the sample in order to achieve sufficient accuracy (Verbeke, 2005).

The precision of the measurements was estimated based on 28 injections of standard gas 300 ppmv (injection pressure ranged between 10 and 99 Torr). We obtained a mean relative error of 2.1%, a standard deviation of 9.8 ppm and a variation coefficient of 3.3%.

III.2.3. Computed parameters

III.2.3.1. Brine volume and Rayleigh number

The brine volume fraction (BrV), a proxy of sea ice permeability, was computed from ice temperature and salinity following the equations of Cox and Weeks (1983) for ice temperature <-2°C and Leppäranta and Manninen (1988) for ice temperature $\geq$ -2°C. We considered that the ice was permeable for a brine volume fraction exceeding 5% (Golden et al., 1998). The Rayleigh number (Ra) was used as a proxy of the intensity of brine convection (Notz and Worster, 2008) which is driven by the density difference between high-salinity brine in sea ice and the seawater underneath (Vancoppenolle et al., 2013a). Theoretically, convection can occur in an ice layer when Ra exceeds a critical value of 10 (Notz and Worster, 2008) or 8 (Zhou et al., 2013) according to experimental studies. The critical value could also be considered as low as 4 (Carnat et al., 2013; Vancoppenolle et al., 2013b) although this critical value is still quite debated and also sensitive to the potential delay between occurrence and observation.

III.2.3.2. DIC

Dissolved inorganic carbon (DIC) was computed from TAf and pH (presented in Figure S1), according to CO_2 acidity constants of Goyet and Poisson (1989) as suggested by Brown et al. (2014) for measurement in brines at sub-zero temperatures, and other constants proposed by DOE (1994). We used TAf for DIC computation in order to avoid bias from the potential dissolution of particulate inorganic carbon (e.g. ikaite formed in sea ice).

DIC and TAf were normalized to a salinity of 6, the mean bulk ice salinity, in order to remove the salinity-related changes (i.e. brine rejection, concentration, and dilution). The normalized DIC and TAf are referenced hereafter as DIC_6 and TAf_6, respectively.

III.2.3.3. NCP from DIC

Net community production based on inorganic carbon deficits (NCP_{DIC}), was computed from changes in observed DIC, TAf, nitrate plus nitrite, and phosphates according to:

$$NCP_{DIC} = -\frac{\triangle DIC}{\triangle t} + 0.5\frac{\triangle TAf + \triangle NO_3^- + \triangle NO_2^- + \triangle PO_4^{3-}}{\triangle t} \tag{12}$$

where $\triangle$t denotes elapsed time between two stations (Delille et al., 2005). The second term of the equation 12 corresponds to the difference in carbonate alkalinity due to the formation or dissolution of calcium carbonate. $\triangle$DIC is the difference between DICt_{n+1} and DICt_n normalized to the St_{n+1}, t_n and t_{n+1} corresponding to the station n and the next station *(n+1)*. $\triangle$TAf, $\triangle \mathrm{NO}_3^-$, $\triangle \mathrm{NO}_2^-$ and $\triangle \mathrm{PO}_4^{3-}$ were computed in the same way. We assumed that no physical process has affected the bulk impurity content of the ice from one station to the next one, and that all these changes are therefore due to biological processes. NCP_{DIC} is given in $\mathrm{mg\,C\,m^{-2}\,d^{-1}}$.

III.2.3.4. NCP from O_2/Ar ratios

Oxygen concentrations in sea ice depend on both biological activity and physical processes. We used argon measurements to remove the influence of physical impact on O_2 concentrations. Argon has indeed no biological sources or sinks but it is affected by physical processes in the same way as oxygen concentrations. O_2 concentrations associated to in situ biological activity ($[\mathrm{O}_2]_{bio}$) were obtained from O_2/Ar ratios and their deviation from saturation as described for seawater by Reuer et al. (2007) and adapted for sea ice by Zhou et al. (2014).

O_2/Ar ratios observed in ice were compared with atmospheric and seawater ratios to determine the abiotic range of O_2/Ar values. Within the abiotic range of O_2/Ar values, it is not possible to discriminate biological processes from physicochemical processes, since changes of O_2/Ar ratio can be ascribed to biological processes but also to the input of atmospheric air or underlying seawater. The atmospheric O_2/Ar ratio is 22.5 based on O_2 and Ar mixing ratios in the atmosphere (NOAA, 1976). Any gas input from the atmosphere or gas bubble formation would push the bulk ice O_2/Ar ratio towards 22.5. At the seawater interface, considering conditions of -1.8°C and a salinity of 34, the O_2/Ar ratio is 20.5 (Garcia and Gordon, 1992; Hamme and Emerson, 2004). Given these ratios, the abiotic range of O_2/Ar in sea ice is determined to lie between 20.5 and 22.5. Out of this range, O_2/Ar values were attributed to the impact of biological activity only and have been considered for computation of net community production.

In order to do so, we first calculated the theoretical brine solubility of each gas using temperature, the salinity of the brine calculated from ice temperature (Cox and Weeks, 1986) and the relationships from Garcia and Gordon (1992) for O_2 and Hamme and Emerson (2004) for Ar. Brine solubility multiplied by the brine volume fraction gives the gas solubility in bulk ice (hereafter referred as $[O_2]_{eq}$ and $[Ar]_{eq}$).

The O_2/Ar deviation from saturation was calculated as follows:

$$\triangle({}^{O_2}/_{Ar}) = \frac{{}^{[O_2]}/_{[Ar]}}{{}^{[O_2]_{eq}}/_{[Ar]_{eq}}} - 1 \tag{13}$$

$[O_2]$ and [Ar] are the sea ice concentrations measured at a vertical resolution of 5 cm and interpolated using the IDL program (Harris Geospatial). O_2 and Ar supersaturation are commonly observed in sea ice (Zhou et al., 2014), indicating that equilibrium concentrations can differ from their solubilities due to physical processes. In order to deal with potential biases while using O_2 and Ar solubilities for $[O_2]_{eq}$ and $[\mathrm{Ar}]_{eq}$, we modified the calculations from Zhou et al. (2014) as follows:

$$[O_2]_{phys} = [O_2]_{eq}({}^{[Ar]}/_{[Ar]_{eq}}) \tag{14}$$

The O_2 concentration associated with in situ biological activity is then defined using the following equation:

$$[O_2]_{bio} = [O_2]_{phys}\triangle({}^{O_2}/_{Ar})(\mu\mathrm{mol\,L^{-1}}) \tag{15}$$

The daily O_2 production is given in $\mu\mathrm{mol\,L^{-1}\,d^{-1}}$. We considered the ice thickness, a O_2/C ratio of 1.43 (Glud et al., 2002) and the molar mass of C in order to derive the C uptake equivalent ($\mathrm{mg\,C\,m^{-2}\,d^{-1}}$).

The propagation of uncertainties on $[O_2]_{bio}$ was estimated using a Monte Carlo approach. We neglected the error on gas diffusion assuming equivalent diffusivities for O_2 and Ar in sea ice as in Crabeck et al. (2014a). Each parameter was given a distribution to represent its uncertainty sampled over 10^5 iterations. Normal or uniform distributions between the mean ± error of measurements were used. Measured parameters (T, S, O_2, Ar) were given normal distribution with the mean population and an error of 0.2 for T, 0.1 for S, 0.7% for O_2 and 2.2% for Ar. The error on ${}^{[O_2]_{eq}}/_{[Ar]_{eq}}$ ratio is prone to larger uncertainties and was therefore given an uniform distribution of 9.9% either side of calculated value to account for gas bubble formation in sea ice (Zhou et al., 2014). The obtained maximum uncertainty of $[O_2]_{bio}$ was 19.6%.

Net community production (NCP) is determined from the change over time of oxygen concentrations associated to in situ biological activity ($[O_2]_{bio}$), as follows:

$$NCP = \frac{[O_2]_{bio}(t_{n+1}) - [O_2]_{bio}(t_n)}{\triangle t}(\mu\mathrm{mol\,L^{-1}\,d^{-1}}) \tag{16}$$

$\triangle$t denotes elapsed time between two stations, t_n and t_{n+1} correspond to the station n and the next station (n+1), respectively.

III.2.3.5. Assessment of calcium carbonate content

Two different indicators were used to assess calcium carbonate precipitation: the overall calcium carbonate content ($[CaCO_3]$) and the saturation state of ikaite (Ω_{ika}).

The overall $CaCO_3$ content was estimated from the difference between total alkalinity of a nonfiltered sample, denoted as bulk alkalinity (TAb) and total alkalinity of the filtered sample, denoted as filtered alkalinity (TAf) (Geilfus et al., 2013), according to

$$[CaCO_3] = \frac{1}{2}(TAb - TAf) \tag{17}$$

Calcium carbonate precipitation (dissolution) can take place if the saturation state of ikaite in brine $\Omega_{ika} > 1$ ($\Omega_{ika} < 1$). The saturation state of ikaite in brine depends on the concentrations of calcium and carbonate in brine and their solubility product described as a function of temperature T(K) by Papadimitriou et al. (2013):

$$pK_{(sp,ikaite)} = -15489.09608 + 623443.70216\ T^{-1} + 2355.14596\ lnT \tag{18}$$

While this solubility product has been established for temperatures above -8°C, we used it below this threshold and assumed it constant. We acknowledge that we neglected some physical processes such as concentration and dilution. This approach thus presents some limitations. We estimated the salinity of brines using a third-order fit from Assur (1958) and Notz (2005). We also computed TA_{brines} and DIC_{brines} by considering their linear dependence to salinity in order to obtain CO_3^{2-} brine concentrations from CO2SYS program for the carbonate system (Lewis et al., 1998). More details can be found in Moreau et al. (2015).

III.3. Results

III.3.1. Sea ice and snow properties

Main sampling took place from late winter (September 2012), when daylight was still short and the air temperature was low (down to -32°C), to late spring (November 2012). Three stations were also carried out in December 2011 with an air temperature above 0°C and high solar irradiance (Figure 21). The mean sea ice thickness ranged between 145 cm and 171.4 cm (Figure 20). The ice texture was homogenous between stations. From top to bottom, we observed a thin layer of granular ice followed by a mixture of granular and columnar ice, a thick layer of columnar ice, columnar ice with isolated platelets and a bottom layer of columnar and platelet ice (Figure 20). The snow cover ranged from 0 to 4 cm thick, with salinities ranging from 7.4 to 24.5.

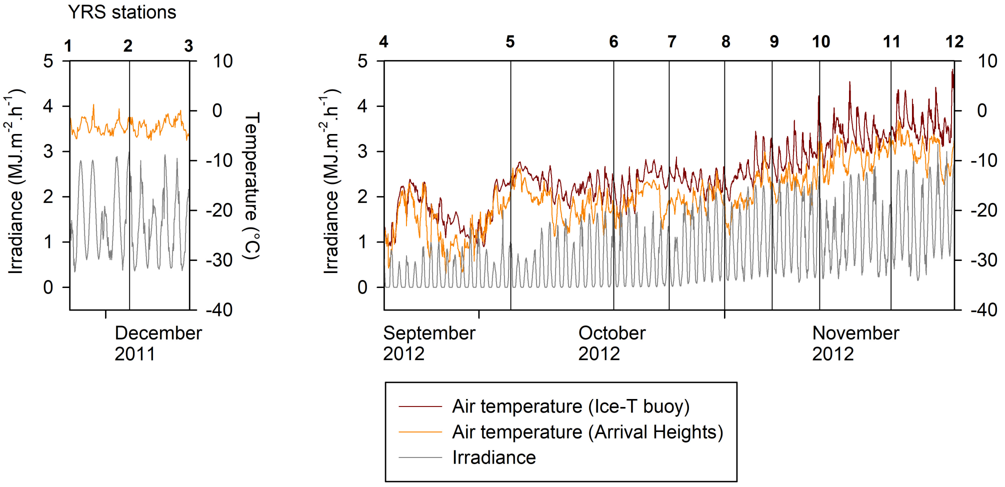

Figure 21: Evolution of air temperature recorded by the ce-T buoy in 2012 (brown line), air temperature (orange line), and solar radiation (gray line) in 2011 and 2012 recorded by the weather station at Arrival Heights (23 km away from sampling location).

The bulk ice temperature ranged from -19.8°C to -0.8°C and showed a strong vertical gradient (Figure 22a). The lowest ice temperature appeared in the upper layer in winter while the temperature in bottom ice was close to the freezing point (i.e. -1.8°C). At the end of the spring (stations YRS1 to YRS3), the ice displayed a nearly isothermal profile. As the ice temperature increased in spring, the ice became fully permeable from station

YRS10 (Figure 22c), when the brine volume fraction exceeded 5%, the threshold for fluid transport (Golden et al., 1998).

The vertical distribution of salinity showed little changes from YRS4 to YRS10 after which surface salinity decreased (Figure 22b). Homogenous salinity profiles were observed in late spring 2012 (stations YRS11 and YRS12) and 2011 (stations YRS1-3). The average bulk salinity for the whole data set was 6. The Rayleigh (Ra) number started to increase at station YRS7 and reached a maximal value of 17 at station YRS11, exceeding the critical convection threshold of 10 (Notz and Worster, 2008). Ra values indicated a convective event in station YRS11 (Figure 22d). However, apart from this specific event, Ra values did not indicate any other obvious convection event, consistently with the salinity distribution.

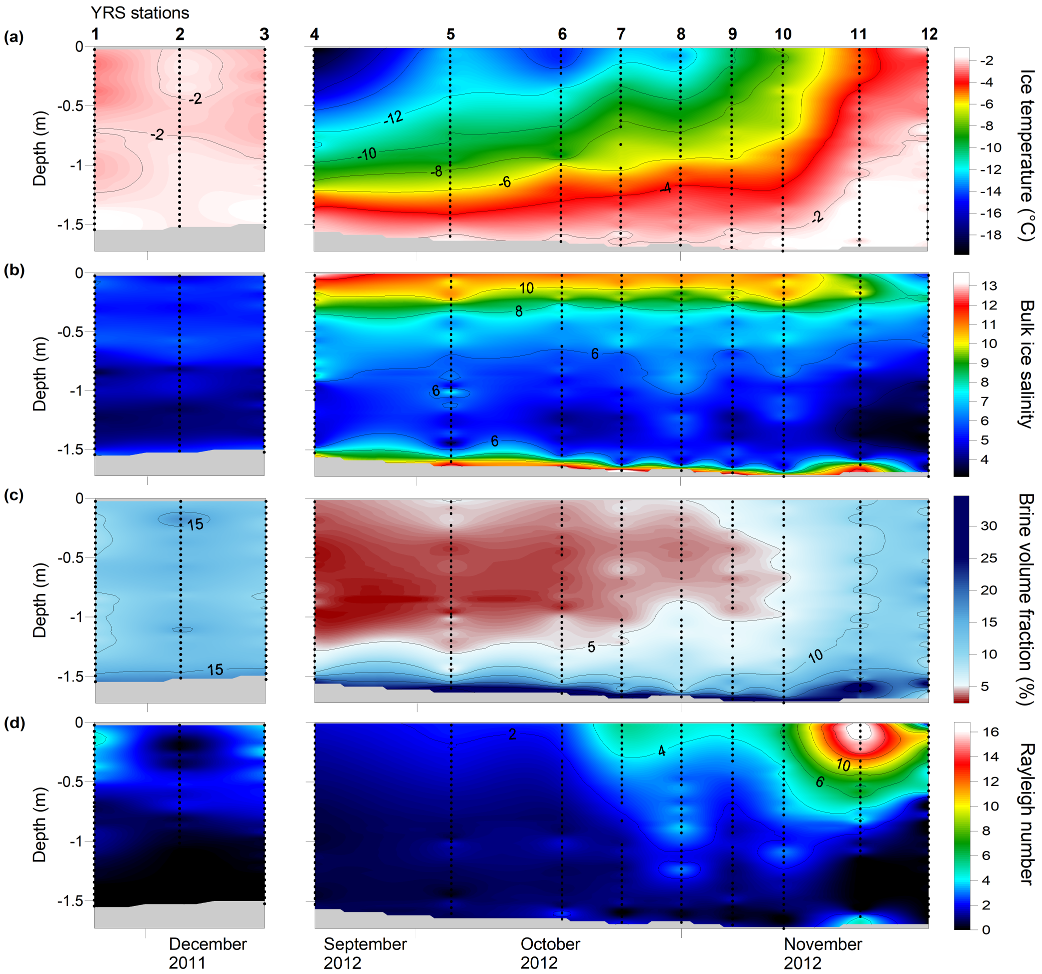

Figure 22: Temporal evolution of (a) ice temperature, (b) bulk ice salinity, (c) brine volume fraction, and (d) Rayleigh number. Plots were produced using the radial basis function method for interpolation in Surfer 8 software. Black dots are data points from field sampling.

III.3.2. Ice carbon content

III.3.2.1. A "three-layers" model based on DIC_6

DIC_6 ranged from 194 to 563 μmol kg^{-1} (Figure 23b) and exhibited strong vertical gradients within the ice column. These gradients were used to discriminate the ice column in three layers: surface, interior, and bottom. The layer between 20% and 83% of the ice thickness is considered as the interior layer and corresponds to relatively constant (standard deviation below 69 μmol kg^{-1}) and highest DIC_6 values (except in late spring from stations YRS1 to YRS3). The surface and bottom layers account for 20% and 17% of the total ice column, respectively (Figure 23b).

DIC_6 increased at all depths from stations YRS4 to YRS6 and then rapidly decreased between stations YRS6 and YRS7. From station YRS7 onwards, DIC_6 values in the surface and bottom layers significantly deviate compared to the mean value observed in the ice interior. Surface DIC_6 oscillated with both increasing and decreasing periods while bottom DIC_6 remained low (<352 μmol kg^{-1} except for station YRS11) and below seawater values (mean DIC_{SW} normalized to salinity 6: 378.8 ± 17.3 μmol kg^{-1} at 0 m depth), although slightly increasing at the end of the study (YRS 11-12). Changes in DIC_6 are mainly due to biogeochemical processes such as CO_2 consumption or production, precipitation, and dissolution of calcium carbonate and exchanges of CO_2(g).

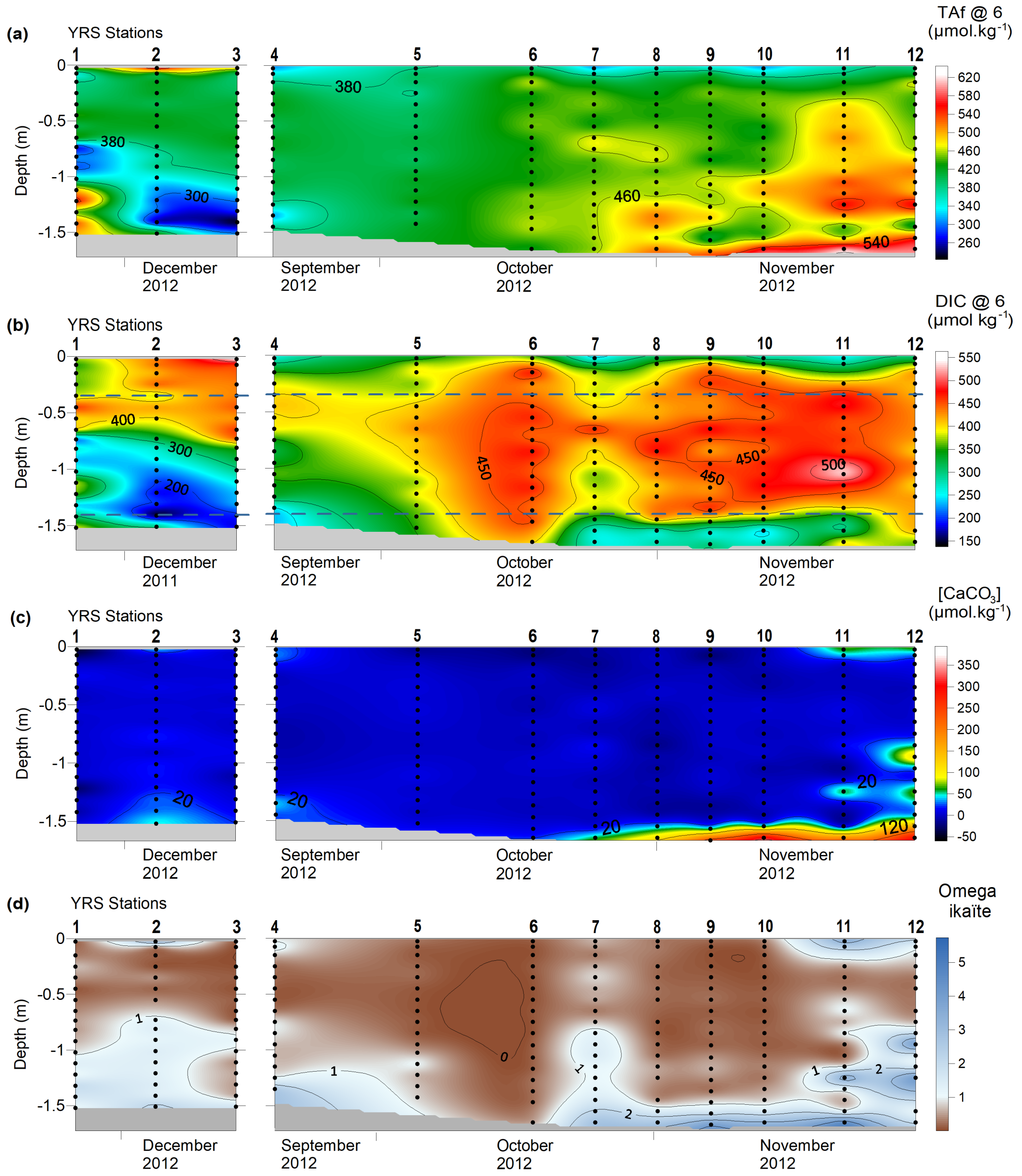

Figure 23: Temporal evolution of (a) TAf_6, (b) DIC_6, (c) $CaCO_3$ content, and (d) omega ikaite. Black dots are data points from field sampling. Horizontal blue lines mark the limits between the surface, interior, and bottom layers of the ice. Plots were produced using the radial basis function method for interpolation in Surfer 8 software.

III.3.2.2. Calcium carbonate precipitation

TAf_6 increased gradually at the bottom of the ice from late winter (station YRS7) to late spring (station YRS12) reaching values up to 550 μmol kg^{-1} (Figure 23a). The $CaCO_3$ content followed the same trend as TAf_6 at the bottom of the ice suggesting localized calcium carbonate precipitation. We estimated that up to 350 μmol kg^{-1} $CaCO_3$ precipitated in late spring (Figure 23c). Accordingly, high Ω_{ika} values were mainly observed at the bottom of the ice from stations YRS7 to YRS12 (Figure 23d). At the sea ice surface, no significant calcium carbonate precipitation occurred except potentially at stations YRS11 and YRS12.

III.3.2.3. Biomass and nitrate concentrations

Most of the ice algal biomass (66 to 99.9%) was concentrated in the bottom 10 cm of the ice (Table S1) with values reaching over 2400 $\mu\text{g}\,\text{L}^{-1}$ in spring (Figure 24a). Under-ice seawater concentrations remained low (<0.41 $\mu\text{g}\,\text{L}^{-1}$) from stations YRS4 to YRS12. The onset of the spring ice-algal bloom was initiated at YRS6 and chl-a was accumulating until station YRS10.

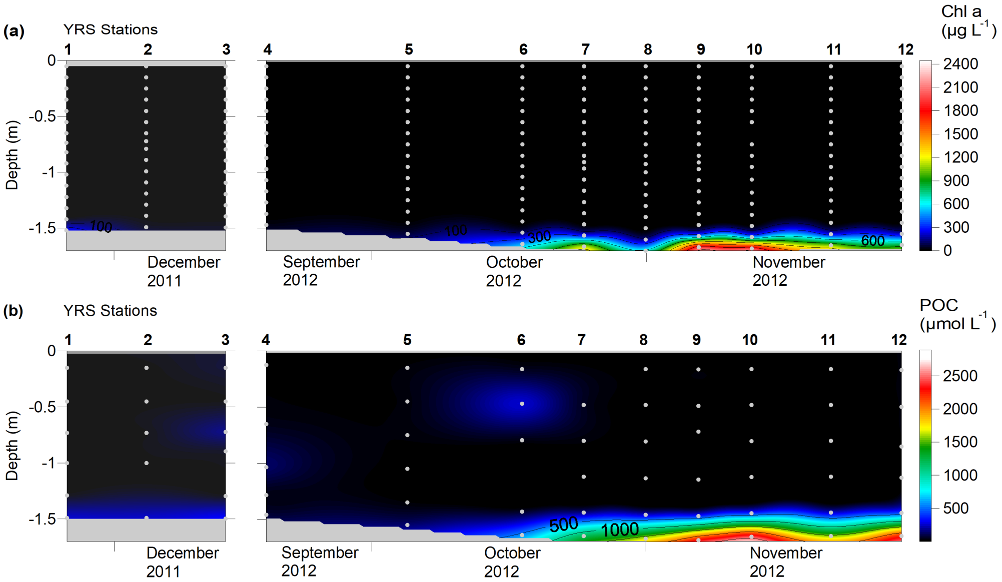

Figure 24: Temporal evolution of (a) chlorophyll a and (b) POC concentrations in sea ice. Plots were produced using the radial basis function method for interpolation in Surfer 8 software. Gray dots are data points from field sampling.

POC accumulated in parallel with the increasing algal biomass in the bottom ice. POC concentrations increased by 1100 $\mu\text{mol}\,\text{L}^{-1}$ between stations YRS8 and YRS10 (in 12 days) to reach maximum value around 2600 $\mu\text{mol}\,\text{L}^{-1}$ in station YRS10 (Figure 24b). Bulk concentrations of nitrate plus nitrite ranged from 0.1 $\mu\text{mol}\,\text{L}^{-1}$ to 97.1 $\mu\text{mol}\,\text{L}^{-1}$ (Figure S2). Changes over time of nitrate plus nitrite concentrations and POC concentrations, calculated using Eq. 11 are shown in the Figure 25a,b. Positive values indicate an increase between the two stations considered while negative values indicate a decrease. Both nitrate plus nitrite and POC concentrations were higher in absolute value at the bottom of the ice than in the ice interior and at the surface. Concentrations increased between each station until YRS10 before collapsing at station YRS11.

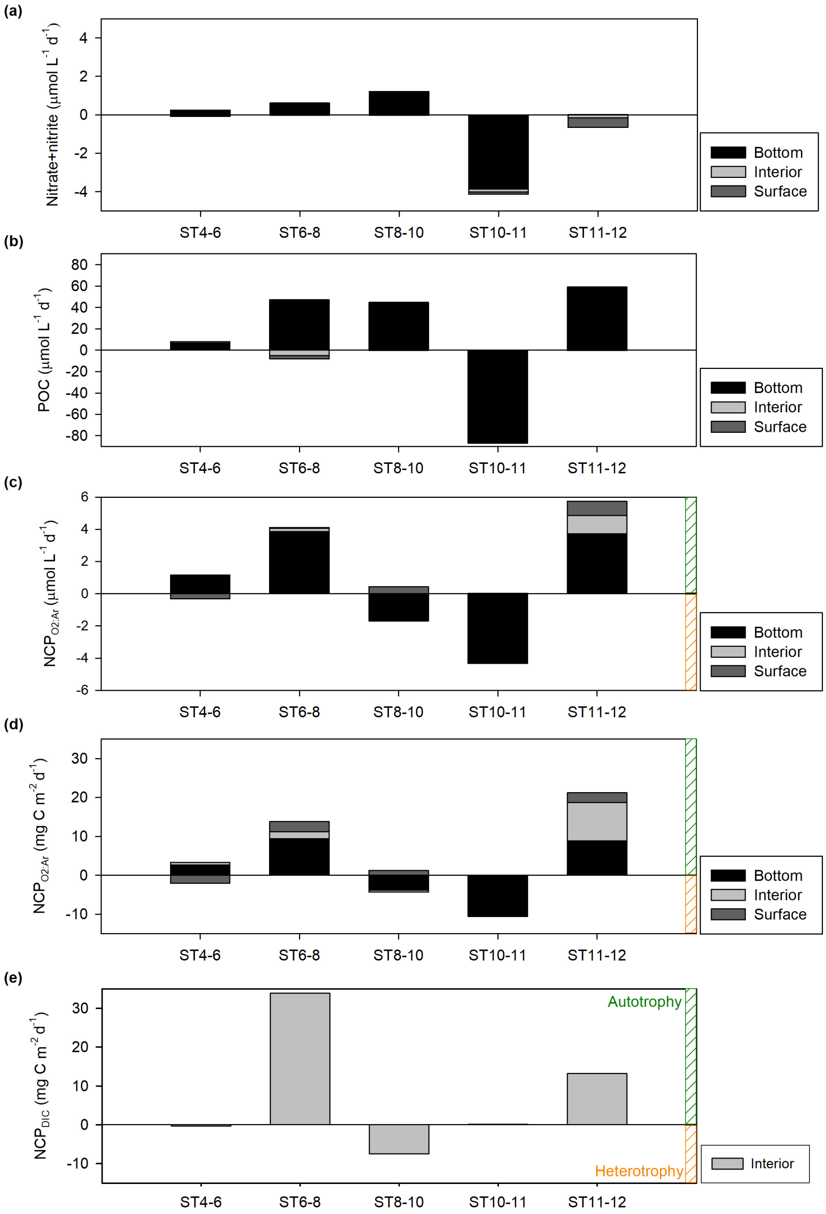

Figure 25: Temporal changes of (a) nitrate plus nitrite concentrations and (b) POC concentrations in surface, bottom, and interior ice layers. Net community production derived from (c, d) O_2/Ar and (e) DIC.

III.3.2.4. Oxygen concentrations

The O_2 and O_{2bio} concentrations ranged from 14 to 272 μmol L^{-1} and -13 to 206 μmol L^{-1}, respectively (Figure 26a, b). The maximum concentrations of O_2 and O_{2bio} were encountered in the bottom sea ice where maximum values of chl-*a* were observed. An increase in oxygen concentrations was observed from YRS4 to YRS8 during the exponential phase of the bloom and a decrease occurred afterward. Our data highlighted a major biogenic contribution to the molecular oxygen pool: O_{2bio} concentrations accounted for 60 to 80% of the O_2 pool at the bottom (Figure 26c).

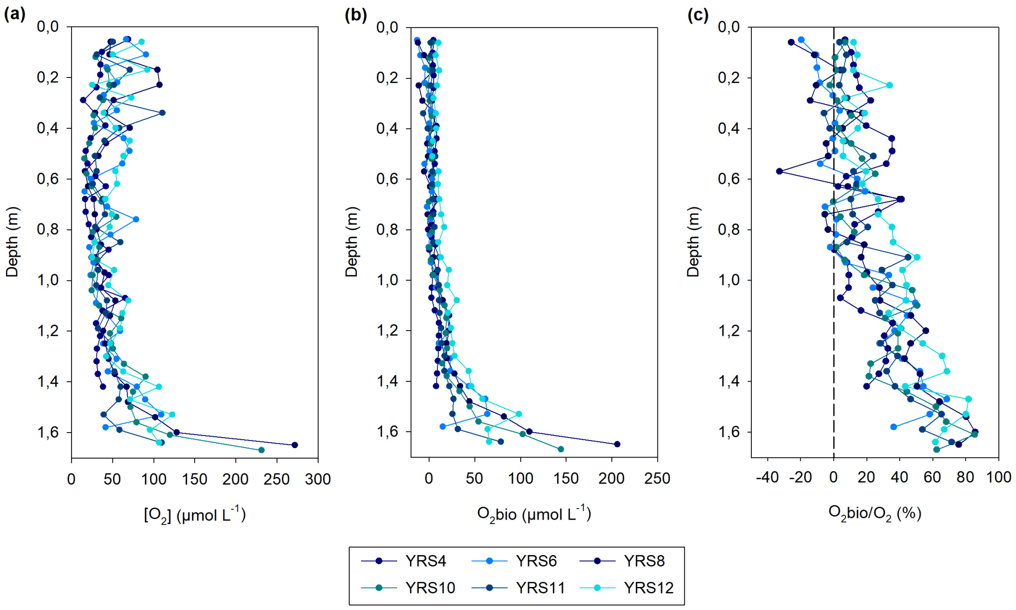

Figure 26: Vertical profiles of (a) O_2 concentrations in bulk ice, (b) $[O_2]_{bio}$ calculated from Equation 15, and (c) O_{2bio}/O_2 ratio.

III.3.2.5. NCP

Figure 25 presents the variables used as tracers of production during this study, which have been computed consistently (i.e. same depths and time steps). Tracers of production are changes in nitrate plus nitrite (in μmol L^{-1} d^{-1}, Figure 25a), POC (in μmol L^{-1} d^{-1}, Figure 25b), NCP derived from O_2/Ar ratios ($NCP_{O_2:Ar}$ in μmol L^{-1} d^{-1}, Figure 25c) and NCP derived from DIC (NCP_{DIC} in mg C m^{-2} d^{-1}, Figure 25e). These assessments are given for each layer (surface, interior, bottom) with the exception of NCP_{DIC} given only for the interior ice. While $NCP_{O_2:Ar}$ accounts for gas exchanges thanks to the use of Ar concentrations to trace physical processes, NCP_{DIC} is sensitive to CO_2 fluxes at the interfaces - surface and bottom layers -, preventing robust estimates in theses layers. In order to allow comparison with the literature, we also provided integrated $NCP_{O_2:Ar}$ (mg C m^{-2} d^{-1}) for the entire ice column (Figure 25d).

Bottom $NCP_{O_2:Ar}$ ranged between -4.3 to 3.8 μmol L^{-1} d^{-1}. Positive NCP indicates an oxygen production (equivalent to an inorganic carbon uptake) while negative NCP corresponds to oxygen consumption (equivalent to inorganic carbon production). We compared our measurements with available data of net community production in Arctic sea ice (Table 3). Our measurements fall within the estimates carried out either by O_2/Ar assessment or oxygen incubation. Our values are at the lower end of previous estimates of NCP for bottom Antarctic sea ice from McMinn et al. (2012) derived from in situ oxygen fluxes across the downwards boundary layer estimated with an oxygen micro-electrode.

NCP$_{O_2:Ar}$ was higher in absolute value in the bottom sea ice compared to the upper layers (Figure 25c). At the bottom, NCP was positive at the end of the winter indicating a net autotrophy (stations YRS4-8), then heterotrophy dominated during spring (YRS8-11) before it turned back to autotrophy at the end of the spring (YRS11-12). In the ice interior, the same pattern was observed, although with a lower amplitude. Autotrophy dominated the sea ice surface except from stations YRS4 to YRS6.

We compared NCP$_{O_2:Ar}$ with NCP$_{DIC}$ for the interior ice. NCP$_{DIC}$ showed similar trends and the same order of magnitude as NCP$_{O_2:Ar}$ for stations YRS8-10 and YRS11-12. A discrepancy in terms of magnitude appeared for stations YRS6-8.

III.3.2.6. pCO$_2$

The sea ice pCO$_2$ ranged from 2 ppm to 810 ppm during the survey (Figure 27). The strongest pCO$_2$ gradient throughout the ice column was observed at YRS6, where the pCO$_2$ increased from 120 ppm at the bottom to 810 ppm at the top of the ice core. In late winter, pCO$_2$ under-saturation relative to the atmosphere was observed at the bottom of the ice while pCO$_2$ increased towards the ice surface where over-saturation conditions prevailed.

The upper 10 cm of sea ice became undersaturated at station YRS9 with surface pCO$_2$ as low as 230 ppm. From station YRS10, the pCO$_2$ decreased throughout the ice column with particularly low pCO$_2$ at the surface ($<$ 45 ppm) for stations YRS11 and YRS12. The YRS3 profile obtained the previous year at a similar stage of the ice melting season showed a similar trend (Figure S3). The entire ice column was under-saturated in late spring.

Bottom pCO$_2$ remained particularly low during the entire study period (below 210 ppm or even below 40 ppm for stations YRS11, 12 and 3).

The pCO$_2$ values observed in this study fall within the same range of previous sea ice measurements in the Southern Ocean (Delille et al., 2014; Geilfus et al., 2014) despite the fact that the measurement methods differ (bulk vs brines). All the studies reported in Table 5 showed recurrent low pCO$_2$ values observed in the ice and brines.

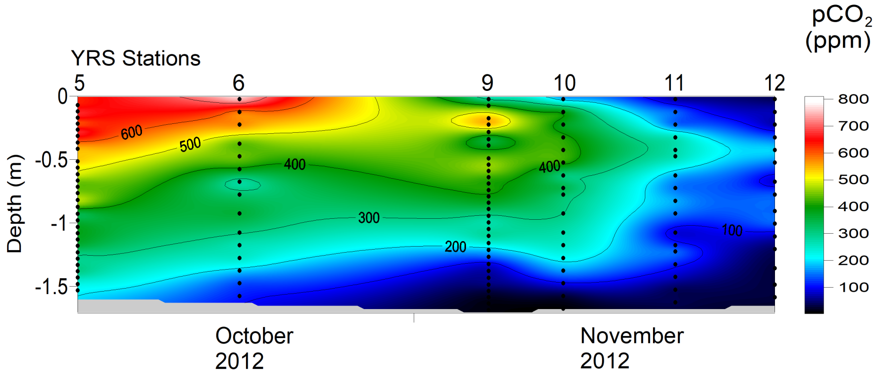

Figure 27: Temporal evolution of pCO$_2$. Samples were analyzed with a standard gas of 300 ppm. Black dots are data points from field sampling. This plot was produced using the radial basis function method for interpolation in Surfer 8 software.

Table 5: Summarized Data for Bulk and Brine pCO$_2$ Records in the Arctic and Southern Oceans as well as in Saroma-Ko.

Location	Ice type	Method	Season	pCO$_2$ (ppm)	Reference
Saroma-Ko, Japan	Landfast ice	Computed from brine DIC/TA	Winter	2.7–195	Nomura et al. (2010b)
Arctic Ocean					
Resolute Passage, Nunavut	Landfast ice (first year)	Computed from brine DIC/TA Brine pCO$_2$ computed from bulk DIC/TA	Spring	200–1128 2–3326	Brown et al. (2015)
Resolute Passage, Nunavut	Landfast ice (1st year)	In situ brine (peepers) In situ bulk Bulk computed from DIC/TA In situ brine	Late Spring	230–1280 6 –182 0–32 20–389	Geilfus et al. (2015)
Point Barrow, Alaska	Landfast ice (1st year)	In situ bulk	Spring	23–442	Geilfus et al. (2012b)
Amundsen Gulf, Beaufort Sea	Pack ice and landfast ice	In-situ brines	Spring	0–1839	Geilfus et al. (2012a)
Nuuk, Greenland	Landfast ice	In situ bulk	Spring	77–330	Crabeck et al. (2014a)
Southern Ocean					
Bellingshausen Sea	Pack ice (1st year)	In situ bulk	Spring	9–193	Geilfus et al. (2014)
Bellingshausen Sea, Weddell Sea, Indian sector of the SO	Pack ice (1st year)	In situ brine	Spring-Summer	28–921	Delille et al. (2014)
Cape Evans (Ross Sea)	Landfast ice	In situ bulk	Spring-Summer	2–810	This study

III.3.2.7. Air-snow-ice CO$_2$ fluxes

The CO$_2$ fluxes measured over bare sea ice and snow ranged from -2.51 $\mathrm{mmol\,m^{-2}\,d^{-1}}$ to 1.81 $\mathrm{mmol\,m^{-2}\,d^{-1}}$, and from -9.76 $\mathrm{mmol\,m^{-2}\,d^{-1}}$ to 6.22 $\mathrm{mmol\,m^{-2}\,d^{-1}}$, respectively. In late winter and early spring (September-October), fluxes at the snow-air interface generally exceeded fluxes over bare ice (Figure 28). In late spring (end of November), both negative and positive fluxes occurred over 24h periods (Figure 29).

Data were slightly higher than values previously reported in Antarctica at the same season and using the chamber technique, although falling within the same order of magnitude (Table 2). Available data showed that both negative and positive fluxes are observed during spring in polar regions.

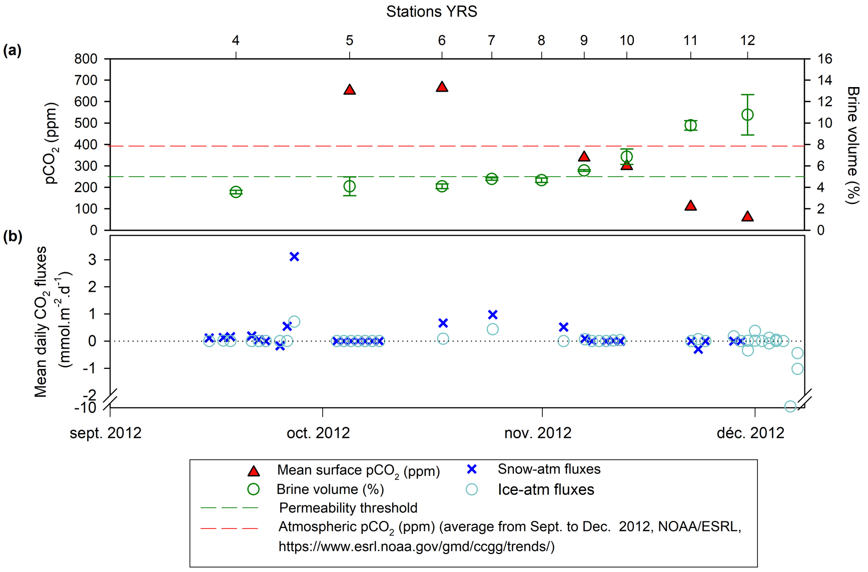

Figure 28: Temporal evolution of (a) mean pCO$_2$ (ppm, red symbols, left axis) for the top 15 cm of the ice and the corresponding mean BrV (%, green symbols, right axis) (b) daily mean CO$_2$ fluxes (mmol m^{-2} d^{-1}) over the ice (light blue open circles) and the snow (dark blue crosses). Positive values indicate CO$_2$ release to the atmosphere, and negative values indicate CO$_2$ uptake.

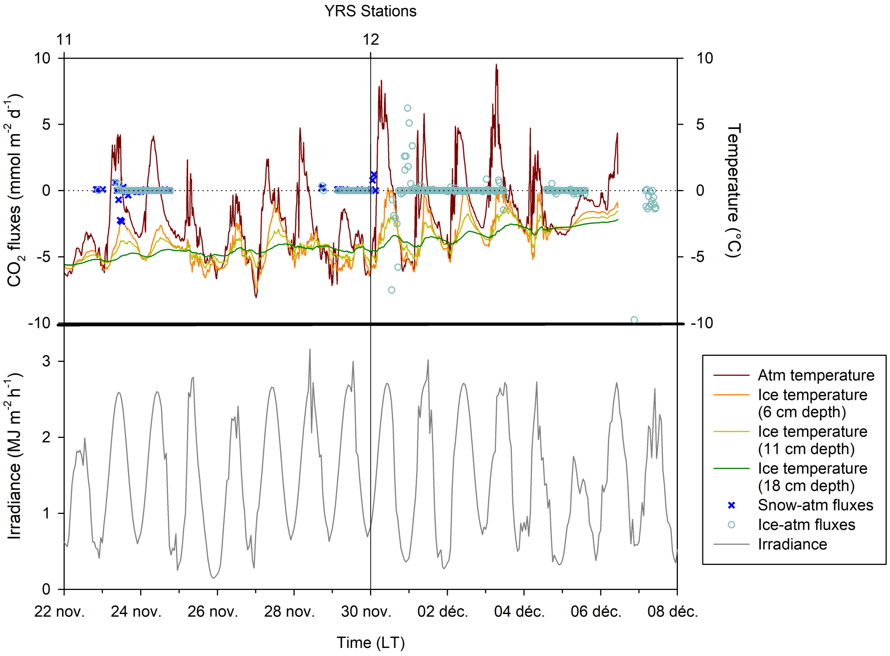

Figure 29: CO$_2$ fluxes in late spring (crosses for snow-atm fluxes and open circles for ice-atm fluxes), air temperature (brown line, recorded at 6 cm above the ice surface with ice-T buoy), ice temperatures (orange, yellow, and green lines, recorded at 6, 11, and 18 cm below the ice surface with ice-T buoy), and irradiance recorded at Arrival Heights (gray line).

III.4. Discussion

III.4.1. The bottom: biofilm implication

III.4.1.1. The high TAf – high Ω_{ika} conundrum

The most striking feature of TAf_6 is the increase in the bottom layers at the end of the spring 2012 (Figure 23a). The dissolution of calcium carbonate crystals (e.g., ikaite) would have increased the TAf_6. However, this increase in TAf_6 co-occurred with calcium carbonate precipitation supported by high Ω_{ika} and high estimated $CaCO_3$ content at the bottom of the ice (Figure 23c,d). We find the origin of this particulate inorganic carbon to be puzzling since inorganic calcium carbonate precipitation or any biogenic calcification (i.e. colonization by planktic foraminifera) would decrease TAf_6 in a closed system, which is opposite to our observations. This implies that excess TAf_6 must have a different origin.

This accumulation of TAf_6 mimics the increase of nutrients at the bottom of the ice during the survey (Figure S2) that has been ascribed to the development of a biofilm (Roukaerts, 2018). Ice-associated biofilms have been suggested in several studies (Boetius et al., 2015; Deming, 2010; Meiners et al., 2003, 2008). Extracellular polysaccharide substances (EPS) secreted by bacteria and algae in sea ice (Krembs and Engel, 2001; Meiners et al., 2003, 2008; Riedel et al., 2006, 2007) are forming a gelatinous network (Decho, 2000; Decho and Gutierrez, 2017; Stewart and Franklin, 2008) and are therefore the backbone of the biofilm. Roukaerts (2018) showed that the development of a biofilm could drive the accumulation of nutrients at the bottom of the ice. In the same way, nutrient trapping was suggested as one of the functions of EPS aggregates and associated biofilm by Stewart and Franklin (2008). Biofilm microenvironments host intense remineralization of organic matter and allow accumulation of nutrients due to the relatively slow diffusion of dissolved compounds between the static biofilm and flowing brine (Stewart, 2003; Stewart and Franklin, 2008). We surmise that the increase in TAf_6 is partly due to the same process or accumulation of dissolved compounds in the biofilm. Besides promoting the storage of calcium carbonate, the presence of the biofilm might also trigger its precipitation. EPS functional groups, mainly negatively charged, can bind to substantial amounts of free Ca^{2+} or other metals (Braissant et al., 2007). This calcium-binding property may initially inhibit calcium carbonate precipitation, but subsequent sequential EPS degradation can create nucleation sites and foster calcium carbonate precipitation (Braissant et al., 2009). The authors developed a conceptual model of microbially mediated calcium carbonate precipitation in the EPS matrix (Figure 30). In the first two steps, the calcium binds to various EPS chemical functional groups (i.e. carboxyl, phosphate, amine, and sulfate esters). This EPS-Ca binding forms a complex with a low-molecular-weight (LMW) organic carbon compound. Upon microbial enzymatic activity, the LMW organic carbon compounds are released and oxidized to bicarbonate, which in turn increases the alkalinity inside the biofilm. Enzymatic activity in sea ice is supported by the presence of cold-active extracellular enzymes able to drive enzymatic hydrolysis or breakdown (Deming, 2007; Helmke and Weyland, 1995; Huston et al., 2000). Finally, the remaining free EPS-Ca sites allow for calcium carbonate precipitation within the EPS matrix. Calcium carbonate precipitation can thus occur in parallel with an increase of alkalinity within the biofilm at the bottom of sea ice, as nitrate plus nitrite concentrations increase in parallel with organic carbon production.

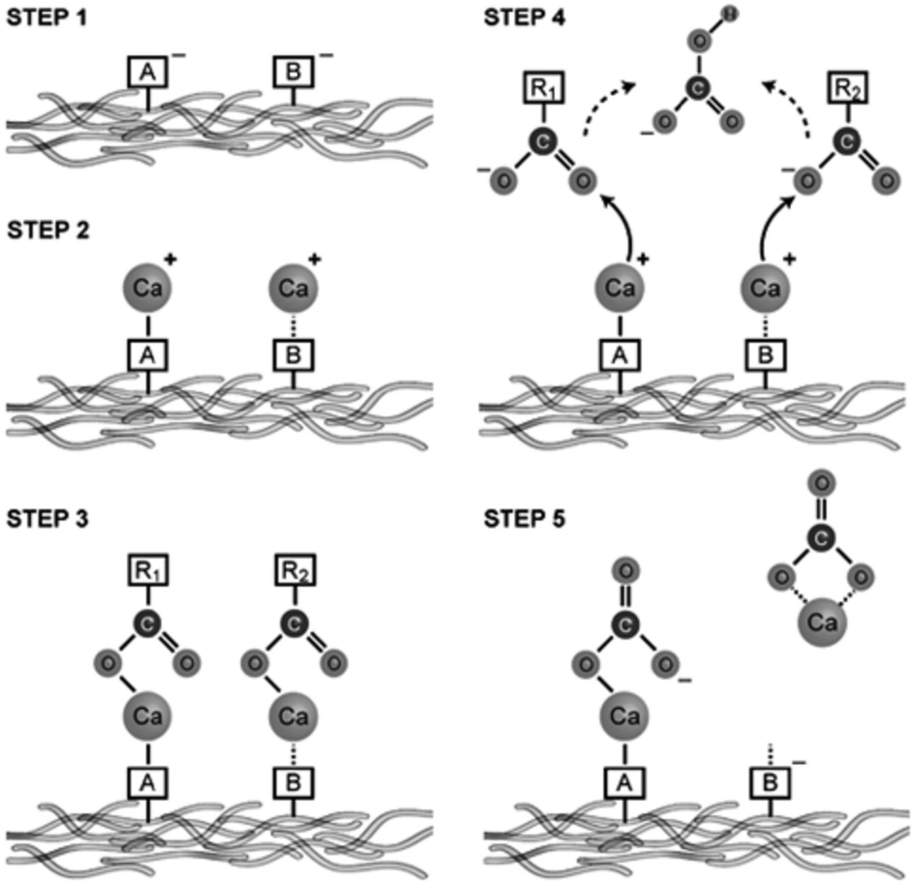

Figure 30: Conceptual model of calcium carbonate precipitation in the biofilm from Braissant et al. (2009). Step 1: EPS functional groups (A and B); step 2: calcium binding more or less tightly to functional groups A and B; step 3: complex formation between LMW organic carbon compound and calcium; step 4: release of LMW organic carbon by microbial activity and oxidation to HCO_3^- which in turn increases TA within the biofilm; step5: $CaCO_3$ formation either on EPS or in pockets within the biofilm. Permission of Federation of European Microbiological Societies.

III.4.1.2. NCP as an indicator of trophic status

The contribution of $O_{2_{bio}}$ to the oxygen pool in sea ice increases steadily with depth. Besides the impact of physical processes (e.g., solubility changes, brine concentration or dilution, vertical transport), biological processes account for up to 80% of the overall oxygen content of the sea ice. The maximal contribution is observed at the bottom of the ice, where the largest biomass concentrations are observed. Sea ice in McMurdo Sound is indeed considered as very productive, with an extremely high build-up of chl-a (Arrigo et al., 1995). Basal concentrations of chl-*a* reached up to 2443 $\mu g\,L^{-1}$ and 2342 $\mu g\,L^{-1}$ (station YRS 9 and YRS10, Figure 24a) and particulate organic carbon up to 2600 $\mu mol\,L^{-1}$. This massive build-up of biomass associated with O_2 accumulation indicates autotrophy. According to the O_2/Ar ratio, autotrophy indeed dominated the bottom sea ice but a transient heterotrophic period was observed between stations YRS8 and YRS11 (Figure 25c,d). Heterotrophy associated with biomass build-up has been reported earlier in the Arctic (Campbell et al., 2017; Rysgaard et al., 2008; Rysgaard and Glud, 2004). To the best of our knowledge, this is the first report of a large biomass build-up associated with a transient heterotrophic period in Antarctic sea ice. The best explanation for such a striking feature at the bottom of the ice is the rapid remineralization of the organic matter (Fripiat et al., 2017, 2014) entrapped within the biofilm (Roukaerts, 2018).

III.4.2. The interior of the sea ice cover

III.4.2.1. NCP

A significant imprint of biological processes on the oxygen pool can also be observed in the ice interior (Figure 26c). $NCP_{O_2:Ar}$ in the ice interior exhibited the same temporal trend as in the bottom ice with dominant autotrophy (Figure 25c,d). NCP values in the interior ice were lower than in the bottom ice, in agreement with biomass concentrations, except for stations YRS11 to YRS12. This higher NCP in the interior at stations YRS11 to YRS12 could be due to upward diffusion of biogenic oxygen enabled with the opening of the brine network (Zhou et al., 2013).

NCP_{DIC} in interior ice showed the same trophic dynamics (autotrophy vs. heterotrophy) as $NCP_{O_2:Ar}$ except for stations YRS4-6 and YRS10-11. From stations YRS11 to YRS12, values agree within 3.4 $mg\,C\,m^{-2}\,d^{-1}$. The largest difference from stations YRS6 to YRS8 is 32 $mg\,C\,m^{-2}\,d^{-1}$. Overall, with the exception of stations YRS6 to YRS8, this suggests that biological activity was the main driver of DIC_6 temporal changes in the ice interior.

III.4.2.2. pCO_2 gradient

Three temporal stages in pCO_2 dynamics have been identified based on physical parameters: (i) super-saturation in the upper half of sea ice (stations YRS5-6) was observed during the winter-spring transition when brine contraction occurred due to cooling, leading to the concentration of salts, CO_2 and other gases associated with brine rejection and upward transport. (ii) Surface under-saturation developed when the top layers become permeable, i.e., when the BrV exceeded 5%, the theoretical permeability threshold for fluid transport through sea ice, according to Golden et al. (1998). pCO_2 at the ice surface decreases below saturation as a first consequence (YRS9 and 10). (iii) Complete under-saturation of the ice column (stations YRS11, 12, and 3 even if preceded by 1 year) was observed by mid-November, with low sea ice pCO_2 as a consequence of ice melting and subsequent brine dilution, brine volume expansion and increase in sea ice permeability.

III.4.3. The surface of the sea ice cover

III.4.3.1. Carbon content

The dissolved inorganic carbon content of sea ice is affected by CO_2 exchanges. DIC_6 concentrations remained low ($< 351\ \mu\mathrm{mol\,kg}^{-1}$) at the top of the ice (first 5 cm), compared to the ice interior. Such a depletion at the top of the ice has been repeatedly observed (Geilfus et al., 2013; Kotovitch et al., 2016; Moreau et al., 2015). This depletion can be ascribed to the CO_2 release to the atmosphere since most primary production was concentrated at the bottom of the ice, and no significant calcium carbonate precipitation occurred at the sea ice surface except potentially at stations YRS11 and YRS12 (Figure 23c,d). CO_2 releases from the ice to the atmosphere occurred throughout all seasons, as explained in the next section.

Precipitation of calcium carbonate at the surface in warm conditions has been rarely reported. It has rather been reported at the surface in cold ice (Nomura et al., 2013a; Rysgaard et al., 2013). However, the slight increase of $CaCO_3$ content at station YRS11 and YRS12 (Figure 23c,d) indicates that precipitation develops at the ice surface consistently with omega ikaite above 1. During the rest of the survey, no precipitation was detected at the surface, while omega ikaite was lower and below 1 in cold surface ice (YRS5-YRS10).

III.4.3.2. pCO_2 and air-snow-ice CO_2 fluxes

CO_2 fluxes exhibited seasonal and diel variations and were likely affected by the thin wet and salty surface snow cover.

III.4.3.2.1. Seasonal variations The seasonal pattern of air-ice CO_2 fluxes direction was consistent with the pCO_2 evolution at the sea ice surface. CO_2 release generally occurred during the sea ice growth when pCO_2 was supersaturated (Figure 28). CO_2 uptake occurred mainly later in the season, during ice decay, when ice became permeable (BrV > 5%), and pCO_2 was undersaturated. This seasonal pattern has also been reported by others (Delille et al., 2014; Miller et al., 2011; Nomura et al., 2010a; Papakyriakou and Miller, 2011). In late spring, fluxes were alternating between release and uptake on a short-time scale.

When the ice was expected to be impermeable during winter, i.e. with brine volume at the sea ice surface below the permeability threshold for fluid transport of 5% (Golden et al., 1998), air-ice fluxes were generally close to zero. However, some significant CO_2 releases over snow-covered ice were observed. These significant winter CO_2 releases have been reported by others using eddy-correlation techniques (Miller et al., 2011; Sievers et al., 2015). This questions the permeability threshold for gas transport in sea ice, permeability being a major control of CO_2 fluxes (Buckley and Trodahl, 1987; Delille et al., 2014). The gas permeability threshold is still debated and has been assessed for brine volumes ranging between 7.5% and 10% according to field observations (Zhou et al., 2013), while models suggest a threshold around 10% of brine volume (Moreau et al., 2014). However, at a smaller scale, the absence of discontinuity in the pCO_2 profiles (Figure S3) can argue for a permeability threshold below 5%.

Indeed, the principle of the pCO_2 measurement method is based on the equilibrium between the ice sample and the gas phase. Hence, the equilibrium depends on the ice permeability for gases. A first-order estimate of this permeability range is the same as the one for liquids (i.e. BrV > 5%). The method should not work below this threshold as reported by Geilfus et al (2012b) in sea ice from Barrow (AK) where pCO_2 in impermeable layers were constant around the concentration of the standard gas. Still, in this study, we carried out pCO_2 measurements for BrV < 5%. The trend was consistent below and within the range of liquid permeability and the pCO_2 exceeded the standard gas concentration in impermeable layers, especially above 130 cm at stations YRS5 and YRS6 (Figure S3). As we did not observe the obvious bias reported by Geilfus et al (2012b) or any significant discontinuity in our pCO_2 profiles, our measurements seem to be valid below the 5%

permeability threshold. This would suggest the BrV threshold for gas permeability to be lower than 5% in sea ice of McMurdo sound. This calls for a better constraint of the permeability threshold for gases.

An alternative explanation for winter CO_2 efflux is the formation of micro-cracks in the landfast sea ice cover. Microcracking has been observed through acoustic studies in the Arctic (Dempsey et al., 2018; Milne, 1972) and Antarctica, especially in McMurdo Sound (Cole and Dempsey, 2004; Dempsey et al., 2018; Langhorne and Haskell, 1996). Ice cracking in the Arctic has been ascribed by Milne (1972) to thermal stress - temperature drop - in winter or spring. Temperature drops induce heat loss at the sea ice surface and subsequent tensile stresses (Ganton and Milne, 1965; Milne, 1972). Cracks, which relieve some of the stresses, are in turn produced along vertical planes and over tens of centimeters (Milne, 1972). Accordingly, visual observations carried out by Light et al. (2003) suggested large changes in microstructure as samples were cooled to -30°C and the presence of microcracks around inclusions while the ice cools and brines are expelled upward. This is consistent with the increase of pressure in sea ice related to ice cooling (Crabeck et al., 2016).

In this study, in early spring (27 September 2012), a sharp air temperature decrease (from -17°C to -25°C) was observed during the night (Figure 31). Ice temperatures followed the same trend and dropped from −17°C to −21°C. Simultaneously, CO_2 efflux up to 6 $\mathrm{mmol\,m^{-2}\,d^{-1}}$ occurred over the snow and the ice. This event is potentially linked to ice cracking. This calls for further investigation of the effect of microcracking on CO_2 release too.

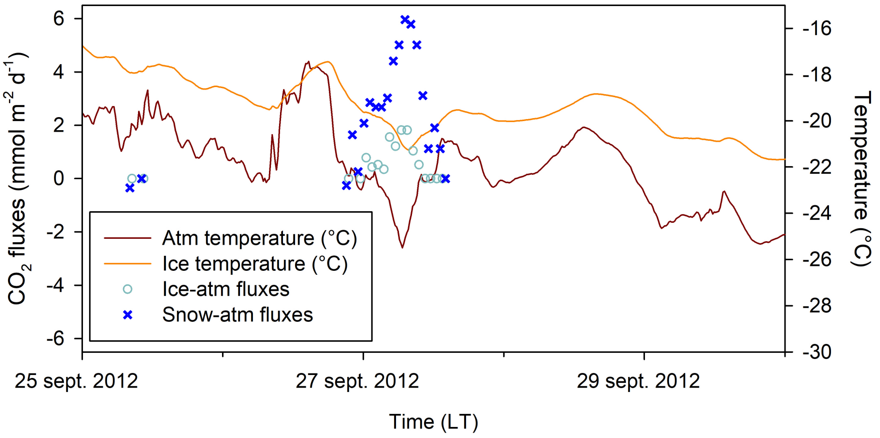

Figure 31: CO_2 fluxes in early spring, air temperature (brown line, recorded at 6 cm above the ice surface with ice-T buoy), and ice temperature (orange line, recorded at 6 cm below the ice surface with ice-T buoy).

III.4.3.2.2. Diel variations in CO_2 fluxes In late spring, both release and uptake of CO_2 occurred over a 24-hour period. Uptake occurred when air and ice temperatures were above 0°C and -5°C, respectively, while release took place when temperatures dropped again below these levels at nighttime (Figure 29).

This diurnal pattern of CO_2 fluxes may be related to an increase of NCP during daylight and a decrease of NCP during nighttime. However, nighttime heterotrophy is questionable since solar irradiance was above 0.4 $\mathrm{MJ\,m^{-2}\,h^{-1}}$ (Figure 29). Then CO_2 release at nighttime should also be ascribed to physical processes. The CO_2 release and uptake sequences could be related to diel temperature variations and the surface freeze-thaw cycles.

Atmospheric temperature variations were mainly affecting the top 6 cm of the ice (Figure 29). We assumed that the surface melt of sea ice was most likely occurring during day time. The subsequent brine dilution can lead to a large decrease of surface pCO_2 as observed at station YRS11 (sampled around midday) and allowed uptake of atmospheric CO_2. The nocturnal refreezing of the ice skin potentially induced CO_2 release to the atmosphere. Similarly, Papakyriakou and Miller (2011) observed prominent diurnal shifts from CO_2 release to CO_2 uptake over landfast sea ice using the eddy covariance technique. The uptake corresponded to local peaks in surface net radiation and air temperature while the release was associated with night-time minima in net radiation and temperature. These authors ascribed the diel variations to cooling and freezing of the brines during the night.

Our results suggest that fluxes are highly variable on a diel cycle and that changes from release to uptake within 24 hours are likely linked to diel changes in NCP or freeze-thaw cycles during spring.

III.4.3.2.3. Effect of thin brine-wetted snow on CO_2 fluxes To date, only a few studies distinguished the snow-air interface and the ice-air interface. We observed larger CO_2 release and uptake over snow than over bare sea ice. Some studies have reported larger fluxes at the snow-air interface (Fischer, 2013; Geilfus et al., 2012a; Nomura et al., 2013a), but in opposite others pointed out impeded CO_2 diffusion over snow-covered sea ice (Nomura et al., 2010b). Indeed, deep snow cover may decrease the magnitude of the fluxes compared to bare ice, especially if superimposed ice -a fresh ice layer formed from snow meltwater- is forming (Delille et al., 2014; Geilfus et al., 2012a; Nomura et al., 2010b; Zemmelink et al., 2006).

Early studies about fresh snow (i.e., snow without salt) over inland terrestrial ecosystems considered snow as an inert layer storing CO_2 and paid little attention to processes within the snow (Brooks et al., 2005; Takagi et al., 2005). Only the impact of biological processes (i.e. microbial respiration) has been studied and was reported not to be significant (Pirk et al., 2016). However, in terrestrial ecosystems close to the sea and even for sea ice, several studies reported chemical and photochemical reactions (see Bartels-Rausch et al. (2014) for a review). Sea salts in snow promote the formation of a surface liquid layer with a high ionic concentration that hosts chemical reactions (Domine and Shespon, 2002).

During this survey, neither snow ice nor superimposed ice formation that could act as a physical barrier to gas exchange were observed. The snow cover was characterized by high salinity (7.4 - 24.5), low thickness (below 4 cm), and high wetness due to brine wicking, i.e. the upward migration of sea salt enriched brines from the sea ice to the snowpack (Domine et al., 2004). Compared to previous studies (Delille et al., 2014; Geilfus et al., 2012a; Nomura et al., 2010b; Papakyriakou and Miller, 2011; Zemmelink et al., 2006), the snow cover was saltier and thinner during our survey. Wet and salty base snow can be viewed as solid snow crystals partially surrounded by liquid (i.e. brine) or disordered air–ice interface (Bartels-Rausch et al., 2014). Such a multiphase medium potentially modifies ice-gas interactions. First, gas adsorption or desorption on snow crystals is proportional to the specific surface area (SSA) – the surface area of snow accessible to gases per mass unit (Legagneux et al., 2002). SSA is changing with snow properties and types (e.g. temperature, density, morphology, crystal structure). Gas interactions within wet snow cover are thus expected to be different from those within dry snow. In addition, CO_2 can dissolve within this multiphase medium. Higher salinity increases the CO_2 buffer capacity of liquids or disordered layers, so that salty snow is likely to have a larger CO_2 storage capacity compared to fresh snow. The CO_2 storage capacity of salty base snow would add up to the total sea ice CO_2 storage capacity so that sea ice with a salty snow cover should have a larger CO_2 storage capacity compared to bare ice. We therefore suggest that the thin salty snow layer observed during the survey allowed CO_2 transport due to its shallowness and provided an enhanced CO_2 storage capacity compared to bare ice and related enhanced CO_2 fluxes.

III.5. Conclusions

We investigated the inorganic carbon dynamics in Antarctic landfast sea ice. Besides the first long-term monitoring of both pCO_2 and CO_2 fluxes at sea ice interfaces from winter to summer, this study also investigated the trophic status of sea ice and proposed a mechanism for calcium carbonate precipitation within the biofilm formed at the bottom of the ice.

Results revealed a succession of heterotrophic and autotrophic phases in the sea ice interior during spring. However, the seasonal pattern of CO_2 fluxes at the air-snow-ice interface was decoupled from the trophic status observed in the ice interior. This seasonal pattern of CO_2 fluxes was mainly driven by changes in pCO_2 at the surface that were related to physical processes. In late spring, diel variations of CO_2 fluxes were superimposed on seasonal variations. It appeared that both biotic and abiotic processes dominated the inorganic carbon dynamics at the sea ice surface in late spring. Diel variations potentially correspond to diel changes in NCP or to freeze-thaw cycles affecting basal snow and ice skin temperatures. As a result, a robust budget of air-snow-ice CO_2 fluxes would require both long term and high-frequency measurements to capture both seasonal and diel patterns.

McMurdo landfast ice is known to accumulate a substantial amount of biomass and is recognized as one of the most productive biotopes of the global ocean. Accordingly, we observed a large biomass build-up at the bottom of the ice but, strikingly associated with transient heterotrophic activity and nitrate plus nitrite accumulation. This counterintuitive observation is likely due to the presence of a biofilm (microbial assemblages embedded in extracellular polymeric substances) where remineralization and accumulation of nutrients are taking place. Our results further suggest that such biofilm also promotes calcium carbonate precipitation, which develops in parallel with an increase of salinity-normalized TA, another counterintuitive observation. EPS functional groups within a biofilm can bind substantial amounts of free calcium. Sequential EPS degradation due to microbial activity creates nucleation sites for calcium carbonate precipitation and provides bicarbonate ions within the biofilm that increase alkalinity. These observations call for further studies on the implication of biofilm formation at the bottom of sea ice.

III.6. Acknowledgments

The authors would like to thank Brian Staite, Bernard Heinesch, Jiayun Zhou, Véronique Schoemann, Thomas Goossens and the Scott Base crew for their assistance during fieldwork. We are indebted to Antarctica New Zealand for their logistical support. The authors are indebted to Nicolas-Xavier Geilfus and Elizabeth Jones for their detailed and constructive comments that greatly improved the overall quality of the manuscript. This research was supported by the F.R.S.-FNRS (project YROSIAE, contract 2.4517.11), Belgian Science Policy (project BIGSOUTH, contract SD/CA/ 05), Antarctica New Zealand (project K131). Fanny Van der Linden, Marie Kotovitch, Sarah Wauthy and Bruno Delille

are PhD students and research associate, respectively, of the F.R.S.-FNRS. The data used within this work are available at the address: http://hdl.handle.net/2268/247284.

III.7. Supporting information

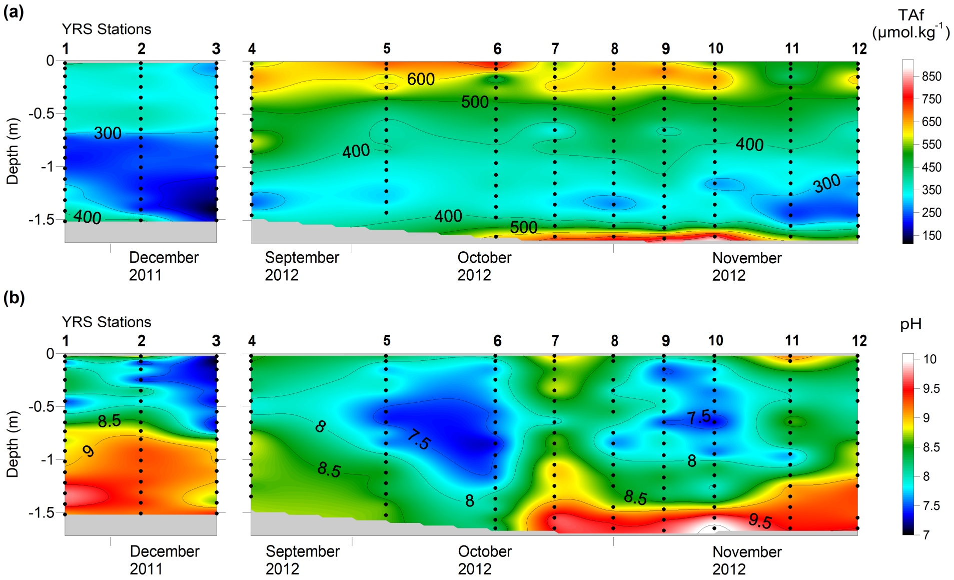

Figure S1: Temporal evolution of (a) filtered alkalinity and (b) pH in landfast sea ice. Plots were produced using the radial basis function method for interpolation in Surfer 8 software. Black dots are data points from field sampling.

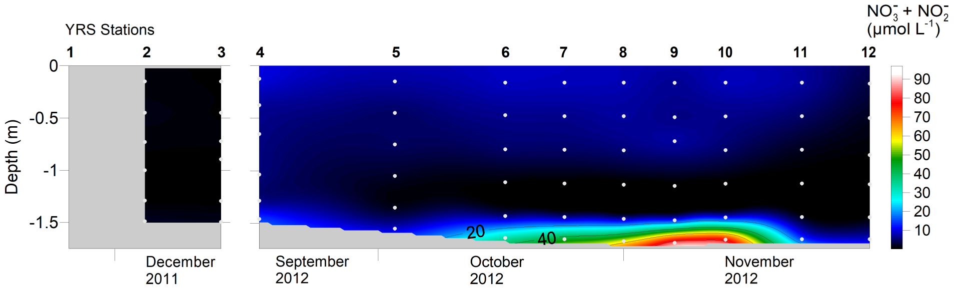

Figure S2: Bulk ice concentrations of nitrate plus nitrite. Plots were produced using the radial basis function method for interpolation in Surfer 8 software. Grey dots are data points from field sampling. Data are missing for station YRS1.

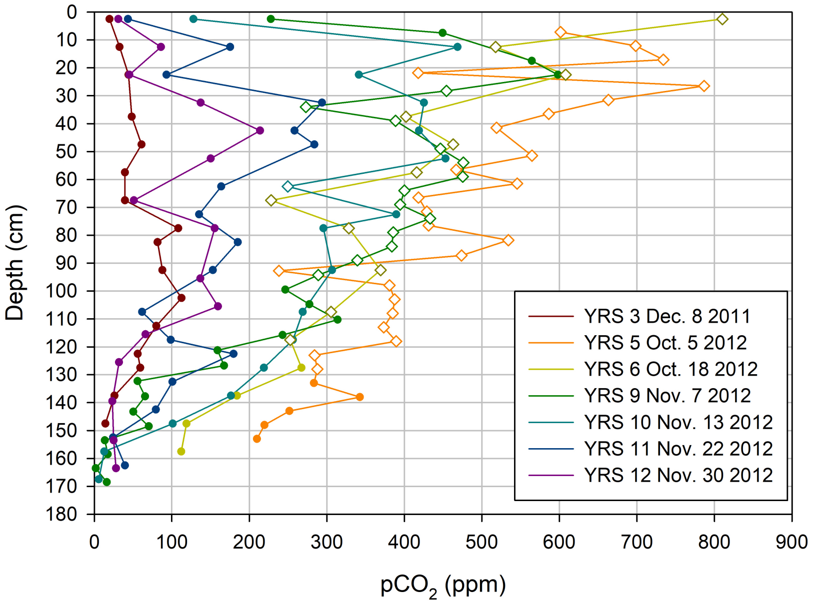

Figure S3: Sea ice pCO$_2$ profiles. Open diamonds indicate impermeable layers (BrV<5%), closed dots indicate permeable layers. Samples were analyzed with a standard gas of 300 ppm.

Table S1: Bottom chl-*a* concentrations and abundances. Total chl-*a* concentration refers to the sum of concentrations measured on the 10 and 0.8 μm filters.

Station number	Station date	Total chl-*a* in the ice column (μg L^{-1})	Total chl-*a* in the bottom 10 cm (μg L^{-1})	Abundance of chl-*a* in the bottom 10 cm relative to the ice column (%)
1	28 November 2011	294.5	285.5	96.9
2	3 December 2011	34.4	22.6	65.8
3	8 December 2011	36.5	24.9	68.2
4	19 September 2012	16.9	13.3	78.8
5	5 October 2012	50.9	45.3	89.0
6	18 October 2012	511.5	506.0	98.9
7	25 October 2012	1446.2	1440.7	99.6
8	1 November 2012	508.2	501.8	98.7
9	7 November 2012	2446.1	2443.4	99.9
10	13 November 2012	2345.6	2342.8	99.9
11	22 November 2012	1221.3	1203.6	98.5
12	30 November 2012	981.8	974.8	99.3

Chapter IV. Bubble-driven gas enrichment in sea ice drives CO_2 release to the atmosphere in autumn.

F. C. Van der Linden, J.-L. Tison, G. Carnat, C. Sapart, J. de Jong, S. Stammerjohn, S. Ackley & B. Delille

This chapter is in preparation for publication.

IV.1. Introduction

Carbon dioxide (CO_2) is a major anthropogenic long-lived greenhouse gas that contributes to about 63% of the total radiative forcing of the Earth (IPCC, 2013). Predicting its future atmospheric concentration is quite challenging because of the lack of knowledge existing on the contribution of its natural sources and sinks (Fischer et al., 2010; Parmentier et al., 2013). Polar oceans in both the Northern and Southern hemispheres are major sinks for atmospheric CO_2 (Gruber et al., 2019b; Takahashi et al., 2002). Sea ice plays a complex yet significant role in the carbon cycle of these polar waters that we recently reviewed in the Arctic Ocean (Lannuzel et al., 2020). In particular, CO_2 fluxes over Arctic and Antarctic sea ice have been repeatedly reported in spring and summer (Brown et al., 2015; Delille et al., 2014; Geilfus et al., 2013, 2012a, 2015, 2014; Nomura et al., 2013a, 2010b). For the Southern Ocean, two large scale assessments of air-ice CO_2 fluxes have been proposed so far (Delille et al., 2014; Rysgaard et al., 2011). Both studies converge and suggest that sea ice in spring and summer would uptake between 0.019 Pg C to 0.052 Pg C of CO_2 from the atmosphere. However, both approaches have the same drawback: they do not account for autumn and winter fluxes. Indeed, little is known about the winter CO_2 exchanges above the sea ice due to the logistical challenges to achieve field observations during winter, especially in the Southern Ocean. CO_2 releases during ice growth have been observed for artificial ice (Geilfus et al., 2016; Kotovitch et al., 2016; Nomura et al., 2006). In the Arctic Ocean, north of Svalbard, Nomura et al. (2018) showed CO_2 releases over young ice (thickness between 15 and 22 cm) and snow-covered ice during winter and spring. Winter CO_2 releases were also reported using eddy covariance techniques in an Arctic polynya in the Amundsen Gulf (Else et al., 2011) or over landfast sea ice of the southern Beaufort Sea (Miller et al., 2011). Using the same method, Sievers et al. (2015) reported periods of strong outgassing during the winter-spring transition (March) over landfast sea ice in northeast Greenland.

In the Southern Ocean, only two studies reported late winter/early spring air-ice CO_2 fluxes measurements. These studies showed contrasting results. In the Bellingshausen Sea at around 70°S, Geilfus et al. (2014) observed that sea ice was under the influence of low-pressure systems that bring heat and lead to marked temperature variations between -20°C and +0.5°C. Early warm-up of sea ice led to negative air-ice CO_2 fluxes (fluxes from the atmosphere to the ice). Further south, in McMurdo Sound, Ross Sea, we reported positive fluxes in very late winter/early spring over snow-covered landfast sea ice (Chapter III.). To our best knowledge, no data of CO_2 fluxes during autumn and winter were reported for the Southern Ocean, even less for early sea ice growth stages during the transition from open to sea-ice covered ocean. Of particular interest to capture this transition are polynyas. Polynyas are recurrent open water and high sea ice production areas where otherwise a thicker ice cover is predominant (Armstrong, 1972; Barber and Massom, 2007). Coastal (or latent-heat) polynyas occur frequently around Antarctica. They are bounded by land, ice shelf, icebergs or glacier tongue on one side (Barber and Massom, 2007), and pack ice on the other side. Their formation is linked to winds or oceanic currents maintaining ice divergence. The Terra Nova Bay polynya (TNBP), a coastal polynya in the western Ross Sea, is bounded to the south by the Drygalski ice tongue and maintained by katabatic winds draining into the Terra Nova Bay.

Air-ice CO_2 fluxes are controlled by the dynamics of dissolved inorganic carbon (DIC) in sea ice. To our best knowledge, the DIC dynamics has not been documented in autumnal natural sea ice. It can be expected that key processes already described for winter ice (Nomura et al. (2018), Chapter III.) control the DIC dynamics in autumn. Among them, the formation of ikaite ($CaCO_3 \cdot 6H_2O$), a metastable form of calcium carbonate, received attention since it has been suggested to act as a sink of CO_2 for the atmosphere (Delille et al., 2014; Rysgaard et al., 2007; Rysgaard et al., 2011). In addition, bacterial respiration (Chapter III., Søgaard et al. (2019), Zhou et al. (2015)) and physical processes, i.e. brine migration, air-sea gas exchange, bubble-driven gas enrichment (Kotovitch et al. (2016), Moreau et al. (2015), Zhou et al. (2013), Chapter III.) are likely majors controls of the DIC dynamics in autumn during sea ice growth.

We present insights from the Polynyas, Ice Production and seasonal Evolution in the Ross Sea (PIPERS) expedition and focus on the temporal and spatial changes of sea ice inorganic carbon content and related air-ice CO_2 fluxes of pack ice during the rapid growth and expansion phase of the Ross Sea ice cover, both inside and outside the polynyas. The main goal of this study is to document the CO_2 dynamics during early sea ice growth, from April to June 2017, and provide the first set of air-ice CO_2 fluxes measured with chambers in an active Antarctic wintertime coastal polynya of the Ross Sea, the Terra Nova Bay Polynya. Multiple sea ice types were sampled (frazil, pancakes, unconsolidated and consolidated ice) in contrasting areas (marginal ice zones, polynyas, and the central Ross Sea).

IV.2. Fieldwork and Methods

IV.2.1. Study site and work settings

The PIPERS survey was carried out in the Ross Sea, aboard the RVIB Nathaniel B. Palmer (NBP), and aimed to investigate autumnal pack ice, particularly the early stages of sea ice formation in the Terra Nova Bay polynya. We focused on 27 biogeochemical ice stations performed between April 19 2017, the day of arrival at the ice edge, and June 4 2017. Unexpectedly, a delayed ice advance was observed in the Ross Sea in autumn 2017 (Ackley et al., 2020; Tison et al., 2020). The ice stations were located in the western Ross Sea, close or within the marginal ice zone (MIZ) (inbound stations PIP1-5), the Central Ross Sea (stations PIP18-25) and the Terra Nova Bay polynya (TNBP) (stations PIP6-16) (Figure 32). These locations allowed us to sample both the main pack and the early stages of ice formation in the TNBP. Three sampling methods were used to overcome logistical constraints: full ice stations (long stations on sea ice), basket stations (short stations on sea ice) and zodiac stations (short stations to sample frazil and very thin ice, e.g. unconsolidated grey ice, proto-pancake or thin pancake ice). Collection of ice cores, snow, brines and seawater down to 30 m (detailed in Tison et al. (2020)) was carried out during the full stations. Limited sampling occurs during the basket and zodiac stations (ice and seawater collection, fluxes measurements whenever possible, no snow or brine sampling). Air-ice fluxes of CO_2 were measured at almost all stations, air-sea fluxes were measured only during zodiac stations.

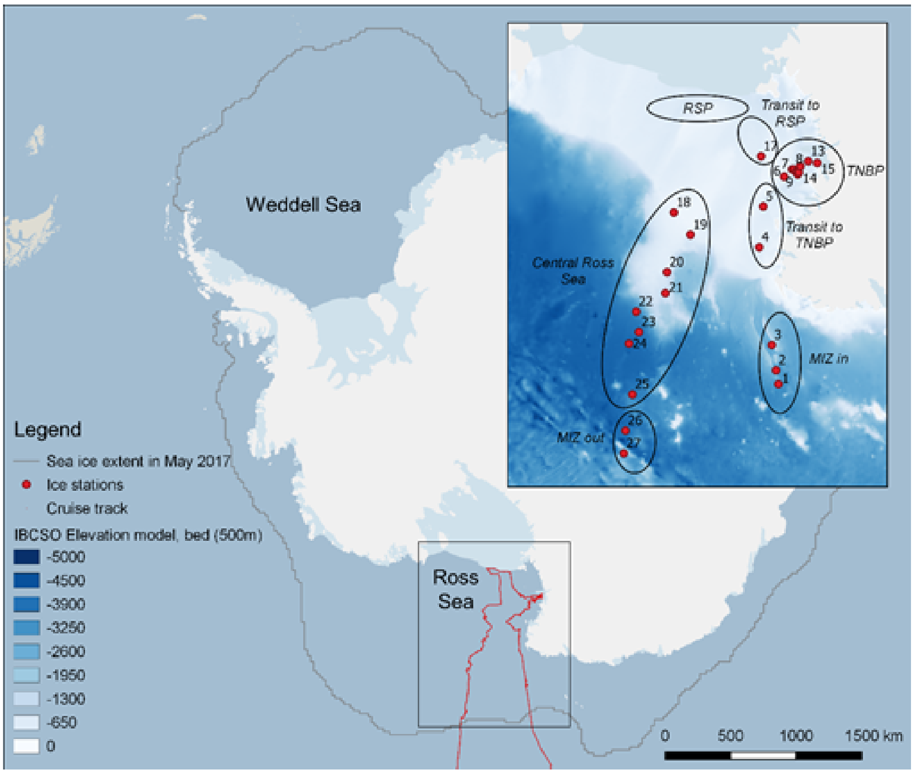

Figure 32: Track of the PIPERS cruise in the Ross Sea and location of the 27 biogeochemical ice stations (red dots). MIZ, TNBP and RSP stand for Marginal Ice Zone, Terra Nova Bay Polynya and Ross Sea Polynya, respectively. Map from Jacques et al. (in prep), created with Quantarctica, from the Norwegian Polar Institute, NSIDC NOAA (https://nsidc.org/data/G02135/versions/3).

IV.2.2. Ice collection

During the so-called "full ice stations" and "basket stations", consolidated ice was collected with an electropolished stainless steel corer. Zodiac stations carried out using rigid inflatable boat allow to sample the early stages of sea ice: free-floating frazil ice, unconsolidated grey ice, proto-pancake or thin pancake ice. Free-floating frazil ice was collected either by filling a polyethene plastic bag directly at the surface (denoted as unfiltered ice) or by filtering water with a handheld sieve (denoted as filtered ice). Whenever possible, we also grabbed by hand grey ice or proto-pancake (denoted as unconsolidated ice), packed it swiftly in a polyethylene bag and placed it in a cooler box with freeze packs (placed in a -20°C or -80°C freezer prior to the ice station) in order to freeze the sample rapidly and therefore prevent brine drainage. We also collected frazil ice and unconsolidated ice at the sea surface within a plastic box placed underneath, containing the under-ice water (Cottier et al., 1999). Ice blocks were extracted with the plastic box (i.e. with the under-ice water) and immediately stored in a freezer at -20°C after the sampling. Once the under-ice water was frozen, the ice blocks were separated from the frozen under-ice water by cutting. Ice collected with this method is denoted "bucket" ice.

Hereafter, when the sampling collection (i.e., filtered, unfiltered, unconsolidated, bucket) is not specified, the collection method corresponds to ice coring and the ice is referred as "consolidated" ice.

IV.2.3. Measured parameters

IV.2.3.1. Ice temperature and bulk ice salinity

Ice temperature measurements were performed on ice cores immediately after collection with a vertical resolution of 5 cm using a calibrated probe TESTO®720 (precision ±0.1°C, accuracy ±0.2°C).

Salinity samples were processed with a Guildline Autosal Salinometer 8400, B calibrated with IAPSO standard seawater at a salinity of 10 to improve the accuracy of the measurements (accuracy better than 0.002 psu). Salinity measurements were performed with a vertical resolution of 5 cm for the top 10 cm of the ice cores and a vertical resolution of 10 cm below.

IV.2.3.2. Total alkalinity and pH

Ice cores were cut into 10 cm sections whenever possible in a cold room (at -25°C). For thinner ice cores, cutting was adapted according to the length of each core. Each section was placed in a gas-tight polyethene/polyamide bag sealed under vacuum with a vacuum sealer. The bagged sea ice samples were then melted in the dark at +4°C on a rotary shaker. The latter speeds up the melting, keeps the water in the bags at a homogenous temperature and allows to avoid hot spot formation detrimental for ikaite crystal preservation (Dieckmann et al., 2008). Attention was paid to treat meltwater as soon as possible after complete melting to avoid meltwater warming and subsequent carbonate dissolution, as suggested by Dieckmann et al. (2008). Meltwater was shaken to resuspend the crystals, and aliquots were collected for pH, bulk alkalinity (TAb) and filtered alkalinity (TAf) analyses. pH was measured using a Metrohm® combined electrode calibrated on the total hydrogen ion scale using NBS standard at pH 4 and 7. The pH measurements were carried out at low temperature (typically below +4°C) to reduce biais due to temperature changes. The accuracy of pH measurements was ±0.01 pH units. Samples for TAf were filtered on 0.2 μm polycarbonate filters. Filtration were carried out at 4°C in order to avoid any dissolution of calcium carbonate. TAb and TAf were poisoned with a saturated mercury chloride solution. Total alkalinity was measured by open-cell titration with HCl 0.1 M on 50 ml aliquots of sea ice melt samples, following Gran (1952) endpoint determination. Titration was stopped for 10 minutes at pH 4.2 to ensure the dissolution of any remaining calcium carbonate crystals before the measurements between pH of 4.2 and 3 required for the Gran function. The accuracy of TA measurements was ±4 μmol kg^{-1}. Data were quality checked with certified reference material from Andrew Dickson (Scripps Institution of Oceanography, University of California, San Diego).

IV.2.3.3. Argon concentration

The dry-crushing technique, developed for gas measurements in continental ice (Raynaud et al., 1982), was used to extract Ar from the ice samples. This technique allows extracting both gas bubbles and gas dissolved in liquid brines. The ice core was cut every 5 cm, and each ice cube of about 60 g was introduced into a vessel, with seven stainless steel balls. The latter was crushed in the vessel as described in Stefels et al. (2012), at a temperature of -25°C and under a vacuum of 10^{-3} torr. The vessel was then kept at -50°C in a cold ethanol bath and connected to the gas chromatograph equipped with a thermal conductivity detector for concentration analyses. We used He (Air Liquide® – Alphagaz 2) as the carrier gas and a 22 ml packed column (Mole Sieve 5A 80/100; 5 m × 1/8 in.). The repeatability of the analyses (i.e., the precision of the gas chromatograph) was 2.3% for Ar (Zhou et al., 2014).

IV.2.3.4. CO_2 fluxes measurements with automatic and floating chambers

CO_2 fluxes were measured using a LI-COR® LI-8100A soil CO_2 flux system. The analyzer was connected to an automatic chamber (LI-COR® 8100-104) for measurements over solid ice. The chamber consists of a metal cylinder, with a diameter of 20 cm and a height of 9.7 cm, closed at the top by a mobile cap to vent the chamber and maintain an ambient pressure inside. A rubber seal surrounds the cylinder and ensures an airtight connection at the chamber-ice interface. The chamber was placed either on the snow or the ice after removing the initial snow cover. For measurements over snow, a stainless-steel seal was mounted at the base of the chamber and pushed down to the ice to enclose snow and prevent lateral diffusion of air in the snowpack. For CO_2 fluxes measurements over open water and unconsolidated ice, the infrared gas analyzer LI-COR® LI-8100A was coupled to POPI (floating Plastic chamber for OPen water and unconsolidated Ice gas fluxes) developed at the University of Liège.

The infrared gas analyzer recorded the pCO_2 during a designated time interval (30 min). The flux was determined by measuring the change of pCO_2 within the chamber. Flux calculations were performed routinely using the LI-COR® SoilFluxPro software, with volumes adjusted to include collar offsets (i.e. rim height above the surface) for the measurement carried out with the automatic chamber, and applying water vapor corrections for dilution and band broadening. The fluxes were determined by the slope of the linear or exponential regression of pCO_2 over time, depending on the best fit. All fluxes were visually checked to discard measurements biased by contamination or poor sealing of the chamber. The uncertainty of the flux computation due to the standard error of the regression slope was ±8%.

IV.2.4. Computed parameters

IV.2.4.1. Brine volume fraction

The brine volume fraction (BrV), a proxy of sea ice permeability, was computed from ice temperature and salinity following the equations of Cox and Weeks (1983) for ice temperature $<$ -2°C and Leppäranta and Manninen (1988) for ice temperature $\geq$ -2°C. We considered that the ice was permeable for a brine volume fraction exceeding 5% (Golden et al., 1998).

IV.2.4.2. Dissolved inorganic carbon

Dissolved inorganic carbon (DIC) was computed from TAf and pH, according to CO_2 acidity constants of GEOSECS (Takahashi et al., 1982), consistently with the use of NBS scale for pH, with K_1 et K_2 from Mehrbach et al. (1973). We used TAf for DIC computation to avoid bias from the potential dissolution of particulate inorganic carbon (e.g., calcium carbonate formed in sea ice). We used DIC normalized to a salinity of 35 (DIC_{35}) in order to distinguish which processes, other than salinity changes, control the carbonate system.

IV.2.4.3. Assessment of calcium carbonate precipitation

The overall $CaCO_3$ content was estimated from the difference between total alkalinity of a nonfiltered sample, denoted as bulk alkalinity (TAb) and total alkalinity of the filtered sample, denoted as filtered alkalinity (TAf) (Geilfus et al., 2013), according to

$$[CaCO_3] = \frac{1}{2}(TAb - TAf) \tag{19}$$

The $CaCO_3$ content is given in μmol kg^{-1}. Based on the spread from observed data, the detection limit was assessed to 50 μmol kg^{-1} of $CaCO_3$ precipitated.

IV.2.4.4. Omega ikaite

The saturation state of brine (Ω_{ika}) depends on the calcium brine concentration, carbonate brine concentration and their solubility product described by Papadimitriou et al. (2013). While the solubility product has been established for temperatures above -8°C, we used it below this threshold and assumed it constant. We acknowledge that we neglected some physical processes, such as concentration and dilution. This approach thus presents some limitations. We estimated the salinity of brines using a third-order fit from Assur (1958) and Notz (2005). We also computed TA$_{brines}$ and DIC$_{brines}$ by considering their linear dependence to salinity in order to obtain CO_3^{2-} brine concentrations from CO2SYS program for the carbonate system (Lewis et al., 1998). More details can be found in Moreau et al. (2015).

IV.3. Results

IV.3.1. Physical and dissolved inorganic carbon parameters in different areas of the western Ross Sea

IV.3.1.1. Inbound transect

The inbound transect includes stations performed in the marginal ice zone (MIZ) on the way in (stations PIP2–3) as well as stations PIP4-5 from 19 April to 25 April 2017 (Figure 32). As observed in Figure 33, the lowest temperatures were observed in the southernmost stations (PIP4-5). These two stations also exhibited spiky profiles consistent with their dynamic origin (rafting and dragon skin process, Tison et al. (2020)). As a result, brine volumes of PIP4 and PIP5 appeared to be below 5% - the threshold of permeability for liquids (Golden et al., 1998) - for the upper part of the ice. The salinity of the northern stations PIP2 and PIP3 increased steadily in the upper part of the ice. Brine volumes were above 5% at all depths at these stations. TAf and DIC mimicked vertical changes of salinity and exhibited an increase at the ice surface. DIC_{35} vertical profiles exhibited less clear patterns, but DIC_{35} values were mostly above mean DIC_{35} of the surface waters.

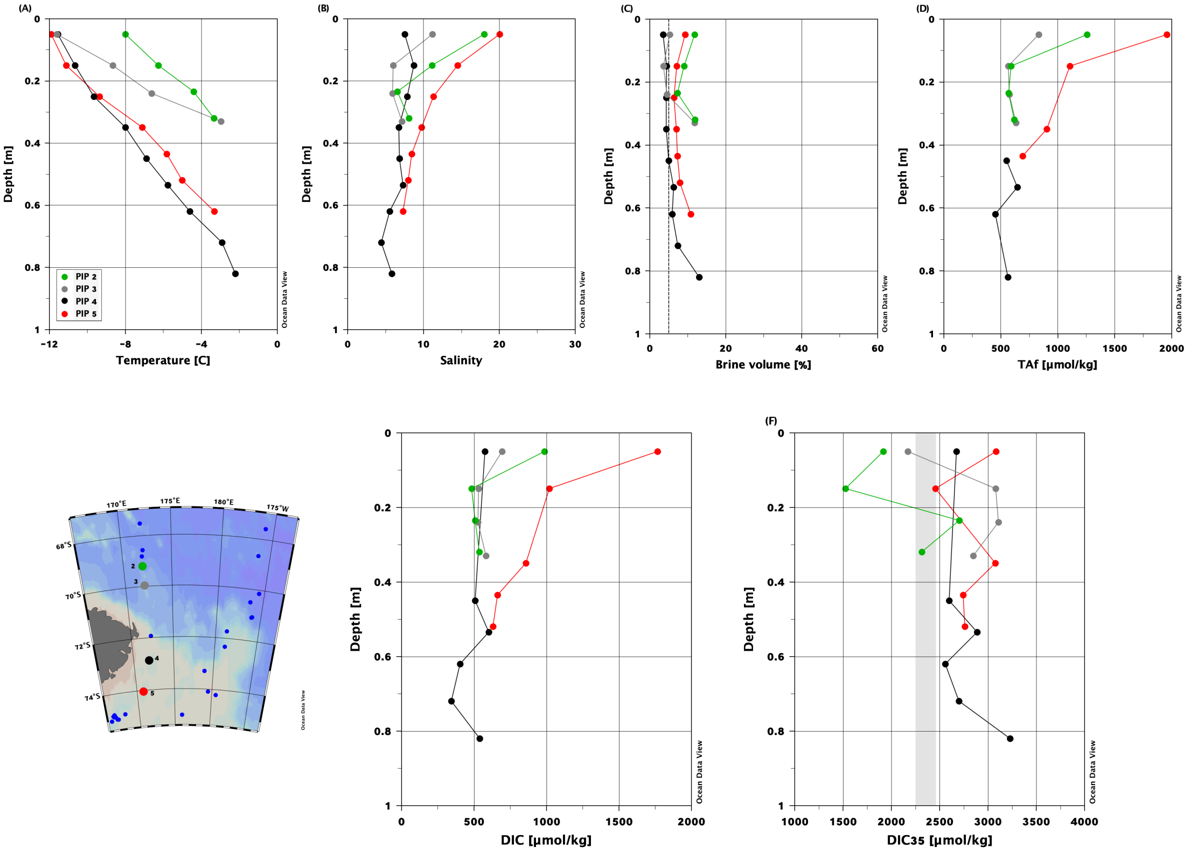

Figure 33: Temperature, salinity, brine volume, TAf, DIC and DIC_{35} vertical profiles in sea ice from inbound stations (PIP2–5). The dashed line in the plot (C) indicates the fluid permeability threshold of 5%. The grey area in plot (F) indicates the seawater range of DIC_{35}.

IV.3.1.2. Terra Nova Bay Polynya

Thin and thick pancakes, and consolidated sea ice were sampled in the TNBP. Low ice thicknesses were observed, with a maximum value of 31 cm. Steep changes were observed for most of the measured parameters in this thin ice cover (Figure 34). Thin pancakes exhibited systematically higher temperatures at the surface compared to thicker pancakes. Salinities were high compared to the values observed in the inbound transect or the central Ross Sea and showed a marked increase at the surface. Consistently with high salinities, brines volumes were above the permeability threshold of 5%, but they exhibited a marked decrease at the surface. TAf and DIC profiles mimicked the vertical changes in salinity. DIC_{35} profiles exhibited lower value at the surface compared to the bottom, with few exceptions.

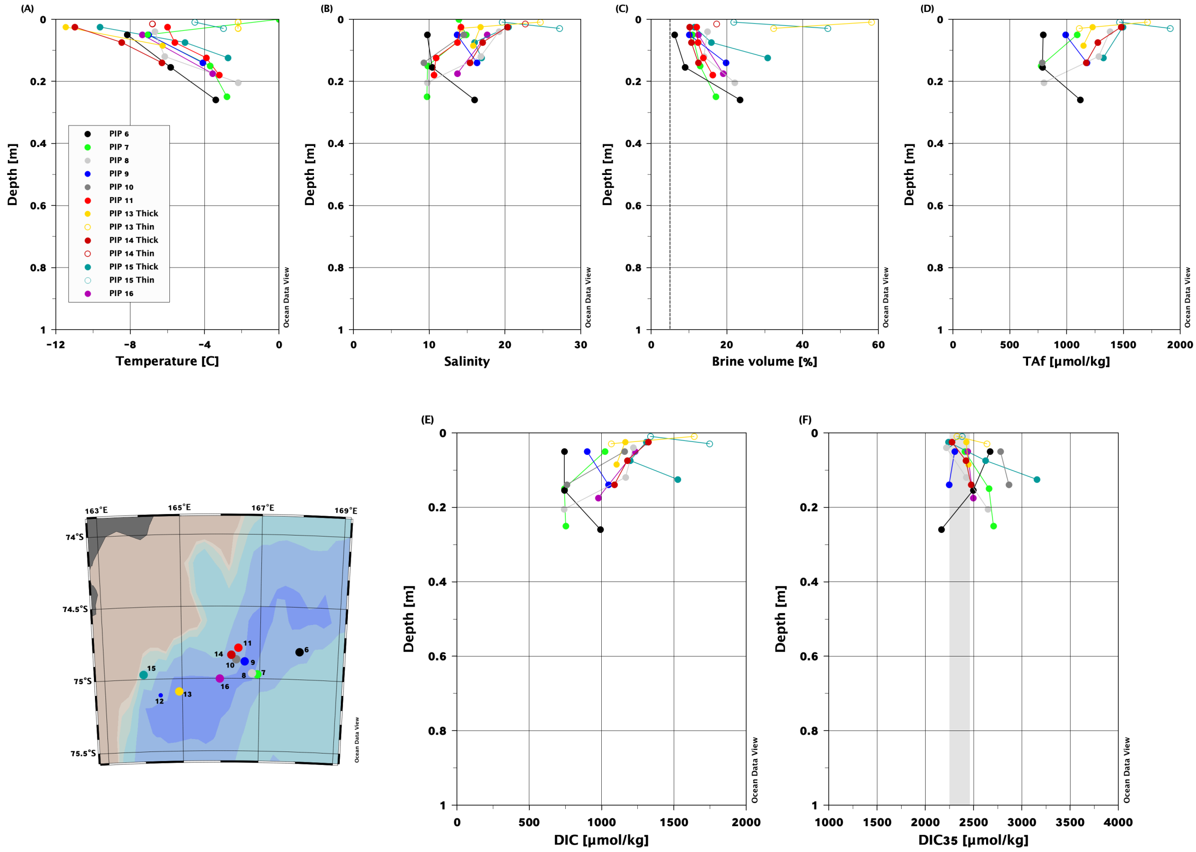

Figure 34: Temperature, salinity, brine volume, TAf, DIC and DIC_{35} vertical profiles profiles in sea ice, thin and thick pancakes from the Terra Nova Bay polynya. The dashed line in the plot (C) indicates the fluid permeability threshold of 5%. The grey area in plot (F) indicates the seawater range of DIC_{35}.

IV.3.1.3. Central Ross Sea

Thicker ice cover was encountered in the central Ross Sea (up to 65 cm at station PIP24). Salinity profiles exhibited a C-shape profile characteristic of growing ice (Figure 35). Impermeable layers were observed at mid-depth, between 7.5 cm and 23 cm. TAf and DIC profiles followed the same trend as salinities profiles. Minimum DIC_{35} values were observed at the surface and were below (stations PIP20, 21 and 24) or around (stations PIP22, 23 and 25) seawater values. We observed a steady increase in DIC_{35} for all stations from the surface to the interior ice. The maximum values (up to 3400 μmol kg^{-1}) were observed between 20 cm and 30 cm. DIC_{35} decreased slightly towards the bottom of the ice. A systematic offset of DIC_{35} values compared to the seawater range was observed at the ice bottom. This offset ranged from 293 μmol kg^{-1} (at PIP24) to 752 μmol kg^{-1} (at PIP22) compared to the highest seawater value.

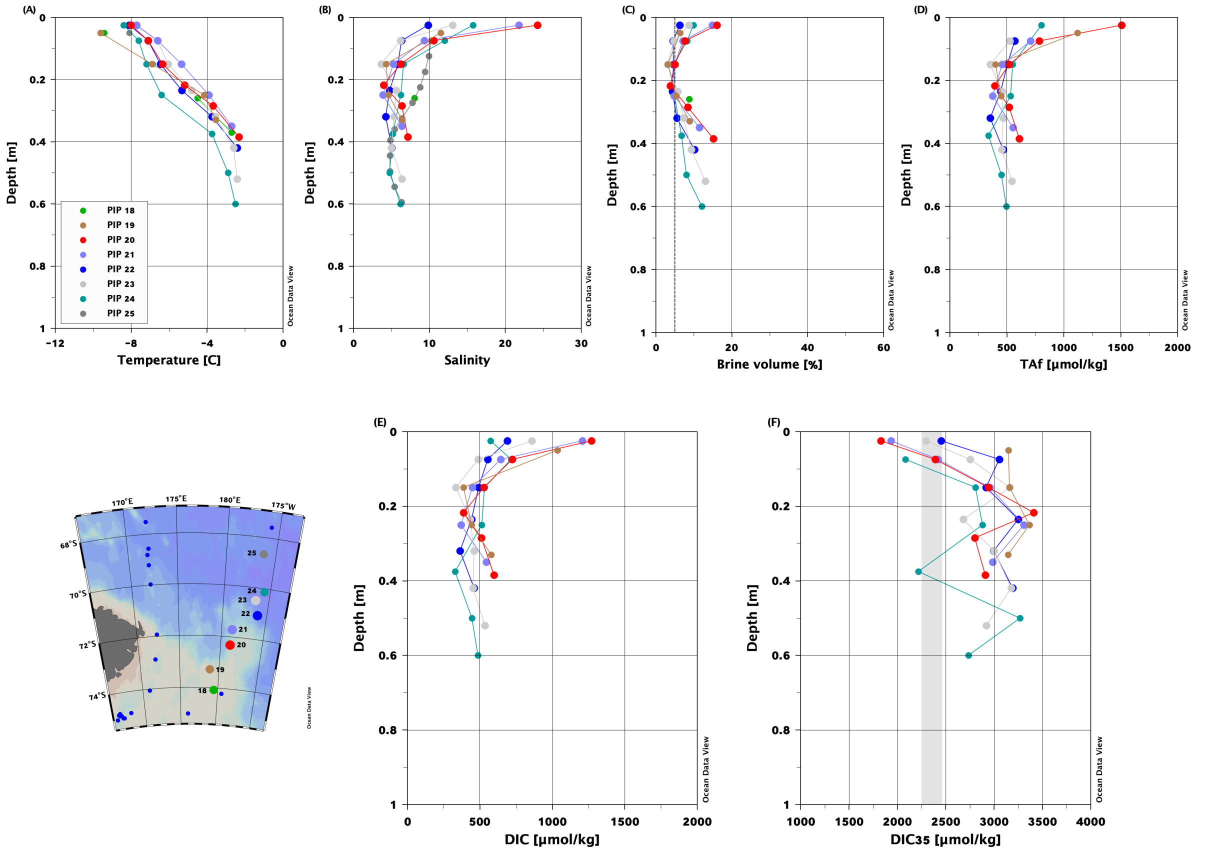

Figure 35: Temperature, salinity, brine volume, TAf, DIC and DIC_{35} vertical profiles in sea ice from the Central Ross Sea. The dashed line in the plot (C) indicates the fluid permeability threshold of 5%. The grey area in plot (F) indicates the seawater range of DIC_{35}. The grey area in plot (F) indicates the seawater range of DIC_{35}.

IV.3.2. CO_2 fluxes at the air-sea, air-ice and air-snow interfaces

The largest CO_2 fluxes were observed during the earliest sea ice growth stages above frazil ice, unconsolidated grey ice and pancake ice (Figure 36) and ranged from 0 to 21.8 $\mathrm{mmol\,m^{-2}\,d^{-1}}$. Both CO_2 releases and uptakes of similar amplitude ranging from -4.4 to 4.9 $\mathrm{mmol\,m^{-2}\,d^{-1}}$ were measured at the air-snow interface over thick (more than 20 cm) consolidated ice (Table 5). These values fall within the range of CO_2 fluxes recorded previously by Geilfus et al. (2016) over Antarctic pack ice in early spring in the Bellingshausen sea, and in the range of our observations in late winter in McMurdo sound (Table 6). Autumn CO_2 fluxes can also be compared with measurements carried out over Arctic pack ice (Nomura et al., 2018) that ranged from 1 to 1.6 $\mathrm{mmol\,m^{-2}\,d^{-1}}$ with an average of 1.3 $\mathrm{mmol\,m^{-2}\,d^{-1}}$ for ice thickness ranging from 15 cm to 22 cm. Autumn CO_2 fluxes were also similar to the observations of Geilfus et al. (2013) in a refrozen lead in the Chukchi Sea that ranged from 4.2 to 9.9 $\mathrm{mmol\,m^{-2}\,d^{-1}}$ over 22 cm thick ice. The mean value of our measurements on snow over consolidated ice was 0.5 $\mathrm{mmol\,m^{-2}\,d^{-1}}$, so that consolidated ice was acting as a source of CO_2 for the atmosphere in autumn.

Measurements carried out on consolidated sea ice after snow removal ranged from 0 to 3.8 mmol m^{-2} d^{-1} and presented less variability that measurements carried out over the snow since they were always positive. Overall, sea ice in autumn was acting as a source of CO_2 for the atmosphere, and the fluxes were enhanced over young thin ice (i.e, grey unconsolidated and pancake ice), compared to consolidated ice.

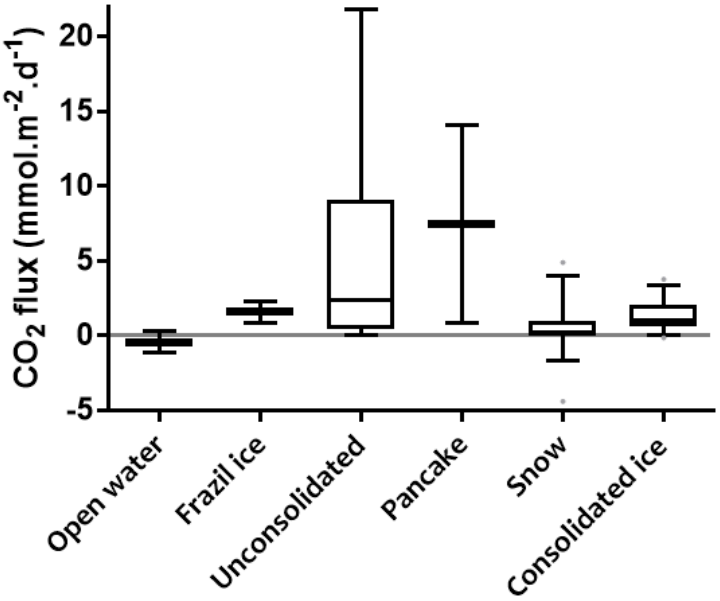

Figure 36: Air-sea, air-ice and snow-ice CO_2 fluxes measured during the PIPERS survey using the chamber technique. Boxes are drawn from the 25th to 75th percentiles, and the medians appear as horizontal lines in boxes. Whiskers indicate the 5th and 95th percentiles and grey dots are outliers.

Table 5: Means and ranges of CO_2 fluxes measured above the frazil ice, unconsolidated grey ice, pancake ice, snow covered consolidated ice and consolidated ice after snow removal. The related mean sea ice depth, temperature, ice salinity and brine volume fraction observed at the top 5 cm of the ice are added.

Ice type	Mean CO_2 fluxes (mmol m^{-2} d^{-1})	Range of CO_2 fluxes (mmol m^{-2} d^{-1})	Mean sea ice depth (cm)	Mean T (°C) at the ice surface	Mean salinity at the ice surface	Mean BrV at the ice surface (%)
Frazil ice	1.6	0.9 to 2.3	n.d.	-1.9	n.d.	n.d.
Unconsolidated grey ice	4.5	0 to 21.8	3	-5	19	23
Pancake ice	8.4	0.9 to 14	16	-5.8	25	21
Snow covered consolidated ice	0.5	-4.4 to 4.9	50	-9.8	16	10
Consolidated ice after snow removal	1.3	0 to 3.8	57	-9.3	14	8

Table 6: Means and ranges of CO_2 fluxes measured over pack ice (PIPERS survey) and landfast ice (YROSIAE survey) at the air-ice and air-snow interfaces.

	Air-ice interface		Air-snow interface	
	Range	Mean	Range	Mean
CO_2 fluxes in September over landfast ice ($\mathrm{mmol\,m^{-2}\,d^{-1}}$)	0 to 1.84	0.08	-0.35 to 5.96	0.55
CO_2 fluxes over pack ice in autumn ($\mathrm{mmol\,m^{-2}\,d^{-1}}$)	0 to 3.8	1.3	-4.4 to 4.9	0.5

IV.3.3. Overall DIC distribution in consolidated ice

DIC_{35} concentrations within consolidated pack ice ranged from 1831 to 3869 $\mu\mathrm{mol\,kg^{-1}}$ (Figure 37). Minimum values were observed in the top 10 cm of the ice with some DIC_{35} values below the seawater range. Lowest DIC_{35} values corresponded to brine volume exceeding 12% (stations PIP20, 21 and 2). Maximum DIC_{35} values were observed between 10 and 30 cm in impermeable layers with BrV as low as 2%. Such feature is observed for several stations in the central Ross Sea (PIP19 - 24, Figure 35).

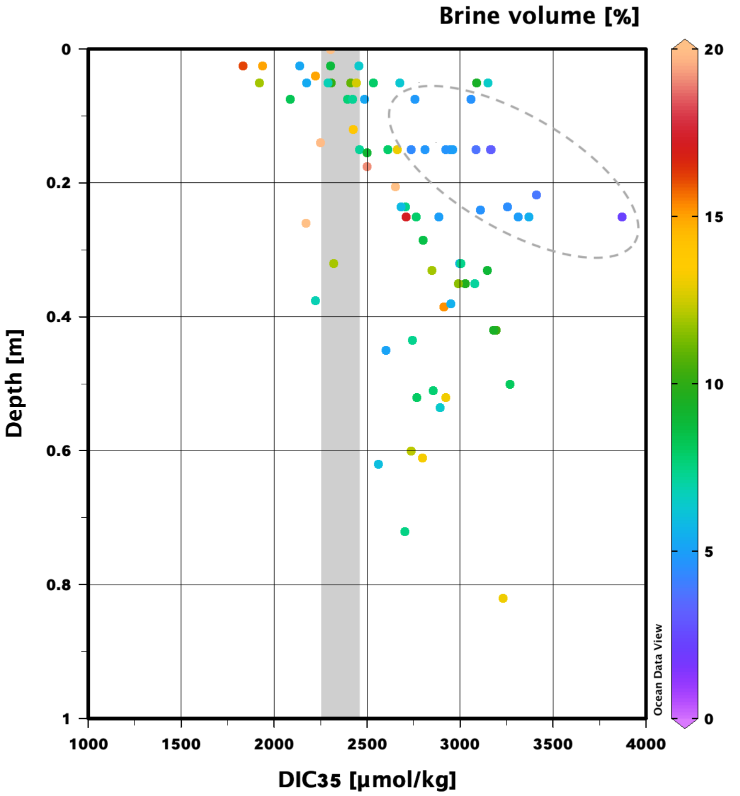

Figure 37: DIC_{35} in consolidated ice as a function of depth (m). The color bar indicates the brine volume fraction (%). The grey area refers to the seawater range of DIC_{35}. The dashed grey contour points out the impermeable layers enriched in DIC_{35}.

IV.3.4. DIC_{35} and Ar_{35} as a function of ice types

Figure 38a presents aggregated DIC_{35} data discriminated by ice type, and vertical distribution for consolidated ice. Lowest DIC_{35} values were encountered in bucket ice and filtered ice. Median values of DIC_{35} of youngest sea ice stages (unconsolidated ice, filtered and unfiltered ice) were close to the mean seawater value. An enrichment in DIC_{35} was observed in older sea ice types, i.e. pancake ice and consolidated ice, particularly between 20 cm and 40 cm. Argon data, normalized to a seawater salinity of 35 (Ar_{35}), were aggregated in the same way as the DIC_{35} data. Ar_{35} presented similar features as DIC_{35} (Figure 38b). The minimum median Ar_{35} value (20.7 $\mu\mathrm{mol\,L^{-1}}$) was observed at the surface, while the maximum median value (23 $\mu\mathrm{mol\,L^{-1}}$) was observed between 20 cm and 40 cm. All median Ar_{35} values of consolidated ice were above the seawater saturation, and the median value at the surface was the closest to the seawater saturation. The median value of Ar_{35} in pancake ice was below the seawater saturation.

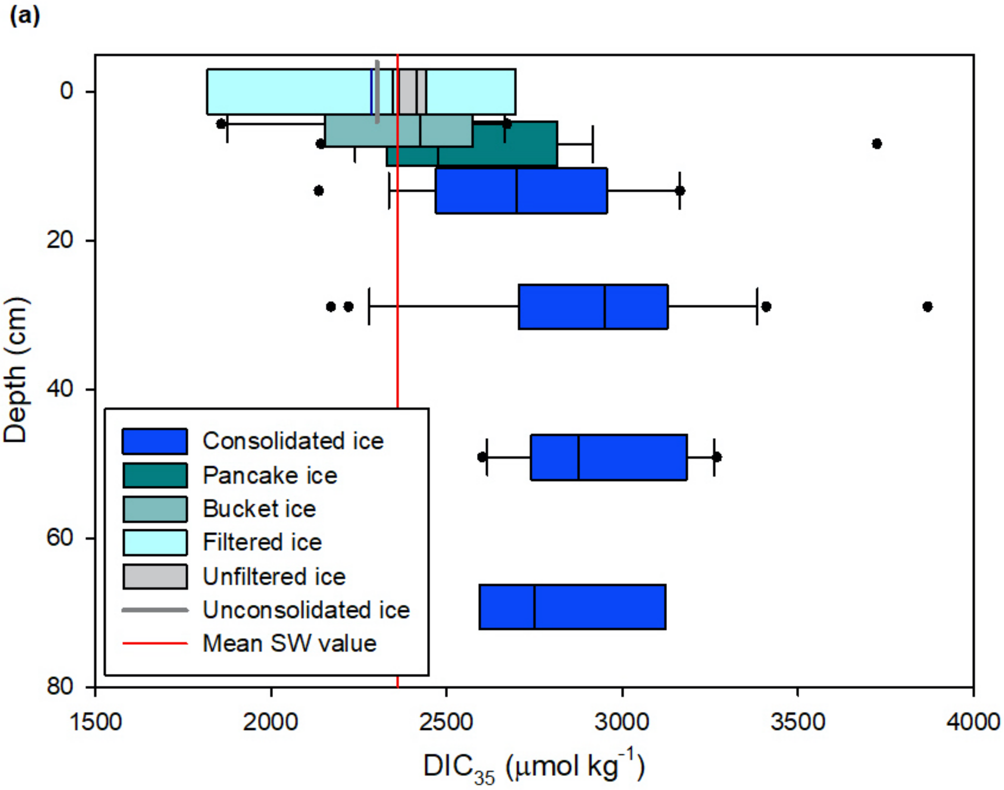

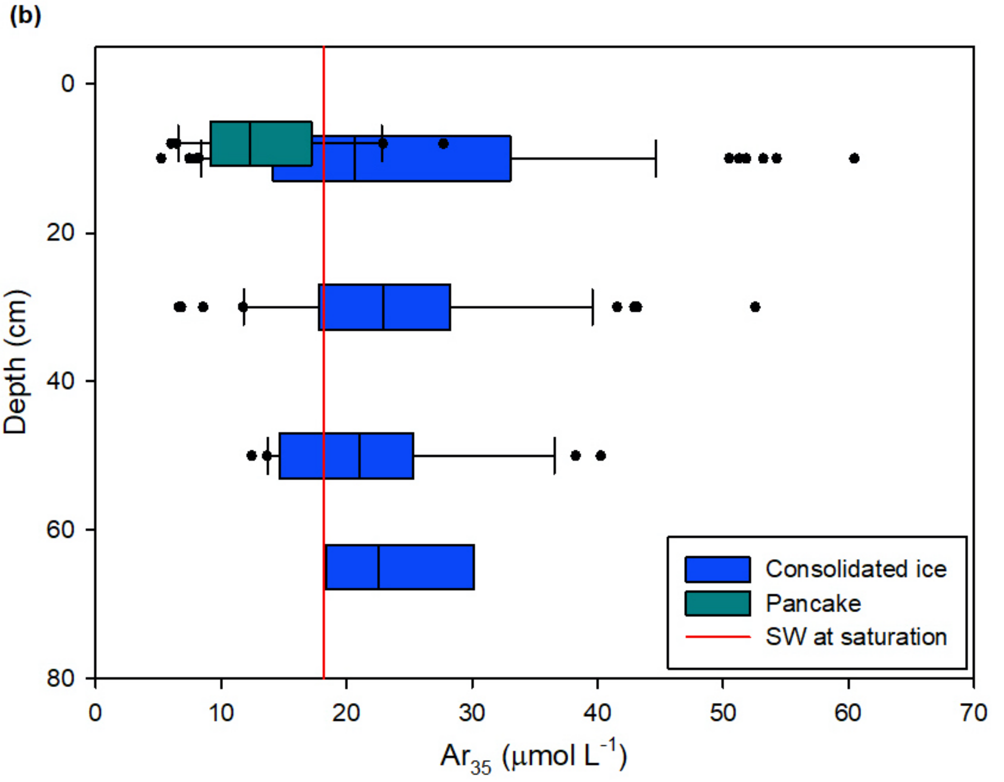

Figure 38: Boxplots of (a) DIC_{35} for pancake, bucket, filtered, unfiltered, unconsolidated ice, and consolidated ice and (b) Ar_{35} concentrations in pancake ice and consolidated ice. Values for consolidated ice are binned into 20 cm intervals. The dashed lines correspond to the mean DIC_{35} of seawater in the plot (a) and the argon saturation of seawater in the plot (b). Boxes are drawn from the 25th to 75th percentiles, and the medians appear as vertical lines in boxes. Whiskers indicate the 5th and 95th percentiles and black dots are outliers.

IV.3.5. Calcium carbonate precipitation

The $CaCO_3$ content (Figure 39) ranged between -50 μmol kg^{-1} and 50 μmol kg^{-1}, except for some outliers. Omega ikaite was mainly below 1, except at the bottom of stations PIP2 and PIP3. However, values above 1 do not correspond to the $CaCO_3$ content outliers.

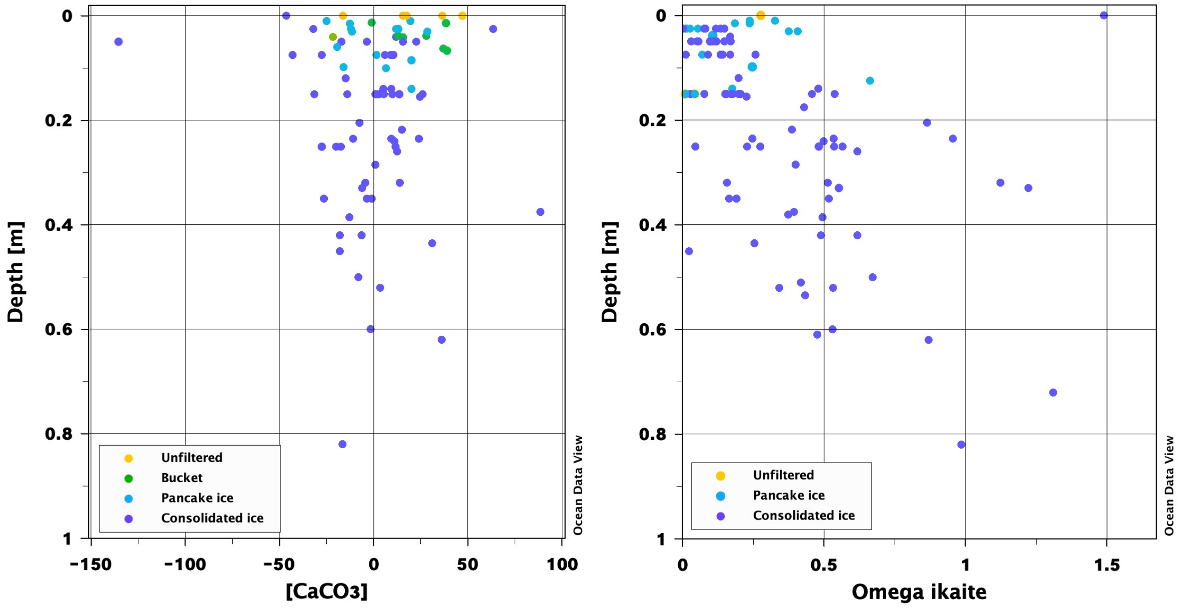

Figure 39: $CaCO_3$ content and omega ikaite in unfiltered, bucket, pancake and consolidated ice.

IV.4. Discussion

IV.4.1. Calcium carbonate precipitation

The $CaCO_3$ content derived from the difference between TAb and TAf can reveal significant calcium carbonate precipitation, as it was observed at the bottom of landfast ice in spring (Chapter III.). Surprisingly, Figure 39 shows meaningless negative values ranging from -50 μmol kg^{-1} to 0 μmol kg^{-1}, as we also reported in Chapter III. (Figure 23, page 62). These negative values correspond to analytical artefacts that result from the cumulative measurement errors in TAb and TAf. We also observed slight differences in salinity between TAb and TAf aliquots from the same sample. These differences are likely to develop due to the filtration or poor conservation of the samples, for instance, if the sampling bottles were not perfectly airtight. Such differences add up to the cumulative error in the measurement of the total alkalinity.

The negative values give some insight into the detection limit of the method. We considered that values in the -50 μmol kg^{-1} to 50 μmol kg^{-1} range were not analytically significant. Therefore, we considered that values below the threshold of 50 μmol kg^{-1} were below the detection limit of the method. Such a relatively high detection limit does not prevent to measure significant precipitation of ikaite as observed during the YROSIAE survey with values up to 350 μmol kg^{-1} (Chapter III.), while value of $CaCO_3$ up to 700 μmol kg^{-1} have been reported in the literature (Table 7).

Except for two outliers, the $CaCO_3$ content in pack ice in autumn during the PIPERS survey was below the detection limit, i.e. 50 μmol kg^{-1}. Consistently, omega ikaite (Figure 39) was generally below the threshold of 1 (with a few exceptions between 1 and 1.5), preventing precipitation of calcium carbonate. Such low values are consistent with our late winter observations in the Ross Sea landfast ice in McMurdo sound that exhibited values below the detection limit. In accordance, a survey in Eastern Antarctic pack ice also reports values ranging between 1 μmol kg^{-1} and 52 μmol kg^{-1} (Fischer et al., 2013).

Significantly larger calcium carbonate content have been reported in Antarctic landfast ice in late spring. In the Chapter III., we observed values up to 350 μmol kg^{-1} in the bottom 20 cm of productive landfast in McMurdo Sound. Fischer et al. (2013) measured calcium carbonate precipitation using inductively coupled plasma optical emission spectrometry with a high vertical resolution and reported repeatedly high $CaCO_3$ values up to 550 μmol kg^{-1} in the top 5 cm of the ice. Still, both studies are converging towards significantly lower values in the ice interior. Fisher et al. (2013) reported values between 10 cm and 30 cm of the ice ranging from 0 to 26 μmol kg^{-1}, while we reported values below 50 μmol kg^{-1} in the ice interior at all time (Table 7).

Overall values in Antarctic sea ice, but also in the Chukchi Sea (Geilfus et al., 2013) or in Fram strait (Nomura et al., 2013a), appear to be significantly lower than values repeatedly reported in landfast ice from Young sound (East Greenland) that ranged from 100 μmol kg^{-1} to 3000 μmol kg^{-1} (Barber et al., 2014; Rysgaard et al., 2013; Søgaard et al., 2019). This challenges the current view of ubiquitous significant (above 50 μmol kg^{-1}) calcium carbonate precipitation in sea ice. Significant calcium carbonate precipitation seems to appear only in late spring at the very top and very bottom of Antarctic landfast ice, or in Young Sound.

In most of the studies, calcium carbonate precipitation is located at the air-ice interface (Barber et al., 2014; Dieckmann et al., 2010; Fischer et al., 2013; Nomura et al., 2013a; Rysgaard et al., 2013). Precipitation at the surface has been ascribed to the lower temperature and higher salinity encountered at the ice surface (Nomura et al., 2013a). This would suggest that the calcium carbonate precipitation would intensify in cold autumn and winter sea ice. However, the lack of precipitation encountered during the PIPERS survey, but also in September and October in McMurdo Sound (Chapter III.), with omega ikaite values below the threshold of 1 in both surveys, shows obviously that cold ice does not favour calcium carbonate precipitation.

In McMurdo sound, we observed the largest calcium carbonate precipitation at the bottom of the ice in late spring in the warmest ice layer (Chapter III.). Clearly, this calcium carbonate precipitation was not related to the decrease of temperature and related increase of salinity, but rather to the decrease of pCO_2 and DIC related to intense primary production, and biofilm growth. Indeed, Papadimitriou et al. (2013) have shown that calcium carbonate precipitation is facilitated in low pCO_2 conditions, i.e. when air-ice CO_2 degassing or primary production maintain the pCO_2 close or below the atmospheric concentration. However, Delille et al. (2014), Geilfus et al. (2012a) and results in our Chapter III. have shown that any decrease of sea ice temperature drives a significant pCO_2 increase in brines in parallel with the increase of brine salinity. For instance, brine pCO_2 is above the saturation for ice temperature below -6°C in the Southern Ocean and -3°C in the Beaufort Sea (Geilfus et al., 2014). Accordingly, high pCO_2 observed in the ice interior at low temperature does not favour calcium carbonate precipitation. As suggested by Rysgaard et al. (2013), in winter, favourable conditions for calcium carbonate precipitation are only found at the top of the ice, where gas exchanges can potentially maintain pCO_2 of brine close to the atmospheric concentration. This challenges the current view that low temperatures - and the related increase in brine salinity - control calcium carbonate precipitation. This is consistent with the lack of relationship between temperature, salinity and calcium carbonate precipitation reported by Nomura et al. (2013a). Instead, we advocate that pCO_2 is a key control of calcium carbonate precipitation and that low pCO_2 is a prerequisite for ikaite formation.

In the model of Mortenson et al. (2018), the value of 54 $\mu\mathrm{mol\,kg^{-1}}$, very close to the detection limit of our method, was used to set the calcium carbonate precipitation within arctic sea ice, and to assess its impact in term of atmospheric CO_2 uptake. Mortenson et al. (2018) suggested that such ikaite precipitation and subsequent dissolution in the water column during ice melt had a small impact on the net ocean carbon uptake estimated at ∼1%. This suggests that calcium carbonate precipitation below our detection limit, i.e. 50 $\mu\mathrm{mol\,kg^{-1}}$, has a limited impact on global carbon fluxes. Overall, low calcium carbonate concentration found in Antarctic ice interior suggests that the significance of this precipitation process in sea ice CO_2 dynamics should not be overrated.

Table 7: Calcium carbonate concentrations in sea ice, snow, frost flowers (FF) or brine skim from different regions of the Arctic and Southern Oceans. SERF refers to Sea-ice Environmental Research Facility (Manitoba).

Location	Type	Season	Ice depth (cm)	Snow depth (cm)	$CaCO_3$ concentrations range (μmol kg^{-1})	Reference
Canada, SERF	FF, artificial sea ice	Winter	20	1-9	2000	Rysgaard et al. (2014)
Arctic Ocean						
Young Sound, Greenland	Thick snow cover (ICE I)	Winter	110	70	430 ± 43	Søgaard et al. (2019)
Young Sound, Greenland	Thin snow cover (POLY I)	Winter	30	17	250 ± 27	Søgaard et al. 2019 (2019)
Young Sound, Greenland	Sea ice (ICE I)	Winter	110	70	100-900	Rysgaard et al. (2013)
Young Sound, Greenland	Sea ice (POLY I)	Winter	30	17	200-700	Rysgaard et al. (2013)
Young Sound, Greenland	FF and brine skim	Spring	5-20	0	500-3000	Barber et al. (2014)
Alaska, Barrow	FF and brine skim	Spring	20	0	15-25	Geilfus et al. (2013)
Greenland , Kapisigdlit	Snow cover (seasonal study)	Winter	0-81	0-7	3-5	Søgaard et al. (2013)
Fram strait, North of Svalbard	Pack ice	Spring	31-500	1-39	30-60	Nomura et al. (2013a)
Southern Ocean						
Weddell Sea	Young and thick lanfast ice	Spring	25-225	N/A	0-103	Dieckmann et al. (2008)
Eastern Antarctica	Top of pack ice	Late winter - Early summer	49-133	N/A	1-52	Fischer et al. (2013)
Adélie Land	Landfast ice	Spring	∼60	∼0	0-26	Fischer et al. (2013)
Adélie Land	Top 5 cm of young landfast ice	Spring	∼15	∼0	25-550	Fischer et al. (2013)
McMurdo Sound, Ross Sea	Landfast ice	Late Winter	150	5	<50	Chapter III.
McMurdo Sound, Ross Sea	Landfast ice (top 5 cm)	Spring	170	5	0-70	Chapter III.
McMurdo Sound, Ross Sea	Landfast ice (ice interior)	Spring	170	5	<50	Chapter III.
McMurdo Sound, Ross Sea	Landfast ice (bottom 20 cm)	Spring	170	5	0-350	Chapter III.
Western Ross Sea	Pack ice	Autumn	20-57	0-20	<50	Present study

IV.4.2. DIC_{35} enrichment in the ice interior

The vertical distribution of DIC_{35} showed an inverse C profile. The main feature was an enrichment in the ice interior and at the bottom compared to the underlying layer. In addition, the maximum DIC_{35} corresponded to the lowest brine volume - i.e. the less permeable layers (Figure 37). We examined the main driving processes that can potentially lead to this DIC_{35} enrichment.

IV.4.2.1. Calcium carbonate precipitation

It should be noted that any precipitation should have decreased DIC_{35}, especially since DIC_{35} was derived from filtered total alkalinity measurements (TAf) where $CaCO_3$ crystals have been removed. Calcium carbonate precipitation cannot lead to a DIC_{35} enrichment. Besides, no significant calcium carbonate precipitation was observed during the PIPERS survey. Overall, calcium carbone precipitation cannot explain the observed DIC_{35} enrichment.

IV.4.2.2. Biological processes

Wauthy et al. (in prep) assessed the net community production (NCP) in the ice derived from O_2:Ar ratios. NCP levels ranged between -8.47 and 31.75 $\mathrm{mg\,C\,m^{-2}\,d^{-1}}$ with a mean value of 1.74 $\mathrm{mg\,C\,m^{-2}\,d^{-1}}$, suggesting that pack ice in the Ross Sea was slightly autotroph. These NCP values were larger than values observed in autumn (Mock et al., 2002) in the Weddell sea, and fell in the lower range of previous estimates of Antarctic sea ice primary production in spring or summer (summarized in Arrigo (2017)). Inbound stations (PIP1–5) showed the highest positive values of NCP at the end of April (April 19 to April 28) while some light was still available as also indicated by the O_2/Ar ratios on the figure 40. In the older ice of the central Ross Sea, heterotrophic activity was observed in interior ice and younger and permeable bottom layers (with the exception of the station PIP23) and at the margin of the TNBP polynya (stations PIP6–8). Overall, limited NCP indicates a low net ecosystem production, that could be expected taking into account (i) both the season and the low latitude of the measurement in the Southern Ocean and related low incoming light (ii) low temperature that neither favours primary production nor respiration. Hence, biological processes were likely playing a minor role in the observed DIC_{35} enrichment.

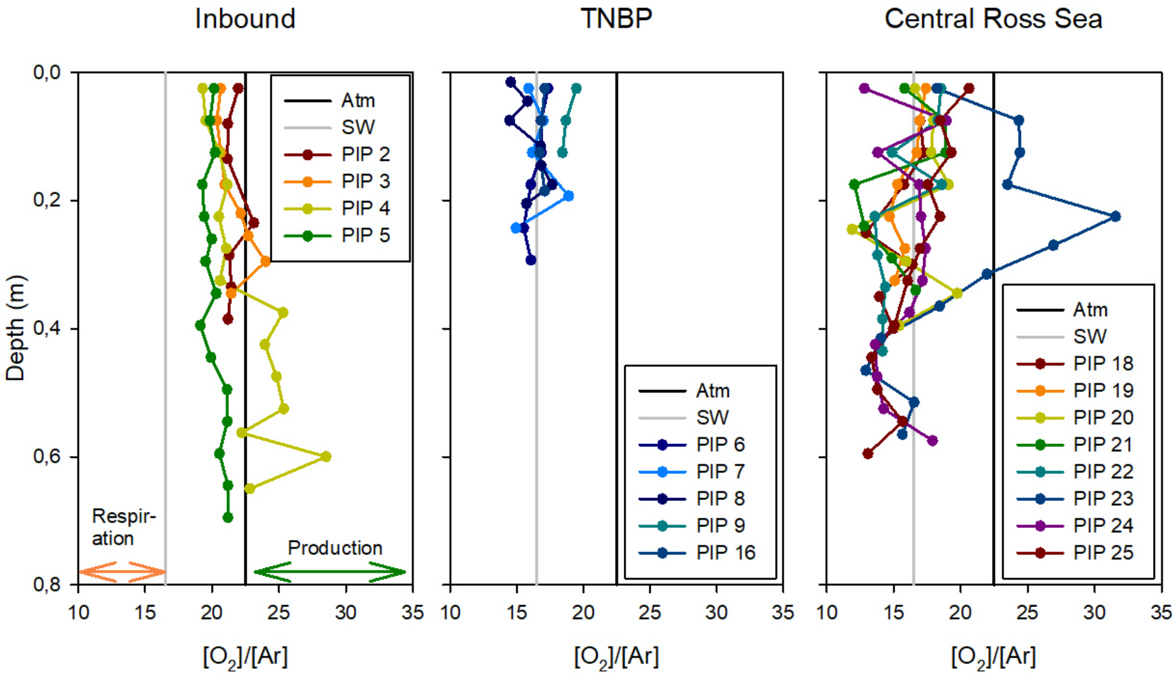

Figure 40: Vertical profiles of O_2/Ar ratios at inbound stations (PIP2-5), Terra Nova Bay Polynya (TNBP, PIP6-16) and central Ross Sea (PIP18-25). The black and grey lines refer to the atmospheric O_2/Ar ratio and the O_2/Ar seawater ratio in TNBP, respectively.

IV.4.2.3. Physical processes

Given the relatively low biological activity, DIC_{35} vertical changes must be explained by a significant impact of physical processes. The DIC_{35} enrichment is most likely related to the decrease of gas solubility and related bubble formation in sea ice as it was observed for Ar, a proxy of physical processes (Tison et al., 2016; Zhou et al., 2013). Briefly, during ice growth, both the increase of gas concentrations and the decrease in gas solubility linked to the salinity increase in brine inclusions with decreasing temperature lead to gas supersaturation and bubbles formation. Once formed, the gas bubbles move upwards due to their buoyancy and remain trapped under the impermeable surface layer while other solutes are expelled downward together with the brines in the underlying water. Moreover, the replacement of brines by underlying seawater during the convection brings new seawater enriched in gases. This incoming seawater will be subjected to the net decrease of gas solubility occurring in brine inclusions, so that repeated convective events are likely raising bulk ice Ar concentration through successive cooling and bubble nucleation and migration (Tison et al., 2016). Hereafter, we denoted this process as “bubble-driven gas enrichment”.

Accordingly, the highest DIC_{35} values are observed in the impermeable layers (Figure 38). This suggests that the bubbles are moving upwards till they reached an impermeable layer. To validate our hypothesis of gas enrichment, we used argon data to track the physical processes. Layers between 20 and 40 cm presented the higher median Ar_{35} concentrations, estimated at 23 μmol L^{-1}, while the seawater value at saturation is 18.2 μmol L^{-1}. This enrichment in argon corresponds exactly to the depth where the highest DIC_{35} values were observed. A slight Ar_{35} enrichment is also observed lower in the ice column. However, the layer between 60 and 70 cm includes only three measurements at two different stations of the MIZ (stations PIP4 and 5) and should be considered cautiously. Overall, vertical distributions of DIC_{35} and Ar_{35} are similar and suggest that the observed enrichment of DIC_{35} in the ice interior is mainly driven by physical processes, i.e. bubble-driven gas enrichment as introduced by Zhou et al. (2013).

IV.4.2.4. DIC_{35}:TAf_{35} relationship

The figure 41 provides insights on the processes occurring within consolidated, pancake and frazil ice during PIPERS. We plotted normalized DIC (DIC_{35}) versus normalized TAf (TAf_{35}) to discard dilution/concentration changes from other processes controlling the carbonate system.

Most of the DIC_{35} and TAf_{35} values of consolidated, pancake and frazil ice in autumn are significantly higher than in the underlying water. An obvious trend ranging between $CaCO_3$ dissolution and CO_2 invasion is observed. As we reported only CO_2 releases to the atmosphere from the air-snow-ice CO_2 fluxes measurements, this suggests that any CO_2 invasion relates mainly to bubble-driven CO_2 enrichment. The latter appears as one of the main processes. The imprint of calcium carbonate dissolution is unclear as we did not detect calcium carbonate crystals. However, we can not exclude that an auto-correlation between DIC and TAf is responsible for this good relationship ($R^2 = 0.94$) along the slope 1:1.

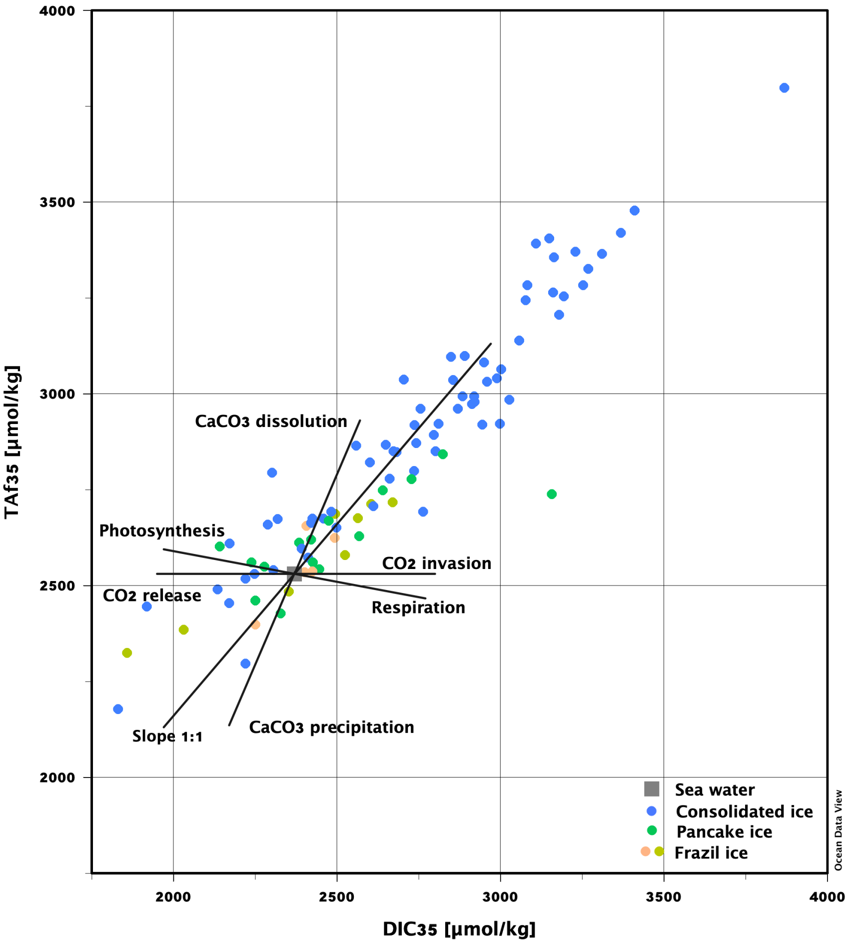

Figure 41: DIC_{35}:TAf_{35} relationship in seawater, consolidated ice, pancake ice and frazil ice samples. The different solid lines represent the theoretical evolution of DIC_{35}:TAf_{35} relationship following a precipitation or dissolution of calcium carbonate, a release of CO_2 or invasion of CO_2 (uptake from the atmosphere or bubble-driven enrichment) and impacts of biological processes.

IV.4.3. DIC depletion at the surface

DIC_{35} and Ar_{35} values were decreasing above the impermeable layers, i.e. in the top 20 cm of the ice (Figure 38). The consistency between DIC_{35} and Ar_{35} distributions suggests that this decrease is related to a physical process, i.e. CO_2 exchanges with the atmosphere. The increase in gas saturation in brines during freezing (Delille et al., 2007; Tison et al., 2016) enhanced by bubble-driven gas enrichment in the ice lead to the oversaturation of gases in brine, a driving force of air-ice gases exchanges. Therefore, gases, in excess in brine inclusions of permeable layers compared to the atmospheric saturation level, are released to the atmosphere. The decrease appears to be limited to the top 20 cm of the ice, in accordance with our observations in landfast ice (Chapter III.) where the top 20% of the ice column were defined as the surface layer under an observable influence of air-ice gas exchanges.

IV.4.4. Air-ice CO_2 release over young ice

Figure 36 presents the CO_2 fluxes to the atmosphere depending on the ice type. Exchanges are enhanced above first stages of ice formation, i.e. unconsolidated grey ice and pancake ice. Over frazil, fluxes are lower than over unconsolidated grey ice and pancake ice as they corresponded to the combination of CO_2 uptake by cold surface water undersaturated in CO_2 compared to the atmosphere and release of CO_2 by growing frazil crystals. The CO_2 release outweighed the uptake by the undersaturated surface water (Figure 36 - open water), resulting in a modest positive flux over frazil ice (Table 5).

Enhanced fluxes of CO_2 over young ice are not surprising. Indeed, young ice is characterized by a high mean brine volume ratio (Table 5) and high permeability that favour brine and gas transports. Nomura et al. (2018) suggested that relatively high temperatures encountered in young sea ice compared to the atmosphere, as we observed during the PIPERS survey (Table 5), promote CO_2 releases. In addition, active brine rejection develops in young ice. Downward brine rejection is an overwhelming transport pathway in sea ice, but some part of the brines is also rejected upwards. Upward brine expulsion (Eicken, 1992) enhances salinity at the surface and leads to high salinities at the bottom of the snowpack, as indicated by the larger salinities in snow (ranging between 0.6 and 53) compared to ice. Upward gas expulsion, along with brine upwards expulsion, very likely contributes to CO_2 releases to the atmosphere. Overall, high permeability, large temperature gradients, and upward brine expulsion processes promote CO_2 release to the atmosphere.

IV.4.5. Impact of snow on air-ice CO_2 fluxes

Generally, snow is expected to hamper air-ice CO_2 fluxes (Delille et al., 2014; Nomura et al., 2010b). This is suggested by the lower mean value of air-snow fluxes compared to air-ice fluxes in autumn (Table 5). However, fluxes over snow exhibited larger variability than fluxes over bare ice after snow removal. Indeed, fluxes over the snow showed both positive and negative values, while fluxes over bare ice showed only positive values (Table 5).The largest CO_2 fluxes were also observed at the air-snow interface. This indicates that in some case, the snow enhances CO_2 fluxes, in agreement with previous observations of Papakyriakou and Miller (2011) and in our Chapter III. In other cases, fluxes above the snow are reversed compared to fluxes over the ice. This suggests that snow is playing a more complex role than a simple transient buffer of air-ice CO_2 fluxes. The impact of snow on air-ice CO_2 fluxes is therefore not fully resolved due to the lack of understanding of CO_2 dynamics in saline snow.

IV.4.6. Significance of CO_2 fluxes over polynyas

The figure 36 shows enhanced fluxes over early sea ice stages. In the table 8, we assessed the significance of CO_2 fluxes over early sea ice stages found in polynyas compared to consolidated pack ice found elsewhere in the Southern Ocean (SO). Our assessment is based on measurements carried out during PIPERS in the Terra Nova Bay Polynya (TNBP). We assumed that only frazil ice was found during katabatic wind events (wind speed > 17 $\mathrm{m\,s^{-1}}$, Thompson et al. (2020)) while unconsolidated ice and pancake ice were found in equal quantity during wind relaxation event. Katabatic wind events were observed 21% of the time spent in the TNBP (Fig. 3 in Thompson et al. (2020)). Using underway visual observations of ice concentration, we derived a mean ice concentration in the TNBP of 0.85% (based on fig 4 in Ackley et al. (2020)). The mean flux over open water measured with our floating chamber was -0.49 $\mathrm{mmol\,m^{-2}\,d^{-1}}$. We expected this number to be underestimated as measurements were carried out only in low wind conditions. Indeed, this value is 40% lower than the mean value for the SO south of 45°S derived from the combined SOCAT and SOCCOM observations (Landschützer et al., 2019). We assessed that the mean daily CO_2 flux in TNBP during PIPERS was 4.55 $\mathrm{mmol\,m^{-2}\,d^{-1}}$ which is large compared to the mean air-sea fluxes in the open ocean south of 45°S derived from SOCAT and SOCCOM measurement (Landschützer et al., 2019). However, taking into account the extent of polynya provided by Kern (2009), we assessed that the overall flux in autumn over polynyas was $1.3\ 10^{-8}$ $\mathrm{Tg\,C\,d^{-1}}$, which is insignificant compared to fluxes over consolidated ice (0.23 $\mathrm{Tg\,C\,d^{-1}}$) or snow covered consolidated ice (0.09 $\mathrm{Tg\,C\,d^{-1}}$). This results from the surface extent of polynya, estimated to 245000 $\mathrm{km^2}$ (Kern, 2009)), which is several order of magnitude lower than the SO sea ice extent, estimated to 14600000 $\mathrm{km^2}$ in September (Parkinson and Cavalieri, 2012).

We assessed the air-sea CO_2 exchanges based on the pCO_2 climatology from Takahashi et al. (2009) for the SO south of 46°S from April to June to -0.77 $\mathrm{Tg\,C\,d^{-1}}$. The SO open water autumn sink is significantly counterbalanced by air-ice and air-snow CO_2 releases. Indeed, air-snow and air-ice CO_2 fluxes account for 12 and 30% of the air-sea CO_2 fluxes, respectively, but with opposite direction.

Table 8: Integration of CO_2 fluxes over polynyas and consolidated pack ice. TNBP and SO refer to Terra Nova Bay Polynya and Southern Ocean, respectively.

Underway measurement of ice concentration during in TNBP during the PIPERS cruise (%)	0.85	Thompson et al. (2020)
Duration of katabatic wind event (wind speed > 17 m s^{-1}) vs wind relaxation period during the PIPERS cruise (%)	21	Ackley et al. (2020)
Coastal polynya extent (km^2)	245000	Kern et al. (2009)
SO sea ice extent (km^2)	14600000	Parkinson and Cavalieri (2012)
Mean CO_2 fluxes ($mmol\,m^{-2}\,d^{-1}$)		
Open water south of 45°S from April to June	-0.82	Landschützer et al. (2019)
Open water in TNBP measured with the floating chamber	-0.49	
Frazil ice	1.57	
Unconsolidated ice	5.42	
Pancake ice	7.45	
Fluxes in TNBP (integrating frazil, unconsolidated ice, pancake ice and open water)	4.55	
Consolidated ice	1.35	
Snow covered consolidated ice	0.51	
Integrated CO_2 fluxes ($Tg\,C\,d^{-1}$)		
Fluxes over polynyas	$1.3\ 10^{-8}$	
Fluxes over snow covered consolidated ice	0.09	
Fluxes over bare ice	0.23	
Air-sea fluxes April to June south of 46°S	-0.77	Takahashi et al. (2009)

IV.4.7. Air-ice CO_2 fluxes in autumn over consolidated ice

Two large scale budgets of air-ice CO_2 exchanges have been proposed (Delille et al., 2014; Rysgaard et al., 2011). Both suggested that the Antarctic sea ice cover would act as a significant sink for atmospheric CO_2 ranging from 0.019 Pg C to 0.052 Pg C for the spring-summer period. Still, both studies do not address autumn and winter fluxes. The budget proposed by Delille et al. (2014) is based on air-snow fluxes and in particular the temperature relationship presented in the Figure 42. This relationship assumes that the ice is impermeable, and fluxes are null accordingly, below a surface temperature of -9°C. This holds true for salinity up to 8.5. However, during PIPERS survey, we observed salinity values at the surface ranging from 14 to 25 for consolidated ice, and brine volume ranging from 5.8% to 19.1%, with a mean around 10%, significantly above the permeability threshold of 5%. As a result, we measured positive air-ice CO_2 fluxes for ice temperatures ranging from -16.5°C to -9°C (Figure 42). Further south in McMurdo sound, we reported positive fluxes, with a lower magnitude, in cold ice in September (Chapter III.). Nomura et al. (2018) reported positive fluxes with a comparable magnitude over arctic ice, North of Svalbard, in the same temperature range. Overall the ice appears to act as a source of CO_2 for the atmosphere in autumn and winter.

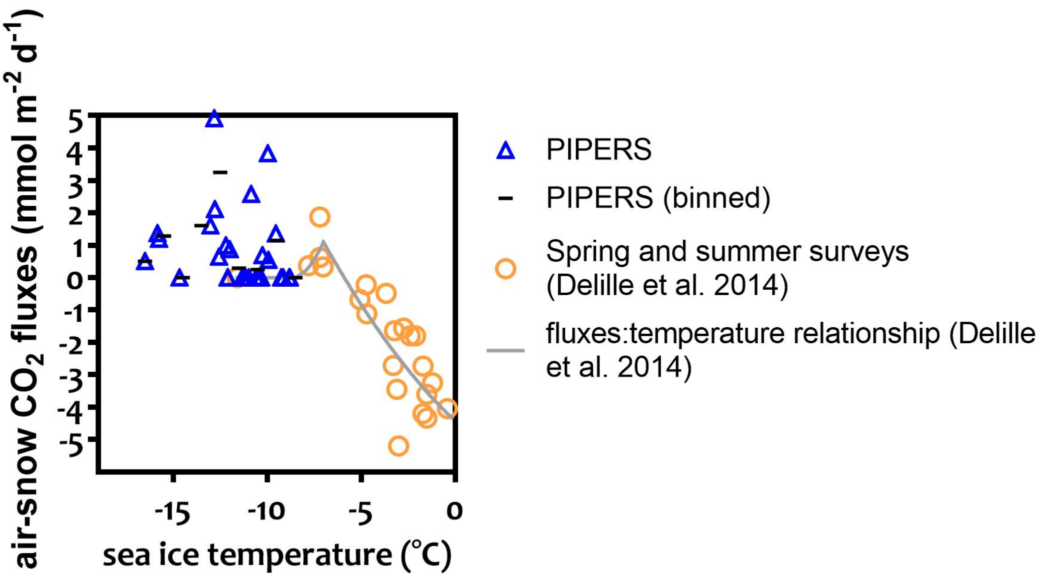

Figure 42: Air-snow CO_2 fluxes over consolidated ice as a function of the ice temperature. Blue triangles correspond to the measurements carried out during the PIPERS survey. For the sake of clarity, fluxes measurements during PIPERS were binned into 1°C interval. Measurements of three other surveys presented in Delille et al. (2014) have been reported (open orange circles).

IV.5. Conclusions

We carefully documented the vertical distribution of $CaCO_3$ in various locations and within various ice types in autumn during the PIPERS cruise. We did not detect significant - i.e. above 50 μmol kg^{-1} - calcium carbonate precipitation. This shows that the decrease of temperature and related increase of salinity does not necessarily trigger calcium carbonate precipitation. Instead, we advocated that pCO_2 is a key control of calcium carbonate precipitation, as suggested by Papadimitriou et al. (2013). The absence of detectable calcium carbonate precipitation in autumn pack ice, and our observations in land fast ice in McMurdo Sound (Chapter III.) indicated that significant calcium carbonate precipitation is limited to the top and the bottom of the ice in spring. This suggests that sea ice calcium carbonate precipitation is not a common feature in the western Ross Sea and that calcium carbonate precipitation, although commonly reported in Fram Strait (Barber et al., 2014; Dieckmann et al., 2010; Nomura et al., 2013a; Rysgaard et al., 2013; Søgaard et al., 2019), is not a ubiquitous process in sea ice, in particular in autumn and late winter.

DIC_{35} and Ar_{35} vertical distributions showed similar behaviour in Antarctic pack ice in autumn. The main features were (i) an enrichment in the interior and bottom ice compared to the seawater surface values (ii) maximum values observed at about 20 cm, corresponding to the impermeable layers (iii) a marked decrease at the top of the ice that led to concentrations close to the seawater value, or even below. The consistency between DIC_{35} and Ar_{35} vertical distributions suggests that the main drivers of DIC_{35} changes in autumn pack ice were physical processes: (i) the bubble-driven gas enrichment as described by Zhou et al. (2014, 2013) and Moreau et al. (2014) within and below the impermeable layers (ii) air-ice gas exchanges above the impermeable layers.

Measurements of CO_2 fluxes carried out during this study provided new data in autumn - a prerequisite to budget air-ice CO_2 fluxes over the year and evaluate the large-scale influence of these fluxes on the annual uptake of CO_2 by ice-covered oceans. Air-ice CO_2 fluxes were enhanced over young ice, compared to consolidated ice, due to the high permeability of young saline ice. High fluxes were supported by active upward brine expulsion and the bubble-driven CO_2 enrichment of the ice, a key process that shapes vertical gas profiles. This abiotic build-up of gases, including CO_2, fuels CO_2 fluxes from the ice to the atmosphere over the western Ross Sea pack ice. This calls for a revision of the current budget of air-ice CO_2 fluxes to account for automnal fluxes at low ice temperature (i.e. below -8°C).

Chapter V. Conclusions and perspectives

The main objectives of this work were to investigate the inorganic carbon processes in both pack and landfast sea ice from the Ross Sea, Antarctica. We focused on the seasonal CO_2 dynamics from autumn to spring, the role of sea ice in the regional carbon cycle (CO_2 source vs sink) and the key physical and biogeochemical processes driving the CO_2 dynamics.

We provided two data sets of CO_2 fluxes measured above Antarctic sea ice, one in autumn and a long-term monitoring from late winter until summer. Major findings are summarized below and placed within the broader context of the polar carbon cycle.

V.1. Sea ice as a significant source of CO_2 in autumn and sink in late spring?

In order to derive seasonal trends, CO_2 fluxes over snow and ice were averaged per month, for both the PIPERS dataset (April-June) and YROSIAE dataset (September-December). The mean CO_2 fluxes range from -0.07 $\mathrm{mmol\,m^{-2}\,d^{-1}}$ to +1.92 $\mathrm{mmol\,m^{-2}\,d^{-1}}$ (Figure 43). Larger mean CO_2 fluxes are observed in winter than in spring.

Positive fluxes (fluxes from the ice to the atmosphere) are reported during sea ice growth. Positive fluxes are expected given the strong abiotic processes taking place in brines at this season (cooling, concentration of solutes in brines and related oversaturation of gases, brine rejection and upward transport). It is consistent with high pCO_2 values observed at the sea ice surface in late winter, and early spring (Figure 28 YRS, Chapter 3). When the sea ice growth slows down in October, the magnitude of the CO_2 fluxes decreases. The transition from a CO_2 source to a CO_2 sink occurs during November while the bulk ice pCO_2 drops below the atmospheric pCO_2. This transition took place later in the season than in previous studies. In the Bellingshausen Sea, at approximately 69°S-71°S, Delille et al. (2014) and Geilfus et al. (2014) observed important negative fluxes in October, pointing out that the transition occurred earlier in the season in that area. While we cannot discard interannual variations in the phenology of sea ice, the late transition in this study can be explained by the sampling location situated in one of the southernmost area of the Southern Ocean (between 67°S-75°S for PIPERS, at 77°38'S for Cape Evans, YROSIAE). In late spring (December), negative fluxes dominate and the sea ice is a net sink.

In April and from September to December, fluxes over snow are larger than fluxes over bare ice (Figure 43). The thin snow layer (max 4 cm in spring and 5 cm in April) appears to enhance gas fluxes. In May and June, the thicker snow layer (up to 20 cm) seems rather to impede fluxes as it has already been suggested by Nomura et al. (2013b). Seeing the snow layer as an inert barrier impeding gas fluxes appears to be too simple to explain our observations. Still, for the time being, very little is known about saline snow chemistry. Additional experiments are required to have a better grasp on snow chemistry and its impact on air-ice fluxes.

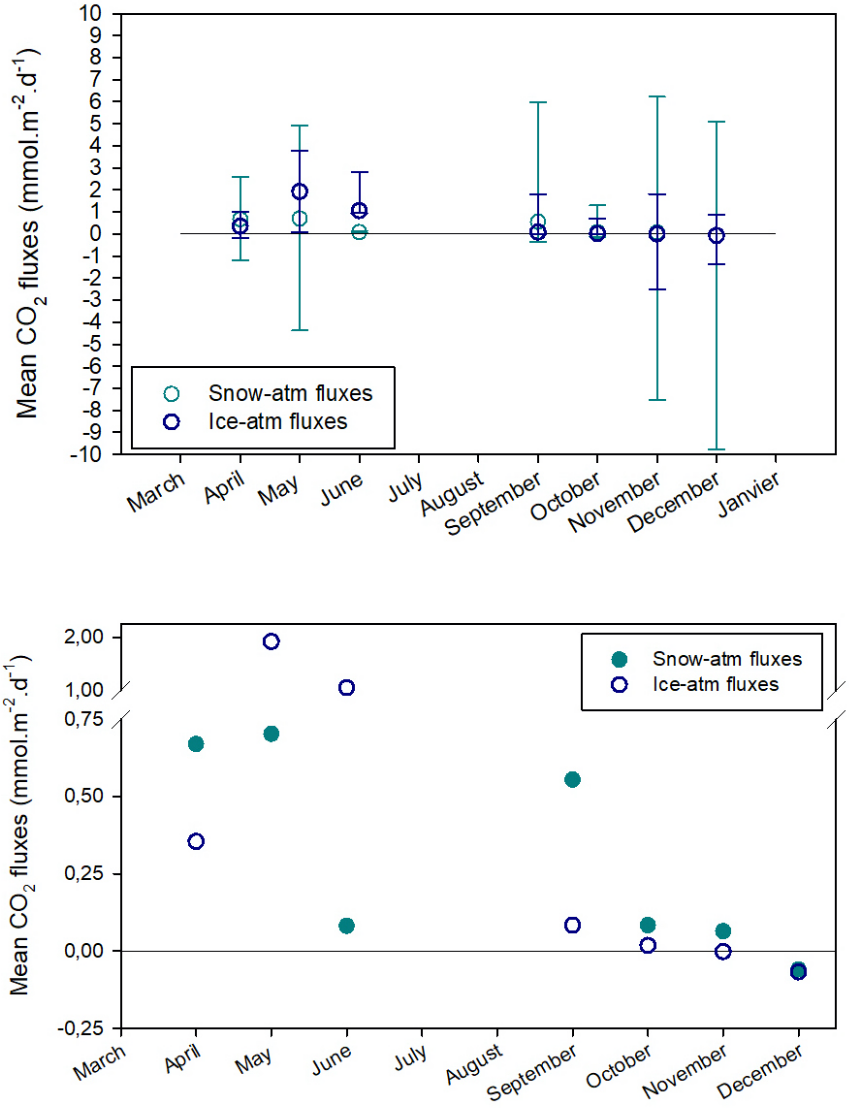

Figure 43: Mean CO$_2$ fluxes over consolidated ice (blue open circles) and snow (blue-green dots) and the associated range of raw CO$_2$ fluxes (a), zoom on the mean CO$_2$ fluxes (b).

V.1.1. Air-snow-ice CO_2 fluxes through seasons

The figure 44 presents the air-snow-ice CO_2 fluxes measurements using the chamber technique through seasons in Saroma-ko, the Arctic and Southern Oceans and allows to place our new data in a broader context. The CO_2 fluxes measured during YROSIAE and PIPERS are in the range of other studies. Our results fill a crucial gap by adding measurements in autumn and late winter. Furthermore, the largest fluxes ever recorded using the chamber technique were observed over young growing sea ice during PIPERS. In winter, large positive fluxes are observed both at YROSIAE and in the Arctic. This was unexpected given the cold and impermeable ice at this period. Furthermore, some negative fluxes were also reported at this season, as in Saroma-ko while the air temperature rose above 0°C during several sampling days. In spring, in the Southern Ocean (SO), mainly negative fluxes were reported, the trend is less clear for the Arctic Ocean with limited fluxes magnitude. During the spring-summer transition, Delille et al. (2014) and Geilfus et al. (2016) observed negative fluxes over pack ice and artificial ice. The role of the snow layer is unclear, sometimes impeding sometimes enhancing CO_2 fluxes.

To provide the mean air-sea CO_2 fluxes in the SO as indicated on the figure 44, we used the free database from Landschützer et al. (2019). The air-sea CO_2 flux estimate is based on the Surface Ocean CO_2 Atlas Database (SOCAT) from 1982 to 2017 and Southern Ocean Carbon and Climate Observations and Modeling (SOCCOM) biogeochemistry floats starting in 2014. Air-sea fluxes of this product are derived using high-resolution Cross-Calibrated Multi-Platform (CCMP) wind speeds (Atlas et al., 2011) and the quadratic gas transfer formulation of Wanninkhof (1992) rescaled to a global mean gas transfer velocity of 16 cm h^{-1}. Among the different products proposed by Landschützer et al. (2019), we used the product based on the raw 2-step neural network sea surface pCO_2 output in μatm from both SOCAT and SOCCOM, with a potential bias of 4 μatm added to the floats. We integrated the air-sea fluxes south of 45°S for each season to compare with snow-ice-air fluxes.

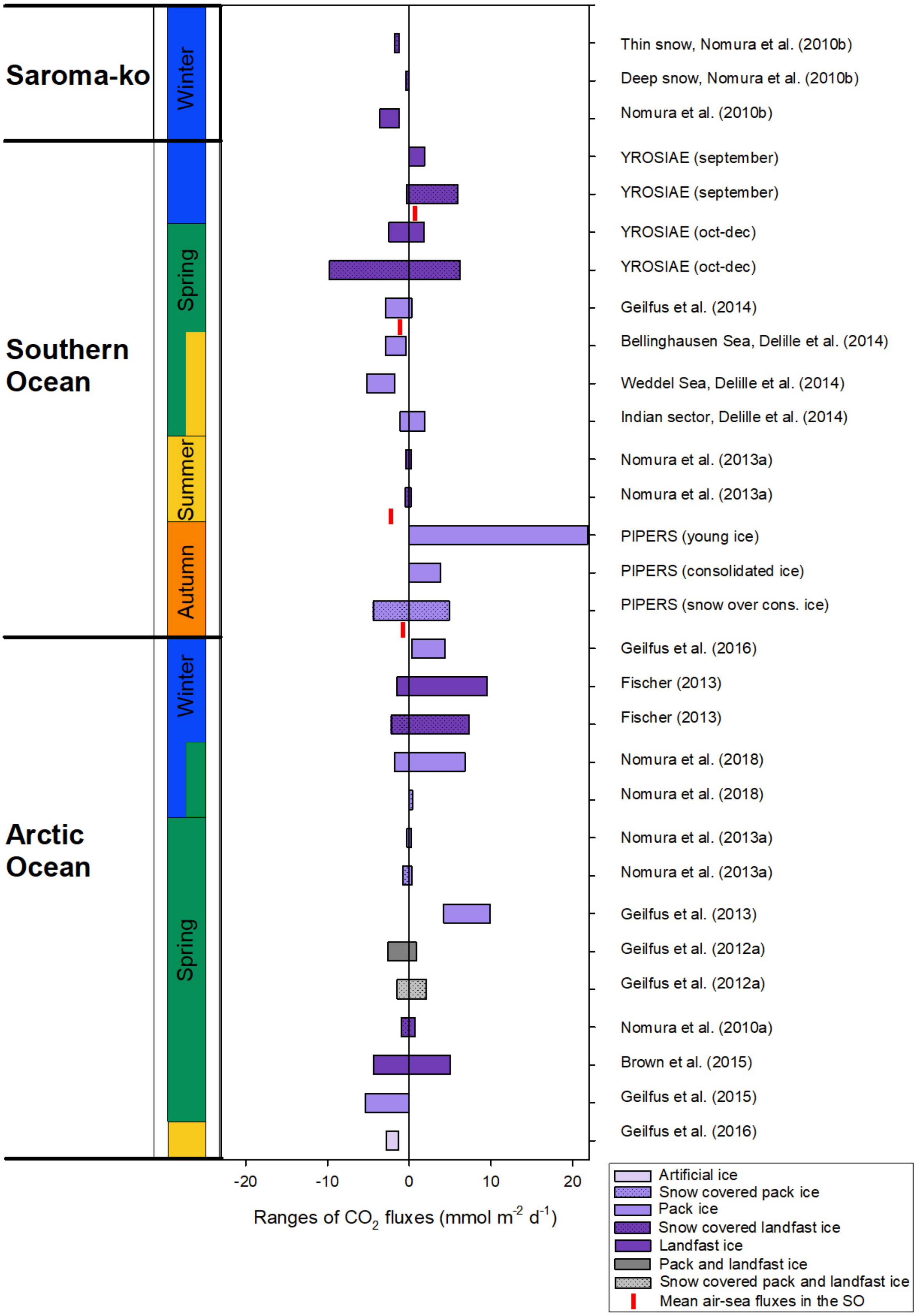

Figure 44: Synthesis of the CO_2 fluxes measurements using the chamber technique through seasons in Saroma-ko, the Arctic and Southern Oceans. Positive fluxes indicate a CO_2 release, negative fluxes indicate a CO_2 uptake. Red vertical lines indicate mean air-sea CO_2 fluxes derived from the combined SOCAT and SOCCOM observations (Landschützer et al., 2019).

V.2. Seasonal DIC dynamics as a function of depth

In order to derive seasonal trends in DIC dynamics, we averaged the DIC data per month. We distinguished three ice layers (i.e. surface, interior, and bottom) to discuss this seasonal DIC dynamics as a function of ice depth. Strong vertical and seasonal changes in DIC were observed within the ice column and over time (Figure 46). These changes are supported by different physical and biogeochemical processes taking place in each layer.

V.2.1. Assessing the depth of the surface layer

Geilfus et al. (2013) estimated the release of CO_2 during ice formation from the observed DIC depletion at the surface of thin landfast sea ice. This DIC depletion refers to the noticeable deviation between the observed DIC and theoretical DIC (DIC_{th}) computed from DIC concentration at 7.5 cm extrapolated to the upper layers assuming a conservative behaviour of DIC relative to the salinity. A similar approach was used in Kotovitch et al. (2016) for young artificial sea ice, they found a DIC anomaly spreading from the top of the surface down to 12.5 cm. This DIC depletion zone corresponds to the ice thickness that is significantly affected by air-ice gas exchanges.

Both Geilfus et al. (2013) and Kotovitch et al. (2016) investigated thin ice. We used the same approach to determine the DIC depletion zone for a consolidated thick ice layer (over 1.5 m) during spring. This DIC depletion zone corresponded to the top 20% of the ice column (or a depth of 33 cm on average). All computations of Chapter III. were performed considering an average DIC depletion zone of 35 cm (Figure 45). This highlights that the ice thickness under the direct and detectable influence of gas exchanges does not exceed 35 cm for a consolidated thick ice layer (over 1.5 m).

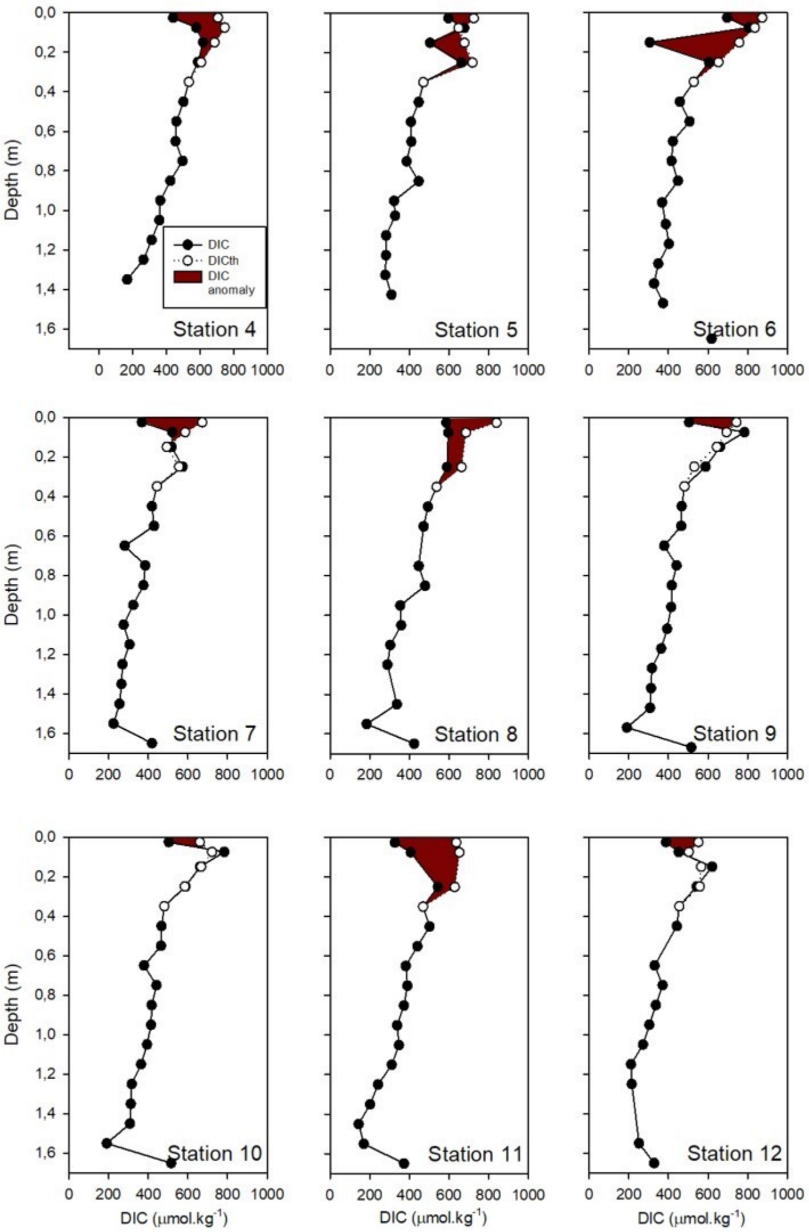

Figure 45: DIC profiles (black dots) and DIC$_{th}$ (open circles) for the stations YRS4 to YRS12. The red area refers to the DIC depletion zone/anomaly.

V.2.2. Assessing the depth of bottom and interior layers

The thickness of the bottom layer was determined by the layer under the influence of seawater allowing replenishment of nutrients and build-up of biomass. We observed that only the bottom 17% of the ice column (22 cm on average) presented a marked decrease in DIC and high nutrient and biomass concentrations (Figures 23, 24 on pages 62, 63). The presence of a microbial biofilm can sustain high nutrient level even during the algae bloom. We surmise that the development of a biofilm probably requires isothermal conditions since large temperature changes and the succession of freezing/melting events would prevent the formation of stable ice walls on which the biofilm can grow. The permeable bottom layers, where the temperature remains at the freezing point, present an ideal media for the development of biofilm and associated large biomass build-up.

The rest of the ice column (between 20% to 83%) was denoted as the ice interior and was characterized by limited vertical gradients in DIC and contrasting values of the main biogeochemical parameters compared to the bottom layer (Figures 23 and 24 on pages 62 and 63). The ice interior is prone to significant seasonal changes in temperature - leading to melting and refreezing events of the ice wall - and limited primary production that both can hamper the biofilm formation.

To sum up, the surface layer where exchanges with the atmosphere occur refers to the top 20% of the ice column. The bottom layer, where significant exchanges with the underlying water take place and the development of a biofilm allows a large build-up of biomass and nutrients, accounts for the last 17% of the ice column and the ice interior extends between 20% and 83% of the ice column. The same references were used to discriminate the pack ice column in autumn, where a clear DIC decoupling is also observed between layers (Figure 38, page 94).

V.2.3. DIC evolution depth by depth

V.2.3.1. Bubble-driven gas enrichment at the beginning of ice formation

Figure 46 shows the evolution of DIC_{35} in consolidated sea ice and surface waters of the Ross Sea from autumn to late spring. An enrichment in DIC_{35} in consolidated sea ice compared to the water column is observed at all depths at the beginning of ice formation in April (Figure 46). It can be ascribed to intense abiotic processes taking place in the ice interior during ice growth while biotic processes appear to be less active. Gas enrichment during ice growth has been first introduced by Zhou et al. (2013), measuring argon concentrations in a nearshore single landfast ice station. This process, denoted as bubble-driven gas enrichment, refers to the increase of gas concentrations and the net decrease of gas solubility linked to the increase of salinity happening in brine inclusions with decreasing temperature, which both lead to gas supersaturation and bubbles formation (Zhou et al., 2013). Once formed, the gas bubbles tend to move upwards due to their buoyancy and remain trapped under the impermeable surface layers. In contrary, other solutes move downward and are expelled from the ice through brine convection. Because of the partition in the gas phase, brine convection does not expel efficiently gas out of the ice to the underlying water. Moreover, the replacement of brine by underlying seawater during the convection brings new sea water enriched in gases. This incoming seawater will be subjected to the net decrease of gas solubility occurring in brine inclusions and leading to the formation of new bubbles. Convective processes at the bottom of the ice therefore fuel the gas-enrichment process. Overall, intense convective processes occurring during ice growth lead to gases and DIC_{35} enrichment compared to salts at all depths in consolidated sea ice.

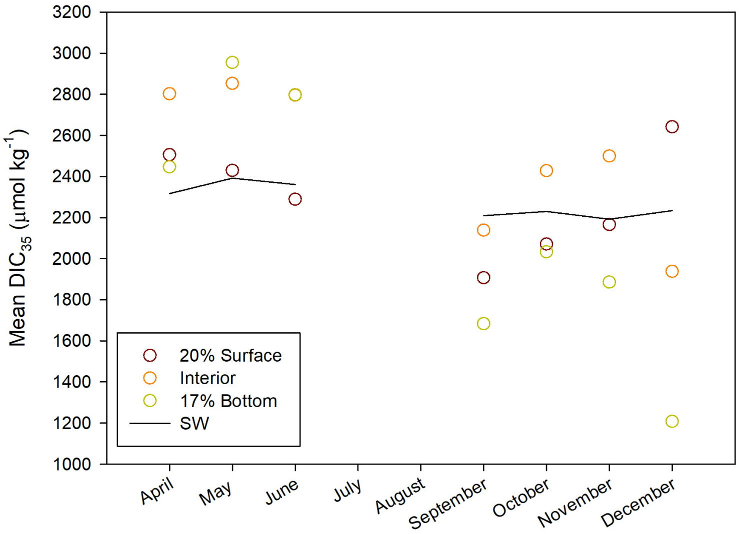

Figure 46: Mean DIC_{35} in layers of consolidated ice (i.e. surface, interior and bottom) during PIPERS (April to June) and YROSIAE (September to December) surveys. The black line presents the DIC_{35} of surface waters averaged per month.

V.2.3.2. Ice surface

At the surface, the initial DIC_{35} enrichment compared to the underlying water disappears rapidly in May and June as the excess of CO_2 is released to the atmosphere. Colder surface temperature and related increase in brine salinity maintain CO_2 oversaturation and sustain important CO_2 release to the atmosphere. The release of CO_2 to the atmosphere drives the decrease in DIC_{35} in surface layers during autumn and winter, which falls below the seawater level in June and reaches a minimum value in September when the coldest ice temperature were observed. In October, the temperature at the surface starts to increase, the pCO_2 decreases (Figure 27, page 67) due to the melting and related brine dilution, but the oversaturation in CO_2 and related CO_2 release to the atmosphere are maintained until November (Figure 43). Despite the observed CO_2 release to the atmosphere, DIC_{35} increases from September to November. A possible explanation of this discrepancy would lie in the onset of bacterial respiration in October and November at the surface as the temperature is increasing. That process would then appear as a significant source of CO_2 in the surface layers. An alternative explanation is brine overturning taking place at the end of November while the surface salinity decreased. In late November, the sea ice surface becomes undersaturated in CO_2 and shifts from a source to a sink of CO_2 for the atmosphere. As a result, DIC_{35} values show a marked increase. Overall, DIC_{35} in the surface layer appears to be mainly controlled by physical processes: (i) air-ice CO_2 exchanges, (ii) brine dilution and concentration (iii) bubble-driven gas enrichment during the ice growth and potential bacterial respiration.

V.2.3.3. Ice interior

In the ice interior, the DIC_{35} enrichment is enhanced compared to the other layers and lasts from April to November (with an exception in September). From September to October, DIC_{35} increases strongly in impermeable layers (BrV $< 5\%$) of landfast sea ice (Figure 22c, on page 60). In the central Ross Sea, internal impermeable layers also show higher values of DIC_{35} (Figure 37, page 92). This DIC_{35} accumulation is observed in first-year consolidated pack ice from the central Ross Sea and first-year landfast ice in interior ice but not in very young and thin ice in autumn. This suggests that the bubble-driven gas enrichment is a slow process that requires time to develop and then significantly affects DIC_{35} content.

A striking feature is the parallel evolution of surface and internal values of DIC_{35}. As sea water is transported from the ice-water interface towards colder (but permeable) ice above, the bubble-driven gas enrichment can temporarily restart and refuel the internal and surface layers in DIC.

Results of our surveys suggest that this mechanism of gas enrichment (i) impacts significantly CO_2 processes (ii) is a common process in sea ice as we observed it in Antarctic pack and landfast ice in numerous locations.

Over the spring, a succession of autotrophic and transient heterotrophic phases was observed in the ice interior but had unclear impact on DIC_{35}. It is only in late spring (i.e. December) that intense autotrophic activity combined with ice melt drove a net decrease in DIC_{35}.

V.2.3.4. Ice bottom

A DIC_{35} enrichment, compared to seawater, was also observed at the bottom during ice growth in autumn. In contrast, in spring as primary production develops at the bottom of the ice, DIC_{35} appears to be depleted compared to seawater values. This depletion increases in late spring, simultaneously with the seasonal peak in biomass. In December, the DIC_{35} exhaustion reaches 45% of the overall seawater DIC_{35} content.

V.3. No impact of calcium carbonate precipitation on CO_2 fluxes?

Calcium carbonate precipitation is potentially a significant process in sea ice altering the carbonate system (Papadimitriou et al., 2004; Papadimitriou et al., 2014; Rysgaard et al., 2007; Rysgaard et al., 2013; Rysgaard et al., 2011). Indeed, this process leads to the decoupling of a solid form of inorganic carbon and dissolved CO_2, with potential impact for atmospheric CO_2 as discussed in Delille et al. (2014). Currently, the significance of this process is still debated.

Although Rysgaard et al. (2011) suggested that this process can act as a significant sink for atmospheric CO_2, several other model studies (Grimm et al., 2016; Moreau et al., 2016) suggested limited impact of calcium carbonate precipitation on the net ocean carbon uptake. Similarly, Mortenson et al. (2018) suggested that an ikaite concentration of 50 $\mu\mathrm{mol\,L^{-1}}$ (i.e. around 54 $\mu\mathrm{mol\,kg^{-1}}$ as reported in Geilfus et al. (2016)) had a limited impact on the net ocean carbon uptake estimated at ∼1%. However, larger ikaite concentrations were reported both in the Arctic and Antarctica (e.g Rysgaard et al. (2013), Fisher et al. (2013) or in this work, Chapter III.). The value used in the model of Mortenson et al. (2018) corresponds to the detection limit of our method to estimate calcium carbonate precipitation. Since we cannot detect lower precipitation and such low precipitation has a limited impact on the net CO_2 uptake as shown by Mortenson et al. (2018), we considered that calcium carbonate precipitation below the threshold of 50 $\mu\mathrm{mol\,kg^{-1}}$ is "not significant".

Significant precipitation at the sea ice surface was expected to occur as a result of low ice temperature (below -19°C), high brine salinity and ikaite saturation state observed in late winter (September). However, only a small amount of calcium carbonate precipitated at the surface during the winter. Surprisingly, high calcium carbonate precipitation was observed at the bottom of the ice (Figure 23c,d, page 62) during the high primary production period and the build-up of EPS rich biofilm. Further north, in young sea ice from the Terra Nova Bay polynya and in pack ice from the central Ross Sea, we hardly detected significant calcium carbonate precipitation (i.e. above 50 $\mu\mathrm{mol\,kg^{-1}}$) during autumn. Calcium carbonate precipitation seems therefore non-ubiquitous in Antarctic sea ice.

V.3.1. Calcium carbonate precipitation in low pCO_2 conditions

A closer look of the YROSIAE survey gives some insights about the lack of significant calcium carbonate precipitation in Antarctic sea ice.

The ikaite saturation state is the driving force for calcium carbonate precipitation. This ikaite saturation state depends on the calcium brine concentration, carbonate brine concentration and their solubility product determined by Papadimitriou et al. (2013). According to Papadimitriou et al. (2013), calcium carbonate precipitation is facilitated in low pCO_2 conditions close to the saturation with the atmosphere. Papadimitriou et al. (2013, 2014) carefully assessed calcium carbonate precipitation during ice growth in laboratory and modeling experiments - Pitzer model of ionic interactions (Marion, 2001) - with “open” and “closed” systems settings. The “open” system corresponded to laboratory experiment or model simulation where pCO_2 is maintained at the atmospheric concentration. The “closed” system corresponded to the setup where pCO_2 increases along with the decrease in temperature and related increase in brine salinity, or due to the release of CO_2 by calcium carbonate precipitation. Both laboratory and model experiments clearly showed that the “closed” system prevents calcium carbonate precipitation, so that precipitation can only develop when pCO_2 remains low as a result of CO_2 exchanges with the atmosphere and/or primary production.

A thorough examination of the Figure 23 (page 62) shows a slight decrease of TAf_6 with values below the seawater value in the top 5 cm of the ice in September and October. This indicates that a limited precipitation may be possible in the surface layer subjected to exchanges with the atmosphere that potentially drive low pCO_2 conditions at the top few cm of the ice. The interface with the atmosphere mimics the “open” system setup of Papadimitriou et al. (2013), so that calcium carbonate precipitation is likely to develop at the very top of the ice in late winter and early spring. Such precipitation of calcium carbonate limited to the skin layer at the ice-snow interface was hardly detectable with our methods. In late spring, while a marked pCO_2 decrease took place (Figure 27, page 67), we observed more clearly calcium carbonate precipitation above the detection limit in parallel with the increase in omega ikaite above the threshold of 1 (Figure 23, page 62).

Calcium carbonate precipitation did not appear in the internal layer where limited transfers of gases take place due to physical settings that mimic the “closed system” setup used by Papadimitriou et al. (2013) which is unfavorable for calcium carbonate precipitation. The simple box model in Table 9, carried out with the CO2SYS program (Lewis et al., 1998), shows that in a closed system, the carbonate concentration in brine does not evolve linearly with salinity and remains low during cooling. Once the system is open and exchanges take place (pCO_2 at equilibrium with the atmosphere), carbonate brine concentration significantly increases, likely promoting calcium carbonate precipitation. Such simulations present limitations and need to be carefully considered since CO2SYS program used the CO_2 dissociation constants of Goyet and Poisson (1989) established for the temperatures and salinities observed in open ocean waters (T > 1°C and salinities of 35).

At the bottom of the ice during YROSIAE, particularly low pCO_2 conditions were reported in spring (below 210 ppm or even below 40 ppm in late spring, Figure 27 on page 67). Simultaneously, large amounts of calcium carbonate precipitation and high omega ikaïte were observed, resulting either of complex processes taking place within the biofilm (Chapter III.) and/or low pCO_2 conditions. In this simulation, such low pCO_2 conditions push up the Ω_{ika} close to 1 while our results showed values higher than 5 (Figure 23 on page 62). The first pCO_2 measurements from the PIPERS study indicate values around 200 ppm. According to our simulation, this corresponds to high calcium carbonate concentrations and an Ω_{ika} around 1.5. However, our dataset presents only some Ω_{ika} values close to 1.5 and all the others below this level (Figure 39, page 95). The actual threshold of Ω_{ika} for significant precipitation can be well above 1. Crystals formation is a complex process that does not rely only on the saturation state.

Table 9: Simulated carbonate brine concentrations and pH conditions in closed and open systems using CO2SYS program and dissociation constant of Goyet and Poisson (1989). Salinity of brines was computed from the temperature, according to Notz et al. (2005). We used mean DIC_{35} and TA_{35} of surface water observed during the YROSIAE survey. The model was forced according to the values in bold. DIC and TA at high salinity are computed assuming a conservative behaviour regarding to the salinity. For the open system, we forced the model using TA and atmospheric pCO_2 (i.e. 410 ppm). The saturation state of brine (Ω_{ika}) was computed following the same method as in Chapter IV. described on page 87

Case	Salinity	T (°C)	TA (μmol kg^{-1})	DIC (μmol kg^{-1})	pH	CO_3^{2-} (μmol kg^{-1})	pCO_2 (ppm)	Ω_{ika}
Observed surface water	**35**	**-1.8**	**2351**	**2210**	8.1	109	301	0.23
Cooling in closed	**87**	**-5**	**5862**	**5470**	8.2	253	1007	0.4
system	**123**	**-8**	**8316**	**7798**	8.7	227	1318	0.33
Open system	**123**	**-8**	**8316**	7089	9.1	550	**410**	0.8
Bottom SI at YRS	**40**	**-2**	**2617**	1949	8.9	450	**40**	0.96
PIPERS first pCO_2 results	**123**	**-8**	**8316**	6556	9.4	859	**200**	1.5

V.3.2. Conceptual representation of our current understanding of calcium carbonate precipitation

To sum up, the figure 47 presents our current view and understanding of calcium carbonate precipitation within sea ice from autumn to spring. At the ice surface, calcium carbonate precipitation is below our detection limit in early spring and becomes significant ($> 50\ \mu\mathrm{mol\,kg^{-1}}$) at the end of the spring, leading to potential CO_2 release since the ice is permeable at that time. At the bottom of the ice, due to the biofilm formation initiated in September providing nucleation sites for calcium carbonate precipitation as described in Chapter III. and/or due to low pCO_2 conditions, significant amounts of calcium carbonate were measured. The fate of the produced CO_2 by calcium carbonate precipitation is still unknown (released to underlying waters, diluted in parallel with ice melting, expelled to the atmosphere or used by algea).

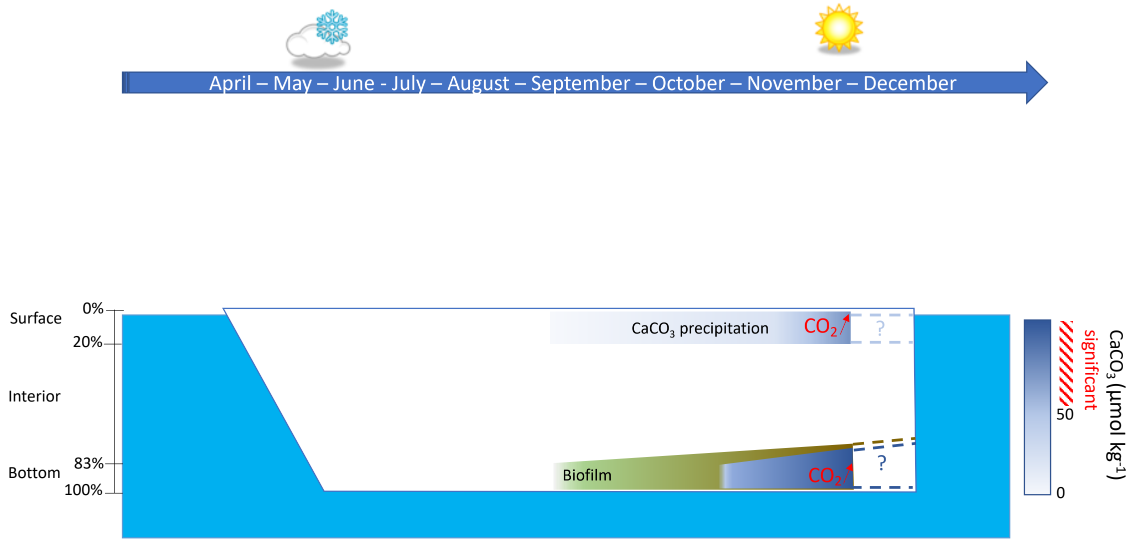

Figure 47: Schematic representation of the Antarctic sea ice active carbon processes of calcium carbonate precipitation and dissolution throughout the year.

V.4. Permeability threshold for gases: a critical issue

In this work, we repeatedly used a first-order estimate of the gas permeability threshold in sea ice, assuming that gas permeability is similar to liquid permeability. Liquid permeability appears to be well constrained, but only in columnar-like ice (Golden et al., 1998). Granular ice appears to be less permeable (Golden, personal communication).

As explained in section V.2.3. (page 114), the DIC accumulates below or in impermeable layers as a result of gas enrichment during the ice growth. The proposed mechanism assumes that the permeability in interior ice layers is large enough to allow the upward migration of gas bubbles and low enough in impermeable layers to allow accumulation. This assumption is currently not verified and difficult to confirm since the permeability threshold for gases is not yet established. The CO_2 releases observed in late winter while the ice surface is considered impermeable raise also questions about the permeability threshold for gases, even if we proposed that winter transport in impermeable conditions is supported by sea ice micro-cracking. Still, sea ice micro-cracking is poorly constrained as well. This inconsistency between fluxes and permeability threshold is still puzzling but critical for our understanding of gas fluxes, and calls for further investigations.

The efficiency of both diffusion processes and bubbles upward migration depends on certain conditions of temperature and ice texture as it has been suggested for fluid transport by Golden et al. (1998). Currently, an higher permeability threshold was discussed for gases (section II.4.4.2., page 26) and potentially ascribed to the tortuosity of brines channels slowing down bubble migration (Crabeck et al., 2014b; Kotovitch et al., 2016; Loose et al., 2010; Moreau et al., 2014). However, given the limited knowledge and literature on the interactions between bubbles themselves and between bubbles and brine channels walls, it is not possible to evaluate the tortuosity effect and validate these estimates of gas permeability threshold. Recent observations of gas bubbles number, size and pressure effects on bubbles nucleation were performed using X-ray tomography (Crabeck et al., 2016) or high-resolution imagery (Crabeck et al., 2019) and could be included in future research and models.

V.5. Perspectives for future research

There has been growing interest in the sea ice carbon cycle and related transfers across the air-ice-ocean interfaces in the last decades. The data presented in this thesis contribute to the understanding of sea ice carbon cycle in Antarctic sea ice, focusing particularly on the seasonal and diel patterns of CO_2 fluxes and the dissolved inorganic carbon dynamics at the early stages of sea ice formation and from late winter to summer. However, open questions remain, and further research is necessary to complete our understanding of the carbon cycle during a complete cycle of sea ice growth and decay.

CO_2 fluxes measurements during winter and summer are of particular interest. Only a few winter expeditions were conducted in Antarctica, even including the two data sets of this thesis, resulting in a critical gap in our knowledge. One of the major aims of the YROSIAE survey was to obtain a temporal series at a dedicated location, allowing us to track seasonal and diurnal variations of CO_2 fluxes. Further long-term and high-frequency measurements, especially during winter and summer, are still necessary to both capture seasonal and diurnal patterns and robustly evaluate the regional carbon budget of sea ice (net source or sink). The closed-path eddy covariance system, recently improved by Butterworth and Else (2018) thanks to the addition of drying devices to remove the moisture of the sampled air, offers the possibility of critical long-term and high-frequency measurements.

Snow properties likely impact CO_2 exchanges. Gas interactions within wet snow cover are expected to be different from those within dry snow as discussed in Chapter III.. The thickness of the snowpack could impact the magnitude of the fluxes. However, the futur snow regime in Antarctica is unknown. The recent IPCC Special Report on the Oceans and Cryosphere in a Changing Climate states that snow accumulation changes in Antarctica are difficult to predict since available data are limited in time and space (Meredith et al., 2019).

- In case of increased snow accumulation, more flooding is expected. Providing fresh nutrients and algae, flooding will increase the primary production and subsequent CO_2 uptake in spring and summer. But more snow tends also to decrease the light availability and the algae productivity, this will contribute to reduce the sea ice CO_2 uptake capacity. The balance depends on when snow accumulation occurs, in winter or during the bloom period. In winter, the snow insulation will enhance the permeability and CO_2 exchanges.
- In case of reduced snow accumulation in winter, shrinking brines channels could hamper CO_2 exchanges while the increased light availability in spring could allow larger primary production and CO_2 uptake.

Future sustained snow observations are needed to evaluate the impact of new snow conditions on CO_2 exchanges.

Unexpected CO_2 releases were observed while the ice was theoretically impermeable in late winter/early spring. In the Chapter III., we suggested the formation of microcracks in the landfast sea ice cover as a potential process triggering these winter CO_2 releases. Microcracking has already been observed through acoustic studies in Antarctica, especially in McMurdo Sound (Cole and Dempsey, 2004; Dempsey et al., 2018; Langhorne and Haskell, 1996). However, the relation between microcracking and CO_2 gas exchanges was never investigated in depth. It might be worth coupling continuous CO_2 fluxes measurements with monitoring of cracking events by using acoustic devices (like transducers mounted in the ice surface).

Recently, the formation of biofilms in sea ice was suggested (Deming, 2010; Meiners et al., 2003, 2008), although not directly observed and not mentioned under that specific name. We reported the presence of microbial biofilm in landfast ice (Roukaerts et al., submitted) at three locations in Antarctica (Ross Sea, Prydz Bay, Terre Adélie). Each site presented simultaneous high biomass and nutrients accumulation at the bottom. In young pack ice, in autumn, neither high biomass accumulation nor nutrients accumulation was detected at the bottom. Autumn pack ice seems therefore be devoid of biofilm formation. Further analyses, on both landfast and pack ice, are required to confirm that the biofilm's formation differs according to ice types and is potentially a seasonal process. Taking a closer look at the conditions required for the biofilm formation (i.e. temperature range, salinity, pH, POC availability), timing and speed of development and its location in the ice column (restricted to ice bottom or not?) could be highly relevant.

Furthermore, the biofilm could play a role in calcium carbonate precipitation. In spring, we found large calcium carbonate precipitation at the bottom of landfast sea ice as a consequence of complex interactions on EPS (Chapter III.). The link between biofilm and calcium carbonate precipitation seems worth exploring. Although several model studies (Grimm et al., 2016; Moreau et al., 2016; Mortenson et al., 2018) suggested limited impact of calcium carbonate precipitation on the net ocean carbon uptake, sea-ice carbon processes need to be considered at a regional scale. These models did not take into account calcium carbonate precipitation at the sea ice bottom supported by biofilm formation. Adding new winter and summer observations of calcium carbonate precipitation could therefore be interesting to obtain a global overview of this process and better estimate its impact at both a regional and global scale. The evolution of the biofilm in warmer climate conditions is, moreover, difficult to predict. In such warmer conditions in Antarctica, the biofilm formation might start earlier in the season and extend higher in a warmer and thinner ice column. This extended biofilm formation might allow larger calcium carbonate precipitation, not restricted to the bottom of sea ice, and in turn impact the sea ice carbon pump.

List of Figures

List of Tables

References

Ackley, S. F., M. J. Lewis, C. H. Fritsen, and H. Xie (2008). Internal melting in Antarctic sea ice: Development of "gap layers". *Geophysical Research Letters* 35.11. DOI: 10.1029/2008GL033644.

Ackley, S. F. and C. W. Sullivan (1994). Physical controls on the development and characteristics of Antarctic sea ice biological communities— a review and synthesis. *Deep Sea Research Part I: Oceanographic Research Papers* 41.10, pp. 1583–1604. DOI: 10.1016/0967-0637(94)90062-0.

Ackley, S. F., S. Stammerjohn, T. Maksym, M. Smith, J. Cassano, P. Guest, et al. (2020). Sea-ice production and air/ice/ocean/biogeochemistry interactions in the Ross Sea during the PIPERS 2017 autumn field campaign. *Annals of Glaciology* 61.82, pp. 181–195. DOI: 10.1017/aog.2020.31.

Ai, X. E., A. S. Studer, D. M. Sigman, A. Martínez-garcía, F. Fripiat, M. Schmitt, et al. (2020). Southern Ocean upwelling, Earth's obliquity, and glacial-interglacial atmospheric CO_2 change. 1.December, pp. 1348–1352.

Aletsee, L and J Jahnke (1992). Growth and productivity of the psychrophilic marine diatoms Thalassiosira antarctica Comber and Nitzschia frigida Grunow in batch cultures at temperatures below the freezing point of sea water. *Polar Biology* 11.8, pp. 643–647. DOI: 10.1007/BF00237960.

Anderson, L. A. (1995). On the hydrogen and oxygen content of marine phytoplankton. *Deep Sea Research Part I: Oceanographic Research Papers* 42.9, pp. 1675–1680. DOI: 10.1016/0967-0637(95)00072-E.

Andreas, E. L. and S. F. Ackley (1982). On the Differences in Ablation Seasons of Arctic and Antarctic Sea Ice. *Journal of the Atmospheric Sciences* 39.2, pp. 440–447. DOI: 10.1175/1520-0469(1982)039⟨0440:OTDIAS⟩2.0.CO;2.

Armstrong, T. (1972). World Meteorological Organization. WMO sea-ice nomenclature. Terminology, codes and illustrated glossary. Edition 1970 . Geneva, Secretariat of the World Meteorological Organization, 1970. [ix], 147 p. [including 175 photos] + corrigenda slip. (WMO/OMM/BM. *Journal of Glaciology* 11.61, pp. 148–149. DOI: 10.3189/S0022143000022577.

Arrigo, K. R. (2002). Ecological impact of a large Antarctic iceberg. *Geophysical Research Letters* 29.7, p. 1104. DOI: 10.1029/2001GL014160.

Arrigo, K. R. (2014). Sea Ice Ecosystems. *Annual Review of Marine Science* 6.1, pp. 439–467. DOI: 10.1146/annurev-marine-010213-135103.

Arrigo, K. R. (2017). Sea ice as a habitat for primary producers. In: *Sea Ice*. Wiley Online Books. Chichester, UK: John Wiley & Sons, Ltd, pp. 352–369. DOI: 10.1002/9781118778371.ch14.

Arrigo, K. R., G. Dieckmann, M. Gosselin, D. H. Robinson, C. H. Fritsen, and C. W. Sullivan (1995). High resolution study of the platelet ice ecosystem in McMurdo Sound, Antarctica:biomass, nutrient, and production profiles within a dense microalgal bloom. *Marine Ecology Progress Series* 127, pp. 255–268. DOI: 10.3354/meps127255.

Arrigo, K. R., G. L. van Dijken, and S. Bushinsky (2008). Primary production in the Southern Ocean, 1997–2006. *Journal of Geophysical Research* 113.C8, p. C08004. DOI: 10.1029/2007JC004551.

Arrigo, K. R., R. B. Dunbar, M. P. Lizotte, and D. H. Robinson (2002). Taxon-specific differences in C/P and N/P drawdown for phytoplankton in the Ross Sea, Antarctica. *Geophysical Research Letters* 29.19, p. 44. DOI: 10.1029/2002GL015277.

Arrigo, K. R. and C. W. Sullivan (1994). A high resolution bio-optical model of microalgal growth: Tests using sea-ice algal community time-series data. *Limnology and Oceanography* 39.3, pp. 609–631. DOI: 10.4319/lo.1994.39.3.0609.

Arrigo, K. R., D. L. Worthen, M. P. Lizotte, P. Dixon, and G. Dieckmann (1997). Primary Production in Antarctic Sea Ice. *Science* 276.5311, 394 LP –397. DOI: 10.1126/science.276.5311.394.

Aslam, S. N., T. Cresswell-Maynard, D. N. Thomas, and G. J. C. Underwood (2012). Production and Characterization of the Intra- and Extracellular Carbohydrates and Polymeric Substances (EPS) of Three Sea-Ice Diatom Species, and Evidence for a Cryoprotective Role for EPS. *Journal of Phycology* 48.6, pp. 1494–1509. DOI: 10.1111/jpy.12004.

Assur, A. (1958). “Composition of sea ice and its tensile strength”. In: *Arctic Sea Ice*. Washington, DC: US National Academy of Sciences (National Research Council Publication 598), pp. 106–138.

Atlas, R., R. N. Hoffman, J. Ardizzone, S. M. Leidner, J. C. Jusem, D. K. Smith, et al. (2011). A cross-calibrated, multiplatform ocean surface wind velocity product for meteorological and oceanographic applications. *Bulletin of the American Meteorological Society* 92.2, pp. 157–174. DOI: 10.1175/2010BAMS2946.1.

Ball, F. K. (1956). The Theory of Strong Katabatic Winds. *Australian Journal of Physics* 9.3, pp. 373–386.

Barber, D. G., J. K. Ehn, M Pućko, S Rysgaard, J. W. Deming, J. S. Bowman, et al. (2014). Frost flowers on young Arctic sea ice: The climatic, chemical, and microbial significance of an emerging ice type. *Journal of Geophysical Research: Atmospheres* 119.20, pp. 11,511–593,612. DOI: https://doi.org/10.1002/2014JD021736.

Barber, D. and R. Massom (2007). The Role of Sea Ice in Arctic and Antarctic Polynyas. In: *Polynyas: Windows to the World*. Ed. by W. O. Smith and D. Barber. Vol. 74. Elsevier. Chap. Chapter 1, pp. 1–54. DOI: 10.1016/S0422-9894(06)74001-6.

Barry, J. and P. Dayton (1988). Current patterns in McMurdo Sound, Antarctica and their relationship to local biotic communities. *Polar Biology* 8.5, pp. 367–376. DOI: 10.1007/BF00442028.

Bartels-Rausch, T., H.-W. Jacobi, T. F. Kahan, J. L. Thomas, E. S. Thomson, J. P. D. Abbatt, et al. (2014). A review of air–ice chemical and physical interactions (AICI): liquids, quasi-liquids, and solids in snow. *Atmospheric Chemistry and Physics* 14.3, pp. 1587–1633. DOI: 10.5194/acp-14-1587-2014.

Bindoff, N., S. Rintoul, and R. Massom (2000). Bottom water formation and polynyas in Adelie Land, Antarctica. *Papers and Proceedings of the Royal Society of Tasmania* 133.3, pp. 51–56. DOI: 10.26749/rstpp.133.3.51.

Boetius, A., A. M. Anesio, J. W. Deming, J. A. Mikucki, and J. Z. Rapp (2015). Microbial ecology of the cryosphere: sea ice and glacial habitats. *Nature Reviews Microbiology* 13.11, pp. 677–690. DOI: 10.1038/nrmicro3522.

Bowman, J. P. (2008). Genomic Analysis of Psychrophilic Prokaryotes. In: *Psychrophiles: from Biodiversity to Biotechnology*. Berlin, Heidelberg: Springer Berlin Heidelberg, pp. 265–284. DOI: 10.1007/978-3-540-74335-4_16.

Braissant, O, A. W. Decho, C Dupraz, C Glunk, K. M. Przekop, and P. T. Visscher (2007). Exopolymeric substances of sulfate-reducing bacteria: Interactions with calcium at alkaline pH and implication for formation of carbonate minerals. *Geobiology* 5.4, pp. 401–411. DOI: 10.1111/j.1472-4669.2007.00117.x.

Braissant, O, A. W. Decho, K. M. Przekop, K. L. Gallagher, C. Glunk, C. Dupraz, et al. (2009). Characteristics and turnover of exopolymeric substances in a hypersaline microbial mat. *FEMS Microbiology Ecology* 67.2, pp. 293–307. DOI: 10.1111/j.1574-6941.2008.00614.x.

Bromwich, D., Z. Liu, A. N. Rogers, and M. L. Van Woert (1998). Winter Atmospheric Forcing of the Ross Sea Polynya. In: *Ocean, Ice, and Atmosphere: Interactions at the Antarctic Continental Margin*. Ed. by S. Jacobs and R. Weiss. Antarctic Research Series. American Geophysical Union, pp. 101–133. DOI: 10.1029/AR075p0101.

Bromwich, D. H. and D. D. Kurtz (1984). Katabatic wind forcing of the Terra Nova Bay polynya. *Journal of Geophysical Research* 89.C3, p. 3561. DOI: 10.1029/JC089iC03p03561.

Brooks, P. D., D. McKnight, and K. Elder (2005). Carbon limitation of soil respiration under winter snowpacks: potential feedbacks between growing season and winter carbon fluxes. *Global Change Biology* 11.2, pp. 231–238. DOI: 10.1111/j.1365-2486.2004.00877.x.

Brown, K., L. Miller, C. Mundy, T. Papakyriakou, R. Francois, M. Gosselin, et al. (2015). Inorganic carbon system dynamics in landfast Artcic sea ice during the early-melt period. *Journal of Geophysical Research: Oceans* 120, pp. 1–25. DOI: 10.1002/2014JC010620.Received.

Brown, K. A., L. A. Miller, M. Davelaar, R. Francois, and P. D. Tortell (2014). Overdetermination of the carbonate system in natural sea-ice brine and assessment of carbonic acid dissociation constants under low temperature, high salinity conditions. *Marine Chemistry* 165, pp. 36–45. DOI: 10.1016/j.marchem.2014.07.005.

Buckley, R. and H. Trodahl (1987). Thermally driven changes in the optical properties of sea ice. *Cold Regions Science and Technology* 14.2, pp. 201–204. DOI: 10.1016/0165-232X(87)90036-X.

Budillon, G, S Gremes Cordero, and E Salusti (2002). On the dense water spreading off the Ross Sea shelf (Southern Ocean). *Journal of Marine Systems* 35.3-4, pp. 207–227. DOI: 10.1016/S0924-7963(02)00082-9.

Budillon, G and G Spezie (2000). Thermohaline structure and variability in the Terra Nova Bay polynya, Ross Sea. *Antarctic Science* 12.4, pp. 493–508. DOI: DOI:10.1017/S0954102000000572.

Butterworth, B. J. and B. G. T. Else (2018). Dried, closed-path eddy covariance method for measuring carbon dioxide flux over sea ice. *Atmospheric Measurement Techniques* 11.11, pp. 6075–6090. DOI: 10.5194/amt-11-6075-2018.

Caldeira, K. and P. B. Duffy (2000). The Role of the Southern Ocean in Uptake and Storage of Anthropogenic Carbon Dioxide. *Science* 287.5453, 620 LP –622. DOI: 10.1126/science.287.5453.620.

Campbell, K, C. J. Mundy, M Gosselin, J. C. Landy, A Delaforge, and S Rysgaard (2017). Net community production in the bottom of first-year sea ice over the Arctic spring bloom. *Geophysical Research Letters* 44.17, pp. 8971–8978. DOI: 10.1002/2017GL074602.

Carnat, G., T. Papakyriakou, N. X. Geilfus, F. Brabant, B. Delille, M. Vancoppenolle, et al. (2013). Investigations on physical and textural properties of arctic first-year sea ice in the Amundsen gulf, Canada, November 2007-June 2008 (IPY-CFL system study). *Journal of Glaciology* 59.217, pp. 819–837. DOI: 10.3189/2013JoG12J148.

Carnat, G., W. Said-Ahmad, F. Fripiat, B. Wittek, J.-L. Tison, C. Uhlig, et al. (2018). Variability in sulfur isotope composition suggests unique dimethylsulfoniopropionate cycling and microalgae metabolism in Antarctic sea ice. *Communications Biology* 1.1, p. 212. DOI: 10.1038/s42003-018-0228-y.

Carnat, G., J. Zhou, T. Papakyriakou, B. Delille, T. Goossens, T. Haskell, et al. (2014). Physical and biological controls on DMS,P dynamics in ice shelf-influenced fast ice during a winter-spring and a spring-summer transitions. *Geophysical Research Letters: Oceans* 119, pp. 2882–2905. DOI: 10.1002/2013JC009381.

Cole, D. M. and J. P. Dempsey (2004). In situ Sea Ice Experiments in McMurdo Sound: Cyclic Loading, Fracture, and Acoustic Emissions. *Journal of Cold Regions Engineering* 18.4, pp. 155–174. DOI: 10.1061/(ASCE)0887-381X(2004)18:4(155).

Costerton, J. W., Z Lewandowski, D DeBeer, D Caldwell, D Korber, and G James (1994). Biofilms, the customized microniche. eng. *Journal of bacteriology* 176.8, pp. 2137–2142. DOI: 10.1128/jb.176.8.2137-2142.1994.

Cottier, F., H Eicken, and P Wadhams (1999). Linkages between salinity and brine channel distribution in young sea ice. *Journal of Geophysical Research: Oceans* 104.C7, pp. 15859–15871. DOI: 10.1029/1999JC900128.

Cox, G. F. N. and W. F. Weeks (1983). Equations for Determining the Gas and Brine Volumes in Sea-Ice Samples. *Journal of Glaciology* 29.102, pp. 306–316. DOI: DOI: 10.3189/S0022143000008364.

Cox, G. and W. Weeks (1986). Changes in the Salinity and Porosity of Sea-Ice Samples During Shipping and Storage. *Journal of Glaciology* 32.112, pp. 371–375. DOI: 10.3189/S0022143000012065.

Crabeck, O., B. Delille, D. Thomas, N.-X. Geilfus, S. Rysgaard, and J.-L. Tison (2014a). CO_2 and CH_4 in sea ice from a subarctic fjord under influence of riverine input. *Biogeosciences* 11.23, pp. 6525–6538. DOI: 10.5194/bg-11-6525-2014.

Crabeck, O, R Galley, B Delille, B Else, N.-X. Geilfus, M Lemes, et al. (2016). Imaging air volume fraction in sea ice using non-destructive X-ray tomography. *The Cryosphere* 10.3, pp. 1125–1145. DOI: 10.5194/tc-10-1125-2016.

Crabeck, O., R. J. Galley, L. Mercury, B. Delille, J. L. Tison, and S. Rysgaard (2019). Evidence of Freezing Pressure in Sea Ice Discrete Brine Inclusions and Its Impact on Aqueous-Gaseous Equilibrium. *Journal of Geophysical Research: Oceans* 124.3, pp. 1660–1678. DOI: 10.1029/2018JC014597.

Crabeck, O., B. Delille, S. Rysgaard, D. N. Thomas, N.-X. Geilfus, B. Else, et al. (2014b). First “in situ” determination of gas transport coefficients (D_{O_2}, DAr, and D_{N_2}) from bulk gas concentration measurements (O_2 , N_2 , Ar) in natural sea ice. *Journal of Geophysical Research: Oceans* 119.10, pp. 6655–6668. DOI: 10.1002/2014JC009849.

Decho, A. W. (2000). Microbial biofilms in intertidal systems: an overview. *Continental Shelf Research* 20.10-11, pp. 1257–1273. DOI: 10.1016/S0278-4343(00)00022-4.

Decho, A. W. and T. Gutierrez (2017). Microbial Extracellular Polymeric Substances (EPSs) in Ocean Systems. eng. *Frontiers in microbiology* 8, p. 922. DOI: 10.3389/fmicb.2017.00922.

Delille, B. (2006). Inorganic carbon dynamics and air-ice-sea CO_2 fluxes in the open and coastal waters of the Southern Ocean. PhD thesis. Université de Liège, p. 307.

Delille, B., J. Harlay, I. Zondervan, S. Jacquet, L. Chou, R. Wollast, et al. (2005). Response of primary production and calcification to changes of pCO_2 during experimental blooms of the coccolithophorid Emiliania huxleyi. *Global Biogeochemical Cycles* 19.2, pp. 1–14. DOI: 10.1029/2004GB002318.

Delille, B., B. Jourdain, A. V. Borges, J.-L. Tison, and D. Delille (2007). Biogas (CO_2, O_2, dimethylsulfide) dynamics in spring Antarctic fast ice. *Limnology and Oceanography* 52.4, pp. 1367–1379. DOI: 10.4319/lo.2007.52.4.1367.

Delille, B., M. Vancoppenolle, N.-X. Geilfus, B. Tilbrook, D. Lannuzel, V. Schoemann, et al. (2014). Southern Ocean CO_2 sink: The contribution of the sea ice. *Journal of Geophysical Research: Oceans* 119.9, pp. 6340–6355. DOI: 10.1002/2014JC009941.

Delille, D., M Fiala, J. Kuparinen, H. Kuosa, and C Plessis (2002). Seasonal changes in microbial biomass in the first-year ice of the Terre Adélie area (Antarctica). *Aquatic Microbial Ecology* 28, pp. 257–265. DOI: 10.3354/ame028257.

Deming, J. W. (2007). Life in Ice Formations at Very Cold Temperatures. In: *Physiology and Biochemistry of Extremophiles.* American Society of Microbiology, pp. 133–144.

Deming, J. W. (2010). Sea Ice Bacteria and Viruses. In: *Sea Ice.* Ed. by D. N. Thomas and G. S. Dieckmann. Oxford, UK: Wiley-Blackwell. Chap. 7, pp. 247–282.

Deming, J. W. and R Eric Collins (2016). Sea ice as a habitat for Bacteria, Archaea and viruses. In: *Sea Ice.* Wiley Online Books. Chichester, UK: John Wiley & Sons, Ltd, pp. 326–351. DOI: 10.1002/9781118778371.ch13.

Dempsey, D. E., P. J. Langhorne, N. J. Robinson, M. J. M. Williams, T. G. Haskell, and R. D. Frew (2010). Observation and modeling of platelet ice fabric in McMurdo Sound, Antarctica. *Journal of Geophysical Research* 115.C1, p. C01007. DOI: 10.1029/2008JC005264.

Dempsey, J. P., D. M. Cole, and S Wang (2018). Tensile fracture of a single crack in first-year sea ice. eng. *Philosophical Transactions of the Royal Society A: Mathematical, Physical and Engineering Sciences* 376.2129, p. 20170346. DOI: 10.1098/rsta.2017.0346.

DeVries, T. (2014). The oceanic anthropogenic CO_2 sink: Storage, air-sea fluxes, and transports over the industrial era. *Global Biogeochemical Cycles* 28.7, pp. 631–647. DOI: 10.1002/2013GB004739.

Dickson, A. (1981). An exact definition of total alkalinity and a procedure for the estimation of alkalinity and total inorganic carbon from titration data. *Deep Sea Research Part A. Oceanographic Research Papers* 28.6, pp. 609–623. DOI: 10.1016/0198-0149(81)90121-7.

DOE (1994). In: *Handbook of methods for the analysis of the various parameters of the carbon dioxide system in sea water. Version 2.* Ed. by A. Dickson and C. Goyet. Oak Ridge, TN: ORNL/CDIAC-74. DOI: 10.2172/10107773.

Dieckmann, G, G Rohardt, H Hellmer, and J Kipfstuhl (1986). The occurrence of ice platelets at 250 m depth near the Filchner Ice Shelf and its significance for sea ice biology. *Deep Sea Research Part A. Oceanographic Research Papers* 33.2, pp. 141–148. DOI: 10.1016/0198-0149(86)90114-7.

Dieckmann, G. S., G Nehrke, C Uhlig, J Göttlicher, S Gerland, M. A. Granskog, et al. (2010). Brief Communication: Ikaite discovered in Arctic sea ice. *The Cryosphere* 4.2, pp. 227–230. DOI: 10.5194/tc-4-227-2010.

Dieckmann, G. S., G. Nehrke, S. Papadimitriou, J. Göttlicher, R. Steininger, H. Kennedy, et al. (2008). Calcium carbonate as ikaite crystals in Antarctic sea ice. *Geophysical Research Letters* 35.8, p. L08501. DOI: 10.1029/2008GL033540.

Domine, F. and P. Shespon (2002). Air-Snow Interactions and Atmospheric Chemistry. *Science* 297.5586, pp. 1506–1510. DOI: 10.1126/science.1074610.

Domine, F., R. Sparapani, A. Ianniello, and H. J. Beine (2004). The origin of sea salt in snow on Arctic sea ice and in coastal regions. *Atmospheric Chemistry and Physics* 4, pp. 2259–2271. DOI: 10.5194/acp-4-2259-2004.

Eicken, H. (1992). Salinity profiles of Antarctic sea ice: Field data and model results. *Journal of Geophysical Research: Oceans* 97.C10, pp. 15545–15557. DOI: https://doi.org/10.1029/92JC01588.

Eicken, H. and M. Lange (1991). Image analysis of sea-ice thin sections: A step towards automated texture classification. *Annals of Glaciology* 15. DOI: 10.1017/S0260305500009745.

Else, B. G. T., T. N. Papakyriakou, R. J. Galley, W. M. Drennan, L. A. Miller, and H. Thomas (2011). Wintertime CO_2 fluxes in an Arctic polynya using eddy covariance: Evidence for enhanced air-sea gas transfer during ice formation. *Journal of Geophysical Research* 116, C00G03. DOI: 10.1029/2010JC006760.

Fischer, H., J. Schmitt, D. Lüthi, T. F. Stocker, T. Tschumi, P. Parekh, et al. (2010). The role of Southern Ocean processes in orbital and millennial CO_2 variations – A synthesis. *Quaternary Science Reviews* 29.1, pp. 193–205. DOI: https://doi.org/10.1016/j.quascirev.2009.06.007.

Fischer, M. (2013). Sea ice and the air-sea exchange of CO_2 (Doctoral dissertation). PhD thesis. Bremen University.

Fischer, M., D. N. Thomas, A. Krell, G. Nehrke, J. Göttlicher, L. Norman, et al. (2013). Quantification of ikaite in Antarctic sea ice. *Antarctic Science* 25.3, pp. 421–432. DOI: 10.1017/S0954102012001150.

Foldvik, A. and T. Kvinge (1974). Conditional instability of sea water at the freezing point. *Deep Sea Research and Oceanographic Abstracts* 21.3, pp. 169–174. DOI: 10.1016/0011-7471(74)90056-4.

Fripiat, F., K. M. Meiners, M. Vancoppenolle, S. Papadimitriou, D. N. Thomas, S. F. Ackley, et al. (2017). Macro-nutrient concentrations in Antarctic pack ice: Overall patterns and overlooked processes. *Elem Sci Anth* 5, p. 13. DOI: 10.1525/elementa.217.

Fripiat, F., D. M. Sigman, S. E. Fawcett, P. A. Rafter, M. A. Weigand, and J.-L. Tison (2014). New insights into sea ice nitrogen biogeochemical dynamics from the nitrogen isotopes. *Global Biogeochemical Cycles* 28.2, pp. 115–130. DOI: 10.1002/2013GB004729.

Fritsen, C. H., V. I. Lytle, S. F. Ackley, and C. W. Sullivan (1994). Autumn Bloom of Antarctic Pack-Ice Algae. *Science* 266.5186, pp. 782–784. DOI: 10.1126/science.266.5186.782.

Frölicher, T. L., J. L. Sarmiento, D. J. Paynter, J. P. Dunne, J. P. Krasting, and M. Winton (2015). Dominance of the Southern Ocean in Anthropogenic Carbon and Heat Uptake in CMIP5 Models. *Journal of Climate* 28.2, pp. 862–886. DOI: 10.1175/JCLI-D-14-00117.1.

Ganton, J. H. and A. R. Milne (1965). Temperature- and Wind-Dependent Ambient Noise under Midwinter Pack Ice. *The Journal of the Acoustical Society of America* 38.3, pp. 406–411. DOI: 10.1121/1.1909697.

Garcia, H. E. and L. I. Gordon (1992). Oxygen solubility in seawater: Better fitting equations. *Limnology and Oceanography* 37.6, pp. 1307–1312. DOI: 10.4319/lo.1992.37.6.1307.

Garrison, D., A. Gibson, S. Coale, M. Gowing, Y. Okolodkov, C. Fritsen, et al. (2005). Sea-ice microbial communities in the Ross Sea: autumn and summer biota. *Marine Ecology Progress Series* 300, pp. 39–52. DOI: 10.3354/meps300039.

Geilfus, N.-X., G. Carnat, G. S. Dieckmann, N. Halden, G. Nehrke, T. Papakyriakou, et al. (2013). First estimates of the contribution of $CaCO_3$ precipitation to the release of CO_2 to the atmosphere during young sea ice growth. *Journal of Geophysical Research: Oceans* 118, pp. 1–12. DOI: 10.1029/2012JC007980.

Geilfus, N.-X., G. Carnat, T. Papakyriakou, J. L. Tison, B. Else, H. Thomas, et al. (2012a). Dynamics of pCO_2 and related air-ice CO_2 fluxes in the Arctic coastal zone (Amundsen Gulf, Beaufort Sea). *Journal of Geophysical Research: Oceans* 117.2. DOI: 10.1029/2011JC007118.

Geilfus, N.-X., B. Delille, V. Verbeke, and J.-L. Tison (2012b). Towards a method for high vertical resolution measurements of the partial pressure of CO_2 within bulk sea ice. *Journal of Glaciology* 58.208, pp. 287–300. DOI: 10.3189/2012JoG11J071.

Geilfus, N.-X., R. J. Galley, O. Crabeck, T. Papakyriakou, J. Landy, J.-L. Tison, et al. (2015). Inorganic carbon dynamics of melt-pond-covered first-year sea ice in the Canadian Arctic. *Biogeosciences* 12.6, pp. 2047–2061. DOI: 10.5194/bg-12-2047-2015.

Geilfus, N.-X., R. J. Galley, B. G. T. Else, K. Campbell, T. Papakyriakou, O. Crabeck, et al. (2016). Estimates of ikaite export from sea ice to the underlying seawater in a sea ice–seawater mesocosm. *The Cryosphere* 10.5, pp. 2173–2189. DOI: 10.5194/tc-10-2173-2016.

Geilfus, N.-X., J.-L. Tison, S. F. Ackley, R. J. Galley, S. Rysgaard, L. Miller, et al. (2014). Sea ice pCO_2 dynamics and air – ice CO_2 fluxes during the Sea Ice Mass Balance in the Antarctic (SIMBA) experiment – Bellingshausen Sea, Antarctica. *The Cryosphere* 8, pp. 2395–2407. DOI: 10.5194/tc-8-2395-2014.

Gleitz, M., M. R. v.d. Loeff, D. N. Thomas, G. S. Dieckmann, and F. J. Millero (1995). Comparison of summer and winter inorganic carbon, oxygen and nutrient concentrations in Antarctic sea ice brine. *Marine Chemistry* 51.2, pp. 81–91. DOI: 10.1016/0304-4203(95)00053-T.

Glud, R., S. Rysgaard, and M. Kühl (2002). A laboratory study on O_2 dynamics and photosynthesis in ice algal communities: quantification by microsensors, O_2 exchange rates, ^{14}C incubations and a PAM fluorometer. *Aquatic Microbial Ecology* 27, pp. 301–311. DOI: 10.3354/ame027301.

Golden, K. M., S. F. Ackley, and V. I. Lytle (1998). The Percolation Phase Transition in Sea Ice. *Science* 282.5397, pp. 2238–2241. DOI: 10.1126/science.282.5397.2238.

Gough, A. J., A. R. Mahoney, P. J. Langhorne, M. J. Williams, N. J. Robinson, and T. G. Haskell (2012). Signatures of supercooling: McMurdo Sound platelet ice. *Journal of Glaciology* 58.207, pp. 38–50. DOI: 10.3189/2012JoG10J218.

Goyet, C. and A. Poisson (1989). New determination of carbonic acid dissociation constants in seawater as a function of temperature and salinity. *Deep-Sea Research* 36, pp. 1635–1654.

Gradinger, R. (2009). Sea-ice algae: Major contributors to primary production and algal biomass in the Chukchi and Beaufort Seas during May/June 2002. *Deep Sea Research Part II: Topical Studies in Oceanography* 56.17, pp. 1201–1212. DOI: 10.1016/j.dsr2.2008.10.016.

Gran, G. (1952). Determination of the equivalence point in potentiometric titrations. Part II. *The Analyst* 77.920, p. 661. DOI: 10.1039/an9527700661.

Grimm, R., D. Notz, R. Glud, S. Rysgaard, and K. Six (2016). Assessment of the sea-ice carbon pump: Insights from a three-dimensional ocean-sea-ice-biogeochemical model (MPIOM/HAMOCC). *Elementa: Science of the Anthropocene* 4, p. 000136. DOI: 10.12952/journal.elementa.000136.

Grossi, S. M., S. T. Kottmeier, R. L. Moe, G. T. Taylor, and C. W. Sullivan (1987). Sea ice microbial communities. VI. Growth and primary production in bottom ice under graded snow cover. *Marine Ecology Progress Series* 35, pp. 153–164.

Gruber, N. (2008). The Marine Nitrogen Cycle: Overview and Challenges. In: *Nitrogen in the Marine Environment.* Ed. by Elsevier, pp. 1–50. DOI: 10.1016/B978-0-12-372522-6.00001-3.

Gruber, N., D. Clement, B. R. Carter, R. A. Feely, S. van Heuven, M. Hoppema, et al. (2019a). The oceanic sink for anthropogenic CO_2 from 1994 to 2007. *Science* 363.6432, 1193 LP –1199. DOI: 10.1126/science.aau5153.

Gruber, N., P. Landschützer, and N. S. Lovenduski (2019b). The Variable Southern Ocean Carbon Sink. *Annual Review of Marine Science* 11.1, pp. 159–186. DOI: 10.1146/annurev-marine-121916-063407.

Haas, C., D. N. Thomas, and J. Bareiss (2001). Surface properties and processes of perennial Antarctic sea ice in summer. *Journal of Glaciology* 47.159, pp. 613–625. DOI: 10.3189/172756501781831864.

Hamme, R. and S. Emerson (2004). The solubility of neon, nitrogen and argon in distilled water and seawater. *Deep Sea Research Part I Oceanographic Research Papers* 51, pp. 1517–1528. DOI: 10.1016/j.dsr.2004.06.009.

Hegseth, E. N. and C. H. Von Quillfeldt (2002). Low phytoplankton biomass and ice algal blooms in the Weddell Sea during the ice-filled summer of 1997. *Antarctic Science* 14.3, pp. 231–243. DOI: 10.1017/S095410200200007X.

Heinze, C, S Meyer, N Goris, L Anderson, R Steinfeldt, N Chang, et al. (2015). The ocean carbon sink – impacts, vulnerabilities and challenges. *Earth System Dynamics* 6.1, pp. 327–358. DOI: 10.5194/esd-6-327-2015.

Helmke, E. and H. Weyland (1995). Bacteria in sea ice and underlying water of the eastern Weddell Sea in midwinter. *Marine Ecology Progress Series* 117.1-3, pp. 269–287. DOI: 10.3354/meps117269.

Hoagland, K. D., J. R. Rosowski, M. R. Gretz, and S. C. Roemer (1993). Diatom extracellular polymeric substances: function, fine structure, chemistry, and physiology. *Journal of Phycology* 29.5, pp. 537–566. DOI: 10.1111/j.0022-3646.1993.00537.x.

Horner, R., S. Ackley, G. Dieckmann, B. Gulliksen, T. Hoshiai, L. Legendre, et al. (1992). Ecology of sea ice biota - 1. Habitat, terminology, and methodology. *Polar Biology* 12.3-4, pp. 417–427. DOI: 10.1007/BF00243113.

Hughes, K. G., P. J. Langhorne, G. H. Leonard, and C. L. Stevens (2014). Extension of an Ice Shelf Water plume model beneath sea ice with application in McMurdo Sound, Antarctica. *Journal of Geophysical Research: Oceans* 119.12, pp. 8662–8687. DOI: 10.1002/2013JC009411.

Huston, A. L., B. B. Krieger-Brockett, and J. W. Deming (2000). Remarkably low temperature optima for extracellular enzyme activity from Arctic bacteria and sea ice. *Environmental Microbiology* 2.4, pp. 383–388. DOI: 10.1046/j.1462-2920.2000.00118.x.

IPCC (2007). *Climate Change 2007: The Physical Science Basis. Contribution of Working Group I to the Fourth Assessment Report of the Intergovernmental Panel on Climate Change*. Ed. by S. Solomon, D. Qin, M. Manning, Z. Chen, M. Marquis, K. Averyt, et al. Cambridge, New York: Cambridge University Press.

IPCC (2013). *Climate Change 2013: The Physical Science Basis. Contribution of Working Group I to the Fifth Assessment Report of the Intergovernmental Panel on Climate Change*. Ed. by T. Stocker, D. Qin, G.-K. Plattner, M. Tignor, S. Allen, J. Boschung, et al. Cambridge University Press.

IPCC (2014). *Climate Change 2014: Synthesis Report. Contribution of Working Groups I, II and III to the Fifth Assessment Report of the Intergovernmental Panel on Climate Change*. Ed. by R. K. Pachauri and L. Meyer. Geneva, Switzerland: IPCC, pp. 1–151.

Jacobs, S. S. and J. C. Comiso (1989). Sea ice and oceanic processes on the Ross Sea continental shelf. *Journal of Geophysical Research: Oceans* 94.C12, pp. 18195–18211. DOI: 10.1029/JC094iC12p18195.

Jacobs, S. S. (2004). Bottom water production and its links with the thermohaline circulation. *Antarctic Science* 16.4, pp. 427–437. DOI: 10.1017/S095410200400224X.

Jeffries, M. O., K Schwartz, K Morris, A. D. Veazey, H. R. Krouse, and S Gushing (1995). Evidence for platelet ice accretion in Arctic sea ice development. *Journal of Geophysical Research: Oceans* 100.C6, pp. 10905–10914. DOI: 10.1029/95JC00804.

Jeffries, M. O., W. F. Weeks, R Shaw, and K Morris (1993). Structural characteristics of congelation and platelet ice and their role in the development of antarctic land-fast sea ice. *Journal of Glaciology* 39.132, pp. 223–238. DOI: 10.3189/S0022143000015884.

Jenkins, A. and A. Bombosch (1995). Modeling the effects of frazil ice crystals on the dynamics and thermodynamics of Ice Shelf Water plumes. *Journal of Geophysical Research: Oceans* 100.C4, pp. 6967–6981. DOI: 10.1029/94JC03227.

Jones, E. P. and A. R. Coote (1981). Oceanic CO_2 produced by the precipitation of $CaCO_3$ from brines in sea ice. *Journal of Geophysical Research: Oceans* 86.C11, pp. 11041–11043. DOI: 10.1029/JC086iC11p11041.

Kattner, G., D. Thomas, C. Haas, H. Kennedy, and G. Dieckmann (2004). Surface ice and gap layers in Antarctic sea ice: highly productive habitats. *Marine Ecology Progress Series* 277.August, pp. 1–12. DOI: 10.3354/meps277001.

Kennedy, H, D. Thomas, G Kattner, C Haas, and G. Dieckmann (2002). Particulate organic matter in Antarctic summer sea ice: concentration and stable isotopic composition. *Marine Ecology Progress Series* 238, pp. 1–13. DOI: 10.3354/meps238001.

Kern, S (2009). Wintertime Antarctic coastal polynya area: 1992–2008. *Geophysical Research Letters* 36.14. DOI: 10.1029/2009GL038062.

Kotovitch, M., S. Moreau, J. Zhou, M. Vancoppenolle, G. S. Dieckmann, K.-U. Evers, et al. (2016). Air-ice carbon pathways inferred from a sea ice tank experiment. *Elementa : Science of the Anthropocene* 4, pp. 1–15. DOI: 10.12952/journal.elementa.000112.

Krell, A., C. Ummenhofer, G. Kattner, A. Naumov, D. Evans, G. S. Dieckmann, et al. (2003). The biology and chemistry of land fast ice in the White Sea, Russia—A comparison of winter and spring conditions. *Polar Biology* 26.11, pp. 707–719. DOI: 10.1007/s00300-003-0543-7.

Krembs, C and A Engel (2001). Abundance and variability of microorganisms and transparent exopolymer particles across the ice-water interface of melting first-year sea ice in the Laptev Sea (Arctic). *Marine Biology* 138.1, pp. 173–185. DOI: 10.1007/s002270000396.

Krembs, C. and J. W. Deming (2008). The Role of Exopolymers in Microbial Adaptation to Sea Ice. In: *Psychrophiles: from Biodiversity to Biotechnology*. Ed. by R. Margesin,

F. Schinner, J.-C. Marx, and C. Gerday. Berlin, Heidelberg: Springer Berlin Heidelberg, pp. 247–264. DOI: 10.1007/978-3-540-74335-4_15.

Krembs, C., H. Eicken, and J. W. Deming (2011). Exopolymer alteration of physical properties of sea ice and implications for ice habitability and biogeochemistry in a warmer Arctic. *Proceedings of the National Academy of Sciences* 108.9, 3653 LP – 3658. DOI: 10.1073/pnas.1100701108.

Krembs, C., H. Eicken, K. Junge, and J. Deming (2002). High concentrations of exopolymeric substances in Arctic winter sea ice: Implications for the polar ocean carbon cycle and cryoprotection of diatoms. *Deep Sea Research Part I: Oceanographic Research Papers* 49, pp. 2163–2181. DOI: 10.1016/S0967-0637(02)00122-X.

Landschützer, P., S. M. Bushinsky, and A. R. Gray (2019). *A combined globally mapped carbon dioxide (CO_2) flux estimate based on the Surface Ocean CO_2 Atlas Database (SOCAT) and Southern Ocean Carbon and Climate Observations and Modeling (SOCCOM) biogeochemistry floats from 1982 to 2017 (NCEI Accession 019.* DOI: 10.25921/9hsn-xq82.

Langhorne, P. and T. Haskell (1996). Acoustic emission during fatigue experiments on first year sea ice. *Cold Regions Science and Technology* 24.3, pp. 237–250. DOI: 10.1016/0165-232X(95)00021-3.

Langway, C. C. (1958). Ice fabrics and the universal stage. *Army Snow Ice and Permafrost Research Establishment* Snow Ice and Permafrost Research Establishment, pp. 1–17.

Lannuzel, D., L. Tedesco, M. van Leeuwe, K. Campbell, H. Flores, B. Delille, et al. (2020). The future of Arctic sea-ice biogeochemistry and ice-associated ecosystems. *Nature Climate Change* 10.11, pp. 983–992. DOI: 10.1038/s41558-020-00940-4.

Lavoie, D., K. Denman, and C. Michel (2005). Modeling ice algal growth and decline in a seasonally ice-covered region of the Arctic (Resolute Passage, Canadian Archipelago). *Journal of Geophysical Research: Oceans* 110.C11. DOI: 10.1029/2005JC002922.

Legagneux, L., A. Cabanes, and F. Dominé (2002). Measurement of the specific surface area of 176 snow samples using methane adsorption at 77 K. *Journal of Geophysical Research: Atmospheres* 107.D17, p. 4335. DOI: 10.1029/2001JD001016.

Legendre, L., S. Ackley, G. Dieckmann, B. Gulliksen, R. Horner, T. Hoshiai, et al. (1992). Ecology of sea ice biota - 2. Global significance. *Polar Biology* 12.3-4. DOI: 10.1007/BF00243114.

Legendre, L., R. B. Rivkin, M. G. Weinbauer, L. Guidi, and J. Uitz (2015). The microbial carbon pump concept: Potential biogeochemical significance in the globally changing ocean. *Progress in Oceanography* 134, pp. 432–450. DOI: 10.1016/j.pocean.2015.01.008.

Leonard, G. H., C. R. Purdie, P. J. Langhorne, T. G. Haskell, M. J. M. Williams, and R. D. Frew (2006). Observations of platelet ice growth and oceanographic conditions during the winter of 2003 in McMurdo Sound, Antarctica. *Journal of Geophysical Research: Oceans* 111.C4. DOI: 10.1029/2005JC002952.

Leppäranta, M. and T. Manninen (1988). *The brine and gas content of sea ice with attention to low salinities and high temperatures*. Tech. rep. Helsinki, Finland: Finnish Institute of Marine Research, pp. 1–14.

Lewis, E., D. Wallace, and L. J. Allison (1998). Program developed for CO_2 system calculations. *Tennesse*.

Light, B, G. A. Maykut, and T. C. Grenfell (2003). Effects of temperature on the microstructure of first-year Arctic sea ice. *Journal of Geophysical Research: Oceans* 108.C2. DOI: 10.1029/2001JC000887.

Lizotte, M. and C. Sullivan (1992). Biochemical composition and photosynthate distribution in sea ice microalgae of McMurdo Sound, Antarctica: evidence for nutrient stress during the spring bloom. *Antarctic Science* 4, pp. 23–30. DOI: 10.1017/S0954102092000063.

Lizotte, M. P. and C. W. Sullivan (1991). Photosynthesis-irradiance relationships in microalgae associated with Antarctic pack ice: evidence for in situ activity. *Marine Ecology Progress Series* 71.2, pp. 175–184.

Long, M. H., D. Koopmans, P. Berg, S. Rysgaard, R. N. Glud, and D. H. Søgaard (2012). Oxygen exchange and ice melt measured at the ice-water interface by eddy correlation. *Biogeosciences* 9.6, pp. 1957–1967. DOI: 10.5194/bg-9-1957-2012.

Loose, B., P. Schlosser, D. Perovich, D. Ringelberg, D. Ho, T. Takahashi, et al. (2010). Gas diffusion through columnar laboratory sea ice: implications for mixed-layer ventilation of CO_2 in the seasonal ice zone. *Tellus B* 63.1, pp. 23–39. DOI: 10.1111/j.1600-0889.2010.00506.x.

Luhtanen, A.-m., E. Eronen-rasimus, H. M. Oksanen, J.-l. Tison, B. Delille, G. S. Dieckmann, et al. (2018). The first known virus isolates from Antarctic sea ice have complex infection patterns. *FEMS Microbiology Ecology* 94.2018, pp. 1–15. DOI: 10.1093/femsec/fiy028.

Mahoney, A. R., A. J. Gough, P. J. Langhorne, N. J. Robinson, C. L. Stevens, M. M. J. Williams, et al. (2011). The seasonal appearance of ice shelf water in coastal Antarctica and its effect on sea ice growth. *Journal of Geophysical Research* 116.C11, p. C11032. DOI: 10.1029/2011JC007060.

Marion, G. M. (2001). Carbonate mineral solubility at low temperatures in the Na-K-Mg-Ca-H-Cl-SO_4-OH-HCO_3-CO_3-CO_2-H_2O system. *Geochimica et Cosmochimica Acta* 65.12, pp. 1883–1896. DOI: 10.1016/S0016-7037(00)00588-3.

Marion, G. M., M. V. Mironenko, and M. W. Roberts (2010). FREZCHEM: A geochemical model for cold aqueous solutions. *Computers & Geosciences* 36.1, pp. 10–15. DOI: 10.1016/j.cageo.2009.06.004.

Marshall, J. and K. Speer (2012). Closure of the meridional overturning circulation through Southern Ocean upwelling. *Nature Geoscience* 5.3, pp. 171–180. DOI: 10.1038/ngeo1391.

Martin, S (2001). Polynyas. In: *Encyclopedia of Ocean Sciences*. Ed. by J. Steele. Oxford: Elsevier, pp. 540–545. DOI: 10.1016/B978-012374473-9.00007-2.

Martin, S., R. S. Drucker, and R. Kwok (2007). The areas and ice production of the western and central Ross Sea polynyas, 1992–2002, and their relation to the B-15 and C-19 iceberg events of 2000 and 2002. *Journal of Marine Systems* 68.1-2, pp. 201–214. DOI: 10.1016/j.jmarsys.2006.11.008.

Marx, J. G., S. D. Carpenter, and J. W. Deming (2009). Production of cryoprotectant extracellular polysaccharide substances (EPS) by the marine psychrophilic bacterium Colwellia psychrerythraea strain 34H under extreme conditionsThis article is one of a selection of papers in the Special Issue on Polar and Al. *Canadian Journal of Microbiology* 55.1, pp. 63–72. DOI: 10.1139/W08-130.

Massom, R. A., P. Harris, K. J. Michael, and M. Potter (1998). The distribution and formative processes of latent-heat polynyas in East Antarctica. *Annals of Glaciology* 27, pp. 420–426. DOI: 10.3189/1998AoG27-1-420-426.

Massom, R. A., H. Eicken, C. Hass, M. O. Jeffries, M. R. Drinkwater, M. Sturm, et al. (2001). Snow on Antarctic sea ice. *Reviews of Geophysics* 39.3, pp. 413–445. DOI: 10.1029/2000RG000085.

Massom, R. A. and S. E. Stammerjohn (2010). Antarctic sea ice change and variability – Physical and ecological implications. *Polar Science* 4.2, pp. 149–186. DOI: 10.1016/j.polar.2010.05.001.

McMinn, A. and C. Ashworth (1998). The use of oxygen microelectrodes to determine the net production by an Antarctic sea ice algal community. *Antarctic Science* 10.1, pp. 39–44. DOI: 10.1017/S0954102098000066.

McMinn, A., C. Ashworth, R. Bhagooli, A. Martin, S. Salleh, P. Ralph, et al. (2012). Antarctic coastal microalgal primary production and photosynthesis. *Marine Biology* 159.12, pp. 2827–2837. DOI: 10.1007/s00227-012-2044-0.

Mehrbach, C, C. H. Culberson, J. E. Hawley, and R. M. Pytkowicx (1973). MEASUREMENT OF THE APPARENT DISSOCIATION CONSTANTS OF CARBONIC ACID IN SEAWATER AT ATMOSPHERIC PRESSURE. *Limnology and Oceanography* 18.6, pp. 897–907. DOI: 10.4319/lo.1973.18.6.0897.

Meiners, K. M., M Vancoppenolle, G Carnat, G Castellani, B. Delille, D Delille, et al. (2018). Chlorophyll-a in Antarctic Landfast Sea Ice: A First Synthesis of Historical Ice Core Data. *Journal of Geophysical Research: Oceans* 123.11, pp. 8444–8459. DOI: 10.1029/2018JC014245.

Meiners, K. M., M Vancoppenolle, S Thanassekos, G. S. Dieckmann, D. N. Thomas, J.-L. Tison, et al. (2012). Chlorophyll a in Antarctic sea ice from historical ice core data. *Geophysical Research Letters* 39.21. DOI: 10.1029/2012GL053478.

Meiners, K., R. Brinkmeyer, M. Granskog, and A Lindfors (2004). Abundance, size distribution and bacterial colonization of exopolymer particles in Antarctic sea ice (Bellingshausen Sea). *Aquatic Microbial Ecology* 35.3, pp. 283–296. DOI: 10.3354/ame035283.

Meiners, K., R. Gradinger, J. Fehling, G. Civitarese, and M. Spindler (2003). Vertical distribution of exopolymer particles in sea ice of the Fram Strait (Arctic) during autumn. *Marine Ecology Progress Series* 248, pp. 1–13. DOI: 10.3354/meps248001.

Meiners, K., C. Krembs, and R. Gradinger (2008). Exopolymer particles: microbial hotspots of enhanced bacterial activity in Arctic fast ice (Chukchi Sea). *Aquatic Microbial Ecology* 52, pp. 195–207. DOI: 10.3354/ame01214.

Meiners, K. M. and C. Michel (2016). Dynamics of nutrients, dissolved organic matter and exopolymers in sea ice. In: *Sea Ice*. Wiley Online Books. Chichester, UK: John Wiley & Sons, Ltd, pp. 415–432. DOI: 10.1002/9781118778371.ch17.

Meredith, M., M. Sommerkorn, S. D. Cassotta, A. Ekaykin, A. Hollowed, G. Kofinas, et al. (2019). Polar Regions. In: *IPCC Special Report on the Ocean and Cryosphere in a Changing Climate*. Ed. by H.-O. Portner, D. Roberts, V. Masson-Delmotte, P. Zhai, M. Tignor, E. Poloczanska, et al.

Middelburg, J. J. (2019). *Marine Carbon Biogeochemistry*. SpringerBriefs in Earth System Sciences. Cham: Springer International Publishing. DOI: 10.1007/978-3-030-10822-9.

Mikaloff Fletcher, S. E., N Gruber, A. R. Jacobson, S. C. Doney, S Dutkiewicz, M Gerber, et al. (2006). Inverse estimates of anthropogenic CO_2 uptake, transport, and storage by the ocean. *Global Biogeochemical Cycles* 20.2. DOI: 10.1029/2005GB002530.

Miller, L. a., T. N. Papakyriakou, R. E. Collins, J. W. Deming, J. K. Ehn, R. W. Macdonald, et al. (2011). Carbon dynamics in sea ice: A winter flux time series. *Journal of Geophysical Research* 116.C2, p. C02028. DOI: 10.1029/2009JC006058.

Milne, A. R. (1972). Thermal tension cracking in sea ice: A source of underice noise. *Journal of Geophysical Research* 77.12, pp. 2177–2192. DOI: 10.1029/JC077i012p02177.

Mock, T, G. Dieckmann, C Haas, A Krell, J. Tison, A. Belem, et al. (2002). Micro-optodes in sea ice: a new approach to investigate oxygen dynamics during sea ice formation. *Aquatic Microbial Ecology* 29, pp. 297–306. DOI: 10.3354/ame029297.

Morales Maqueda, M. A., A. J. Willmott, and N. R. T. Biggs (2004). Polynya Dynamics: a Review of Observations and Modeling. *Reviews of Geophysics* 42.1. DOI: 10.1029/2002RG000116.

Moreau, S., M. Vancoppenolle, L. Bopp, O. Aumont, G. Madec, B. Delille, et al. (2016). Assessment of the sea-ice carbon pump: Insights from a three-dimensional ocean-sea-ice biogeochemical model (NEMO-LIM-PISCES). *Elementa: Science of the Anthropocene* 4, p. 000122. DOI: 10.12952/journal.elementa.000122.

Moreau, S., M. Vancoppenolle, B. Delille, J.-L. Tison, J. Zhou, M. Kotovitch, et al. (2015). Drivers of inorganic carbon dynamics in first-year sea ice: A model study. *Journal of Geophysical Research: Oceans* 120.January, pp. 471–495. DOI: 10.1002/2014JC010388.

Moreau, S., M. Vancoppenolle, J. Zhou, J. L. Tison, B. Delille, and H. Goosse (2014). Modelling argon dynamics in first-year sea ice. *Ocean Modelling* 73, pp. 1–18. DOI: 10.1016/j.ocemod.2013.10.004.

Morrison, A. K., T. L. Frölicher, and J. L. Sarmiento (2015). Upwelling in the Southern Ocean. *Physics Today* 68.1, pp. 27–32. DOI: 10.1063/PT.3.2654.

Mortenson, E., N. Steiner, A. H. Monahan, L. A. Miller, N. Geilfus, and K. Brown (2018). A Model-Based Analysis of Physical and Biogeochemical Controls on Carbon Exchange in the Upper Water Column, Sea Ice, and Atmosphere in a Seasonally Ice-Covered Arctic Strait. *Journal of Geophysical Research: Oceans* 123.10, pp. 7529–7549. DOI: 10.1029/2018JC014376.

Mundy, C., D. Barber, and C Michel (2005). Variability of snow and ice thermal, physical and optical properties pertinent to sea ice algae biomass during spring. *Journal of Marine Systems* 58.3-4, pp. 107–120. DOI: 10.1016/j.jmarsys.2005.07.003.

Niemi, A., C. Michel, K. Hille, and M. Poulin (2011). Protist assemblages in winter sea ice: setting the stage for the spring ice algal bloom. *Polar Biology* 34.12, pp. 1803–1817. DOI: 10.1007/s00300-011-1059-1.

NOAA (1976). *U.S. Standard Atmosphere, 1976*. NOAA - SIT 76-1562. National Oceanic and Amospheric Administration.

NOAA/ESRL (2020). *Trends in Atmospheric Carbon Dioxide*. URL: www.esrl.noaa.gov/gmd/ccgg/trends/ (visited on 02/27/2020).

Nomura, D, M. A. Granskog, A Fransson, M Chierici, A Silyakova, K. I. Ohshima, et al. (2018). CO_2 flux over young and snow-covered Arctic pack ice in winter and spring. *Biogeosciences* 15.11, pp. 3331–3343. DOI: 10.5194/bg-15-3331-2018.

Nomura, D., P. Assmy, G. Nehrke, M. A. Granskog, M. Fischer, G. S. Dieckmann, et al. (2013a). Characterization of ikaite ($CaCO_3{\cdot}6H_2O$) crystals in first-year Arctic sea ice north of Svalbard. *Annals of Glaciology* 54.62, pp. 125–131. DOI: 10.3189/2013AoG62A034.

Nomura, D., H. Eicken, R. Gradinger, and K. Shirasawa (2010a). Rapid physically driven inversion of the air-sea ice CO_2 flux in the seasonal landfast ice off Barrow, Alaska after onset of surface melt. *Continental Shelf Research* 30.19, pp. 1998–2004. DOI: 10.1016/j.csr.2010.09.014.

Nomura, D., M. A. Granskog, P. Assmy, D. Simizu, and G. Hashida (2013b). Arctic and Antarctic sea ice acts as a sink for atmospheric CO_2 during periods of snowmelt and surface flooding. *Journal of Geophysical Research: Oceans* 118.12, pp. 6511–6524. DOI: 10.1002/2013JC009048.

Nomura, D., H. Yoshikawa-Inoue, and T. Toyota (2006). The effect of sea-ice growth on air–sea CO_2 flux in a tank experiment. *Tellus B: Chemical and Physical Meteorology* 58.5, pp. 418–426. DOI: 10.1111/j.1600-0889.2006.00204.x.

Nomura, D., H. Yoshikawa-Inoue, T. Toyota, and K. Shirasawa (2010b). Effects of snow, snowmelting and refreezing processes on air–sea-ice CO_2 flux. *Journal of Glaciology* 56.196, pp. 262–270. DOI: 10.3189/002214310791968548.

Norman, L., D. N. Thomas, C. A. Stedmon, M. A. Granskog, S. Papadimitriou, R. H. Krapp, et al. (2011). The characteristics of dissolved organic matter (DOM) and chromophoric dissolved organic matter (CDOM) in Antarctic sea ice. *Deep Sea Research Part II: Topical Studies in Oceanography* 58.9-10, pp. 1075–1091. DOI: 10.1016/j.dsr2.2010.10.030.

Notz, D. (2003). Impact of underwater-ice evolution on Arctic summer sea ice. *Journal of Geophysical Research* 108.C7, p. 3223. DOI: 10.1029/2001JC001173.

Notz, D. (2005). Thermodynamic and fluid-dynamical processes in sea ice (Doctoral dissertation). PhD thesis. University of Cambridge, p. 238.

Notz, D. and M. G. Worster (2008). In situ measurements of the evolution of young sea ice. *Journal of Geophysical Research* 113.C3, p. C03001. DOI: 10.1029/2007JC004333.

NSIDC (2019). *Charctic Interactive Sea Ice Graph.* URL: https://nsidc.org/arcticseaicenews/charctic-interactive-sea-ice-graph/ (visited on 03/26/2020).

NSIDC (2020a). *Arctic Sea Ice News and Analysis.* URL: http://nsidc.org/arcticseaicenews/ (visited on 03/25/2020).

NSIDC (2020b). *Sea Ice Index: Arctic- and Antarctic-wide changes in sea ice.* URL: https://nsidc.org/data/seaice_index/.

Ohshima, K., K. Yoshida, H. Shimoda, M. Wakatsuchi, T. Endoh, and M. Fukuchi (1998). Relationship between the upper ocean and sea ice during the Antarctic melting season. *Journal of Geophysical Research* 103, pp. 7601–7616. DOI: 10.1029/97JC02806.

Orsi, A. H. and C. L. Wiederwohl (2009). A recount of Ross Sea waters. *Deep Sea Research Part II: Topical Studies in Oceanography* 56.13, pp. 778–795. DOI: 10.1016/j.dsr2.2008.10.033.

Papadimitriou, S, H Kennedy, G Kattner, G. Dieckmann, and D. Thomas (2004). Experimental evidence for carbonate precipitation and CO_2 degassing during sea ice formation. *Geochimica et Cosmochimica Acta* 68.8, pp. 1749–1761. DOI: 10.1016/j.gca.2003.07.004.

Papadimitriou, S., H. Kennedy, L. Norman, D. P. Kennedy, G. S. Dieckmann, and D. N. Thomas (2012). The effect of biological activity, $CaCO_3$ mineral dynamics, and CO_2 degassing in the inorganic carbon cycle in sea ice in late winter-early spring in the Weddell Sea, Antarctica. *Journal of Geophysical Research* 117.C8, p. C08011. DOI: 10.1029/2012JC008058.

Papadimitriou, S, D. N. Thomas, H Kennedy, C Haas, H Kuosa, A Krell, et al. (2007). Biogeochemical composition of natural sea ice brines from the Weddell Sea during early austral summer. *Limnology and Oceanography* 52.5, pp. 1809–1823. DOI: 10.4319/lo.2007.52.5.1809.

Papadimitriou, S., H. Kennedy, P. Kennedy, and D. N. Thomas (2013). Ikaite solubility in seawater-derived brines at 1atm and sub-zero temperatures to 265K. *Geochimica et Cosmochimica Acta* 109.0, pp. 241–253. DOI: 10.1016/j.gca.2013.01.044.

Papadimitriou, S., H. Kennedy, P. Kennedy, and D. N. Thomas (2014). Kinetics of ikaite precipitation and dissolution in seawater-derived brines at sub-zero temperatures to 265 K. *Geochimica et Cosmochimica Acta* 140, pp. 199–211. DOI: 10.1016/j.gca.2014.05.031.

Papakyriakou, T. and L. Miller (2011). Springtime CO_2 exchange over seasonal sea ice in the Canadian Arctic Archipelago. *Annals of Glaciology* 52.57, pp. 215–224. DOI: 10.3189/172756411795931534.

Parish, T. R. and D. H. Bromwich (1989). Instrumented Aircraft Observations of the Katabatic Wind Regime Near Terra Nova Bay. *Monthly Weather Review* 117.7, pp. 1570–1585. DOI: 10.1175/1520-0493(1989)117⟨1570:IAOOTK⟩2.0.CO;2.

Parkinson, C. L. and D. J. Cavalieri (2012). Antarctic sea ice variability and trends, 1979-2010. *The Cryosphere* 6.4, pp. 871–880. DOI: 10.5194/tc-6-871-2012.

Parkinson, C. L. (2019). A 40-y record reveals gradual Antarctic sea ice increases followed by decreases at rates far exceeding the rates seen in the Arctic. *Proceedings of the National Academy of Sciences* 116.29, 14414 LP –14423. DOI: 10.1073/pnas.1906556116.

Parkinson, C. L. and J. C. Comiso (2013). On the 2012 record low Arctic sea ice cover: Combined impact of preconditioning and an August storm. *Geophysical Research Letters* 40.7, pp. 1356–1361. DOI: 10.1002/grl.50349.

Parmentier, F.-J. W., T. R. Christensen, L. L. Sørensen, S. Rysgaard, A. D. McGuire, P. A. Miller, et al. (2013). The impact of lower sea-ice extent on Arctic greenhouse-gas exchange. *Nature Climate Change* 3.3, pp. 195–202. DOI: 10.1038/nclimate1784.

Paterson, H. and J. Laybourn-Parry (2012). Sea ice microbial dynamics over an annual ice cycle in Prydz Bay, Antarctica. *Polar Biology* 35.7, pp. 993–1002. DOI: 10.1007/s00300-011-1146-3.

Paytan, A. and K. McLaughlin (2007). The Oceanic Phosphorus Cycle. *Chemical Reviews* 107.2, pp. 563–576. DOI: 10.1021/cr0503613.

Perovich, D. (2011). The Changing Arctic Sea Ice Cover. *Oceanography* 24.3, pp. 162–173. DOI: 10.5670/oceanog.2011.68.

Petrich, C. and H. Eicken (2016). Overview of sea ice growth and properties. In: *Sea Ice*. Ed. by D. Thomas. Third edit. Wiley Online Books. Chichester, UK: John Wiley & Sons, Ltd. Chap. Chapter 1, pp. 1–41. DOI: 10.1002/9781118778371.ch1.

Pirk, N., M. P. Tamstorf, M. Lund, M. Mastepanov, S. H. Pedersen, M. R. Mylius, et al. (2016). Snowpack fluxes of methane and carbon dioxide from high Arctic tundra. *Journal of Geophysical Research: Biogeosciences* 121.11, pp. 2886–2900. DOI: 10.1002/2016JG003486.

Poulin, M., N. Daugbjerg, R. Gradinger, L. Ilyash, T. Ratkova, and C. von Quillfeldt (2011). The pan-Arctic biodiversity of marine pelagic and sea-ice unicellular eukaryotes: a first-attempt assessment. *Marine Biodiversity* 41.1, pp. 13–28. DOI: 10.1007/s12526-010-0058-8.

Ratkova, T, A. Sazhin, and K. Kosobokova (2004). Unicellular Inhabitants of the White Sea Underice Pelagic Zone during the Early Spring Period. *Oceanology* 44, pp. 240–246. DOI: 44(2):240246.

Raynaud, D, R Delmas, J. Ascencio, and M Legrand (1982). Gas Extraction From Polar Ice Cores: A Critical Issue For Studying The Evolution of Atmospheric CO_2 and Ice-Sheet Surface Elevation. *Annals of Glaciology* 3, pp. 265–268. DOI: 10.3189/S0260305500002895.

Redfield, A., B. Ketchum, and F. Richards (1963). The influence of organisms on the composition of sea-water. In: *The Sea.* Ed. by M. N. Hill. New York: Wiley Interscience, pp. 26–77.

Reuer, M. K., B. A. Barnett, M. L. Bender, P. G. Falkowski, and M. B. Hendricks (2007). New estimates of Southern Ocean biological production rates from O_2/Ar ratios and the triple isotope composition of O_2. *Deep Sea Research Part I: Oceanographic Research Papers* 54.6, pp. 951–974. DOI: 10.1016/j.dsr.2007.02.007.

Riedel, A., C. Michel, and M. Gosselin (2006). Seasonal study of sea-ice exopolymeric substances on the Mackenzie shelf: implications for transport of sea-ice bacteria and algae. *Aquatic Microbial Ecology* 45.2, pp. 195–206. DOI: 10.3354/ame045195.

Riedel, A., C. Michel, M. Gosselin, and B. LeBlanc (2007). Enrichment of nutrients, exopolymeric substances and microorganisms in newly formed sea ice on the Mackenzie shelf. *Marine Ecology Progress Series* 342, pp. 55–67. DOI: 10.3354/meps342055.

Riedel, A., C. Michel, M. Gosselin, and B. LeBlanc (2008). Winter–spring dynamics in sea-ice carbon cycling in the coastal Arctic Ocean. *Journal of Marine Systems* 74.3-4, pp. 918–932. DOI: 10.1016/j.jmarsys.2008.01.003.

Rintoul, S. R. (2013). On the Origin and Influence of Adélie Land Bottom Water. In: *Ocean, Ice, and Atmosphere: Interactions at the Antarctic Continental Margin.* Ed. by S. Jacobs and R. Weiss. Antarctic Research Series. Washington, DC: American Geophysical Union, pp. 151–171. DOI: 10.1029/AR075p0151.

Robinson, N. J., M. J. M. Williams, P. J. Barrett, and a. R. Pyne (2010). Observations of flow and ice-ocean interaction beneath the McMurdo Ice Shelf, Antarctica. *Journal of Geophysical Research* 115.C3, p. C03025. DOI: 10.1029/2008JC005255.

Robinson, N. J., M. J. M. Williams, C. L. Stevens, P. J. Langhorne, and T. G. Haskell (2014). Evolution of a supercooled Ice Shelf Water plume with an actively growing subice platelet matrix. *Journal of Geophysical Research: Oceans* 119.6, pp. 3425–3446. DOI: 10.1002/2013JC009399.

Roukaerts, A. (2018). Novel insights in nitrogen and carbon biogeochemistry of Antarctic sea ice: the potential role of a microbial biofilm. PhD thesis. Vrije Universiteit Brussel, p. 216.

Roukaerts, A., A.-J. Cavagna, F. Fripiat, D. Lannuzel, K. M. Meiners, and F. Dehairs (2016). Sea-ice algal primary production and nitrogen uptake rates off East Antarctica. *Deep Sea Research Part II: Topical Studies in Oceanography* 131, pp. 140–149. DOI: 10.1016/j.dsr2.2015.08.007.

Roukaerts, A., F. Deman, F. Van der Linden, G. Carnat, A. Bratkic, S. Moreau, et al. "The biogeochemical role of a microbial biofilm in sea ice: Antarctic landfast sea ice as a case study." Submitted to Elementa: Science of the Anthropocene.

Rysgaard, S, R. N. Glud, K Lennert, M Cooper, N Halden, R. J. G. Leakey, et al. (2012). Ikaite crystals in melting sea ice – implications for pCO_2 and pH levels in Arctic surface waters. *The Cryosphere* 6.4, pp. 901–908. DOI: 10.5194/tc-6-901-2012.

Rysgaard, S., R. N. Glud, M. K. Sejr, J. Bendtsen, and P. B. Christensen (2007). Inorganic carbon transport during sea ice growth and decay: A carbon pump in polar seas. *Journal of Geophysical Research* 112.C3, p. C03016. DOI: 10.1029/2006JC003572.

Rysgaard, S, D. H. Søgaard, M Cooper, M Pućko, K Lennert, T. N. Papakyriakou, et al. (2013). Ikaite crystal distribution in winter sea ice and implications for CO_2 system dynamics. *The Cryosphere* 7.2, pp. 707–718. DOI: 10.5194/tc-7-707-2013.

Rysgaard, S., F. Wang, R. J. Galley, R. Grimm, D. Notz, M. Lemes, et al. (2014). Temporal dynamics of ikaite in experimental sea ice. *The Cryosphere* 8.4, pp. 1469–1478. DOI: 10.5194/tc-8-1469-2014.

Rysgaard, S., J. Bendtsen, B. Delille, G. S. Dieckmann, R. N. Glud, H. Kennedy, et al. (2011). Sea ice contribution to the air–sea CO_2 exchange in the Arctic and Southern Oceans. *Tellus B: Chemical and Physical Meteorology* 63.5, pp. 823–830. DOI: 10.1111/j.1600-0889.2011.00571.x.

Rysgaard, S., R. N. Glud, M. K. Sejr, M. E. Blicher, and H. J. Stahl (2008). Denitrification activity and oxygen dynamics in Arctic sea ice. *Polar Biology* 31.5, pp. 527–537. DOI: 10.1007/s00300-007-0384-x.

Rysgaard, S. and R. N. Glud (2004). Anaerobic N_2 production in Arctic sea ice. English. *Limnology and Oceanography* 49.1, pp. 86–94. DOI: 10.4319/lo.2004.49.1.0086.

Sabine, C. L. (2004). The Oceanic Sink for Anthropogenic CO_2. *Science* 305.5682, pp. 367–371. DOI: 10.1126/science.1097403.

Saenz, B. T. and K. R. Arrigo (2014). Annual primary production in Antarctic sea ice during 2005–2006 from a sea ice state estimate. *Journal of Geophysical Research: Oceans* 119.6, pp. 3645–3678. DOI: 10.1002/2013JC009677.

Sarmiento, J. L. and N. Gruber (2006). *Ocean Biogeochemical Dynamics*. Princeton University Press.

Schlitzer, R. (2000). Applying the adjoint method for biogeochemical modeling: Export of participate organic matter in the world ocean. In: *Inverse Methods in Global Biogeochemical Cycles*. Geophysical Monograph Series, pp. 107–124. DOI: 10.1029/GM114p0107.

Sievers, J, L. L. Sørensen, T Papakyriakou, B Else, M. K. Sejr, D Haubjerg Søgaard, et al. (2015). Winter observations of CO_2 exchange between sea ice and the atmosphere in a coastal fjord environment. *The Cryosphere* 9.4, pp. 1701–1713. DOI: 10.5194/tc-9-1701-2015.

Sigman, D. M., M. P. Hain, and G. H. Haug (2010). The polar ocean and glacial cycles in atmospheric CO_2 concentration. *Nature* 466.7302, pp. 47–55. DOI: 10.1038/nature09149.

Smedsrud, L. H. and A. Jenkins (2004). Frazil ice formation in an ice shelf water plume. *Journal of Geophysical Research: Oceans* 109.C3. DOI: 10.1029/2003JC001851.

Smith, I. J., P. J. Langhorne, T. G. Haskell, H. Joe Trodahl, R. Frew, and M. Ross Vennell (2001). Platelet ice and the land-fast sea ice of McMurdo Sound, Antarctica. *Annals of Glaciology* 33.1, pp. 21–27. DOI: 10.3189/172756401781818365.

Smith, R., M Gosselin, S Kudoh, B Robineau, and S Taguchi (1997). DOC and its relationship to algae in bottom ice communities. *Journal of Marine Systems* 11.1-2, pp. 71–80. DOI: 10.1016/S0924-7963(96)00029-2.

Smith, S. D., R. D. Muench, and C. H. Pease (1990). Polynyas and leads: An overview of physical processes and environment. *Journal of Geophysical Research: Oceans* 95.C6, pp. 9461–9479. DOI: 10.1029/JC095iC06p09461.

Smith, W., P. Sedwick, K. Arrigo, D. Ainley, and A. Orsi (2012). The Ross Sea in a Sea of Change. *Oceanography* 25.3, pp. 90–103. DOI: 10.5670/oceanog.2012.80.

Søgaard, D., J. Deming, L Meire, and S Rysgaard (2019). Effects of microbial processes and $CaCO_3$ dynamics on inorganic carbon cycling in snow-covered Arctic winter sea ice. *Marine Ecology Progress Series* 611, pp. 31–44. DOI: 10.3354/meps12868.

Søgaard, D., M Kristensen, S Rysgaard, R. Glud, P. Hansen, and K. Hilligsøe (2010). Autotrophic and heterotrophic activity in Arctic first-year sea ice: seasonal study from Malene Bight, SW Greenland. *Marine Ecology Progress Series* 419, pp. 31–45. DOI: 10.3354/meps08845.

Søgaard, D. H., D. N. Thomas, S. Rysgaard, R. N. Glud, L. Norman, H. Kaartokallio, et al. (2013). The relative contributions of biological and abiotic processes to carbon dynamics in subarctic sea ice. *Polar Biology* 36.12, pp. 1761–1777. DOI: 10.1007/s00300-013-1396-3.

Steele, D. J., D. J. Franklin, and G. J. C. Underwood (2014). Protection of cells from salinity stress by extracellular polymeric substances in diatom biofilms. eng. *Biofouling* 30.8, pp. 987–998. DOI: 10.1080/08927014.2014.960859.

Steemann-Nielsen, E. (1952). The Use of Radio-active Carbon (C14) for Measuring Organic Production in the Sea. *ICES Journal of Marine Science* 18.2, pp. 117–140. DOI: 10.1093/icesjms/18.2.117.

Stefels, J., G. Carnat, J. W. Dacey, T. Goossens, J. T. M. Elzenga, and J.-L. Tison (2012). The analysis of dimethylsulfide and dimethylsulfoniopropionate in sea ice: Dry-crushing and melting using stable isotope additions. *Marine Chemistry* 128-129, pp. 34–43. DOI: 10.1016/j.marchem.2011.09.007.

Stewart, P. S. (2003). Diffusion in Biofilms. *Journal of Bacteriology* 185.5, pp. 1485–1491. DOI: 10.1128/JB.185.5.1485-1491.2003.

Stewart, P. S. and M. J. Franklin (2008). Physiological heterogeneity in biofilms. *Nature Reviews Microbiology* 6.3, pp. 199–210. DOI: 10.1038/nrmicro1838.

Takagi, K., M. Nomura, D. Ashiya, H. Takahashi, K. Sasa, Y. Fujinuma, et al. (2005). Dynamic carbon dioxide exchange through snowpack by wind-driven mass transfer in a conifer-broadleaf mixed forest in northernmost Japan. *Global Biogeochemical Cycles* 19.2. DOI: 10.1029/2004GB002272.

Takahashi, T., R. Williams, and D. Bos (1982). Carbonate chemistry. In: *GEOSECS Pacific Expedition, Vol. 3, Hydrographic Data.* Washington, D.C: National Science Foundation, pp. 77–82.

Takahashi, T., S. C. Sutherland, C. Sweeney, A. Poisson, N. Metzl, B. Tilbrook, et al. (2002). Global sea–air CO_2 flux based on climatological surface ocean pCO_2, and seasonal biological and temperature effects. *Deep Sea Research Part II: Topical Studies in Oceanography* 49.9-10, pp. 1601–1622. DOI: 10.1016/S0967-0645(02)00003-6.

Takahashi, T., S. C. Sutherland, R. Wanninkhof, C. Sweeney, R. A. Feely, D. W. Chipman, et al. (2009). Climatological mean and decadal change in surface ocean pCO_2, and net sea–air CO_2 flux over the global oceans. *Deep Sea Research Part II: Topical Studies in Oceanography* 56.8-10, pp. 554–577. DOI: 10.1016/j.dsr2.2008.12.009.

Tamaru, Y., Y. Takani, T. Yoshida, and T. Sakamoto (2005). Crucial role of extracellular polysaccharides in desiccation and freezing tolerance in the terrestrial cyanobacterium Nostoc commune. eng. *Applied and environmental microbiology* 71.11, pp. 7327–7333. DOI: 10.1128/AEM.71.11.7327-7333.2005.

Tauber, G. M. (1960). “Characteristics of Antarctic katabatic winds on Antarctic meteorology”. In: *Papers Proceedings of a Symposium.* Kidlington: Pergamon Press, pp. 52–64.

Thomas, D. N. and G. S. Dieckmann (2010). *Sea Ice 2nd Edition.* Oxford, UK: Wiley-Blackwell, p. 621.

Thomas, D. N., G. Kattner, R. Engbrodt, V. Giannelli, H. Kennedy, C. Haas, et al. (2001). Dissolved organic matter in Antarctic sea ice. *Annals of Glaciology* 33, pp. 297–303. DOI: 10.3189/172756401781818338.

Thomas, D. N., S. Papadimitriou, and C. Michel (2010). Biogeochemistry of Sea Ice. In: *Sea Ice*. Wiley Online Books. Oxford, UK: Wiley-Blackwell, pp. 425–467. DOI: 10.1002/9781444317145.ch12.

Thompson, L., M. Smith, J. Thomson, S. Stammerjohn, S. Ackley, and B. Loose (2020). Frazil ice growth and production during katabatic wind events in the Ross Sea, Antarctica. *Cryosphere* 14.10, pp. 3329–3347. DOI: 10.5194/tc-14-3329-2020.

Tison, J.-L., R. D. Lorrain, A. Bouzette, M. Dini, A. Bondesan, and M. StiéVenard (2013). Linking Landfast Sea Ice Variability to Marine Ice Accretion at Hells Gate Ice Shelf, Ross Sea. In: *Antarctic Sea Ice: Physical Processes, Interactions and Variability*. Ed. by M.O. Jeffries. Antarctic Research Series, pp. 375–407. DOI: 10.1029/AR074p0375.

Tison, J.-L., B. Delille, and S. Papadimitriou (2016). Gases in sea ice. In: *Sea Ice*. Wiley Online Books. Chichester, UK: John Wiley & Sons, Ltd, pp. 433–471. DOI: 10.1002/9781118778371.ch18.

Tison, J.-L., T. Maksym, A. D. Fraser, M. Corkill, N. Kimura, Y. Nosaka, et al. (2020). Physical and biological properties of early winter Antarctic sea ice in the Ross Sea. *Annals of Glaciology*, pp. 1–19. DOI: 10.1017/aog.2020.43.

Ugalde, S. C., K. J. Westwood, R. van den Enden, A. McMinn, and K. M. Meiners (2016). Characteristics and primary productivity of East Antarctic pack ice during the winter-spring transition. *Deep Sea Research Part II: Topical Studies in Oceanography* 131, pp. 123–139. DOI: 10.1016/j.dsr2.2015.12.013.

UNESCO (1966). *International oceanographic tables*. Paris: National Institute of Oceanography of Great Britain and UNESCO.

Van Leeuwe, M., L. Tedesco, K. R. Arrigo, P. Assmy, K. Campbell, K. M. Meiners, et al. (2018). Microalgal community structure and primary production in Arctic and Antarctic sea ice: A synthesis. *Elem Sci Anth* 6.1, p. 4. DOI: 10.1525/elementa.267.

Vancoppenolle, M, D Notz, F Vivier, J Tison, B Delille, G Carnat, et al. (2013a). Technical Note: On the use of the mushy-layer Rayleigh number for the interpretation of sea-ice-core data. *The Cryosphere Discuss.* 2013, pp. 3209–3230. DOI: 10.5194/tcd-7-3209-2013.

Vancoppenolle, M., K. M. Meiners, C. Michel, L. Bopp, F. Brabant, G. Carnat, et al. (2013b). Role of sea ice in global biogeochemical cycles: emerging views and challenges. *Quaternary Science Reviews* 79, pp. 207–230. DOI: 10.1016/j.quascirev.2013.04.011.

Verbeke, V. (2005). Concentrations en gaz dans la glace de mer: développements techniques et implications environnementales (Doctoral dissertation). PhD thesis. Université Libre de Bruxelles.

Wanninkhof, R. (1992). Relationship between wind speed and gas exchange over the ocean. *Journal of Geophysical Research* 97.C5, pp. 7373–7382. DOI: 10.1029/92JC00188.

Weeks, W (2010). *On Sea Ice*. University of Alaska Press.

Weeks, W. F. and S. F. Ackley (1986). The Growth, Structure, and Properties of Sea Ice. In: *The Geophysics of Sea Ice*. Ed. by N. Untersteiner. Boston, MA: Springer US, pp. 9–164. DOI: 10.1007/978-1-4899-5352-0_2.

Werner, I., J. Ikävalko, and H. Schünemann (2007). Sea-ice algae in Arctic pack ice during late winter. *Polar Biology* 30.11, pp. 1493–1504. DOI: 10.1007/s00300-007-0310-2.

Zeebe, R. E and D. Wolf-Gladrow (2001). *CO_2 in sea water: Equilibrium, Kinetics, Isotopes*. Elsevier.

Zemmelink, H. J., B. Delille, J. L. Tison, E. J. Hintsa, L. Houghton, and J. W. H. Dacey (2006). CO_2 deposition over the multi-year ice of the western Weddell Sea. *Geophysical Research Letters* 33.13, p. L13606. DOI: 10.1029/2006GL026320.

Zhou, J, M Kotovitch, H Kaartokallio, S Moreau, J.-L. Tison, G Kattner, et al. (2015). The impact of dissolved organic carbon and bacterial respiration on pCO_2 in experimental sea ice. *Progress in Oceanography* 141, pp. 153–167. DOI: 10.1016/j.pocean.2015.12.005.

Zhou, J., B. Delille, F. Brabant, and J.-L. Tison (2014). Insights into oxygen transport and net community production in sea ice from oxygen, nitrogen and argon concentrations. *Biogeosciences* 11.18, pp. 5007–5020. DOI: 10.5194/bg-11-5007-2014.

Zhou, J., B. Delille, H. Eicken, M. Vancoppenolle, F. Brabant, G. Carnat, et al. (2013). Physical and biogeochemical properties in landfast sea ice (Barrow, Alaska): Insights on brine and gas dynamics across seasons. *Journal of Geophysical Research: Oceans* 118.6, pp. 3172–3189. DOI: 10.1002/jgrc.20232.

Appendices

In addition to the two manuscripts presented in this thesis, I also participated to the writing of three peer-reviewed publications listed below and attached in the following appendix. Another publication was recently submitted to *Elementa: Science of the Anthropocene*.

- **Publications as a first author presented in this thesis :**

  Van der Linden, F., Tison, J.-L., Champenois, W., Moreau, S., Carnat, G., Kotovitch, M., Fripiat, F., Deman, F., Roukaerts, A., Dehairs, F., Wauthy, S., Lourenço, A., Vivier, F., Haskell, T., and Delille, B. (2020, May 13). Sea ice CO_2 dynamics across seasons: impact of processes at the interfaces. *Journal of Geophysical Research. Oceans*, 125, e2019JC015807.

- **Publications:**

  Roukaerts A., Deman F., Van der Linden F., Carnat G., Bratkic A., Moreau S., Lannuzel D., Dehairs F., Delille B., Tison J.-L. and Fripiat F. The biogeochemical role of a microbial biofilm in sea ice: Antarctic landfast sea ice as a case study. Submitted to *Elementa:Science of the Anthropocene*, January 2021.

  Lannuzel, D., Tedesco, L., van Leeuwe, M., Campbell, K., Flores, H., Delille, B., Miller, L., Stefels, J., Assmy, P., Bowman, J., Brown, K., Castellani, G., Chierici, M., Crabeck, O., Damm, E., Else, B., Fransson, A., Fripiat, F., Geilfus, N. X., Jacques, C., Jones, E., Kaartokallio, H., Kotovitch, M., Meiners, K., Moreau, S., Nomura, D., Peeken, I., Rintala, J. M., Steiner, N., Tison, J. L., Vancoppenolle, M., Van der Linden, F., Vichi, M., and Wongpan, P. (2020). The future of Arctic sea-ice biogeochemistry and ice-associated ecosystems. *Nature Climate Change*, 10, 983–992.

  Tison, J.-L., Maksym, T., Fraser, A. D., Corkill, M., Kimura, N., Nosaka, Y., Nomura, D., Vancoppenolle, M., Ackley, S., Stammerjohn, S., Wauthy, S., Van der Linden, F., Carnat, G., Sapart, C., de Jong, J., Fripiat, F., and Delille, B. (2020, June 24). Physical and biological properties of early winter Antarctic sea ice in the Ross Sea. *Annals of Glaciology*, 1-19.

  Kotovitch, M., Moreau, S., Zhou, J., Vancoppenolle, M., Dieckmann, G. S., Evers, K.-U., Van Der Linden, F., Thomas, D. N., Tison, J.-L., and Delille, B. (2016, June). Air-ice carbon pathways inferred from a sea ice tank experiment. *Elementa: Science of the Anthropocene*, 4: 000112.

Appendix A: Air-ice carbon pathways inferred from a sea ice tank experiment

ELEMENTA
Science of the Anthropocene

Air-ice carbon pathways inferred from a sea ice tank experiment

Marie Kotovitch[1,2]* • Sébastien Moreau[3] • Jiayun Zhou[1,2,4] • Martin Vancoppenolle[5] • Gerhard S Dieckmann[6] • Karl-Ulrich Evers[7] • Fanny Van der Linden[1] • David N Thomas[8,9] • Jean-Louis Tison[2] • Bruno Delille[1]

[1]Unité d'Océanographie Chimique, MARE, Université de Liège, Liège, Belgium
[2]Laboratoire de Glaciologie, DSTE, Université Libre de Bruxelles, Brussels, Belgium
[3]Institute for Marine and Antarctic Studies, University of Tasmania, Hobart, Tas, Australia
[4]Division of Earth and Ocean Sciences, Nicholas School of the Environment, Duke University, Durham, North Carolina, United States
[5]Sorbonne Universités, UPMC Paris 6, LOCEAN-IPSL, CNRS/IRD/MNHN, France
[6]Alfred Wegener Institute, Helmholtz Center for Polar and Marine Research, Bremerhaven, Germany
[7]Arctic Technology Department, HSVA, Hamburg, Germany
[8]Marine Research Centre, Finnish Environment Institute (SYKE), Helsinki, Finland
[9]School of Ocean Sciences, Bangor University, Menai Bridge, United Kingdom

*Marie.Kotovitch@ulg.ac.be

Abstract

Given rapid sea ice changes in the Arctic Ocean in the context of climate warming, better constraints on the role of sea ice in CO_2 cycling are needed to assess the capacity of polar oceans to buffer the rise of atmospheric CO_2 concentration. Air-ice CO_2 fluxes were measured continuously using automated chambers from the initial freezing of a sea ice cover until its decay during the INTERICE V experiment at the Hamburg Ship Model Basin. Cooling seawater prior to sea ice formation acted as a sink for atmospheric CO_2, but as soon as the first ice crystals started to form, sea ice turned to a source of CO_2, which lasted throughout the whole ice growth phase. Once ice decay was initiated by warming the atmosphere, the sea ice shifted back again to a sink of CO_2. Direct measurements of outward ice-atmosphere CO_2 fluxes were consistent with the depletion of dissolved inorganic carbon in the upper half of sea ice. Combining measured air-ice CO_2 fluxes with the partial pressure of CO_2 in sea ice, we determined strongly different gas transfer coefficients of CO_2 at the air-ice interface between the growth and the decay phases (from 2.5 to 0.4 mol m^{-2} d^{-1} atm^{-1}). A 1D sea ice carbon cycle model including gas physics and carbon biogeochemistry was used in various configurations in order to interpret the observations. All model simulations correctly predicted the sign of the air-ice flux. By contrast, the amplitude of the flux was much more variable between the different simulations. In none of the simulations was the dissolved gas pathway strong enough to explain the large fluxes during ice growth. This pathway weakness is due to an intrinsic limitation of ice-air fluxes of dissolved CO_2 by the slow transport of dissolved inorganic carbon in the ice. The best means we found to explain the high air-ice carbon fluxes during ice growth is an intense yet uncertain gas bubble efflux, requiring sufficient bubble nucleation and upwards rise. We therefore call for further investigation of gas bubble nucleation and transport in sea ice.

Domain Editor-in-Chief
Jody W. Deming, University of Washington

Associate Editor
Stephen F. Ackley, University of Texas at San Antonio

Knowledge Domain
Ocean Science

Article Type
Research Article

Part of an *Elementa* Special Feature
Biogeochemical Exchange Processes at Sea-Ice Interfaces (BEPSII)

Received: May 29, 2015
Accepted: May 19, 2016
Published: June 8, 2016

1. Introduction

Among the natural systems, the role of sea ice in CO_2 cycling is not well constrained. Several studies report air-ice CO_2 fluxes that show that sea ice is a permeable medium under certain conditions of temperature and salinity (Semiletov et al., 2004; Nomura et al., 2006, 2010b; Miller et al., 2011b; Delille et al., 2014), thereby refuting the assumption that sea ice impedes the air-ocean gas exchange. However, observational difficulties, in particular the lack of continuous observations covering the entire ice growth and decay cycle, hinder the understanding of carbon exchange processes in ice-covered seas. Some studies suggest that active sea ice processes are significant (Rysgaard et al., 2011; Delille et al., 2014), while others assume them to be negligible (Cross et al., 2014). Given the rapid sea ice changes in the Arctic Ocean in the context of global warming (IPCC, 2013), better constraints on the role of sea ice in CO_2 cycling are needed to assess the future capacity of polar oceans to buffer the rise of atmospheric CO_2 concentration.

Sea ice is a composite of pure ice, brine and gas inclusions. Various biological, chemical and physical parameters may affect the concentration of gases in sea ice (e.g., Tsurikov, 1979; Zhou et al., 2014a). Temperature appears to be one of the main controls of CO_2 concentration in sea ice (Geilfus et al., 2012a; Delille et al., 2014). When temperature decreases, brine inclusions shrink, concentrating salts, gases and other impurities in the brine. In contrast, when temperature increases, the melting of ice with the increase in size of brine inclusions dilutes their content (e.g., Vancoppenolle et al., 2013; Delille et al., 2014). The increasing concentration of gases in brine due to the shrinking of brine inclusions triggers the nucleation of bubbles (Tsurikov, 1979; Killawee et al., 1998; Tison et al., 2002; Light et al., 2003). Gases are therefore found in sea ice in both dissolved (i.e., brines) and gaseous forms (i.e., bubbles). Bubbles are indeed observed at the onset of sea ice growth, when air inclusions are trapped within the ice structure. Crabeck et al. (2014b) and Zhou et al. (2014a) suggested that bubbles further develop during ice growth when the gases concentrates within the brine. Conversely, during ice decay, brine dilution and the related decrease of gas concentration is hypothesized to promote the dissolution of gases in the brines.

Sea ice is considered as permeable when the brine fraction is above 5% (Golden et al., 1998). As sea ice becomes permeable, air-ice gas exchange increases (Delille et al., 2014). Brine convection or gravity drainage (Notz and Worster, 2009; Hunke et al., 2011) is the main process responsible for the rejection of dissolved gases to the ocean during ice growth (Moreau et al., 2014). In the absence of convection, the diffusion of dissolved gases becomes the main pathway to transport dissolved gas across the ice (Gosink et al., 1976; Loose et al., 2011; Shaw et al., 2011). This diffusive flux is driven by dissolved gas gradients (Delille et al., 2007; Nomura et al., 2010b; Miller et al., 2011b). Gas bubbles may provide an alternative gas transport pathway (Zhou et al., 2013; Crabeck et al., 2014a). The efficiency of this pathway depends on whether bubbles can only diffuse molecularly (Loose et al., 2011) or rise due to their buoyancy (Moreau et al., 2014).

Considering the need to better understand carbon cycling in ice-covered seas, the absence of measurements over the whole ice growth and decay cycle and the difficulty of performing these measurements on natural sea ice, we carried out a controlled ice growth and decay experiment during which the air-ice CO_2 fluxes were monitored using the chamber method. The CO_2 transfer coefficient during both ice growth and ice decay was computed and compared to a sea ice model integrating carbon dynamics.

2. Methods

2.1 Experimental setting

The experiment was carried out at the Arctic Environmental Test Basin facility of the Hamburg Ship Model Basin (http://www.hsva.de) in the framework of the INTERICE V project. Eleven polyethylene bags of 1.2 m^3 were filled with about 1000 L of filtered seawater from the North Sea. The experiment reproducing ice growth and ice decay took place over a period of 19 days. The day "0" of the experiment was 30 May 2012. The air temperature above the mesocosms was set to –14 °C the first 14 days (hereafter denoted as the"growth phase"), then to –1 °C until the end of the experiment (the "melting phase"). More information about the experimental settings are provided by Zhou et al. (2014b).

We carried out continuous *in situ* measurements of ice temperature and air-ice CO_2 fluxes: A chain of 10 thermistors was placed at 2 cm intervals through the whole ice thickness. Ice cores were also collected regularly (every 1 to 3 days). On a given day, all samples (ice, under-ice water) came from the same mesocosm. Once the ice in a mesocosm was sampled, it was compromised and not used again in the experiment. So each sampling day corresponded to a different mesocosm, except on day 19, when we sampled two mesocosms. Ice cores were wrapped in polyethylene bags for storage below –25 °C in the dark and for subsequent measurements of bulk ice salinity, total alkalinity (TA) and partial pressure of CO_2 (pCO_2).

2.2 Ice pCO_2 at high vertical resolution

We applied the method developed by Geilfus et al. (2012b) and reviewed by Crabeck et al. (2014b) and Geilfus et al. (2015) for the measurement of the bulk pCO_2 (denoted as $pCO_{2\,bulk}$) within permeable sea ice. The goal is to equilibrate the sea ice samples with a N_2/CO_2 gas mixture of known concentration at a temperature as close as possible to the *in situ* temperature (the temperature of the ice upon sampling). Samples were cut to fit tightly into a square container, 4 x 4 cm, that was 4.4 cm high to minimize the headspace. The container containing the sample was sealed and connected to a vacuum pump for 15 min. A standard gas of known concentration (500 ppm of CO_2) was then injected at a pressure of 1013 mbar. Standard gas and ice sample were equilibrated for 20 hours in a constant temperature bath at the *in situ* temperature. Gas was then recovered and injected in a Varian 3300 gas chromatograph to measure the CO_2 concentration. Shortly afterward, the sample temperature was measured to check for experimental drift. Measured $pCO_{2\,bulk}$ was corrected for the temperature difference between the sample and the *in situ* temperature according to the corrections proposed by Copin-Montegut (1988).

2.3 Total alkalinity

We measured total alkalinity (TA) on melted sea ice (TA_{bulk}) using 50 g of sea ice melt collected at a 2 cm vertical resolution. TA was measured on all mesocosms except SW 9. We derived TA for all SW 9 ice sections using the strong linear regression between salinity and TA observed for all of the other samples. We also collected seawater for TA measurement. Melted bulk ice and seawater samples were poisoned with a solution of super-saturated $HgCl_2$ and then stored in the dark, until analysis (one year after the sampling). TA was measured by open-cell titration with 0.11 M HCl and the endpoints were determined according to Gran (1952). Routine analyses of Certified Reference Materials (provided by A. G. Dickson, Scripps Institution of Oceanography) ensured that the uncertainty of the TA measurements was less than 4 µmol kg^{-1}.

2.4 Dissolved inorganic carbon

We computed the dissolved inorganic carbon of bulk ice from TA_{bulk} and $pCO_{2\,bulk}$ using a 2 step computation. We estimated the salinity of brines according to the ice temperature using the relationship of Cox and Weeks (1983) derived from data compiled by Assur (1960). We then computed TA_{brines} at the salinity of brines from the linear relationship between TA and salinity. We computed the total dissolved inorganic carbon (DIC) of brines (denoted as DIC_{brines}) from TA_{brines} and $pCO_{2\,bulk}$ using the CO2SYS program for the carbonate system (Lewis and Wallace, 1998). We used the CO_2 dissociation constants of Mehrbach (1973) refitted by Dickson and Millero (1987) and the other constants advocated by Dickson and Goyet (1994). We then converted DIC_{brines} to DIC_{bulk} assuming a linear relationship between DIC and salinity. Nonetheless, there are some limitations with this approach that should be noted: the dissociation constants have been established for the ranges of temperatures and salinities of open ocean waters (i.e., temperatures above 1 °C and salinities of 35). We assumed that the CO_2 dissociation constants were applicable at sub-zero temperatures, as suggested by Marion (2001) and Delille et al. (2007). We refer the reader to Brown et al. (2014) for a discussion on the validity of the constants.

2.5 Seawater pCO_2

To measure the underlying seawater pCO_2 a hole was drilled through the sea ice cover. Seawater was pumped from the hole using a peristaltic pump (Masterflex® - Environmental Sampler) and supplied to a sea ice equilibrator system (SIES; Delille et al., 2007) for measurements of the pCO_2 and recycled back to the seawater through the same hole. The SIES is based on a membrane contractor equilibrator (Membrana® Liqui-cell) coupled to an infrared gas analyzer (IRGA, Li-Cor® 6262). Seawater flowed into the equilibrator at a maximum rate of 1 L min^{-1} and a closed air loop ensured circulation through the equilibrator and the IRGA at a rate of 3 L min^{-1}. The IRGA was calibrated before and after the experiment with N_2 and CO_2:N_2 mixtures with mixing ratios of 388 and 813 ppm supplied by Air Liquide Belgium. During the experiment, the drift of the IRGA was corrected with N_2. Uncertainty during this experiment was less than 6 µatm.

2.6 Air–ice CO_2 fluxes

2.6.1 Measurements at the automated chamber

In this paper, positive CO_2 flux refers to CO_2 flux from the ice to the atmosphere, while negative CO_2 flux refers to a flux from the atmosphere to the ice. We measured air-ice CO_2 fluxes using an automated chamber placed above the water surface or on top of the ice. The chamber consisted of a mobile cap and a plastic cylinder, or so-called collar, with a diameter of 20 cm and a height of 9.7 cm. A rubber seal surrounded the cylinder and ensured an airtight connection between the ice and the chamber. Each hour, the cap closed the chamber and the pCO_2 was measured over 15 min. At the beginning of the experiment one chamber was set above the surface of the water with the collar lowered a few millimetres below the water surface of a dedicated mesocosm apart from the 21 mesocosms used for ice collection. However, ice freezing and consolidation pushed the collar upward so that the collar was not properly sealed. After the fifth day of the experiment, the chamber was therefore moved to mesocosm 11 and was properly sealed. A pump within the LI-COR Multiplexer (LI-8150) circulated the air in the chamber at a flow rate of 2.1 L min^{-1}. When the pCO_2 of ice is higher than atmospheric pCO_2, CO_2 is transferred from the ice to the atmosphere and the automated chamber records a positive flux. A negative flux is observed in the opposite case. Water-corrected CO_2 flux was computed automatically with LI-8100 File Viewer 3.1.0 package provided by LI-COR Biosciences. The flux was either calculated with a linear or an empirical exponential regression depending on which method provided the best fit (assessed from the normalized sums of the squares of the residuals).

2.6.2 Computation of a gas transfer coefficient for CO_2

As described above, gases are transported through sea ice to the atmosphere by convection, diffusion and/or the ascent of bubbles to the ice surface. In the present study, we calculated an effective gas transfer coefficient for CO_2 (K, in mmol m^{-2} d^{-1} atm^{-1}), using the equation developed by Liss and Slater (1974) and Sarmiento and Gruber (2004):

$$F = K\,(pCO_{2\ bulk} - pCO_{2\ air}) \tag{1}$$

where F is the air-ice CO_2 flux in mmol m^{-2} d^{-1}, $pCO_{2\ bulk}$ is the pCO_2 in the ice and $pCO_{2\ air}$ is the pCO_2 in the air, both expressed in atm. In this equation we assume that F and K reflect both diffusive flux and bubble buoyancy (i.e., the rise of bubbles to the ice surface).

2.7 Assessment of the precision of derived variables

A Bootstrap resampling statistical analysis procedure, using random values of the measured parameters (temperature, salinity, pCO_2, DIC and TA) between the mean ± precision over 1000 iterations, was used to estimate the propagation of errors to the computed parameters (ΔDIC and K). This method was used as a way to show the effects of the imprecision of the data set on the calculated parameter.

2.8 Modelling air-ice CO_2 fluxes

In order to understand the factors that drive air-ice CO_2 fluxes during the experiment, we ran a one-dimensional thermodynamic sea ice model representing sea ice halo-thermodynamics and carbon dynamics, including air-ice CO_2 fluxes (Vancoppenolle et al., 2010; Moreau et al., 2015). Vertical carbon transport and air-ice carbon fluxes are explicitly separated between dissolved and gaseous form contributions.

The dissolved gas pathway combines the vertical transport of dissolved inorganic carbon in brine and the diffusive air-ice CO_2 flux, F^{CO_2} (mmol m^{-2} d^{-1}), which is assumed proportional to the CO_2 partial pressure (pCO_2) difference between the surface brine (in the top 5 cm of the ice) and the atmosphere, and is a function of the near-surface brine fraction:

$$F^{CO_2} = k^{CO_2} \cdot e^{2/3} \cdot (\zeta^{CO_2} - K_0 f^{CO_2}) \tag{2}$$

where k^{CO_2} (m s^{-1}) is the piston velocity, e is the brine fraction near the ice surface, $e^{2/3}$ represents the fractional surface open to brine-air diffusive CO_2 fluxes, ζ^{CO_2} is the brine CO_2 concentration (mmol m^{-3}), f^{CO_2} is the atmospheric CO_2 fugacity (atm), and K_0 is the Henry's constant (mmol m^{-3} atm^{-1}). We consider that $f^{CO_2} = p_{atm} * r^{CO_2}{}_{,atm}$, where p_{atm} is the atmospheric pressure (atm) and $rCO_{2,atm}$ is the atmospheric CO_2 mixing ratio measured within the chamber. The piston velocity is calculated from the molecular diffusion coefficient of dissolved CO_2 (D_{diff} in m^2 s^{-1}) and the thickness of the diffusive boundary layer (z_{BL} in μm):

$$k^{CO_2} = D_{diff} / z_{BL} \tag{3}$$

This piston velocity neglects the effects of snow and wind, absent in these tank experiments, and only includes the contribution of dissolved CO_2. In contrast, equation 1 includes both gas bubble and dissolved contributions as F and $pCO_{2\ bulk}$ are direct measurements without distinction between dissolved and gaseous forms. The z_{BL} is highly uncertain and therefore has been used as a tuning parameter to adjust the magnitude of air-ice CO_2 fluxes, whereas D_{diff} is better constrained by observations. For our control simulation (CTRL), we used $D_{diff} = 0.97\ 10^{-9}$ m^2 s^{-1} (the diffusion coefficient of CO_2 in water from Broecker and Peng, 1974) and $z_{BL} = 0.5$ μm (Moreau et al., 2015; Table 1).

The gas bubble pathway was developed in the model to simulate Argon dynamics (Moreau et al., 2014) and implies explicit gas bubble reservoirs in every layer. The gas concentration in the bubble reservoir changes due to bubble nucleation/dissolution, upward migration of buoyant gas bubbles, and bubble escape to the atmosphere. Nucleation of gas bubbles transfers dissolved CO_2 from brine to the bubble compartment as a function of the CO_2 super-saturation. At each time step, a fraction R^{bub} of the CO_2 super-saturation is transferred to bubbles. The bubbles migrate upward when the brine network is connected, which is assumed to happen above a given brine fraction threshold (e.g., $e_T{}^{gas} = 0.07$, Zhou et al., 2013; Moreau et al., 2014). If the fraction of sea ice with $e > e_T{}^{gas}$ includes the ice surface, all gas bubbles escape to the atmosphere and contribute to the air-ice CO_2 flux. For our CTRL simulation, we used $R^{bub} = 10\%\ h^{-1}$ and $e_T{}^{gas} = 0.07$ (Table 1).

In order to understand the potential reasons to explain the underestimation of the observed air-ice CO_2 fluxes by the model, we performed three series of sensitivity experiments (Table 1). First, we tested the impact of a more intense dissolved CO_2 pathway, by changing D_{diff} and z_{BL} (runs 2–4). The D_{diff} value of Broecker and Peng (1974) is derived from seawater and only includes diffusive effects. We tested the slightly higher D_{diff} value of Loose et al. (2011), derived from sea ice experiments, which can potentially include both diffuse and bubble contributions. A lower z_{BL} (0.05 μm) value was also tested. In a second series of experiments

Table 1. Description of the sensitivity runs used to test the sensitivity of air-ice CO_2 fluxes to model parameterization[a]

Run	Name	R^{bub}	e_T^{gas}	D_{diff}	z_{BL}	Ikaite precipitation	Number of ice layers	Misfit
1	CTRL	10	0.07	0.97	0.5	Yes	10	0.1
2	Loose-D_{diff}[b]	0	0.07	24	0.5	Yes	10	0.08
3	No-bub	0	0.07	0.97	0.5	Yes	10	0.08
4	Low-z_{BL}	0	0.07	0.97	0.05	Yes	10	0.08
5	No-ikaite	0	0.07	0.97	0.5	No	10	0.10
6	20-layers	0	0.07	0.97	0.5	Yes	20	0.06
7	Low-bub	1	0.07	0.97	0.5	Yes	10	0.07
8	High-bub	20	0.07	0.97	0.5	Yes	10	–0.05
9	Moreau-bub[c]	0.1	0.07	0.97	0.5	Yes	10	0.08

[a] Different parameterizations include the bubble formation rate (R^{bub}, % h^{-1}), the molecular diffusion rate (D_{diff}, 10^9 m^{-2} s^{-1}), the boundary layer thickness (z_{BL}, um), ikaite precipitation and the number of vertical ice layers. Model-data misfit (mmol m^{-2} d^{-1}) are also presented for each run.

[b] Loose et al. (2011)

[c] Moreau et al. (2015)

doi: 10.12952/journal.elementa.000112.t001

(runs 5–6), the impacts of higher resolution (20 layers instead of 10) and ikaite precipitation/dissolution were investigated. Third, we tested the impact of a more intense gas bubble pathway by changing R^{bub}, the bubble nucleation rate (runs 7–9), which is highly uncertain.

To evaluate which scenario is closest to the observed fluxes, we computed a model-data misfit for each of the model runs. The misfit were computed from the difference between the flux observed and the flux modelled. We report averages for each of the model runs in Table 1.

All other parameters are from Moreau et al. (2015). The simulation spans 31 May – 18 June 2012. The time step is 1 h. Based on the present observations, initial seawater TA and DIC concentrations were set to 2300 mmol m^{-3} and 2090 mmol m^{-3}, and sea ice TA and DIC concentrations were set to 850 mmol m^{-3} and 750 mmol m^{-3}.

3. Results and discussion

Detailed information about sea ice physical properties can be found in Zhou et al. (2014b). Briefly, the first phase of the experiment – the growth phase – lasted from day 1 to day 15. Air temperature above the tank was set to –15 °C and sea ice grew continuously, reaching a maximum thickness of 24 cm. A strong temperature gradient was observed between the top and the bottom of the ice. Salinity exhibited a typical C-shape profile with a lower salinity at the ice interior compared to the top and the bottom of the ice. Then from day 16 to 19, the air temperature was set to –1 °C, sea ice thickness slightly decreased, temperature exhibited a more homogeneous profile through the whole thickness, and salinity decreased in the top and bottom parts. The brine volume fraction remained above 5% during the whole experiment. On the whole, the sea ice remained thin, warm and permeable during both the growth and the melting phase.

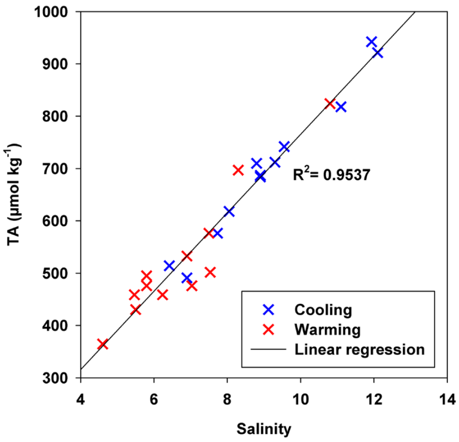

Figure 1

Linear regression between TA and salinity within bulk sea ice.

The ice growth and melting phases are colored in blue and red, respectively.

doi: 10.12952/journal.elementa.000112.f001

3.1 Total alkalinity

TA concentrations in bulk sea ice (i.e., melted sea ice) are consistent with the values reported in the literature (Gleitz et al., 1995; Delille et al., 2007; Nomura et al., 2010b; Fransson et al., 2011; Miller et al., 2011a; Geilfus et al., 2012a; Rysgaard et al., 2013) and were highly correlated with salinity ($r^2 = 0.95$; Figure 1).

The repeated inspection of freshly melted ice using a binocular microscope (Leitz Laborlux® with 125 to 500 x magnification) did not reveal the presence of ikaite, a hydrated calcium carbonate polymorph ($CaCO_3{\cdot}6H_2O$). Taking into account the thermodynamic constraints (Papadimitriou et al., 2013) and the kinetics to simulate the ikaite precipitation (Papadimitriou et al., 2014), the maximum value of ikaite simulated by the model in the ice surface layer was 13 µmol kg^{-1}, whereas the error on TA measurement was 4 µmol kg^{-1}.(parameters from the CTRL simulation of Moreau et al., 2015). This concentration falls at the lower end of the range of ikaite concentrations reported in sea ice (7–93 µmol kg^{-1} in Dieckmann et al., 2008; 15–19 µmol kg^{-1} in Geilfus et al., 2013; 100–900 µmol kg^{-1} in Rysgaard et al., 2013). This evidence indicates that if ikaite precipitated during the experiment, it was not significant.

3.2 CO_2 exchange at the air-ice interface

3.2.1 Continuous measurements of air-ice CO_2 fluxes

During seawater cooling, and before the formation of the ice crystals, CO_2 fluxes measured with the automated chamber showed negative values, down to −6 mmol m^{-2} d^{-1} (Figure 2). Within hours after the formation of the first ice crystals, CO_2 fluxes became mostly positive (ranging between −0.4 mmol m^{-2} d^{-1} and 0.75 mmol m^{-2} d^{-1} with an average of 0.2 mmol m^{-2} d^{-1} for the growth phase), consistent with the observed super-saturation of CO_2 in bulk ice (i.e., $pCO_{2\,bulk}$ above 400 ppm). During the melting phase, CO_2 fluxes turned to negative (ranging between −2.1 mmol m^{-2} d^{-1} and 0 mmol m^{-2} d^{-1} with an average of −0.24 mmol m^{-2} d^{-1}) in parallel with the decrease of $pCO_{2\,bulk}$ that passed below saturation. The pCO_2 of the underlying seawater remained under-saturated during the whole experiment, while the surface (first 5 cm) $pCO_{2\,bulk}$ showed values above or below the atmospheric pCO_2 during the growth and the melting phase, respectively.

Although the chamber was not properly sealed between day 0 and day 5, air-ice CO_2 fluxes from the whole measurement period were consistent with previous measurements carried out with chambers over artificial sea ice (between 0 and 0.27 mmol m^{-2} d^{-1}; Nomura et al., 2006) and slightly lower than measurements over natural sea ice. Delille et al. (2014) measured CO_2 fluxes ranging from −5.2 mmol m^{-2} d^{-1} to 1.9 mmol m^{-2} d^{-1} on Antarctic pack ice in spring, and ascribed these fluxes to seasonal pCO_2 gradients between the brine and the atmosphere. Geilfus et al. (2012a) measured CO_2 fluxes at the sea ice interface ranging from −2.63 mmol m^{-2} d^{-1} up to 0.84 mmol m^{-2} d^{-1} in the Arctic coastal zone, while Nomura et al. (2010a) measured CO_2 fluxes ranging from -1 mmol m^{-2} d^{-1} to 0.7 mmol m^{-2} d^{-1} over land fast ice in Barrow at the end of spring.

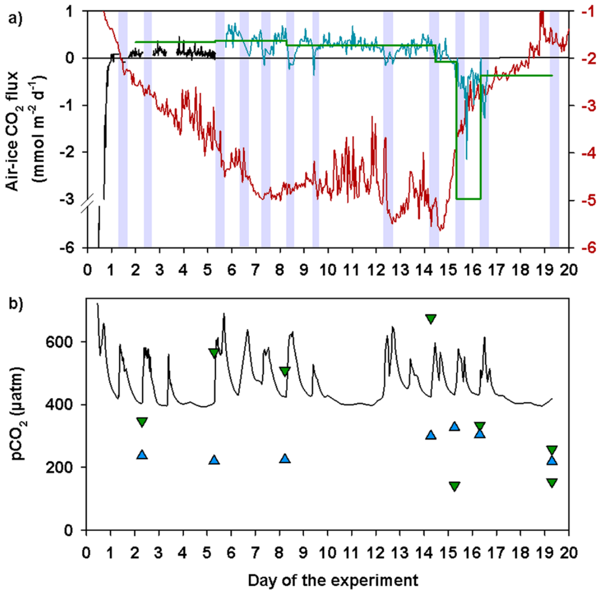

Figure 2

Air-ice CO_2 fluxes, sea ice surface temperature and pCO_2 over time.

a) Evolution of the air-ice CO_2 flux (black corresponds to a period with the chamber not properly sealed, blue to a period with a correct sealing of the chamber) and temperature 2 cm above the air-ice interface (in red). The green horizontal step line corresponds to the flux calculated from the DIC anomaly. The shaded areas refer to working hours and the related increase of atmospheric pCO_2. b) Atmospheric (black line), ice surface (green triangles down) and seawater (blue triangles up) pCO_2. The ice surface pCO_2 corresponds to the first 5 cm of the bulk sea ice measured with the method of high vertical resolution.

doi: 10.12952/journal.elementa.000112.f002

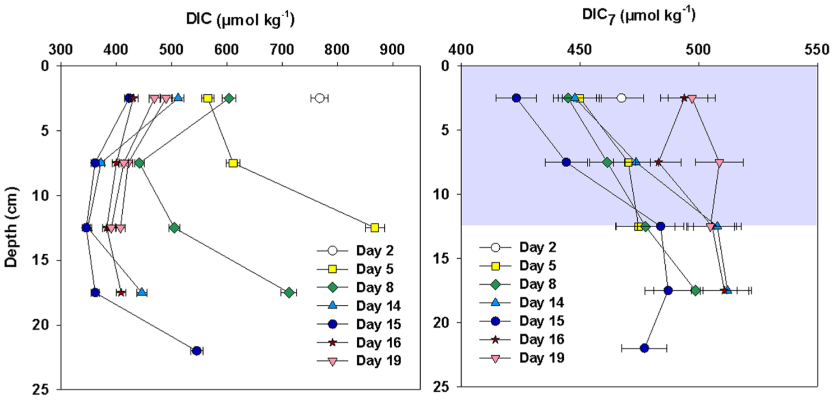

Figure 3

Bulk sea ice DIC and surface DIC depletion during ice growth.

a) Bulk DIC profiles and b) DIC profiles normalized to a salinity of 7 (DIC_7), where the grey area refers to the DIC depletion zone.

doi: 10.12952/journal.elementa.000112.f003

The temperature and the $pCO_{2\ air}$ measured within the automated chamber exhibited daily variations, rising during "working hours" due to the presence of the researchers in the experimental room and decreasing outside "working hours". The pattern of air-ice CO_2 fluxes is clearly opposite and strongly affected by the rise of atmospheric pCO_2 during working hours. These imperfections are inherent to the environmental constraints of this experimental study and could hardly be avoided. Nevertheless, the results can still be interpreted in terms of the main factors driving the CO_2 fluxes, and the overall pattern of observed air-ice CO_2 fluxes is consistent with *in situ* observation of a seasonal cycle, with upward CO_2 fluxes during ice growth (Nomura et al., 2010a; Geilfus et al., 2012a; Delille et al., 2014) and downward CO_2 fluxes during ice melt (Delille et al., 2014; Geilfus et al., 2015).

3.2.2 Integrated estimates of air-ice CO_2 fluxes

In parallel with direct measurements of air-ice CO_2 fluxes, we derived air-ice CO_2 fluxes from DIC depletion in the top layers of the ice (Geilfus et al., 2013). DIC was normalized to a salinity of 7 (7 corresponds to the mean bulk ice salinity during the whole experiment, noted as DIC_7) to remove the salinity-related changes (brine rejection, concentration and dilution; Figure 3). If no biogeochemical processes occurred (biological activity, $CaCO_3$ precipitation, CO_2 transfer to the gas phase and CO_2 exchange with the atmosphere), DIC_7 profiles should be homogeneous over the ice column. During the growth phase, a clear decrease in the top 12.5 cm of the young ice was measured compared to the bottom ice horizons. Because no significant primary production was possible due to absence of primary producers (Zhou et al., 2014b) and ikaite precipitation was insignificant (section 3.1), we assumed that DIC_7 depletion in the top 12.5 cm of the growing ice was due to CO_2 release from the super-saturated ice to the atmosphere above. Whereas, during the melting phase we observed a DIC_7 increase in the top 12.5 cm. This increase can be linked to the downward air-ice CO_2 flux measured during the melting phase.

Besides the measurements of air-ice CO_2 fluxes, the amount of CO_2 released to the atmosphere during the sea ice growth was assessed using a method proposed by Geilfus et al. (2013). First, a "theoretical DIC" (DIC_{th}) was calculated from the raw DIC concentration at 12.5 cm ($DIC_{12.5\,cm}$), assuming that, if biogeochemical processes are null, DIC and salinity (S) should follow a linear relationship:

$$DIC_{th,\,i} = DIC_{12.5\,cm} \cdot (S_i / S_{12.5\,cm}) \tag{4}$$

where $DIC_{th,\,i}$ and $DIC_{12.5\,cm}$ are computed for each sampling event and expressed in µmol kg^{-1}. The index, i, refers to the upper two sampling depths, 2.5 cm and 7.5 cm. From the theoretical DIC, we derive the "DIC anomaly" for each sampling day (ΔDIC_t in mmol m^{-2}):

$$\Delta DIC_t = \Sigma\ (i = 2.5 \text{ to } 12.5 \text{ cm})\ (DIC_{th,\,i} - DIC_i) \tag{5}$$

As the DIC anomaly was mainly due to the release of CO_2 from the ice to the atmosphere during the present experiment (see above), integrating DIC anomalies over time gives the theoretical air-ice CO_2 flux between two sampling events:

$$F = ((\Delta DIC_{t+\Delta t} - \Delta DIC_t) / \Delta t) \cdot dx \cdot \rho \tag{6}$$

Table 2. Gas transfer coefficient calculated for each day of the experiment[a]

Day of the experiment	*T*	*Bulk S*	*K*
2	–3.0	11.5	2.43 (± 0.9)
5	–5.1	8.8	2.59 (± 0.9)
8	–5.0	9.5	2.66 (± 0.9)
14	–5.8	8.0	2.22 (± 0.9)
15[b]	–3.3	3.0	2.1
16[b]	–2.5	6.1	2.9
19	–1.8	6.9	0.5 (± 0.08)
19	–1.8	6.9	0.3 (± 0.08)

[a] Mean ice surface temperature (*T*, °C), bulk salinity (*Bulk S*) and gas transfer coefficient for CO_2 at the air-ice interface (*K*, mol m^{-2} d^{-1} atm^{-1}) for each day of the experiment

[b] Refers to the transition period

doi: 10.12952/journal.elementa.000112.t002

where Δt is the time frame between two sampling events in days, *dx* is the distance in meters between two sampling depths, and ρ is the sea ice density for each layer defined from temperature and salinity and using relationships given by Cox and Weeks (1982), in kg m^{-3}. Based on the precision of the measured variables (salinity, temperature, TA, pCO_2; see Methods section), the precision on *F* is assessed at ± 0.03 mmol m^{-2} d^{-1} (which represents an error of 15% for the averaged CO_2 flux of 0.2 mmol m^{-2} d^{-1}).

From these DIC anomalies, the calculated air-ice CO_2 fluxes (black triangles in Figure 2a) are in good agreement with the observed air-ice CO_2 fluxes, except on day 16 where the difference represents more than 1 mmol m^{-2} d^{-1}; integrated measurements cannot accurately capture the rapid transition from the freezing to the melting decay phase. With the exception of this transition phase, the consistency between the continuous and integrated fluxes suggest that in an indoor experiment, the automated chamber provides accurate measurements of air-ice CO_2 fluxes when snow cover is absent, despite the large variation of the atmospheric pCO_2.

3.3 Determination of a gas transfer coefficient for CO_2 in artificial sea ice

Using equation 1 for gas exchange, we calculated a gas transfer coefficient for CO_2 at the air-ice interface for each sampling day of the experiment (see *K*; Table 2), where *F* corresponds to the air-ice CO_2 fluxes measured with the automated chamber, $pCO_{2\,air}$ to the pCO_2 at the air interface and $pCO_{2\,bulk}$ to the pCO_2 at the ice interface (0 cm to 5 cm). The numbers in light grey in Table 2 refer to the transition phase which was not taken into account in the final value computed for *K*. The values for *K* and ancillary data detailed in Table 2 are close during the whole growth period. The mean *K* for the sea ice growth period, from day 2 to day 14 inclusive, is $K = 2.5$ mol m^{-2} d^{-1} atm^{-1}. A Bootstrap resampling statistical analysis of the propagation of the uncertainties of the measured variables (salinity, temperature, measured CO_2 fluxes, $pCO_{2\,bulk}$ and $pCO_{2\,air}$) gives an uncertainty for *K* of 0.9 mol m^{-2} d^{-1} atm^{-1} where standard error deviation is only 0.25 mol m^{-2} d^{-1} atm^{-1}. For the melting phase (which corresponds to two measurements on day 19) the mean *K* value was 0.4 mol m^{-2} d^{-1} atm^{-1} (the uncertainty derived from a Bootstrap resampling statistical analysis was 0.08 mol m^{-2} d^{-1} atm^{-1}). *K* was therefore 6 times higher during the growth phase than during the melting phase.

In order to get a measure of gas exchange that does not depend on the gas solubility, Wanninkhof (1992) proposed to use *k*, the gas transfer velocity, defined from:

$$K = k.\ Sol \tag{7}$$

where *Sol* (mmol m^{-3} atm^{-1}) is the solubility of CO_2 in salt water (here brine), a function of temperature (*T*) and salinity (*S*), following Weiss (1974):

$$\ln \mathrm{Sol} = A_1 + A_2(100/T) + A_3 \ln(T/100) + S\,[B_1 + B_2(T/100) + B_3(T/100)^2] \tag{8}$$

We used the *T* and *S* of sea ice brine. The resulting value, k = **0.164 (± 10%)** cm h^{-1}, falls within the range of values given by Liss and Merlivat (1986) for a smooth surface regime and the values given by Crusius and Wanninkhof (2003) for gas exchange over a lake at low wind speed. However, solubility as described by eq. 8 is most likely not adequate for the range of temperature and salinity encountered within sea ice, as suggested by Zhou et al. (2014a). *K*, the gas transfer coefficient, is solely deduced from measurements and does not depend on an uncertain solubility value.

Thin sections of the ice cores were processed following Tison et al. (2002). Bubbles were observed during the growth phase, particularly near the ice surface (Figure 4). We suggest that these bubbles (trapped at the very beginning of ice growth or newly formed) were likely moving upward due to their own buoyancy. Once

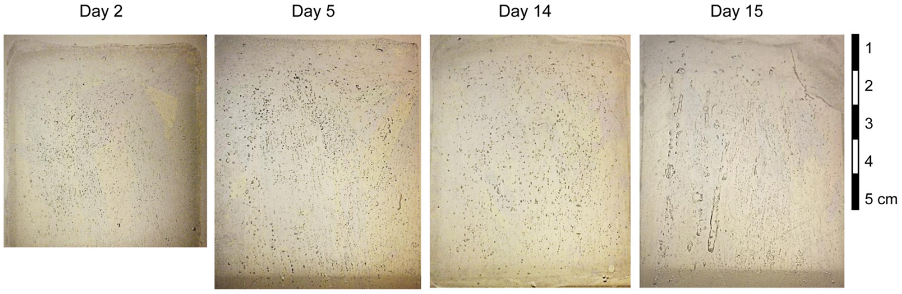

Figure 4

Thin sections of surface ice cores.

Thin sections of ice cores for day 2, 5, 14 and 15 of the experiment. The contrasted circles and tubes are bubbles while the gray-shaded features are brine inclusions.

doi: 10.12952/journal.elementa.000112.f004

bubbles reached the ice surface, they collapsed and CO_2 was released to the atmosphere, corresponding to an ebullition flux. K-values calculated during the growth and melting phases indicate that gas transport was about 6 times faster during ice growth than during ice decay. We hypothesize that air-ice CO_2 fluxes during the melting phase are driven mainly by molecular diffusion, while during the growth phase, ebullition fluxes add to molecular diffusion. This hypothesis suggests that the ebullition fluxes are a dominant pathway for gas transport and exchange during the growth phase.

3.4 Model sensitivity experiments on the CO_2 transport pathways through sea ice

Here we use the model to frame the CO_2 flux into further theoretical considerations. The various model simulations described in Table 1 are compared to the observations, in order to understand which parameters are most influential in shaping the model response (Figure 5).

First, the sign of the CO_2 flux is consistent between observations and all model simulations. All model runs show an efflux of CO_2 during the growth period and an influx during the melt period. The direction of the flux depends mostly on the dissolved gas pathway, itself driven by the air-brine pCO_2 difference, ultimately set by the near-surface ice temperature evolution, which is quite well understood. In addition, some of the short-term variations of the observed CO_2 fluxes are reproduced. The model gives a good estimation of downward CO_2 fluxes during ice melting although the time of the onset of downward CO_2 fluxes occurs earlier than observed in the model.

By contrast, the magnitude of the air-ice CO_2 flux is highly variable among the different model runs, in particular during the growth phase. The most influential but uncertain factors clearly lie within the gas bubble pathway (Figure 5c). By contrast, the dissolved pathway is found rather insensitive to parameterization choices (e.g., gas diffusivity D_{diff}, boundary layer thickness z_{BL}, vertical resolution, ikaite, etc.). In turn, the total (dissolved + bubble) air-ice CO_2 flux is essentially determined by the gas bubble nucleation rate R^{bub}, which acts as a bottleneck parameter for the efflux of CO_2 to the atmosphere via the gas bubble pathway. This bottleneck effect explains why R^{bub} was used as a tuning parameter, set to 10% h^{-1} in the CTRL run, the value that gave the best agreement with observations.

Why is the dissolved pathway rather insensitive between the different runs? As in Moreau et al. (2015), we investigated whether the dissolved gas pathway could have been more intense than simulated. To answer this question, we tested to what extent modifying the uncertain parameters z_{BL} and D_{diff} could increase the upward CO_2 fluxes during ice growth. None of our trials was successful. For example, increasing D_{diff} up to 2.4×10^{-8} m^2 s^{-1} (run 2: Loose-D_{diff}) barely affects the upward CO_2 fluxes during ice growth. Decreasing z_{BL} down to 0.05 μm did not significantly increase the simulated air-ice CO_2 fluxes either. This model behavior arises because the ultimate limitation for the air-ice CO_2 diffusive flux is the near surface stock of DIC: supply to the near-surface DIC is not rapid enough to sustain CO_2 fluxes to the observed magnitude. This result was already obtained by Moreau et al. (2015; see their Figure 9b where the simulated outward CO_2 fluxes during winter at Barrow reach asymptotically 1.3 mmol m^{-2} d^{-1} when z_{BL} is decreased down to 10^{-3} μm). By contrast, the gas bubble pathway is much more variable between the different runs and characterized by much larger uncertainties, because gas bubble flux can originate further down in the ice and is not limited by near-surface DIC stocks. The model-data misfit presented in Table 1 shows that the best model-observation agreement was achieved for a strong gas bubble pathway, which corresponds to high values of R^{bub} (10-20% h^{-1}). Yet, the bubble nucleation rate R^{bub} is far from being well constrained from observations. In Moreau et al. (2014), this value was tuned to 0.1% h^{-1}, corresponding to a characteristic time scale of 40 days, in order to match observed gas bubble concentrations over simulations spanning several months. In the present context (curve Moreau-bub in Figure 5c), such value gives a weak gas bubble pathway and an underestimation of CO_2 fluxes by the model. Forty days is rather long for bubble nucleation, much larger than expected, typically less than one hour (see, e.g., Brennen, 1995). The most obvious reason why such an unrealistically large 40 day

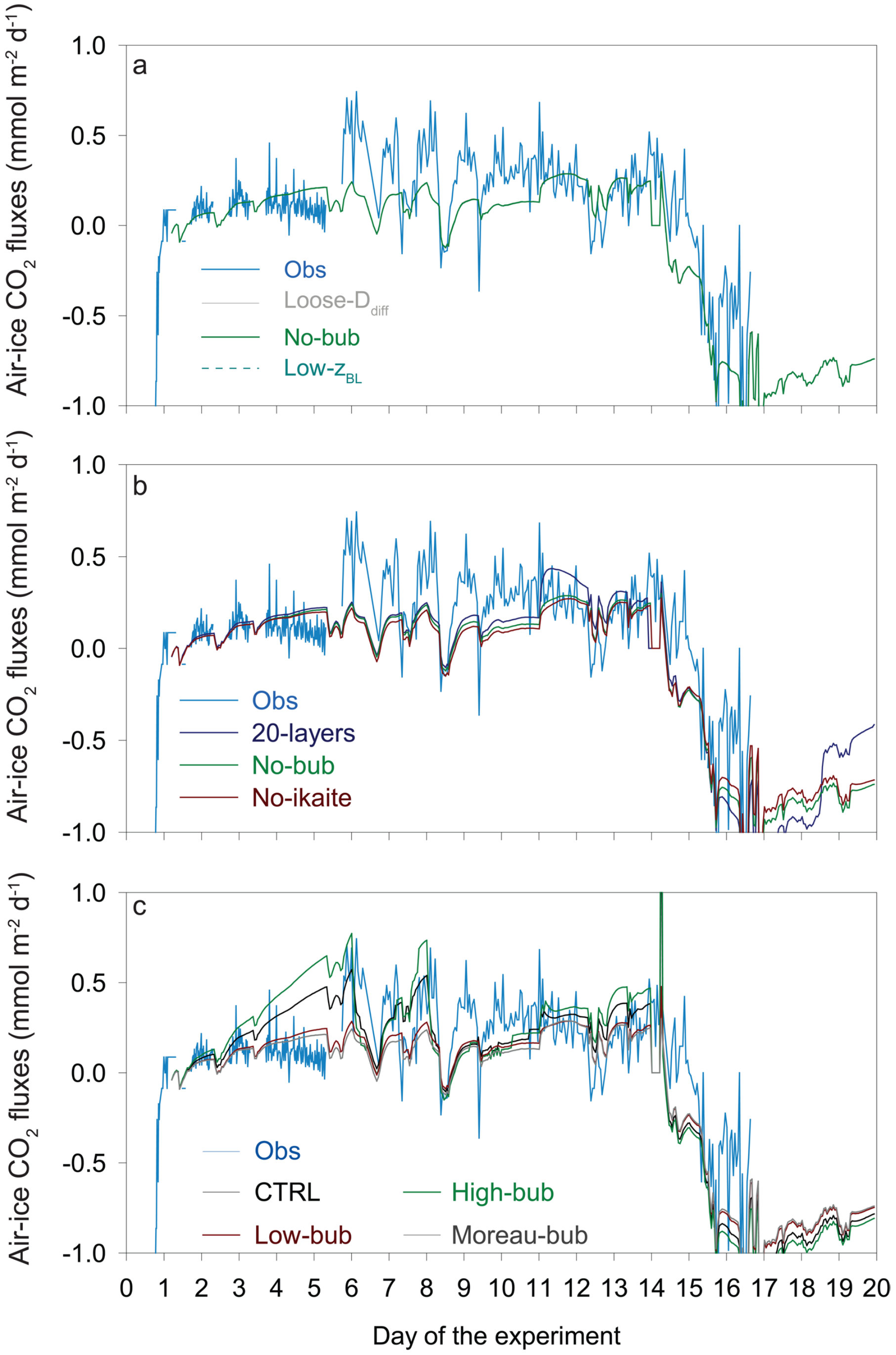

Figure 5

Observed and simulated air-ice CO$_2$ fluxes.

a) Simulated air-ice CO$_2$ fluxes (mmol m^{-2} d^{-1}) for runs Loose-D$_{diff}$ (grey, where D_{diff} = 24 10^{-9} m^2 s^{-1}), No-bub (green, where R^{bub} = 0% h^{-1} and D_{diff} = 0.97 10^{-9} m^2 s^{-1}) and Low-z_{BL} (dark blue in dash, where z_{BL} = 0.05 µm). The three curves for runs Loose-D_{diff}, No-bub and Low-z_{BL} are confounded on the plot. Observed CO$_2$ fluxes are given in blue.

b) Simulated air-ice CO$_2$ fluxes (mmol m^{-2} d^{-1}) for runs No-ikaite (dark red, where there is no ikaite precipitation) and 20-layers (dark blue, where the number layers of ice was set to 20 instead of 10). Observed CO$_2$ fluxes are given in blue.

c) Simulated air-ice CO$_2$ fluxes (mmol m^{-2} d^{-1}) for runs CTRL (in black), Low-bub (grey, where R^{bub} = 1% h^{-1}), High-bub (cyan, where R^{bub} = 20% h^{-1}) and Moreau-bub (dark grey, R^{bub} = 0.1% h^{-1}). Observed CO$_2$ fluxes (mmol m^{-2} d^{-1}) are given in blue.

doi: 10.12952/journal.elementa.000112.f005

value had to be used by Moreau et al. (2014) is that pressure effects are missing in the model, which should quickly inhibit gas bubble nucleation once a large enough stock of gas bubbles is built up, which would typically occur for impervious sea ice over a few days. Larger R^{bub} values of 10–20% h^{-1} strongly intensify the gas bubble pathway. They also correspond to more realistic time scales for gas bubble nucleation (4–8 hours).

The influence of several other processes, known to occur in natural conditions and contribute to the ice-air CO$_2$ fluxes, was also considered. As far as frost flowers are concerned, they were not observed in the tank experiment, and hence are not relevant to the present discussion of air-ice CO$_2$ fluxes. The precipitation of ikaite could have influenced ice-atmosphere CO$_2$ fluxes (e.g., Geilfus et al., 2013; Rysgaard et al., 2014);

however, as discussed above, ikaite precipitation was not observed under the microscope and the model CTRL simulation predicts a rather low ikaite concentration of 13 µmol kg^{-1}. The lack of ikaite influence is further corroborated by the model run with no ikaite precipitation (and no bubbles; Run 6, Table 1) which barely differs from the no-BUB run in terms of air-ice CO_2 flux (Figure 5b).

We also tested the role of vertical resolution of the simulated CO_2 fluxes by running the model with 20 vertical ice layers instead of 10, and with no bubbles (Figure 5b). More layers better resolve and increase the near-surface pCO_2, which slightly intensifies the dissolved gas pathway during the growth phase.

3.5 Synthesis

As detailed in Zhou et al. (2014b), the artificial sea ice was likely permeable to gas exchange during the whole experiment. Convection was likely only present during the growth period and limited to near the ice-water interface (see Rayleigh numbers in Figure 3 of Zhou et al., 2014b) and was nearly negligible during the whole period of decay. We therefore consider that only diffusion and/or buoyancy processes occurred in the upper parts of the ice. Both the computation of the gas transfer coefficient and the model sensitivity analysis support this assumption. As described previously, bubbles were observed during the growth phase, particularly near the ice surface (Figure 4).

The values of *K* were about 6 times lower during the melting phase as compared with the growth phase (Table 2). At this stage, based on model simulations, we cannot explain this difference without assuming a significant contribution of the gas bubble pathway during the growth of sea ice. However, this explanation is not based on direct observation of gas bubble processes but rather on inference from model simulations characterized by large uncertainties, in particular in terms of the gas bubble nucleation rate. The latter is the key tuning bottleneck parameter sourcing gas bubbles to the model gas bubble ice-atmosphere pathway. All the other surface processes that we could envision were, to the best of our present investigation capability, not able to supply enough carbon to the atmosphere. During ice melt, the model is in agreement with the much lower *K* values, suggesting that air-ice CO_2 fluxes are dominated by the dissolved pathway, apart from the short under-sampled transition period when other processes such as episodic convection events might have taken place.

Using our best model run (CTRL), we compared the contribution of all processes based on the computation of the model DIC budget, following Moreau et al. (2015; see Figure 6). Sea ice is gaining DIC throughout its growth (Figure 6a). Large quantities of DIC are incorporated into sea ice by growth, although 80% of this DIC is rejected through brine drainage (Figure 6b). Ikaite precipitation does not significantly contribute to the budget of DIC. Ice-atmosphere CO_2 fluxes (Figure 6c) are dominated by the escape of gas bubbles during ice growth. However, only the dissolved pathway affects CO_2 fluxes during ice melt. As suggested by Moreau et al. (2015) the budget of DIC in sea ice is driven mainly by physics while biogeochemical processes (only chemical here), although significant, are secondary.

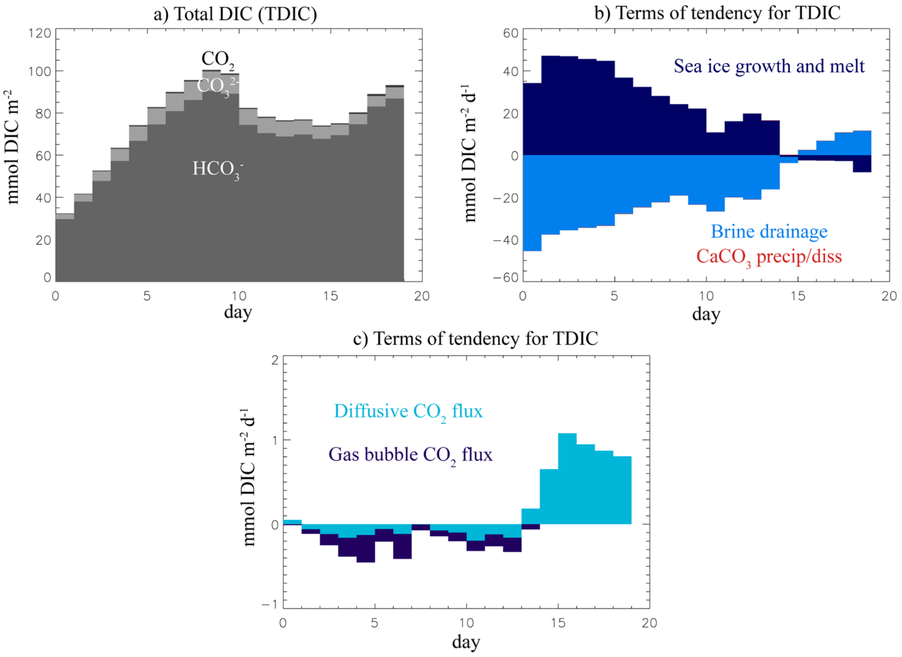

Figure 6

CO_2 budget.

a) Daily budget of vertically integrated DIC (TDIC, mmol m^{-2}) dissolved into CO_2 (black), CO_3^{2-} (light grey), and HCO^{3-} (grey) for the CTRL run. b) Corresponding daily mean changes (mmol m^{-2} day^{-1}) in TDIC due to total sea ice growth and melt (dark blue), brine drainage (light blue), and ikaite precipitation/dissolution (red). c) Corresponding daily mean changes (mmol m^{-2} day^{-1}) in TDIC due to diffusive CO_2 fluxes (light blue) and gas bubble fluxes (dark blue).

doi: 10.12952/journal.elementa.000112.f006

Based on these considerations, we expand to ice-atmosphere exchanges of CO_2 the suggestion that gas bubbles provide important contributions to the stocks of gaseous compounds in sea ice (Mock, 2002; Tison et al., 2002; Rysgaard and Glud, 2004; Zhou et al., 2013; Moreau et al., 2014). The conceptual view that we propose is based on three key arguments. **1.** Gas bubbles easily form in sea ice because brine shrinking with temperature induces drastic increases in gas concentrations, and because there is a net decrease in gas solubility with decreasing temperature in brine inclusions. **2.** Gas bubbles in the liquid brine rise upward if the connectivity of the brine network is sufficient. **3.** The dilution of brines during warming brings CO_2 concentration in brine below saturation, which brings trapped gas bubbles back into dissolved form. Because there is no analytical method to assess the partitioning of gases between dissolved and gaseous forms in sea ice brine, it is difficult for the time being to confirm this conceptual view directly. In natural sea ice, other surface processes likely affect air-ice CO_2 fluxes as well (e.g., the formation of frost flowers, brine skim; Geilfus et al., 2013; Barber et al., 2014). In the present experiments, however, they were not observed.

Finally let us stress that there are only a few processes able to sustain enhanced CO_2 fluxes during a long period. The presence of frost flowers would be transient and have only short-term effects on CO_2 fluxes. Other processes (e.g., melting/freezing cycle of the ice surface) modulate air-ice CO_2 fluxes, but few of them can actually sustain CO_2 fluxes for extended periods of time as we observed during the experiment. Processes that sustain CO_2 for extended periods of time must involve either the production of CO_2, like bacterial respiration, or the transfer of CO_2 from a large reservoir (like the ice interior or the ocean) to the surface.

4. Conclusions

The first aim of this study was to determine experimentally the air-ice CO_2 transfer coefficient from continuous CO_2 flux measurements during an ice growth and decay cycle in an ice-tank experiment. Discrete measurements of air-ice pCO_2 gradients and DIC anomalies reflected well the amplitude and the patterns of the air-ice CO_2 fluxes, supporting the reliability of our methods and results, including the calculation of a bulk gas transfer coefficient. The second aim was to discriminate the different drivers of air-ice CO_2 fluxes using a 1D sea ice carbon cycle model (Vancoppenolle et al., 2010; Moreau et al., 2015), including explicit empirical representations of dissolved gas and gas bubble ice-atmosphere pathways and testing for several gases (Ar, O_2, CO_2) at a few locations.

There are three key findings in the paper. **1.** The observation-based gas transfer coefficient, retrieved by dividing the observed CO_2 flux by the air-brine pCO_2 difference, was ~6 times higher during growth ($K = 2.5$ mol m^{-2} d^{-1} atm^{-1}) than during melt ($K = 0.4$ mol m^{-2} d^{-1} atm^{-1}). **2.** The time evolution of the sign of the air-ice CO_2 flux, characterized by an efflux from the ice during growth and an influx during melting, was consistent between observations and the nine model simulations, as well as with previous literature (Nomura et al., 2010a; Geilfus et al., 2012a; Delille et al., 2014; Geilfus et al., 2015). Such evolution must therefore be seen as typical and robust. **3.** The magnitude of the observed CO_2 flux is consistent with previous literature but not between the different model simulations. The simulated dissolved CO_2 flux clearly underestimates the observed value because of an intrinsic limitation by DIC stocks in the model already identified by Moreau et al. (2015). The observed magnitude of the ice-air CO_2 flux can only be reached in the model by invoking an intense escape of gas bubbles through an ice-atmosphere pathway. Such an intense pathway was achieved by tuning the gas bubble nucleation time scale down to a few hours, which contrasts with the value of a few weeks used in a previous 6-month simulation of Argon dynamics in natural sea ice (Moreau et al., 2014).

Based on these concordant findings, we infer that the gas bubble ice-atmosphere pathway is likely a significant contributor to air-ice flux in young growing sea ice, next to diffusion. This intense gas bubble pathway in growing sea ice proposed here is plausible at this stage but subject to caution, because it does not rely on direct process observations, but rather on inference from air-ice CO_2 flux and a single sea ice model, characterized by a number of assumptions. Further evaluation of the proposed scenario and reduction of uncertainties rely on improvements of both observation and modelling techniques. Observations of gas bubbles from X-ray tomography (Crabeck et al., 2016) provide new insights on gas bubble size and number distribution, and might be used to document the upward migration of gas bubbles. Future models should include at least pressure effects on gas bubble nucleation and perhaps tortuosity effects on gas bubble rise, as well as improved representations of brine dynamics (e.g., Griewank and Notz, 2013; Turner et al., 2013; Rees Jones and Worster, 2014).

The multiphase nature of CO_2 in sea ice is well established, with contributions of dissolved species, gas bubbles (Tison et al., 2002; Zhou et al., 2013; Crabeck et al., 2014a; Moreau et al., 2014, 2015) and ikaite crystals (Papadimitriou et al., 2004; Dieckmann et al., 2008), a solid inorganic compound that contains inorganic carbon. This multiphase nature of CO_2 is, to our best knowledge, a unique feature in marine environments. Clarifying the partitioning of CO_2 between the gaseous and dissolved phases and the gas transport pathways, as well as the contribution of surface ice processes, is a critical challenge for future research related to gas dynamics and the carbon cycle in ice-covered seas.

References

Assur A. 1960. Composition of sea ice and its tensile strength. *SIPRE Research Report 44*.

Barber DG, Ehn JK, Pućko M, Rysgaard S, Deming JW, et al. 2014. Frost flowers on young Arctic sea ice: The climatic, chemical, and microbial significance of an emerging ice type. *J Geophys Res-Atmos* **119**(20): 11,593–11,612. doi: 10.1002/2014JD021736.

Brennen C. 1995. Cavitation and bubble dynamics. *Oxford University Press*.

Broecker WS, Peng T. 1974. Gas exchange rates between air and sea. *Tellus* **26**(1–2): 21–35.

Brown KA, Miller LA, Davelaar M, Francois R, Tortell PD. 2014. Over-determination of the carbonate system in natural sea-ice brine and assessment of carbonic acid dissociation constants under low temperature, high salinity conditions. *Mar Chem* **165**: 36–45. doi: 10.1016/j.marchem.2014.07.005.

Copin-Montegut C. 1988. A new formula for the effect of temperature on the partial pressure of CO_2 in seawater. *Mar Chem* **25**(1): 29–37. doi: 10.1016/0304-4203(88)90012-6.

Cox GFN, Weeks WF. 1983. Equations for determining the gas and brine volumes in sea ice samples. *J Glaciol* **29**(102): 306–316.

Crabeck O, Delille B, Rysgaard S, Thomas DN, Geilfus N-X, et al. 2014a. First "in situ" determination of gas transport coefficients (DO_2, DAr, and DN_2) from bulk gas concentration measurements (O_2, N_2, Ar) in natural sea ice. *J Geophys Res-Oceans* **119**(10): 6655–6668: doi: 10.1002/2014JC009849.

Crabeck O, Delille B, Thomas DN, Geilfus N-X, Rysgaard S, et al. 2014b. CO_2 and CH_4 in sea ice from a subarctic fjord under influence of riverine input. *Biogeosciences* **11**(23): 6525–6538: doi: 10.5194/bg-11-6525-2014.

Crabeck O, Galley RJ, Delille B, Else BGT, Geilfus N-X, et al. 2016. Imaging air volume fraction in sea ice using non-destructive X-ray tomography. *The Cryosphere* **10**(3): 1125–1145: doi: 10.5194/tc-10-1125-2016.

Cross JN, Mathis JT, Frey KE, Cosca CE, Danielson SL, et al. 2014. Annual sea-air CO_2 fluxes in the Bering Sea: Insights from new autumn and winter observations of a seasonally ice-covered continental shelf. *J Geophys Res-Oceans* **119**(10): 6693–6708: doi: 10.1002/2013JC009579.

Crusius J, Wanninkhof R. 2003. Gas transfer velocities measured at low wind speed over a lake. *Limnol Oceanogr* **48**(3): 1010–1017: doi: 10.4319/lo.2003.48.3.1010.

Delille B, Jourdain B, Borges A V, Tison J, Delille D. 2007. Biogas (CO_2, O_2, dimethylsulfide) dynamics in spring Antarctic fast ice. *Limnol Oceanogr* **52**(4): 1367.

Delille B, Vancoppenolle M, Geilfus N-X, Tilbrook B, Lannuzel D, et al. 2014. Southern Ocean CO_2 sink: The contribution of the sea ice. *J Geophys Res-Oceans* **119**(9): 6340–6355: doi: 10.1002/2014JC009941.

Dickson AG, Goyet C. 1994. *Handbook of Methods for the Analysis of the Various Parameters of the Carbon Dioxide System in Sea Water*. Oak Ridge, TN. doi: 10.2172/10107773.

Dickson AG, Millero FJ. 1987. A comparison of the equilibrium constants for the dissociation of carbonic acid in seawater media. *Deep-Sea Res* **34**(10): 1733–1743.

Dieckmann GS, Nehrke G, Papadimitriou S, Göttlicher J, Steininger R, et al. 2008. Calcium carbonate as ikaite crystals in Antarctic sea ice. *Geophys Res Lett* **35**(8): L08501. doi: 10.1029/2008GL033540.

Fransson A, Chierici M, Yager PL, Smith WO. 2011. Antarctic sea ice carbon dioxide system and controls. *J Geophys Res-Oceans* **116**(C12).

Geilfus N-X, Carnat G, Dieckmann GS, Halden N, Nehrke G, et al. 2013. First estimates of the contribution of $CaCO_3$ precipitation to the release of CO_2 to the atmosphere during young sea ice growth. *J Geophys Res-Oceans* **118**(1): 244–255.

Geilfus N-X, Carnat G, Papakyriakou T, Tison J, Else B, et al. 2012a. Dynamics of pCO_2 and related air-ice CO_2 fluxes in the Arctic coastal zone (Amundsen Gulf, Beaufort Sea). *J Geophys Res-Oceans* **117**(C9).

Geilfus N-X, Delille B, Verbeke V, Tison J-L. 2012b. Towards a method for high vertical resolution measurements of the partial pressure of CO_2 within bulk sea ice. *J Glaciol* **58**(208): 287–300.

Geilfus N-X, Galley RJ, Crabeck O, Papakyriakou T, Landy J, et al. 2015. Inorganic carbon dynamics of melt pond-covered first year sea ice in the Canadian Arctic. *Biogeosciences Discussions* **11**(5): 7485–7519. doi: 10.5194/bgd-11-7485-2014.

Gleitz M, Thomas DN, Dieckmann GS, Millero FJ. 1995. Comparison of summer and winter inorganic carbon, oxygen and nutrient concentrations in Antarctic sea ice brine. *Mar Chem* **51**(2): 81–91.

Golden KM, Ackley SF, Lytle VI. 1998. The percolation phase transition in sea ice. *Science* **282**(5397): 2238–2241.

Gosink TA, Pearson J, Kelley JJ. 1976. Gas movement through sea ice. *Nature* **263**(5572): 41–42.

Gran G. 1952. Determination of the equivalence point in potentiometric titrations. Part II. *Analyst* **77**(920): 661–671.

Griewank PJ, Notz D. 2013. Insights into brine dynamics and sea ice desalination from a 1-D model study of gravity drainage. *J Geophys Res-Oceans* **118**(7): 3370–3386. doi: 10.1002/jgrc.20247.

Hunke EC, Notz D, Turner AK, Vancoppenolle M. 2011. The multiphase physics of sea ice: A review for model developers. *The Cryosphere* **5**(4): 989–1009.

IPCC. 2013. *Climate Change 2013: The Physical Science Basis. Contribution of Working Group I to the Fifth Assessment Report of the Intergovernmental Panel on Climate Change*. Cambridge University Press, NY, USA. 1535 pp: doi: 10.1017/CBO9781107415324.

Killawee JA, Fairchild IJ, Tison J-L, Janssens L, Lorrain R. 1998. Segregation of solutes and gases in experimental freezing of dilute solutions: Implications for natural glacial systems. *Geochim Cosmochim Ac* **62**(23): 3637–3655.

Lewis E, Wallace D. 1998. Program developed for CO_2 system calculations. *ORNL/CDIAC-105*. Oak Ridge, Tennessee. pp. 1–21.

Light B, Maykut GA, Grenfell TC. 2003. Effects of temperature on the microstructure of first-year Arctic sea ice. *J Geophys Res* **108**(C2): 3051. doi: 10.1029/2001JC000887.

Liss PS, Merlivat L. 1986. Air-sea gas exchange rates: Introduction and synthesis. *The role of air-sea exchange in geochemical cycling*. Springer. pp. 113–127.

Liss PS, Slater PG. 1974. Flux of gases across the air-sea interface. *Nature* **247**(5438): 181–184: doi: 10.1038/247181a0.

Loose B, Schlosser P, Perovich D, Ringelberg D, Ho DT, et al. 2011. Gas diffusion through columnar laboratory sea ice: Implications for mixed layer ventilation of CO_2 in the seasonal ice zone. *Tellus B* **63**(1): 23–39.

Marion GM. 2001. Carbonate mineral solubility at low temperatures in the Na-K-Mg-Ca-H-Cl-SO_4-OH-HCO_3-CO_3-CO_2-H_2O system. *Geochim Cosmochim Ac* **65**(12): 1883–1896.

Mehrbach C. 1973. Measurement of the apparent dissociation constants of carbonic acid in seawater at atmospheric pressure. *Limnol Oceanogr* **18**(6): 897–907.

Miller LA, Carnat G, Else BGT, Sutherland N, Papakyriakou TN. 2011a. Carbonate system evolution at the Arctic Ocean surface during autumn freeze-up. *J Geophys Res-Oceans* **116**(C9).

Miller LA, Papakyriakou TN, Collins RE, Deming JW, Ehn JK, et al. 2011b. Carbon dynamics in sea ice: A winter flux time series. *J Geophys Res-Oceans* **116**(C2).

Mock T. 2002. In situ primary production in young Antarctic sea ice. *Hydrobiologia* **470**(1–3): 127–132.

Moreau S, Vancoppenolle M, Delille B, Tison J-L, Zhou J, et al. 2015. Drivers of inorganic carbon dynamics in first-year sea ice : A model study. *J Geophys Res-Oceans* **120**(1): 471–495. doi: 10.1002/2014JC010388.

Moreau S, Vancoppenolle M, Zhou J, Tison J-L, Delille B, et al. 2014. Modelling argon dynamics in first-year sea ice. *Ocean Modelling* **73**: 1–18.

Nomura D, Eicken H, Gradinger R Shirasawa K. 2010a. Rapid physically driven inversion of the air–sea ice CO_2 flux in the seasonal landfast ice off Barrow, Alaska after onset of surface melt. *Cont Shelf Res* **30**(19): 1998–2004.

Nomura D, Inoue HY, Toyota T. 2006. The effect of sea ice growth on air–sea CO_2 flux in a tank experiment. *Tellus B* **58**(5): 418–426.

Nomura D, Inoue HY, Toyota T Shirasawa K. 2010b. Effects of snow, snowmelting and refreezing processes on air-sea-ice CO_2 flux. *J Glaciol* **56**(196): 262–270: doi: 10.3189/002214310791968548.

Notz D, Worster MG. 2009. Desalination processes of sea ice revisited. *J Geophys Res-Oceans* **114**(C5).

Papadimitriou S, Kennedy H, Kattner G, Dieckmann GS, Thomas DN. 2004. Experimental evidence for carbonate precipitation and CO_2 degassing during sea ice formation. *Geochim Cosmochim Ac* **68**(8): 1749–1761.

Papadimitriou S, Kennedy H, Kennedy P, Thomas DN. 2013. Ikaite solubility in seawater-derived brines at 1atm and sub-zero temperatures to 265K. *Geochim Cosmochim Ac* **109**: 241–253. doi: 10.1016/j.gca.2013.01.044.

Papadimitriou S, Kennedy H, Kennedy P Thomas DN. 2014. Kinetics of ikaite precipitation and dissolution in seawater-derived brines at sub-zero temperatures to 265K. *Geochim Cosmochim Ac* **140**: 199–211. doi: 10.1016/j.gca.2014.05.031.

Rees Jones DW, Worster MG. 2014. A physically based parameterization of gravity drainage for sea-ice modeling. *J Geophys Res-Oceans* **119**(9): 5599–5621. doi: 10.1002/2013JC009296.

Rysgaard S, Bendtsen J, Delille B, Dieckmann GS, Glud RN, et al. 2011. Sea ice contribution to the air–sea CO_2 exchange in the Arctic and Southern Oceans. *Tellus B* **63**(5): 823–830.

Rysgaard S, Glud RN. 2004. Anaerobic N_2 production in Arctic sea ice. *Limnol Oceanogr* **49**(1): 86–94. doi: 10.4319/lo.2004.49.1.0086.

Rysgaard S, Søgaard DH, Cooper M, Pucko M, Lennert K, et al. 2013. Ikaite crystal distribution in winter sea ice and implications for CO_2 system dynamics. *Cryosphere* **7**(2): 707–718.

Rysgaard S, Wang F, Galley RJ, Grimm R, Notz D, et al. 2014. Temporal dynamics of ikaite in experimental sea ice. *The Cryosphere* **8**(4): 1469–1478. doi: 10.5194/tc-8-1469-2014.

Sarmiento JL, Gruber N. 2004. *Ocean Biogeochemical Dynamics*. Princeton University Press.

Semiletov I, Makshtas A, Akasofu S, Andreas EL. 2004. Atmospheric CO_2 balance: The role of Arctic sea ice. *Geophys Res Lett* **31**(5): doi: 10.1029/2003GL017996.

Shaw MD, Carpenter LJ, Baeza-Romero MT, Jackson AV. 2011. Thermal evolution of diffusive transport of atmospheric halocarbons through artificial sea–ice. *Atmos Environ* **45**(35): 6393–6402. doi: 10.1016/j.atmosenv.2011.08.023.

Tison J-L, Haas C, Gowing MM, Sleewaegen S, Bernard A. 2002. Tank study of physico-chemical controls on gas content and composition during growth of young sea ice. *J Glaciol* **48**(161): 177–191.

Tsurikov VL. 1979. The formation and composition of the gas content of sea ice. *J Glaciol* **22**(86): 67–81.

Turner AK, Hunke EC, Bitz CM. 2013. Two modes of sea-ice gravity drainage: A parameterization for large-scale modeling. *J Geophys Res-Oceans* **118**(5): 2279–2294. doi: 10.1002/jgrc.20171.

Vancoppenolle M, Goosse H, De Montety A, Fichefet T, Tremblay B, et al. 2010. Modeling brine and nutrient dynamics in Antarctic sea ice: The case of dissolved silica. *J Geophys Res-Oceans* **115**(2). 1–18: doi: 10.1029/2009JC005369.

Vancoppenolle M, Notz D, Vivier F, Tison J, Delille B, et al. 2013. Technical Note: On the use of the mushy-layer Rayleigh number for the interpretation of sea-ice-core data. *The Cryosphere Discussions* **7**(4): 3209–3230.

Wanninkhof R. 1992. Relationship between wind speed and gas exchange over the ocean. *J Geophys Res-Oceans* **97**(C5): 7373–7382.

Weiss RF. 1974. Carbon dioxide in water and seawater: The solubility of a non-ideal gas. *Mar Chem* **2**(3): 203–215.

Zhou J, Delille B, Brabant F, Tison J-L. 2014a. Insights into oxygen transport and net community production in sea ice from oxygen, nitrogen and argon concentrations. *Biogeosciences Discussions* **11**(2): 2045–2081.

Zhou J, Delille B, Eicken H, Vancoppenolle M, Brabant F, et al. 2013. Physical and biogeochemical properties in landfast sea ice (Barrow, Alaska): Insights on brine and gas dynamics across seasons. *J Geophys Res-Oceans* **118**(6): 3172–3189.

Zhou J, Delille B, Kaartokallio H, Kattner G, Kuosa H, et al. 2014b. Physical and bacterial controls on inorganic nutrients and dissolved organic carbon during a sea ice growth and decay experiment. *Mar Chem* **166**: 59–69.

Contributions

- Lead of the INTERICE V experiment: DT
- Contributed to planning and experimental design: DT, GD, K-UE, J-LT, BD
- Contributed to carry out the experiment and acquisition of data: JZ, GD, K-UE, DT, J-LT, BD
- Contributed to analysis and interpretation of data: MK, SM, JZ, FVdL, J-LT, BD, MV
- Contributed to the model simulations and interpretation: SM, MV
- MK wrote the paper, with the help of SM, JZ, BD, MV and comments and inputs from all coauthors.

Acknowledgments

The authors would like to thank the Hamburg Ship Model Basin (HSVA), and the ice tank crew, for the hospitality, technical and scientific support and the professional execution of the test program in the Research Infrastructure ARCTICLAB. We are grateful to Michael Fischer for his help with the deployment of the automated chambers and treatment of flux data, to Nicolas-Xavier Geilfus, one anonymous reviewer, the Editor Jody Deming and the associate editor for their comments that improve the overall quality of the manuscript.

Funding information

This study was supported by the European Community's 7th Framework Programme through the grant to the budget of the Integrated Infrastructure Initiative HYDRALAB-IV, Contract no. 261520. The work was supported by a FiDiPro award by the Academy of Finland, the Walter and Andree Nottbeck Foundation, and the BIGSOUTH project funded by the Belgian Science Federal Policy Office. MK and JZ, SM and BD are respectively research fellows, postdoctoral researcher and research associate of the Fonds de la Recherche Scientique – FNRS. MV acknowledges support from the EU, through BISICLO (FP7 CIG grant no 321938). This is a MARE contribution.

Competing interests

The authors have declared that no competing interests exist.

Data accessibility statement

The observation data and the model code will be made available to any scientist upon request and which is encouraged in order to reproduce the computations and test the model results in other locations (contacts: marie.kotovitch@ulg.ac.be, s.moreau@uclouvain.be and bruno.delille@ulg.ac.be).

Appendix B: Physical and biological properties of early winter Antarctic sea ice in the Ross Sea

Annals of Glaciology

Paper

Cite this article: Tison J-L et al. (2020). Physical and biological properties of early winter Antarctic sea ice in the Ross Sea. *Annals of Glaciology* 1–19. https://doi.org/10.1017/aog.2020.43

Received: 16 December 2019
Revised: 16 May 2020
Accepted: 18 May 2020

Key words:
Antarctic glaciology; biogeochemistry; sea ice

Author for correspondence:
Jean-Louis Tison,
E-mail: Jean-Louis.Tison@ulb.be

cambridge.org/aog

Physical and biological properties of early winter Antarctic sea ice in the Ross Sea

Jean-Louis Tison[1], Ted Maksym[2], Alexander D. Fraser[3,4], Matthew Corkill[3,4], Noriaki Kimura[5], Yuichi Nosaka[6], Daiki Nomura[7,8,9], Martin Vancoppenolle[10], Steve Ackley[11], Sharon Stammerjohn[12], Sarah Wauthy[1], Fanny Van der Linden[1,13], Gauthier Carnat[1], Célia Sapart[1], Jeroen de Jong[1], François Fripiat[1] and Bruno Delille[13]

[1]PROPICE Unit, Laboratoire de Glaciologie, Université Libre de Bruxelles, Bruxelles, Belgium; [2]Department of Applied Ocean Physics and Engineering, Woods Hole Oceanographic Institution, Woods Hole, USA; [3]Institute for Marine and Antarctic Studies, University of Tasmania, Hobart, Tasmania, Australia; [4]Antarctic Climate and Ecosystems Cooperative Research Centre, University of Tasmania, Hobart, Tasmania, Australia; [5]Atmosphere and Ocean Research Institute, University of Tokyo, Tokyo, Japan; [6]School of Biological Sciences, Tokai University, Tokyo, Japan; [7]Faculty of Fisheries Sciences, Hokkaido University, Hakodate, Japan; [8]Arctic Research Center, Hokkaido University, Sapporo, Japan; [9]Global Station for Arctic Research, Global Institution for Collaborative Research and Education, Hokkaido University, Sapporo, Japan; [10]Laboratoire d'Océanographie et du Climat, Institut Pierre-Simon Laplace, Paris, France; [11]Department of Geological Sciences, University of Texas at San Antonio, San Antonio, USA; [12]Institute of Arctic and Alpine Research, University of Colorado, Boulder, USA and [13]Unité d'Océanographie Chimique, Freshwater and Oceanic sCience Unit reSearch (FOCUS), Université de Liège, Liège, Belgium

Abstract

This work presents the results of physical and biological investigations at 27 biogeochemical stations of early winter sea ice in the Ross Sea during the 2017 PIPERS cruise. Only two similar cruises occurred in the past, in 1995 and 1998. The year 2017 was a specific year, in that ice growth in the Central Ross Sea was considerably delayed, compared to previous years. These conditions resulted in lower ice thicknesses and Chl-*a* burdens, as compared to those observed during the previous cruises. It also resulted in a different structure of the sympagic algal community, unusually dominated by *Phaeocystis* rather than diatoms. Compared to autumn-winter sea ice in the Weddell Sea (AWECS cruise), the 2017 Ross Sea pack ice displayed similar thickness distribution, but much lower snow cover and therefore nearly no flooding conditions. It is shown that contrasted dynamics of autumnal-winter sea-ice growth between the Weddell Sea and the Ross Sea impacted the development of the sympagic community. Mean/median ice Chl-*a* concentrations were 3–5 times lower at PIPERS, and the community status there appeared to be more mature (decaying?), based on Phaeopigments/Chl-*a* ratios. These contrasts are discussed in the light of temporal and spatial differences between the two cruises.

Introduction

Sea ice plays a major role in the Earth System: It greatly increases the albedo of the ice-free open ocean (e.g. Perovich, 1996), it is an important driver of global oceanic circulation through bottom water formation (e.g.Williams and others, 2008; Oshima and others, 2013), and it acts as a dynamic biogeochemical reactor at the interface between the ocean and the atmosphere (e.g. Tison and others, 2017*a*). Sea ice hosts microbial communities throughout the year and actively or passively controls gas, energy and matter exchanges between the ocean and the atmosphere (e.g. Arrigo and Thomas, 2004; Arrigo and others, 2010; Dieckmann and Hellmer, 2010; Rysgaard and others, 2011; Zhou and others, 2013, 2014; Delille and others, 2014). It also plays a major ecological role in the polar ocean systems (e.g. Bluhm and others, 2010; Leu and others, 2011; Flores and others, 2012).

Major changes are clearly occurring in the Arctic sea-ice system, with an indisputable trend of reduced ice cover, both at minimum and maximum extent (IPCC and others, 2013; IPCC, 2019). Antarctica, on the contrary, and in contradiction with global climate model outputs, showed a slight increase in circumpolar averaged extent for most of the last four decades (since satellite observations consistently began in the late 1970s). This circumpolar increase masks large regional contrasts however, with longer sea-ice seasons in the Weddell and Ross Seas and shorter sea-ice seasons in the Bellingshausen-Amundsen Seas and in the Amery Ice Shelf sector (Stammerjohn and others, 2008). There has been however a marked change toward record low circumpolar sea ice since late 2016 (Parkinson, 2019).

Global biogeochemical models have been developed only relatively recently, and are still in need of fully incorporating the processes at work in sea ice. This is particularly true for winter processes, given the relative scarcity of observations during that period, especially in the Antarctic. A better knowledge of winter sea-ice behavior is however also crucial to yearly budgeting exchange processes between the ocean and the atmosphere in polar regions, and in understanding their trends in a changing climate.

In a recent publication, Tison and others (2017*b*) presented the physical and biological properties of winter pack ice in the Weddell Sea during the AWECS (Antarctic Winter Climate Ecosystem Study) 2013 cruise. This was the most recent of only three winter sea-ice studies in the Central Weddell Sea (1986, 1992 and 2013). The winter 2013 showed a relatively warm sea-ice cover, due to the combined effect of a deep snow cover and warm cyclone events progressing southward from the open Southern Ocean. This resulted in high ice permeability and frequent formation of 'brine tubes' from cyclic events of brine movements within the sea-ice cover and the consequent development of an internal microbial community, evidenced by relatively high Chl-*a* concentrations. The authors also showed that large-scale sea-ice model simulations suggest a trend of deeper snow, warmer ice and larger brine volume fractions across the three observational years.

In this paper, we present results from the Polynyas, Ice Production and seasonal Evolution in the Ross Sea (PIPERS) cruise, devoted to the space/time evolution of air–ice–ocean interactions during autumn and early winter 2017 in the Ross Sea. The cruise documented a full set of physical and biogeochemical properties of the whole atmosphere–sea-ice–ocean system, with a specific focus on the Terra Nova Bay and Ross Sea Polynyas (TNBP and RSP). Here we will focus on the basic physical and biological properties of the sea-ice cover in the context of a delayed autumn sea-ice advance, in line with the recent decrease in Antarctic sea-ice extent that started late 2016 (Turner and others, 2017; Parkinson, 2019), and see how it might have affected the sea-ice biogeochemistry. Physical data are presented in order to document the specific environmental constrains for the biological components of the ecosystem.

Field work and analytical methods

The PIPERS cruise

The PIPERS cruise sampled the Ross Sea pack ice between 19 April 2017 (Julian Day 109) and 4 June 2017 (Julian Day 155) (Fig. 1, see Ackley and others (2020) in this volume for an overview of the cruise). A total of 27 biogeochemistry sites were occupied. The aim was to gather a suite of physical and biogeochemical parameters in order to decipher winter sea-ice biogeochemical dynamics and the control it potentially exerts on exchanges across the atmosphere–ice–ocean interfaces. Although the initial goal was to sample both the TNBP and the RSP as well as the main pack, unfortunately biogeochemical stations could not be conducted in the RSP for logistical reasons. It was however possible to document the sea-ice cover of the Western Ross Sea on its southbound leg to Terra Nova Bay (TNB, ice stations 1–5) and the sea-ice cover of the Central Ross Sea (CRS) on its northbound leg from the Ross Sea Polynya (ice stations 18–24). Six main groups of stations will therefore be discussed: the marginal ice zone on the way in (MIZ-in, stations 1–3), the transit to TNBP (Transit TNBP, stations 4 and 5), the TNBP (stations 6–16), the transit to the RSP (Transit RSP, station 17), the CRS (stations 18–25) and the marginal ice zone on the way out (MIZ-out, stations 26–27). Sea-ice sampling was also performed at additional stations for physical properties only. These will only be used briefly here to assess the representativeness of the biogeochemical stations and discussed in detail elsewhere.

Field work

At each of the biogeochemical stations (BGC, stations 1–27), we attempted to collect the full set of physical and biogeochemical parameters. For safety reasons however, especially in the TNBP, with its dynamic ice cover of thin ice pancakes, sampling could only be done from man-basket or zodiac, reducing the sampling time to less than an hour. At those stations, only a limited number of sea-ice samples could be collected, reducing the breadth of variables measured. Otherwise, the sampling procedure was similar to the one applied during the 2013 AWECS cruise in the Weddell Sea (Tison and others, 2017*b*). It is briefly summarized here below.

Once the ice floe had been selected and the ship anchored to it, a trace metal clean biogeochemical 10 × 10 m sampling site was chosen and flagged. Access was only permitted to operators wearing clean suits to prevent contamination (Lannuzel and others, 2006). Snow samples were first collected in the central part of the restricted area. Then, a first core was drilled and its vertical temperature profile was measured. The core was then immediately placed into a plastic bag and stored with −30°C cooling bags within a core storage box, to prevent brine drainage and limit microbial activity. The core was later cut into 0.05 m thick sections for bulk ice salinity measurements onboard the ship. A set of 12 supplementary ice cores were collected at a maximum spatial spacing of ~0.20 m to limit the effects of spatial differences. These cores were dedicated to a whole suite of biogeochemical measurements (nutrients, POC, DOC, PON, DON, gases, texture, fabrics, etc.) either on-board the ship or later in the laboratory. Cores were stored and transported below −25°C and in the dark at all times. Most of the cores were retrieved using 0.10 or 0.14 m electropolished stainless steel core barrels. For thin ice stations (below 15–20 cm), cutting of sea-ice blocks was preferred, using a non-contaminating curved hand-saw.

The drill hole of the temperature/salinity core was used to sample sea water at various depths, and brine 'sackholes' (incomplete ice core holes reaching a specific depth into sea ice) were drilled to collect the brine. Finally, gas fluxes (CO_2, N_2O) were measured at the surface of the ice and at the surface of the snow using the 'chamber' technique (Tison and others, 2017*a*).

Only the basic physical (texture, temperature, bulk ice salinity, brine salinity, brine volume, Rayleigh numbers, brine upward velocities) and biological (Chl-*a*, Phaeopigments) properties will be discussed in this paper.

Direct measurements

Ice temperature measurements were performed using a calibrated probe (Testo 720). The probe was inserted into holes matching the diameter of the probe, drilled perpendicular to the ice core axis or to the ice block surface, with a depth resolution of 0.02–0.05 m. Precision of the probe was ±0.1°C. As recommended by Pringle and Ingham (2009), temperature measurements were completed within 5 min after ice core extraction.

Bulk ice salinity was measured at a depth resolution of 0.02–0.05 cm, on melted ice samples at room temperature, using a portable electrical conductivity meter (Orion Star Series meter WP-84TP, calibrated before and after the cruise). Cores were cut horizontally such that samples were centered on the depths of the discrete temperature measurements. To improve the accuracy of the measurements (<±0.1), the same samples were re-measured in Europe on a Guildline Autosal Salinometer 8400, B calibrated with IAPSO standard sea water (precision better than 0.002 psu). A calibration curve was then established to correct the conductimeter salinities according to salinometer salinities. The latter are used here.

Ice thin sections (~600 µm thick) were produced following the standard procedure of Langway (1958), using a microtome (Leica SM2400). The sections were examined and photographed between crossed polarizers on a universal stage system.

Chl-a and Phaeopigments were measured on a dedicated ice core or ice block, cut at a 0.05–0.10 m vertical resolution. Samples were melted in 0.2 µm filtered sea water (1:4 volume ratio) to avoid osmotic stress, in the dark. Melted samples were

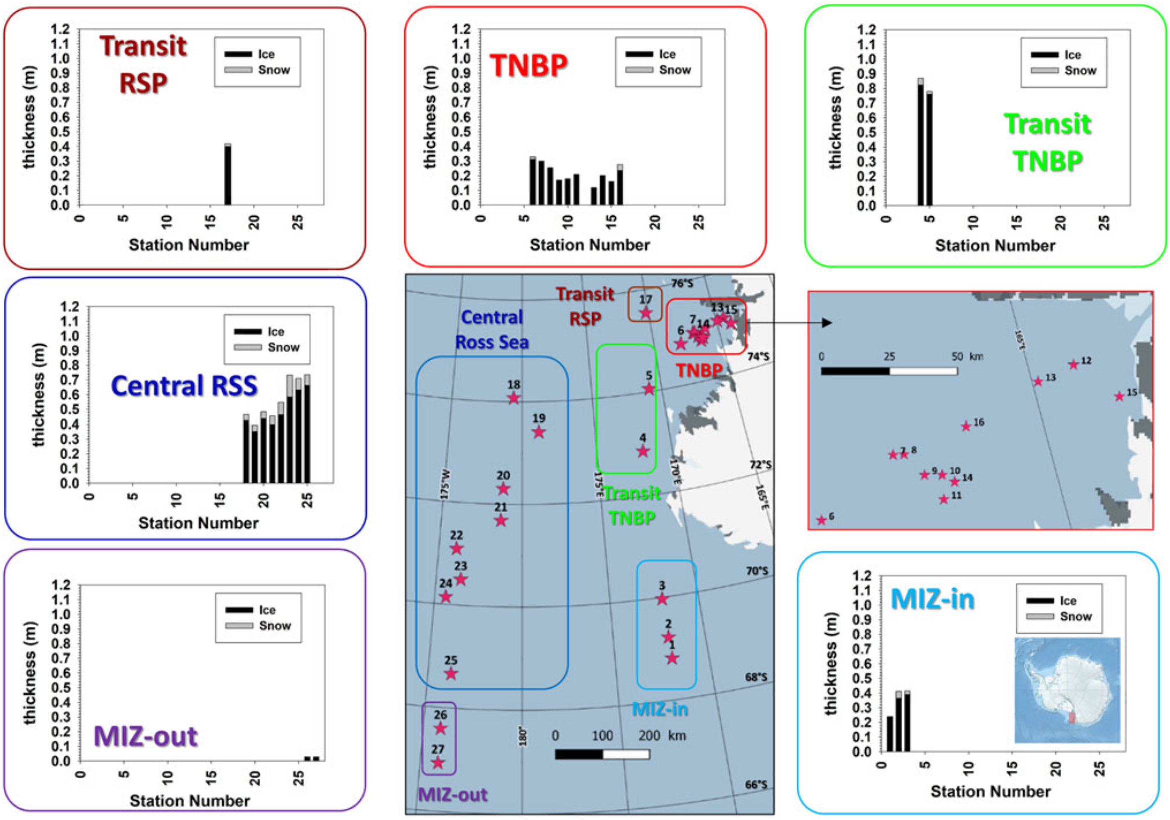

Fig. 1. Location of the 27 PIPERS biogeochemical stations, and mean ice (black) and snow (grey) thicknesses for the major groups of stations. The global area of investigations is shown as a red rectangle on the Antarctic map of the lower-right insert. The Terra Nova Bay area is enlarged at the black arrow.

size fractionated by filtering on 10 then 0.8 µm polycarbonate filters. This allows differentiation of larger microalgae species from the smaller ones. Filters were analyzed by fluorometry, according to standard protocols (Arar and Collins, 1997).

Species cell counting for ice algae community assemblages was performed at specific stations, at a 10–20 cm resolution, on Lugol-preserved samples. Identification of ice algae was determined following Thomas (1997) and Scott and Marchant (2005). The sample was concentrated using a sedimentation tube. Cell counting was performed using a microscope (Olympus, IMT-2, Tokyo, Japan) with 10× oculars and 40× objective. For each sample, three countings were done, and, for each counting, 100 µL of the sample was placed on a counting plate (50 µm slits). Results are given as average ±1 std dev. ($n = 3$).

Data processing

Based on ice temperature (T) and bulk ice salinity (S) measurements, a series of descriptors of phase composition and of fluid transport through sea ice were derived.

The *phase composition properties*, namely brine salinity (S_{br}) and brine mass fraction (Φ), as well as the sea-water freezing point were derived from the $T - S$ data, using the FREZCHEM phase diagram equations (Vancoppenolle and others, 2018), based on the resolution of the Gibbs–Pitzer equations for standard sea water (Marion and others, 2010). As demonstrated in Vancoppenolle and others (2018), brine mass fraction and brine volume fraction are quasi-linearly related and differ by a very small amount (<1% absolute difference and <10% of relative difference, in our natural sea-ice range). For coherence with previous studies, we are using the latter. Brine volume fraction controls permeability and therefore the mobility of biogeochemical compounds within sea ice and across its interfaces with the atmosphere and the ocean. For brine in columnar sea ice, it has been shown (Golden and others, 1998; Freitag, 1999; Eicken and others, 2004) that permeability increases by at least 1 order of magnitude above a relative brine volume of 5% (Golden and others, 1998). This threshold might be higher for gases in sea ice (7%, Zhou and others, 2013) or for brine in fine grained granular ice (10%, personal communication from Golden, 2016).

The *fluid transport properties* were calculated on a vertical grid composed of the midpoint of the core sections, and an extra point at the bottom of the ice core, required to have well-posed Rayleigh number and upwelling convective velocity calculations. The calculation nodes are labelled from top to bottom ($i = 1, \ldots, N + 1$). Observed temperatures were taken from the exact same core when possible (in the majority of the cases), or from the nearest core (typically <10 m distance) taken on the same day and at the sampling station. At the core bottom, S and T were not measured. There, S is assumed to be of 34 g kg^{-1}, representative of surface waters in the area, assuming continuity at the ice–ocean interface (Notz and Worster, 2009). Temperature at the base was considered to be at the freezing point T_{fr}, calculated with a salinity of 34 g kg^{-1}.

The porous-medium Rayleigh number (Ra, Notz and Worster, 2008), is here defined following Rees Jones and Worster (2014) and Thomas and others (2020):

$$\mathrm{Ra}(z) = \frac{cg\beta[S_{\mathrm{br}}(z) - S_{\mathrm{w}}]\bar{\Pi}}{k\nu}(h - z), \tag{1}$$

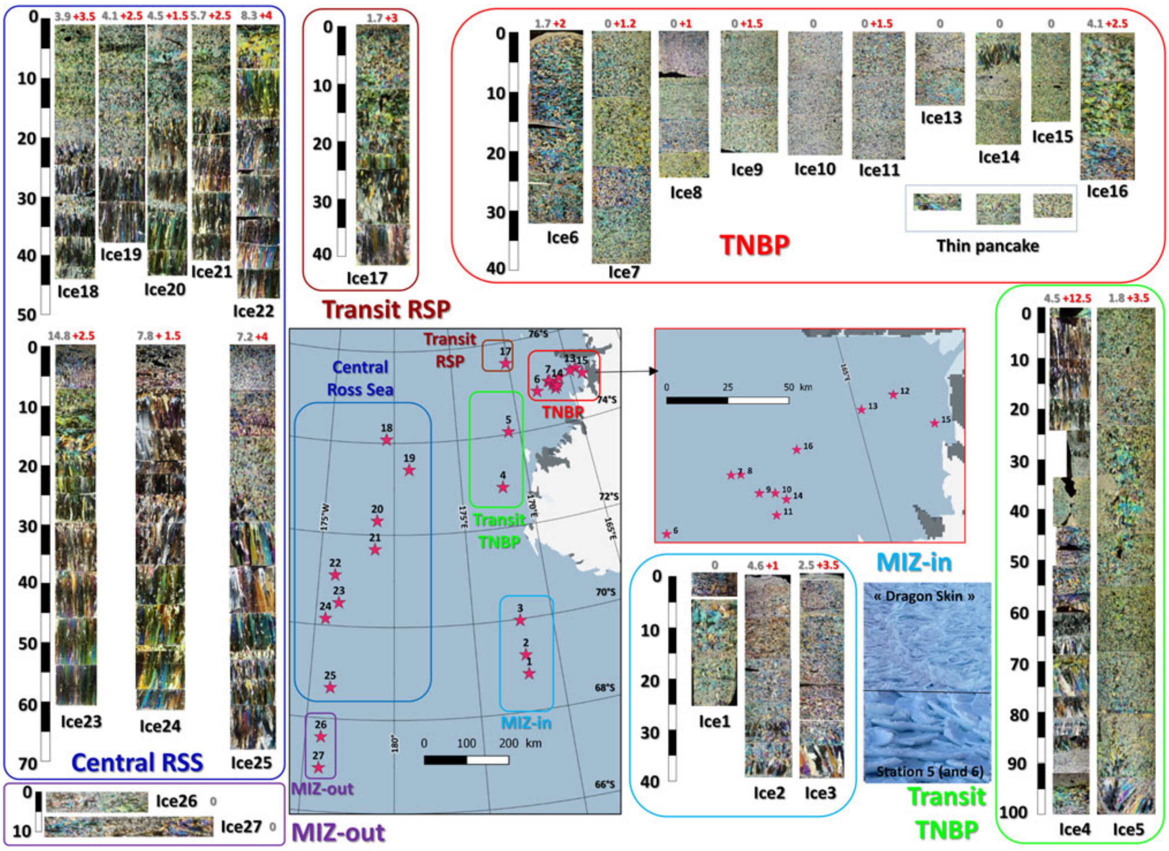

Fig. 2. Textural properties (ice types) at the 27 PIPERS biogeochemical stations, shown as vertical thin sections visualized under crossed polarizers. Surface properties of 'dragon skin', mainly seen at stations 5 and 6, are illustrated. Grey and red numbers on top of each core section are mean snow thickness (ten measurements) and freeboard in centimeters, respectively. Ice core numbering corresponds to the station numbering.

where z is the depth counted from the upper sea-ice surface and is positive downward, and h is the sea-ice thickness. S_w is the ocean salinity (34 g kg^{-1}, see above) and $\beta = 7.5 \times 10^{-4}$ kg g^{-1} is the saline density coefficient. $\bar{\Pi}$ is the effective permeability, taken as the harmonic mean of permeability from between depths z and h. Permeability is computed from the formulation of Freitag (1999). The formulation of Freitag (1999) for permeability was developed for young sea ice (<30 cm), and a more appropriate formula would be the one of Eicken and others (2004) derived from first-year ice at Barrow. However, we chose to compute permeability using the formulation of Freitag (1999) for consistency with the calculations of Thomas and others (2020). g is the acceleration due to gravity, whereas $c = 4 \times 10^6$ J m^{-3} K^{-1}, $k = 0.523$ W m^{-1} K^{-1}, and $\nu = 1.8 \times 10^{-6}$ m^{2}s^{-1} are reference values for the volumetric heat capacity, thermal conductivity and kinematic viscosity of brine, respectively.

Ra is often used as a proxy for gravity drainage (i.e. brine convection), which would initiate once Ra surpasses a critical threshold value (Notz and Worster, 2008). This threshold however is still not very well constrained (Notz and Worster, 2009; Hunke and others, 2011; Carnat and others, 2013), with values ranging from 2 to 10 and depending on many assumptions in the calculations. The interpretation can therefore still only be qualitative today, especially in the context of discrete measurements in time and space.

Upwelling convective velocity profiles were computed following methods elaborated in Thomas and others (2020) based on the concepts developed by Wells and others (2011), Griewank and Notz (2013) and Rees Jones and Worster (2014). The convective upwelling velocity, as introduced by Rees Jones and Worster (2014), informs on the theoretical intensity of the net salt loss (and of all other solutes). In this calculation, it is implicitly assumed that a convective circulation holds, made of a downwelling flow within infinitely narrow brine channels and an upwelling flow within the rest of porous ice.

The calculated convective upwelling velocity is from a recast version of the parameterization of Griewank and Notz (2013):

$$w = -\frac{\alpha}{\rho} \sum_{i=1}^{k} \max\{\mathrm{Ra}_i - \mathrm{Ra}_c, 0\} \Delta z_i, \tag{2}$$

where $\alpha = 6.67 \times 10^{-3}$ kg m^{-3}s^{-1} is the convection strength parameter, $\varrho_{br} = 1020$ kg m^{-3} is a reference brine density, Ra_i is the porous-medium Rayleigh number in the i^{th} layer, $\mathrm{Ra}_c = 2.4$ is a critical Rayleigh number, and Δz_i is the thickness of the i^{th} core section. Both α and Ra_c are parameters, tuned by Thomas and others (2020) within the exact same calculation framework, as to minimize the difference between simulated and observed salinity and rhodamine in artificially grown sea-ice experiments.

Crystal sizes have been estimated from detailed high-resolution thin-section photographs for the TNBP stations 6–16. At each station, a set of six lines were randomly chosen across the thin section, and individual crystals counted along each line. The length of the line is then divided by the number of crystals counted to give an estimate of individual crystal diameters. This method,

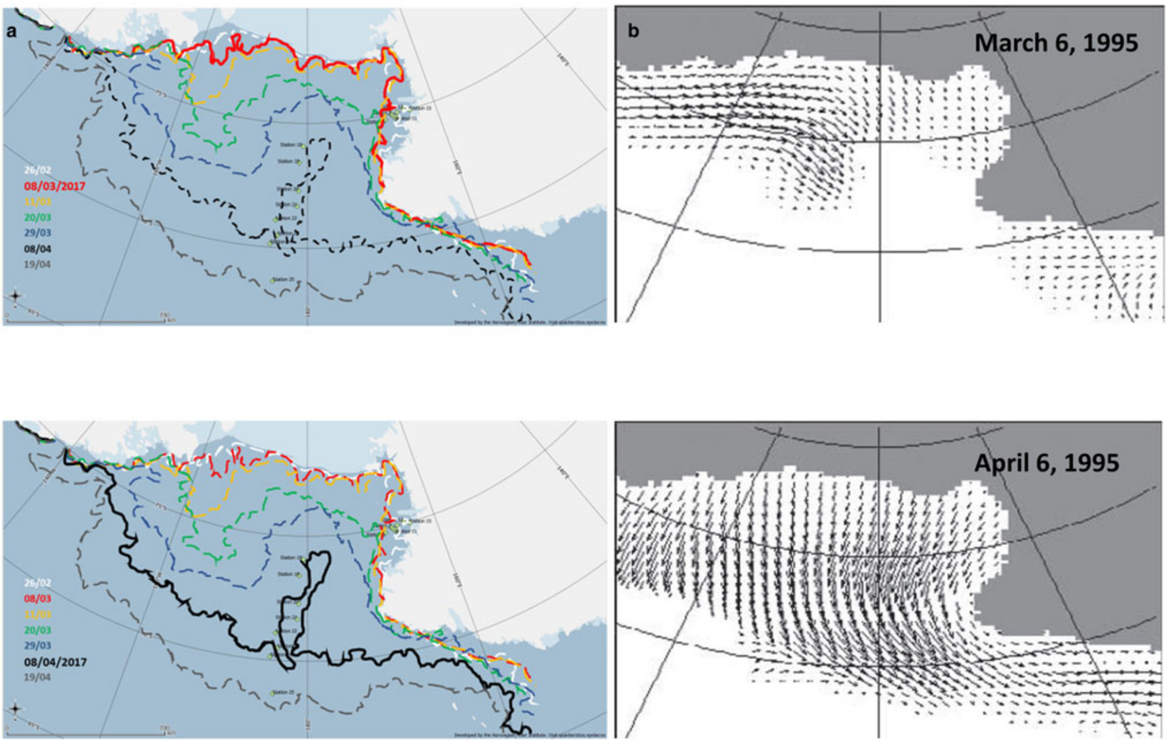

Fig. 3. (a) Reconstructed sea-ice margin at various dates in 2017 (red: 8 March; orange: 11 March; green: 20 March; blue: 29 March; black: 8 April and grey: 19 April), from high-resolution AMSR2 satellite imagery (Beitsch and others, 2014; Bremen, 2018); (b) arrows show fields of sea-ice movement for April–March 1995 from Arrigo and others (2003).

referred as the 'Linear intercept method', is of course semi-quantitative, due to the irregular shape of the crystals and the fact that they are rarely cross-cut along their mean dimension. Another indicator is also calculated, the 'equivalent disc area', which is the area of a circular disk of equivalent diameter.

To describe the peculiar evolution of the sea-ice cover on that year and understand stations locations in this context, *Ice margin tracking* was reconstructed from high-resolution AMSR2 imagery, using the approach of Beitsch and others (2014). Daily sea-ice concentration maps were retrieved from the open access server at the Universität Bremen (2018) from January to June 2017. These images were georeferenced and introduced into the Quantarctica GIS (Matsuoka and others, 2013). Comiso and others (2003) proposed the threshold of 10% sea-ice concentration as the limit between sea ice and open ocean. For readability reasons, we have kept the 10–20% interval to track the temporal evolution of the ice margin within Quantarctica.

Ice margin tracking integrates both dynamic (ice drift) and thermo-dynamic (ice growth) sea-ice processes, and does not allow reconstruction of specific growth history at a given station. To address this, we used *backward motion trajectories* to retrace the location of each sampled ice floe during PIPERS. Trajectories were calculated using a dataset of AMSR2 maximum cross correlation-derived sea-ice motion vectors (Kimura, 2004). We use the station location of each sampled floe as an end point for the backward trajectory calculation, which is advected with the nearest-neighbor velocity and run for up to 200 d. On occasion, to produce longer trajectories in the case of missing data, we substitute the mean velocity field of up to eight nearest neighbors. Back trajectories were truncated when they came within 60 km of the coastal mask due to coastal contamination of the underlying velocity dataset. Time series of sea-ice *divergence/convergence* at each station's location was also calculated from the sea-ice motion dataset. The discrete partial derivative of x and y velocities were added together to calculate the divergence, using the four nearest neighbors.

A suite of *drifting sea-ice buoys* was deployed at ice stations at the outflow of the TNBP and in the CRS on the transit out of the ice. Here, we show tracks for five GPS buoys that were deployed at, or very near to several of the biogeochemistry ice stations and survived for several months. Theses buoys were comprised of a NAL Research Corporation 9602-LP low-power Iridium satellite tracker with built-in GPS that reported position every 30 min. These were enclosed in a waterproof enclosure and fixed to the floe.

Results and discussion

Ice and snow thicknesses, freeboard, ice types and ice growth history

The mean ice thickness at the biogeochemical stations was 0.35 m. It was however biased toward low thicknesses due to the denser sampling in the TNBP (Fig. 1). Maximum ice thicknesses were encountered both in the northern CRS (up to 0.71 m at station 25) and on the Western Ross Sea continental shelf area (transit to TNB, 1.02 and 0.69 m at stations 4 and 5, respectively). Quite low snow thicknesses were observed overall at the biogeochemical stations, with a mean value of 0.04 m (Figs 1 and 2). The highest snow thicknesses (up to 0.15 m) were found on the thicker, older ice of the northern CRS.

Freeboards (red numbers in Fig. 2) were positive at all stations, with very rare evidence for previous flooding events, although some flooding was observed around ridged areas, not sampled for biogeochemistry. This observation is consistent with the

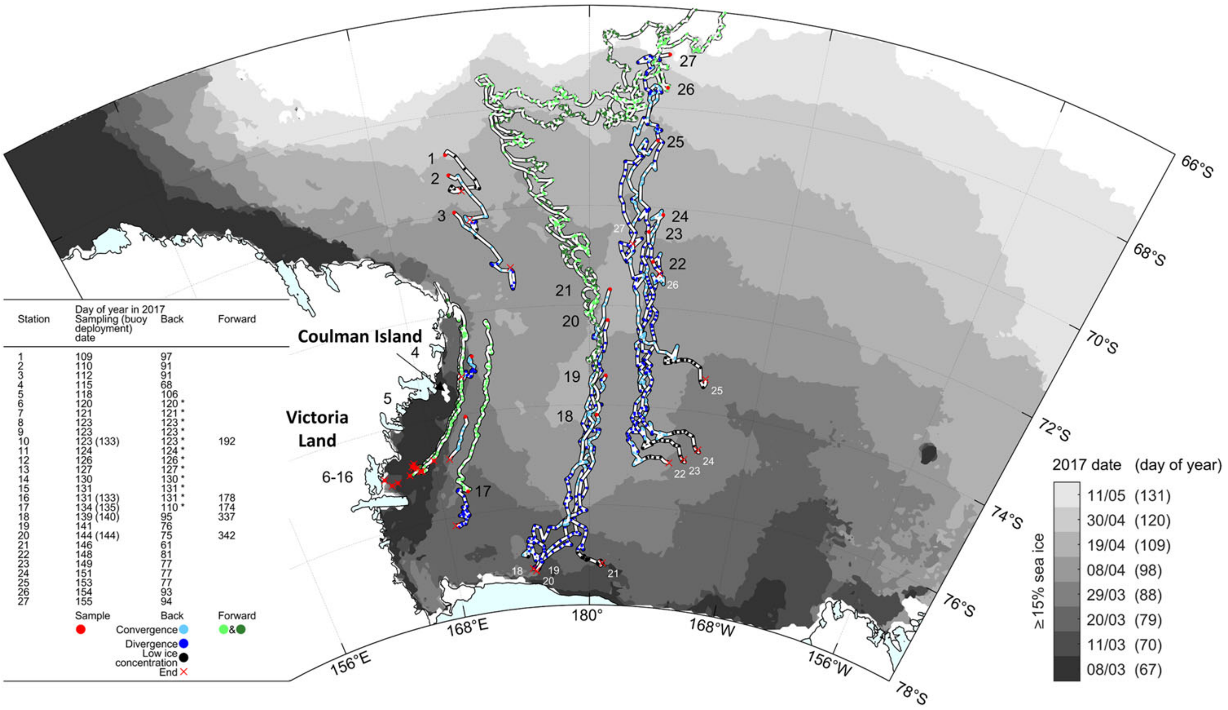

Station	Day of year in 2017 Sampling (buoy deployment) date	Back	Forward
1	109	97	
2	110	91	
3	112	91	
4	115	68	
5	118	106	
6	120	120 *	
7	121	121 *	
8	123	123 *	
9	123	123 *	
10	123 (133)	123 *	192
11	124	124 *	
12	126	126 *	
13	127	127 *	
14	130	130 *	
15	131	131 *	
16	131 (133)	131 *	178
17	134 (135)	110 *	174
18	139 (140)	95	337
19	141	76	
20	144 (144)	75	342
21	146	61	
22	148	81	
23	149	77	
24	151	77	
25	153	77	
26	154	93	
27	155	94	

Fig. 4. Calculated back trajectories (blue) and observed buoy trajectories ('Forward', green) for some of the 27 PIPERS stations (red dots). Back trajectories are shown with convergent (light blue) and divergent (dark blue) status. Each blue or green dot corresponds to a daily position, allowing semi-quantitative visual reconstruction of the velocity. Red crosses indicate the origin of the ice sampled at a given station (station number recalled in white in Central Ross Sea). Black dots indicate days where there was not enough data to calculate an 11 d-centered moving average for divergence/convergence due to low ice concentrations – '*' in the left table indicate stations for which back trajectories could not be fully reconstructed due to the proximity of the coast at early stages of growth (coastal contamination of the sea-ice velocity dataset). Light and dark green are used to decipher overlapping buoys trajectories. Some of the buoys were laid on the sea-ice cover at the biogeochemistry stations, others at locations nearby. Ice shelves are overlaid on the coastline in cyan (Rignot and others, 2013; Greene and others, 2017; Mouginot and others, 2017). Periodic sea-ice extents are indicated by filled greyscale contours (Spreen and others, 2008).

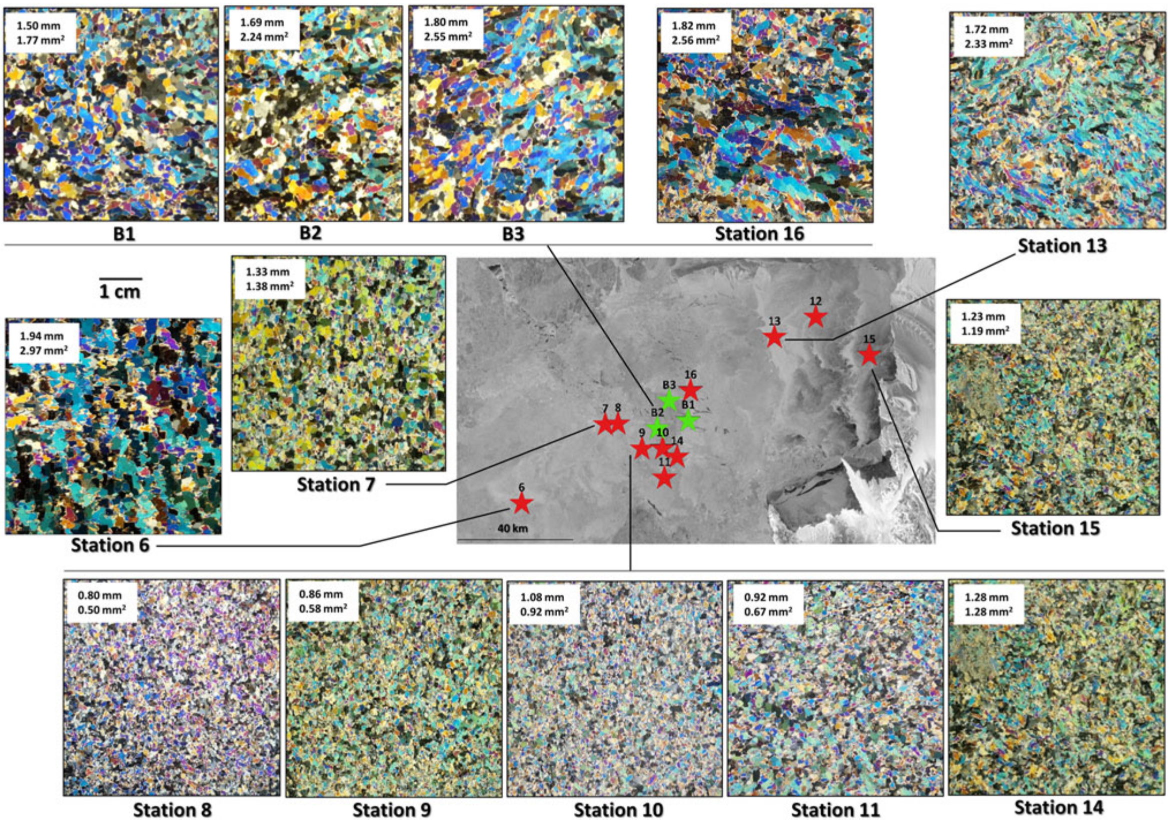

Fig. 5. Close up of textural properties of PIPERS Terra Nova Bay polynya biogeochemical stations 6–16. All pictures are illustrative vertical thin sections viewed under crossed polarizers, at the same scale. Numbers in the top left corner of each picture are respectively 'mean grain diameter' (top) and 'equivalent disk area'. The 'mean grain diameter' is obtained by the 'linear intercept method' and the 'equivalent disk surface' is the surface of a circular grain of equivalent diameter (see methods). Red stars are locations of biogeochemical stations and green stars are locations of complementary physics stations. No data are available for station 12. Satellite image is Terra SAR-X from DLR (German Aerospace Centre).

very small amounts of snow ice observed during the cruise, as discussed in more details in a companion paper.

Figure 2 shows a clear textural contrast between the marginal ice zone (MIZ) and the TNBP on the one hand, and the CRS and the continental shelf stations of the Western Ross Sea (transit to TNB) on the other hand. TNBP and the MIZ share a dominant granular ice texture (frazil), while the CRS is predominantly of columnar texture. A distinction can be made in the latter between the stations 18–22, showing decreasing granular ice contribution northwards, and a surprisingly constant thickness over nearly 4 degrees of latitude (70–74°S), and the thicker northerly stations 23–25, showing either a contribution from snow ice (23, 24) or increasing granular ice (25) at the top.

These characteristics of the CRS pack ice agree well with the peculiar sea-ice growth conditions of the autumn 2017. Indeed, Figure 3a shows the sea-ice margin at various dates in March/April 2017 (just before our access to the ice), from high-resolution AMSR2 satellite imagery (see methods). Figure 3b shows sea-ice motion vectors for April–March 1995, from a study of Arrigo and others (2003). Clearly, while the whole of the Ross Sea was already covered with sea ice on 6 April 1995, there is still open water present in the CRS on 8 April 2017 (black line). The area lies just north of Pennel Bank, a shelf break promontory, that protrudes northward of the mean east-west trending shelf break. Reports of very high ocean to ice heat fluxes, up to 35 Wm^2, in this area during the cruise (personal communication from T. Maksym), suggest that these might result from obstructions of the westward flowing slope current near the shelf break that may have caused local upwelling of warm Circumpolar Deep Water.

The Central Ross Sea

Figure 4, a plot of backward trajectories with divergence/convergence history at each station, together with selected observed (forward) buoy trajectories, on top of the same sea-ice margin evolution as in Figure 3, allows further interpretation of the history of the ice at each station. In the CRS, for stations 18–21, sea ice originates along the outflow of the RSP, at a similar distance from the ice-shelf front. The steadily decreasing lifetime from station 18 to 21 explains why these stations show an initial contribution of frazil accumulation from the RSP of decreasing proportion going north (Fig. 2). Advection of that ice over an area of very high ocean–ice heat fluxes would have retarded further basal growth and maintained a relatively constant ice thickness (~0.4 m).

Over that part of the cruise track, the sea-ice cover was very uniform, with few indications of dynamical thickening. This is consistent with the predominance of divergent flow conditions (i.e. unfavorable conditions for ridging or rafting, dark blue dots, Fig. 4). The same holds for the ice cover at station 17, situated in the outflow of the McMurdo Sound polynya. The ice cover at stations 22–24 originated further to the north and shows a lower (and relatively constant) frazil/granular ice layer at the top. Their trajectory is also located East of the remnant open water area (that was initially observed in the CRS; cf. Figs 3 and 4), suggesting that the ice cover might have been somewhat

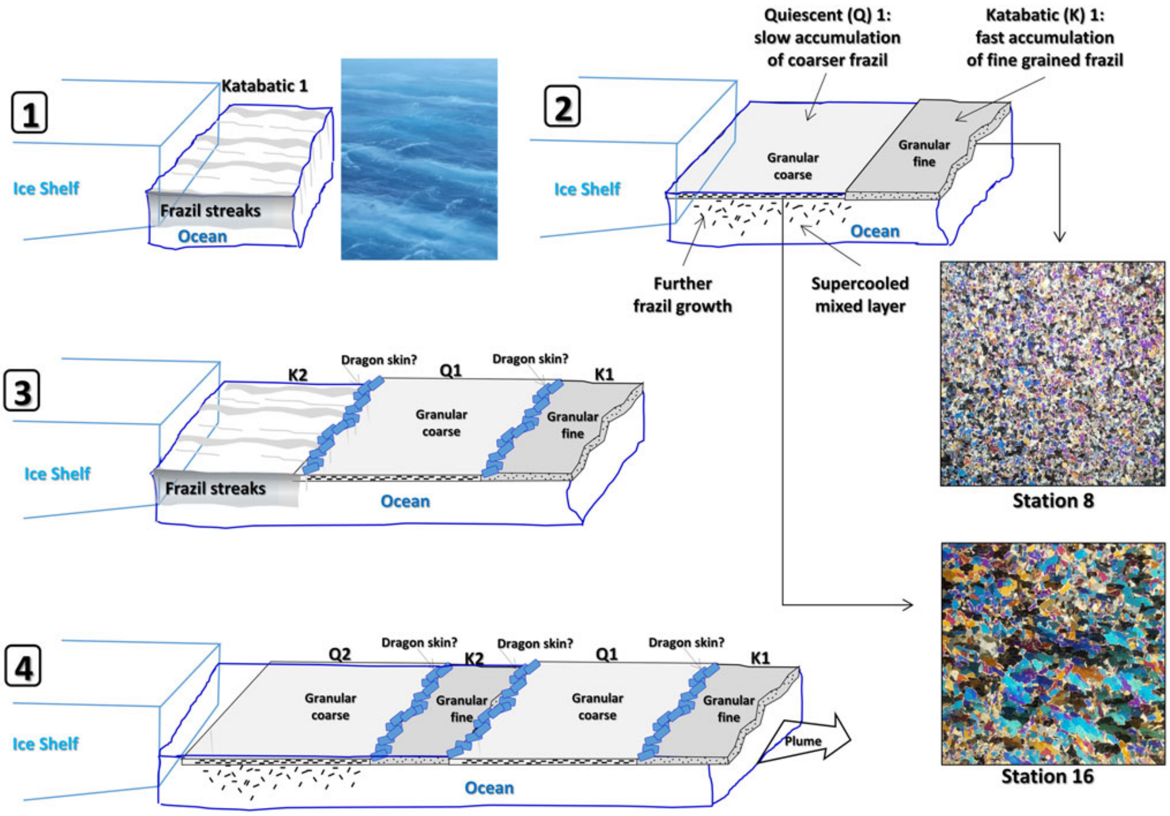

Fig. 6. Schematic showing the proposed mechanism generating crystal size and textural banding in the Terra Nova Bay polynya, as a result of the alternation of periods of high katabatic winds and quieter conditions.

more removed from the high oceanic heat flux (that was assumed to have been present in the remnant open water area), and therefore show a larger ice thickness for a similar initial growth date. It is indeed interesting to note that stations 23–25 all initiated growth within a very short time window (around year day 77), illustrating the very fast growth that eventually occurred in the remnant open water area. Sea ice at station 25 formed in a period of fast marginal expansion, fully outside the Ross Sea embayment, which might explain the larger proportion of frazil/granular ice in the upper section of the cores (Fig. 2).

Overall, the forward buoys trajectories shown in Figure 4 clearly indicate that, around mid-August 2017 (about day 225, when buoys launched at stations 18 and 20 take a sharp turn East), a general pattern of eastward circulation was initiated, as the sea-ice cover was caught up into the ACC (Antarctic Circumpolar Current). This is similar to what has been previously described for the outer Ross Sea, although it was then happening much earlier on in the year (mid-May) (e.g. Arrigo and others (2003), their Figure 4).

The Terra Nova Bay Polynya

Details of the textural properties of the TNBP stations are shown in Figure 5. A clear grain size contrast exists between stations 6, B1 to B3, 16 and 13 showing larger grain sizes (1.7–2.97 mm^2) and stations 8–11 with smaller grain sizes (0.50–0.92 mm^2). Stations 7, 14 and 15 show intermediary values (1.19–1.38 mm^2). The spatial arrangement of these grain size contrasts is not random as these differences roughly correspond with backscatter banding in satellite synthetic aperture radar (SAR) imagery (Fig. 5). We suggest that smaller grain sizes correspond to very fast ice growth during strong katabatic wind episodes (three of these occurred between sampling of stations 7 and 8, 11 and 12 and 13 and 14), while larger grains denote quieter times, allowing further crystal growth in the surface water, before aggregation as pancakes. Thin pancakes (a few centimeters) formed during the quieter phases of sampling indeed show larger grain sizes, often with elongated disk-like shapes (not shown, but similar to those seen at stations 26–27 in Fig. 2). Figure 6 proposes a schematic of the process of this 'banding' buildup, following successive episodes of katabatic winds. This is supported by the SAR imagery, with brighter bands, indicative of rougher ice formed from the original outflow of an ice plume during a katabatic event, having typically finer grained ice, while the coarser grained ice formed in the darker, more quiescent bands that subsequently formed behind the lighter bands. Dragon skin ice (see above, and Worby and others (1998) for full description) has mainly been observed at the outer margin of the polynya, where it accumulates and meets drifting coastal sea ice from the South, but it has also occasionally been seen within the polynya itself.

Apparently, as shown by the forward buoys trajectories in Figure 4, the ice from the TNBP (buoys from stations 10 and 16) appears to join the pack ice originating from further south (i.e. the McMurdo Sound area – buoy from station 17) and to be pushed further northward along the Victoria Land Coast past Coulman island, at least until midwinter (end of tracks on Julian Day 177–192, i.e. 26 June–11 July). Nonetheless, the TNB sea ice does not seem to contribute significantly to the pack ice in the CRS, given that its trajectory remains close to the Victoria Land Coast. This might also explain the difficulties the N.B. Palmer had during its southbound leg into TNB, it was basically traversing this coastal convergent flow.

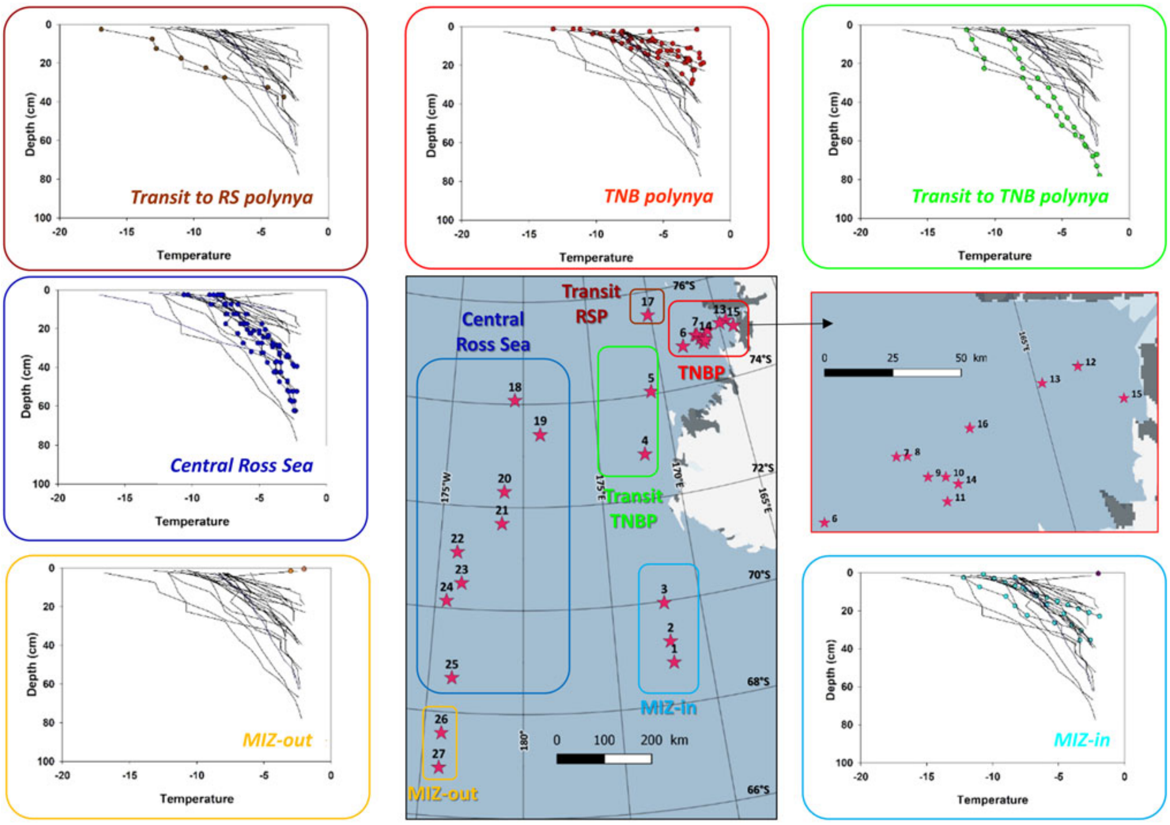

Fig. 7. Temperature profiles at the 27 PIPERS biogeochemical stations. Profiles for all cores are shown in each panel as thin black lines. Profiles for the cores within each indicated group are shown as color dots.

The Western Ross Sea

The western shelf sea-ice stations 4 and 5 both show peculiar textures (Fig. 2), but of potentially different origin. Station 4 remained in nearly the same position for a month and a half (Fig. 4), and shows clear signs of rafting processes (Fig. 2, also confirmed with the bulk ice salinity profiles, see below), with recurrent alternation between granular and columnar ice, oblique crystal elongations and ice type boundaries. These dynamical features could be expected in a more coastal area where locally formed land-fast sea ice meets granular pack ice drifting northwards. Station 5 is fully granular, but with large crystal size changes, oblique layering in the granular ice (only apparent in the bottom 0.70–0.90 m in Fig. 2, but present nearly everywhere) and oblique growth of bottom columnar ice. This also suggests an important dynamical component to ice thickening, confirmed by the large-scale ‘dragon skin’ characteristic of the sea-ice surface in that area (both at stations 5 and 6, see picture insert in lower left part of Fig. 2). We propose that these specific dynamical features result from the convergence of pancake ice pushed out from TNB by katabatic-driven winds, joined with coastal pancake ice drifting northwards from the southern McMurdo Sound area. Clearly, the history of stations 4 and 5 is one of convergent flow (light blue dots in Fig. 4).

Ice thermohaline properties

Profiles of ice temperature, bulk ice salinity, brine volume fraction, Rayleigh numbers and brine upwards velocities are presented in Figures 7–11, respectively. All profiles are shown for each group, and the profiles specific to the group enhanced with color dots.

All temperatures display near-equilibrium profiles, monotonically increasing downwards (Fig. 7), to the exception of surface samples, adjusting to air temperatures at the time of sampling. The southernmost station (17, −17°C) shows the coldest profile, and some of the TNB stations show colder surface temperatures (−12 to −13°C).

The remaining of the stations show a surface temperature hovering between −8 and −10°C. Warmer surface temperatures occur in the MIZ.

Salinity profiles (Fig. 8) generally show a ‘classical’ C-shape (growing ice), with the exception of some MIZ and TNBP stations (a few) and the western shelf stations, in Transit TNBP. The MIZ stations show a clear transition from isohaline (station 1) to C-shaped profiles (stations 2 and 3), as thickness increases. Both stations 4 and 5 show a vertically ‘jagged’ profile, consistent with their dynamic origin (rafting and dragon skin process, see above). The mean salinity profile is higher in the MIZ and the TNBP than in the CRS and Transit TNBP and RSP (less mature brine drainage processes in these young ice stations).

All brine volume fractions (Fig. 9) are above the permeability threshold of 5% in the TNBP and in the MIZ, with the exception of the more southerly station 3 that already shows impermeable layers at mid-depth. Impermeable layers at mid-depth are a common feature at both the CRS stations and the transit stations. Station 25 is however slightly above the permeability threshold at all depths, probably due to its slightly younger age.

Rayleigh numbers are shown in Figure 10. They generally reflect the age and maturity of the sea-ice cover. The younger

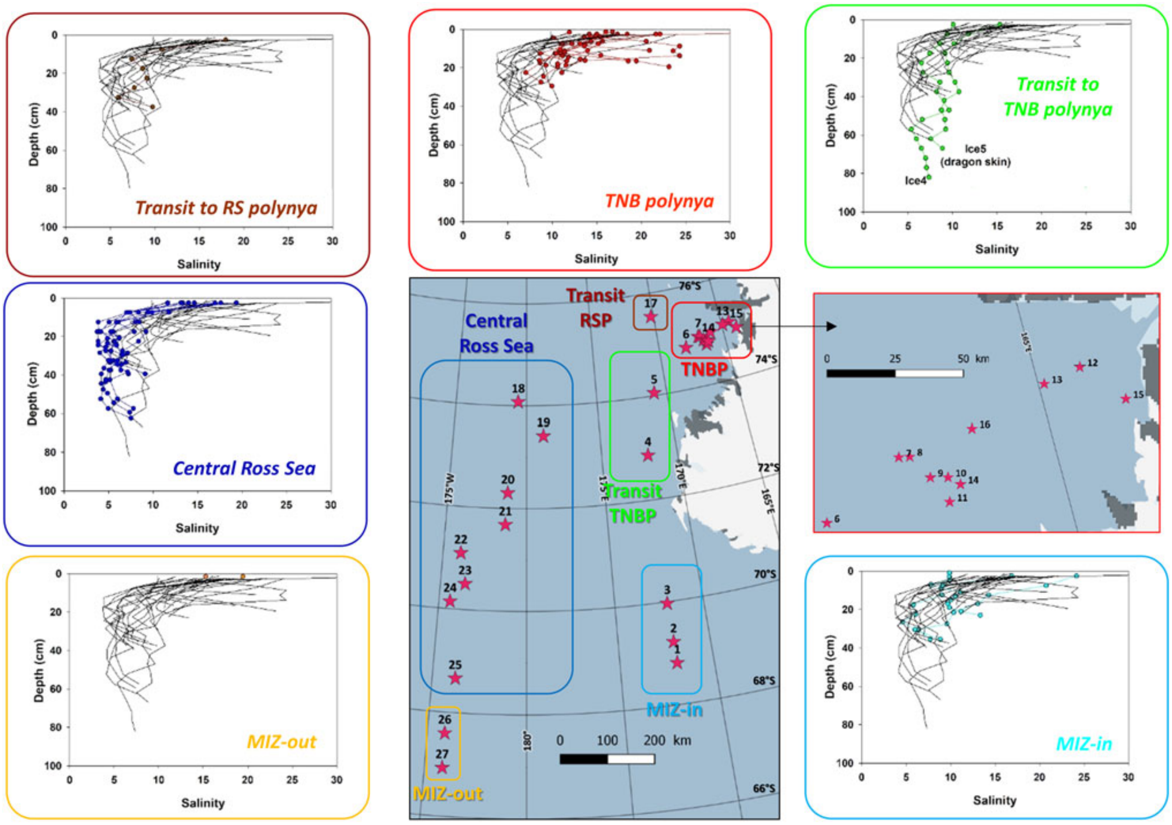

Fig. 8. Bulk ice salinity profiles at the 27 PIPERS biogeochemical stations. Profiles for all cores are shown in each panel as thin black lines. Profiles for the cores within each indicated group are shown as color dots.

ice, such as the one in the TNBP and at the MIZ, shows record values (maximum close to 200, a record for sea ice in the existing literature), mostly at or far way above the conservative critical value of 10, above which convection is expected to occur. In the more mature ice of the CRS or the Transit RSP, only the very bottom value, the few centimeters where the ice might still be actively growing, is above 10. Note the contrast for the transit stations to the TNBP, where station 5 is fully convective, while station 4 is entirely below the threshold.

An illustrative way to show the potential impact of brine overturning that avoids the uncertainty in the value of the critical Rayleigh number above which convection occurs is to examine the theoretical upwards brine velocities derived from the mushy layer theory (Thomas and others (2020), see methods). These are plotted in Figure 11 for the PIPERS stations. They clearly provide a more gradual view of the efficiency of the overturning in the brine system, with low values overall (approximately below maximum 2.10^{-5} m s^{-1}, i.e. ~7 cm h^{-1}) in the CRS vs values up to more than five times higher in the TNBP. A good illustration of the interest of plotting vertical brine velocities is the enhanced contrast between the profiles of the CRS and those of the western transit stations to the TNBP (stations 4 and 5), where the slightly higher Rayleigh numbers correspond to considerably higher brine upwards velocities. These contrasts between the two approaches have a clear significance for sea-ice biogeochemistry, nutrient transport and spatial variability.

Figure 12c illustrates the relationship between the vertically averaged Rayleigh numbers (Ra, Eqn (1)) and the vertically averaged upwards brine velocities (w, Eqn (2)). A strict relationship exists up to about Ra = 5, after which considerably higher brine velocities occur for a slightly higher Ra value, suggesting that Ra = 10 maybe a rather 'conservative' threshold for Ra$_c$. Figures 12a and b show the general direct/indirect relationships of w to mean bulk ice salinity (S)/mean ice temperature (T), respectively.

Algal standing stocks (Chl-a), size distribution, species and health state

Figure 13 shows Chl-a concentration in green (μg L^{-1}), which can be used as a proxy of algal standing stocks. Sea-water values (indicated at the bottom of each graph) are very low at all stations (0.02–0.2 μg L^{-1}), the maximum being observed at one of the polynya stations (station 9).

In the ice of the MIZ, Chl-a values become significant (above 1 μg L^{-1}, commonly referred to as a 'bloom' threshold in the ocean water) and the community switches from internal communities (station 1) to bottom communities (stations 2 and 3) as the ice thickens and ages. The ice is also dominated by large organisms (dark green in the profiles), a common feature for a 'well-established' sea-ice community in unflooded sea ice (e.g. Carnat and others, 2014; Carnat and others, 2016; Tison and others, 2017*b*). A similar evolution is seen for the ice in the TNBP. Starting from an internal community with low Chl-a concentrations (≤1 μg L^{-1}), the ice cover then develops a bottom community with an increasing concentration toward the margin of the polynya (stations 6 and 7, showing continuity with older stations 4 and 5, to the north, showing the highest concentrations encountered during the cruise). This is also the typical signature of the southern CRS stations (18–22), as the ice sourced from the RSP quickly advects into the area of delayed freezing (Figs 3 and 4).

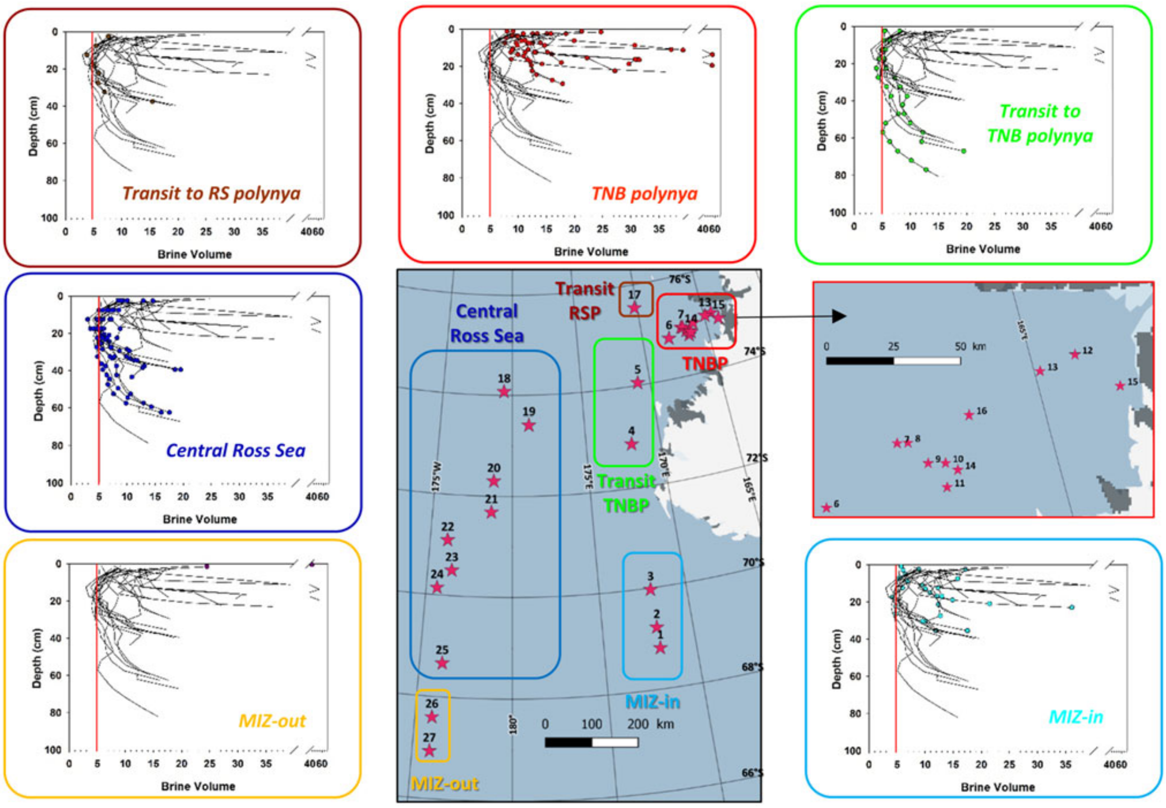

Fig. 9. Brine volume fraction profiles at the 27 PIPERS biogeochemical stations. Profiles for all cores are shown in each panel as thin black lines. Profiles for the cores within each indicated group are shown as color dots.

The thicker northern CRS stations (23–25) similarly show a low Chl-*a* (1–2 µg L^{-1}) internal community, with the exception of larger concentrations observed at station 23.

A major contrast, however, between the Central and the Western Ross Sea stations is in the algal size distribution. While the western shelf stations are dominated by large size algae (>10 µm), the CRS stations generally show a larger proportion of small size algae (0.8–10 µm), to the exception of a few bottom layers. In a recent study, De Jong and others (2017) describe that *Phaeocystis antarctica* and diatoms are the two major phytoplankton groups in the Ross Sea sea water, with *Phaeocystis* blooms occurring in the CRS in the summer, followed by diatom blooms later in the season in the Western Ross Sea Sector. Arrigo and others (2000) and Arrigo and Van Dijken (2004) also previously observed blooms of *P. antarctica* in the unstratified waters north of the Ross Ice Shelf in the Spring (October to mid-December), followed by diatom blooms later in the year (December–January), in association with the highly stratified surface waters of the western shelf, including TNB. Close to our study cruise track, Garrison and others (2005) compare sympagic (sea ice) communities in the Ross Sea during the Nathaniel B. Palmer (US) autumn-winter cruise ('NBP 98-3', same season as PIPERS 'NBP17-04') and summer NBP99-01 cruise. Similar to our observations, during their autumn-winter cruise, most of the biomass was found within ice floes as interior and bottom layer communities. During summer, surface-layer slush communities occurred throughout the ice-covered regions. The authors state that, although the biomass was highly variable throughout the study region during both cruises, diatoms dominated the internal and bottom autotrophic biomass. This was also true in terms of mean cell abundance (Diatoms: 2.4 10^{6} cells L^{-1} in autumn and 2.7 10^{6} cells L^{-1} in summer; *Phaeocystis*: 2.6 10^{5} cells L^{-1} in autumn and 2.3 10^{5} cells L^{-1} in summer). The summer surface communities were however dominated by *Phaeocystis*, *Pyramimonas* and *Gymnodium*.

Given that diatoms and *Phaeocystis* can be considered as the two major phytoplankton groups in the Ross Sea, and given their large size difference, we can surmise, as a first approximation, that our large size class is dominated by diatoms, while *Phaeocystis* might significantly contribute to the small size class. Following that rationale, we see that our CRS stations in 2017 show a different picture from the year 1998, both sampled at nearly the same period (NBP 98-3 covered Julian days 129–162 while PIPERS covered Julian days 109–155). Instead of being dominated by large size algae (presumably diatoms), small sizes are the rule (presumably *Phaeocystis*). This specificity can be related to the peculiar sea-ice growth history in 2017, as discussed above. The delayed but then very fast ice cover progression between 29 March and 8 April (blue line to black line in Fig. 3) likely resulted in entrapment of small size algae from the sea water within the growing columnar ice (presumably *Phaeocystis* present in surface waters of the CRS), with not enough time available or no suitable conditions for the transition toward a larger size diatoms community before the permeability closes-off, to the exception of the more permeable bottom layers (e.g. below 0.40 m at stations 22–24, Fig. 13). It has indeed been shown recently, in an Arctic case of algal colonization of young Arctic sea ice in the Spring, that there is a progressive shift from a ciliate, flagellate and dinoflagellate 'sea-water inherited' community (biomass fluctuating between 3 and 42 mg C m^{-3}) toward a pennate

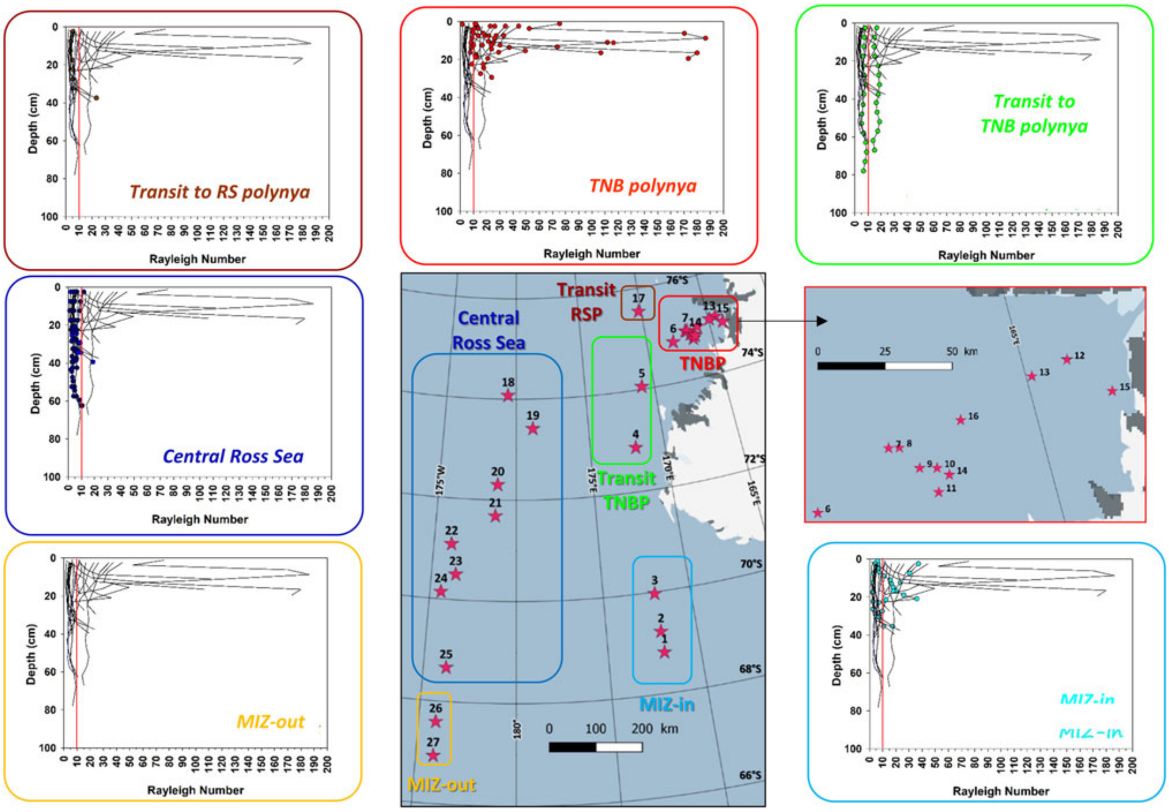

Fig. 10. Rayleigh number profiles at the 27 PIPERS biogeochemical stations. Profiles for all cores are shown in each panel as thin black lines. Profiles for the cores within each indicated group are shown as color dots. Red line shows conservative Ra threshold=10.

diatoms community (biomass steadily increasing from 0 to >500 mg C m^{-3}) in ~2 or 3 weeks (Kauko and others, 2018, their Figure 5). This suggests that the delayed but fast sea-ice growth resulted in a shift of algal speciation in the CRS in 2017, as compared to 1998.

To test this hypothesis further, we have performed cell abundance counts at three contrasted PIPERS stations: station 3 for the MIZ (unfortunately, only the bottom ice was available), station 4 for the Western Ross Sea and station 23 for the CRS (Table 1, Fig. 14). Clearly, *Phaeocystis* is the more abundant in all layers, with the exception of the bottom of stations 3 and 23, supporting our interpretation. However, this dataset also underlines the limitations of our working hypothesis. Indeed, station 4 showing overwhelming large size fractions Chl-*a* (Fig. 13) is actually dominated by *Phaeocystis* cells. Conversion of cell abundance to Chl-*a* concentrations is not trivial. Indeed, Chl-*a* cell quotas for a given species largely depend on environmental factors (temperature, salinity, light conditions) and individual sizes. This is especially true for diatoms, less for *Phaeocystis*. However, using an upper bound value of the Chl-*a* cell quota of 1.68 pg Chl-*a* $cell^{-1}$ for polar *Phaeocystis* in the literature (Baumann and others, 1994; Schoemann and others, 2005), conversion of cell number in the 0.2–0.4 m interval at station 23 gives 2.5 µg Chl-*a* L^{-1}, a value reasonably close to the observed value of 2.41 µg Chl-*a* L^{-1}, given the uncertainties. Therefore, using the same cell quota to convert our *Phaeocystis* cell counts at station 4 into Chl-*a* concentrations, we obtain estimates for 0.8–10 µm Chl-*a* concentrations on the average four times higher, and maximum ten times higher than observations. This suggests that some of the *Phaeocystis* cells could have been in the colonial form, and therefore be collected as part of the large size cells (>10 µm). Preservation in Lugol for several months before cell abundance counting might have deconstructed most of these colonies. Another potential explanation of the discrepancies at station 4 is that the size of the diatom cells was there on the high side, therefore boosting the Chl-*a* concentration of the large size cells. The rafted nature of station 4 could have easily brought large size diatoms, initially at the bottom, further up in the ice cover. On the contrary, diatoms in the internal layers of unrafted station 23, incorporated during fast columnar ice growth, might have remained on the low size side. A first semi-quantitative estimate partly supports this hypothesis, with diatoms sizes ranging 58–120 µm × 4–65 µm at station 4 and 20–25 µm × 4 µm at station 23.

As shown in Figure 15 and consistent with the associated single-cell biomass of the two phytoplankton groups, the late sea-ice growth in 2017 resulted in a generally lower *Chl-a* burden than in 1998 for the same period. Dejong and others (2017, 2018) have recently looked at late-summer frazil ice-associated algal blooms around Antarctica using daily MODIS visible spectral band satellite imagery. They produced a map of the percent of years between 2003 and 2017, where polynyas around Antarctica in March appear green from high photosynthetic productivity on the satellite images. TNB (greenest hot spot in the whole dataset) and the RSP were blooming between 61 and 100% of the time for the months and period considered. The authors suggest that the heavy frazil ice production in the polynyas enhances convective processes and deepens the mixed layer so that nutrients are efficiently delivered to the surface water, favoring surface photosynthesis, as long as light is available. De Jong and others (2017) surmise that this sustained polynya production is

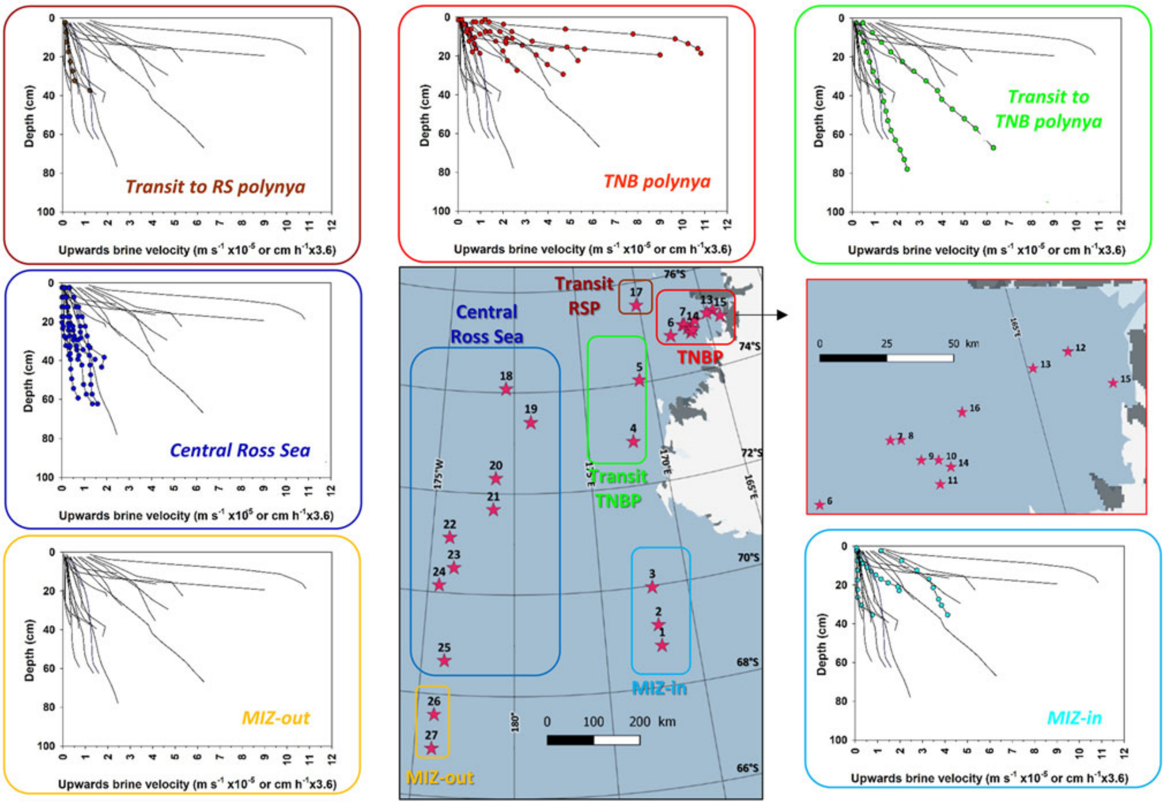

Fig. 11. Brine upward velocity profiles at the 27 PIPERS biogeochemical stations. Profiles for all cores are shown in each panel as thin black lines. Profiles for the cores within each indicated group are shown as color dots.

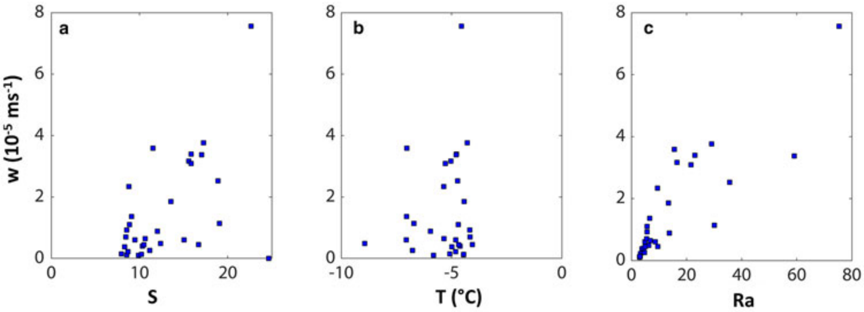

Fig. 12. Upwards brine velocities (w) vs (a) bulk ice salinity (S), (b) bulk ice temperature (T) and (c) bulk ice Rayleigh number (Ra) for all 27 PIPERS stations. Each data point is a mean vertical value for the considered variables for a given ice core, at a given location.

quickly exported below 200 m depth in the Polynya itself. This planktonic material could nevertheless be the seeding source for the ice exported from the polynyas. We however could not find any significant *Chl-a* accumulation in the top granular ice of the cores from the TNBP or from the southernmost CRS stations ($<1\,\mu g\,L^{-1}$, Fig. 13) that would have been inherited from potentially sustained production in the source polynyas earlier in the year. Satellite imagery of the TNBP in 2017 indicated clear discoloration prior to our arrival on site (personal communication from Jan Lieser), but nothing could be detected from the ship's deck during our stay. The higher Chl-*a* levels observed at stations 4–7 could however be partly inherited from earlier production in TNB, given the specific sea-ice dynamics in the area, as described above.

Finally, as already shown for the winter sea ice from the Weddell Sea (Tison and others, 2017*b*), sea-ice Phaeopigments/*Chl-a* ratios are very different from those in the sea water below (Fig. 13). While sea-water Phaeopigments concentrations are generally 2–3 times higher than *Chl-a* concentrations (with very low concentrations for both), in sea ice this ratio generally remains much lower. As discussed in Tison and others (2017*b*), the Phaeopigments/*Chl-a* ratio can be interpreted in terms of algal community health (proportion of living cells vs dead cells) and active growth. Several examples from the Arctic and the Antarctic (Mock and others, 1997; Mock and Gradinger, 1999; Krembs and others, 2011; Arrigo and others, 2014; Zhou and others, 2014) show that Spring/early Summer sea ice, with active primary production, is characterized by low

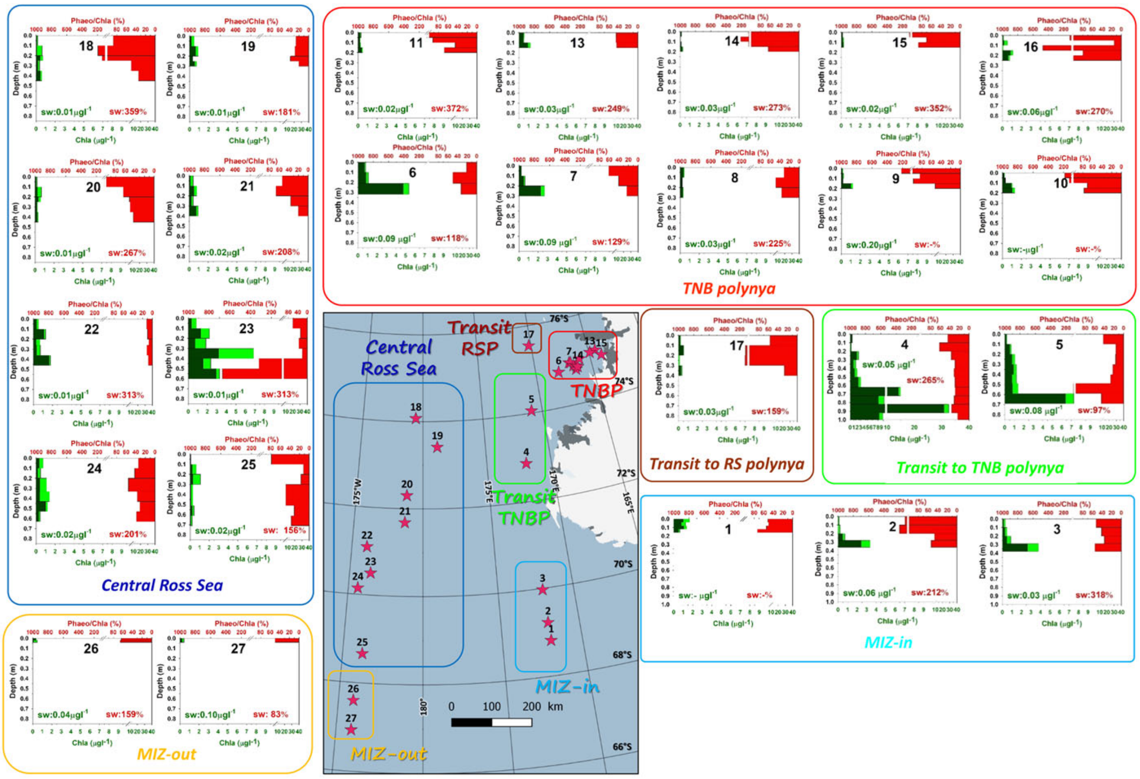

Fig. 13. Chl-*a* and Phaeopigments profiles at the 27 PIPERS biogeochemical stations. Chl-*a* is shown in green, with light green for the small algae (0.8–10 µm) and dark green for the large algae (>10 µm). The Phaeopigments/Chl-*a* ratios are shown in red. Sea-water values (sw), when available, are also indicated at the bottom of each graph.

Phaeopigments/*Chl-a* ratios which then increases steadily as ice ages and decays. The same should be true for active autumnal sympagic communities, therefore implying that most of our PIPERS stations are ‘healthy’ and possibly actively growing. The main exception is the bottom ice of station 23 with ratios equal or higher than sea-water values.

Ross Sea vs Weddell Sea

In this section, we will place our PIPERS dataset in perspective, comparing it to recent winter pack ice observations in the Weddell Sea (The AWECS cruise (Tison and others, 2017*b*)). The AWECS cruise took place in June–August 2013, or mid-late winter, while PIPERS took place a few months earlier during the autumn freeze-up. It is nevertheless worth the comparison, given the scarcity of data from these seasons.

Figure 16 compares physical and biological properties during the AWECS (blue) and PIPERS (red) winter cruises. To enlarge the statistical validity of our approach, we have also considered ice thickness, snow thickness and freeboard datasets that were, for both cruises, collected by dedicated ice physics teams. These are usually transects of 50–100 m sampled at a 1 m spatial resolution. Transects are chosen to be representative of the various ice types found at a given station, while the biogeochemical stations are usually biased toward thinner level ice.

During the AWECS cruise, the distribution of the BGC ice thicknesses (Fig. 16b) was similar to that sampled along the physics transects (Fig. 16a, blue bars). This was clearly not the case for the PIPERS BGC stations where the ice was generally thinner and level compared to the physics transects which were designed to cross deformed ice (mean of 0.38 vs 0.79 m, respectively, Figs 16a and b, red bars). This is easily understood, when looking at the respective locations of the BGC and the physics transects sections (Fig. 16o). Only one out of nine physics transects locations was performed at the margin of the TNBP, while 11 out of 27 BGC stations were located within the thin ice of the polynya. Snow thicknesses at BGC stations were generally consistent with the physics transects during both cruises (Figs 16c and d). Although not apparent in the frequency distributions, the mean and median snow thicknesses at PIPERS however suggest a bias toward thinner snow at the BGC stations, due to the higher proportion of snow-depleted polynya stations.

No significant difference exists in overall ice thickness distribution between AWECS and PIPERS (Fig. 16a). There are however differences in terms of ice texture, ice types and their spatial distribution. Granular ice dominates the Weddell Sea ice samples, due to the combination of the pancake cycle in the region (frazil ice and rafting) with the greater occurrence of snow ice (present at nearly all stations, with thicknesses between a few and 0.40 m (Tison and others, 2017*b*, their Fig. 5)). This is consistent with seasonal differences in snow ice formation (Jeffries and others, 2001). Columnar ice was dominant at only one AWECS near-coastal station close to the Antarctic Peninsula. In the Ross Sea, during our 2017 cruise, granular frazil ice dominates the ice cover in the polynyas and downstream of it, and in the MIZ. The CRS, on the contrary, has columnar ice as the principal component. Snow ice was only present in some of the CRS samples and in the MIZ, with a thickness between 0.05 and 0.40 m (a more detailed study of the snow ice dynamics at PIPERS is beyond the scope of this paper and will be presented elsewhere).

Mean snow thickness is clearly lower at PIPERS stations (mean of 0.07 vs 0.27 m at AWECS, Fig. 16c), resulting in a freeboard distribution shifted toward positive values (Fig. 16e) and scarce observations of flooding. Brine tubes, thought to result from the combination of flooding and frequent alternation of warm and cold spells (Tison and others, 2017*b*), were observed regularly

Table 1. Cell abundance (cells mL^{-1}) for selected PIPERS stations

Microorganism	PIPERS 3	PIPERS 4									PIPERS 23		
	0.29–0.39 m	0–0.10 m	0.10–0.20 m	0.20–0.30 m	0.30–0.40 m	0.40–0.50 m	0.50–0.62 m	0.62–0.72 m	0.72–0.82 m	0.82–0.92 m	0–0.20 m	0.20–0.40 m	0.40–0.60 m
Diatoms													
Fragilariopsis sp.	414 ± 33	20 ± 15	37 ± 4	24 ± 11	36 ± 8	41 ± 7	85 ± 11	89 ± 13	64 ± 6	641 ± 81	47 ± 5	476 ± 63	156 ± 29
Pseudo-nitzschia s	0	0	13 ± 4	10 ± 4	3 ± 1	6 ± 3	21 ± 3	23 ± 7	20 ± 9	143 ± 24	2 ± 1	10 ± 8	20 ± 4
Corethron sp.	0	6 ± 1	8 ± 1	10 ± 3	1 ± 1	18 ± 6	32 ± 7	53 ± 5	24 ± 4	27 ± 9	0	0	0
Chaetoceros sp.	2 ± 3	5 ± 3	28 ± 4	19 ± 0	1 ± 2	8 ± 2	27 ± 6	22 ± 10	19 ± 5	20 ± 3	0	0	0
Thalassiosira sp.	0	20 ± 15	2 ± 1	6 ± 1	0	0	3 ± 1	2 ± 3	2 ± 1	7 ± 1	1 ± 1	1 ± 1	0
Asteromphalus sp.	0	0	2 ± 1	0	0	0	1 ± 0	7 ± 5	0	12 ± 5	0	0	0
Nitzschia sp.	0	0	0	1 ± 1	2 ± 1	0	7 ± 2	8 ± 3	4 ± 2	10 ± 4	0	12 ± 6	9 ± 2
Dactyliosolen sp.	0	1 ± 1	2 ± 0	1 ± 0	0	2 ± 0	2 ± 1	2 ± 2	0	0	0	0	0
Coscinodiscus sp.	0	0	0	1 ± 1	0	1 ± 1	0	1 ± 1	0	0	0	0	0
Prymnesiophyceae													
Phaeocystis sp.	104 ± 10	511 ± 52	550 ± 17	528 ± 61	920 ± 81	1766 ± 47	495 ± 50	2519 ± 19	2885 ± 107	3012 ± 138	105 ± 38	1473 ± 144	85 ± 23
Dinoflagellata	9 ± 2	8 ± 1	5 ± 0	5 ± 1	10 ± 2	4 ± 1	2 ± 0	3 ± 1	6 ± 1	5 ± 1	35 ± 5	6 ± 1	20 ± 8
Silicofagellata													
Dictyocha sp.	1 ± 1	0	0	0	0	0	0	0	0	0	0	0	0

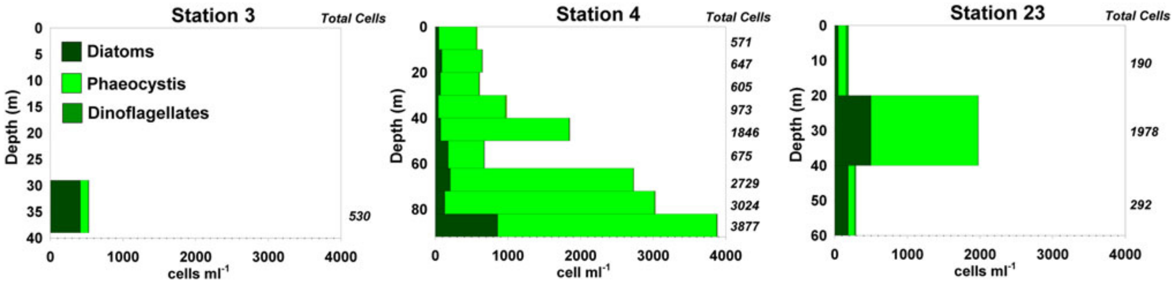

Fig. 14. Profiles of cell abundance for selected PIPERS stations. Diatoms have been grouped for clarity. Full dataset is presented in Table 1. Only bottom sample was available at station 3.

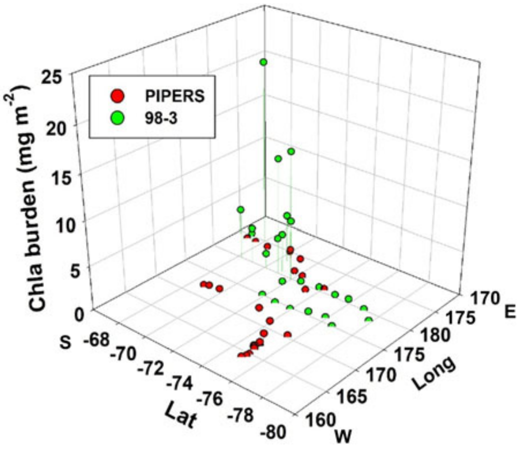

Fig. 15. Compared *Chl-a* burden (mg m^{-2}) between the PIPERS 2017 cruise (red dots) and the NBP 98-3 cruise (green dots) as a function of position. The two cruises occurred at a similar period (April–June), but the PIPERS cruise spent more time in the Terra Nova Bay polynya, therefore under-sampling the Ross Sea Polynya.

during AWECS, while not seen at all during PIPERS. Despite a temperature distribution skewed toward lower values (Fig. 16f), higher bulk ice salinities (especially in the TNB and MIZ areas) resulted in higher mean and median relative brine volumes at PIPERS (Figs 16g and h). Note, however, that, for both cruises, a minority of brine volumes were below the 5% permeability threshold. PIPERS stations are clearly more convective than AWECS, as shown by the comparison of the Rayleigh numbers in Figure 16i, but it should however be remembered that the PIPERS distribution is somewhat biased toward thin, young ice in the TNBP.

With similar values observed in the water for the two cruises (Fig. 16m), mean/median *Chl-a* concentrations in the ice are 5–3 times lower at PIPERS, with a narrower distribution (Fig. 16k). Although in both cruises ice (Fig. 16l) appears much more biologically 'healthier' than water (Fig. 16n), PIPERS stations are shifted toward more 'mature' (larger proportion of dead cells vs living cells) ice and water Phaeopigments/*Chl-a* ratios (Figs 16l and n respectively).

The comparison above is clearly affected by important sampling spatio-temporal differences between the two studies: (a) PIPERS stations are spanning a more southerly latitudinal range (67–76°S vs 60–71°S at AWECS), potentially implying colder conditions and lesser influence from synoptic conditions (snow precipitations and warmer temperatures) and (b) PIPERS cruise occurred earlier in the winter. The lower *Chl-a* concentrations at PIPERS could result from the fact that the ice is younger and thinner because of (a) the bias from over-representation of polynya samples and/or (b) the earlier time of the year. Figure 16j shows a moderate correlation between ice thickness and *Chl-a* burden for our PIPERS stations. However, if we trust this correlation and move our mean BGC ice thickness (0.39 m) toward the physics stations mean ice thickness (0.79 m), to take our polynya bias into account, it would only increase the burden by 0.301 mg m^{-2}, with a rather insignificant corresponding increase of *Chl-a* concentration of 0.012 µg l^{-1}. Autumnal growth, as opposed to winter, should favor higher *Chl-a* at PIPERS (autumnal blooms) although this might be counterbalanced by the more southerly location of the PIPERS stations. Clearly, the polynya blooms detected in March 2017 (in satellite data) had disappeared by the time of our arrival in the TNBP (April–May 2017).

A significant factor influencing the spatio-temporal differences discussed above is the observation that the Ross Sea ice growth was delayed in 2017 (Parkinson, 2019), resulting in thinner ice and lower *Chl-a* concentration compared to the NBP98-3 cruise, within the same time window. This is part of a recent trend in the Ross Sea pack ice cycle. For the last decades, both the Weddell and the Ross Sea were characterized by a longer ice season (earlier growth and later decay (Stammerjohn and others, 2008)). As suggested by Tison and others (2017*b*), this longer ice season in the Weddell Sea would have resulted in thicker, more concentrated ice and sufficient increase in snow depth to warm the ice, increased flooding, brine tubes formation and boosting of an internal sympagic community. The delay in ice growth in the Ross Sea in 2017, on the contrary, has limited the potential for developing that community and establishing the typical diatom-dominated sympagic speciation. With later growth, in this colder more southerly (Ross Sea) region, the lack of light, thinner snow depths limiting flooding and the impermeable status of internal layers should not favor major biomass increases and species shifts later in the winter. In that respect, the higher Phaeopigments/*Chl-a* ratio in the Ross Sea vs the Weddell Sea might be an early sign of the decaying trend of the sympagic community in the Ross Sea.

Our PIPERS dataset suggests that, if the autumn ice advance continues to be delayed, as might be expected if we are now seeing the foreseen long-term decline of the Antarctic sea-ice cover, that trend in ice seasonality could have important implications for the sea-ice sympagic community in the Ross Sea.

Conclusions

Early winter sea ice is typically under-sampled in terms of both physical and biogeochemical properties. Links between polynya activity and pack ice seasonal growth are still often debated. The Ross and the Weddell Seas have both been characterized by a longer sea-ice season on the long term. However, recent anomalies in the observed trend of a generally increasing Antarctic sea-ice extent make it even more important to document

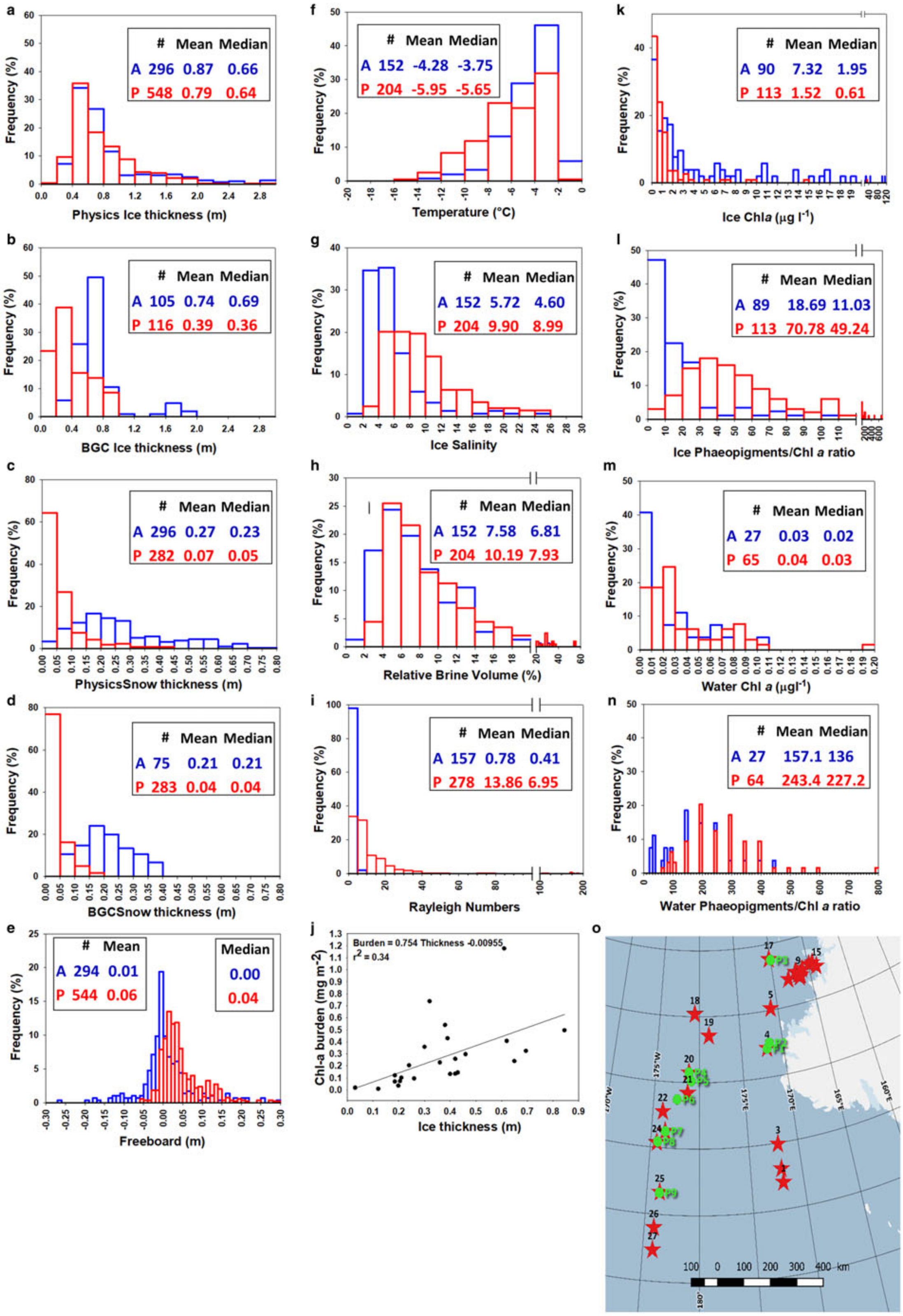

Fig. 16. Comparison of physical and biological properties during winter cruises AWECS (Weddell Sea, June–August 2013, blue symbols, A) and PIPERS (Ross Sea, April–June 2017, red symbols, P): ice thickness at physics transects (a) and BGC stations (b); snow thickness at physics transects (c) and BGC stations (d); freeboard at physics transects (e); temperature (f), salinity (g), relative brine volume (h) and Rayleigh number (i) at BGC stations; ice Chl-*a* (k) and Phaeopigments/Chl-*a* (l) at BGC stations; water Chl-*a* (m) and Phaeopigments/Chl-*a* (n) at BGC stations. Map of physics transects (green dots) and BGC locations (red stars) (o). Relationship between Chl-*a* burden and ice thickness at BGC stations (j). See text for details.

Antarctic winter sea-ice behavior and changes, and its potential impact on ecosystems.

Here, we have documented the late development of the CRS sea-ice extent in 2017, and show how it has affected its physicochemical and biological properties: thinner ice, with less early winter snow cover, seeded by granular ice from the RSP, but dominated by columnar ice growth, however slowed down by a larger than usual oceanic heat flux. This has resulted in a less 'mature', internal, sympagic community with a majority of small cells and a lower total biomass in the CRS.

Sea-ice growth and discharge from the TNBP is shown to mainly feed the coastal Western Ross Sea, in a very dynamic environment favoring rafting and dragon skin ice formation. The biological community there shows higher biomass, dominated by large celled communities and developing clearer bottom ice locations.

These properties are in clear contrasts with those recently observed in the Central Weddell Sea, demonstrating the crucial interest of enlarging our sea-ice biogeochemical database to winter times, a mandatory step to unbiased yearly budgets.

Acknowledgements. We are indebted to N.B. Palmer crew for their logistical support during the 2017 PIPERS cruise. S. Stammerjohn was supported by the PIPERS and LTER Programs of the U.S. National Science Foundation, ANT-1341606 (S. Stammerjohn and J. Cassano, U Colorado) and ANT-0823101 (H. Ducklow, LDEO/Columbia University), respectively. Steve Ackley (UTSA) was supported by the PIPERS program of the U.S. National Science Foundation ANT-1341717 and by NASA Grant 80NSSC19M0194 to the Center for Adv. Meas. in Extreme Environments at UTSA.Ted Maksym (WHOI) was supported by the PIPERS program of the U.S. National Science Foundation ANT-1341513. This research was supported by the Belgian F.R.S-FNRS (project ISOGGAP and IODIne, contract T.0268.16 and J.0262.17, respectively). Fanny Van der Linden, Sarah Wauthy, Gauthier Carnat, Célia Sapart and Bruno Delille are PhD students, postdoctoral researchers and research associate, respectively, of the Belgian F.R.S.-FNRS. This work was also supported by the Australian Government's Cooperative Research Centre program through the Antarctic Climate & Ecosystems Cooperative Research Centre, and by the Australian Research Council's Special Research Initiative for Antarctic Gateway Partnership (Project ID SR140300001). Daiki Nomura was supported by grants from the Japan Society for the Promotion of Science (#17H04715) and the National Institute for Polar Research through Project Research KP-303 (ROBOTICA) and #28-14. We thank Dr Jan Lieser for his constructive remarks and suggestions about primary production in Antarctic Polynya, in the early stages of this work.

References

Ackley SF and 12 others (2020) Sea ice production and air-ocean-ice biogeochemistry interactions in the Ross Sea during the PIPERS 2017 autumn field campaign. *Annals of Glaciology* (82), 1–15. https://doi.org/10.1017/aog.2020.31.

Arar EJ and Collins GB (1997) Method 445.0 In vitro determination of chlorophyll a and Pheophytin in marine and freshwater algae by fluorescence. U.S. Environmental Protection Agency 309417.

Arrigo KR and 6 others (2000) Phytoplankton taxonomic variability and nutrient utilization and primary production in the Ross Sea. *Journal of Geophysical Research* **105**, 8827–8846.

Arrigo KR, Brown ZW and Mills MM (2014) Sea ice algal biomass and physiology in the Amundsen Sea, Antarctica. *Elementa: Science of the Anthropocene* **2**(28). doi: 10.12952/journal.elementa.000028.

Arrigo KR, Mock T and Lizotte MP (2010) Primary producers and sea ice. In Thomas DNAD and Dieckmann GS (eds), *Sea Ice*. Oxford, UK: Blackwell Publishing Ltd, p. 621.

Arrigo KR, Robinson DH, Dunbar RB, Leventer AR and Lizotte MP (2003) Physical control of chlorophyll a, POC, and PON distributions in the pack ice of the Ross Sea, Antarctica. *Journal of Geophysical Research* **108**(10). doi: 10.1029/2001JC001138.

Arrigo KR and Thomas DN (2004) Large scale importance of sea ice biology in the Southern Ocean. *Antarctic Science* **16**, 471–486.

Arrigo KR and Van Dijken GL (2004) Annual changes in sea ice, chlorophyll *a*, and primary production in the Ross Sea, Antarctica. *Deep Sea Research Part II: Topical Studies in Oceanography* **51**(1–3), 117–138.

Baumann MEM, Lancelot C, Brandini FP, Sakshaug E and John DM (1994) The taxonomic identity of the cosmopolitan prymnesiophyte *Phaeocystis*: a morphological and ecophysiological approach. *The Journal of Marine Systems* **5**, 5–22.

Beitsch A, Kaleschke L and Kern S (2014) Investigating high-resolution AMSR2 sea ice concentrations during the February 2013 fracture event in the Beaufort sea. *Remote Sensing* **6**(5), 3841–3856.

Bluhm BA, Gradinger RR and Schnack-Schiel SB (2010) Sea ice Meio- and Macrofauna. In Thomas DN and Dieckmann GS (eds), *Sea Ice*. Oxford, UK: Blackwell Publishing Ltd, p. 621.

Carnat G and 8 others (2013) Investigations on physical and textural properties of Arctic first-year sea ice in the Amundsen Gulf, Canada, November 2007–June 2008 (IPY-CFL system study). *Journal of Glaciology* **59**(217), 819–837. doi: http://dx.doi.org/10.3189/2013JoG12J148.

Carnat G and 8 others (2014) Physical and biological controls on DMS, P dynamics in ice shelf-influenced fast ice during a winter-spring and spring-summer transition. *Journal of Geophysical Research: Oceans* **119**, 2882–2905.

Carnat G and 7 others (2016) Influence of short-term synoptic events and snow depth on DMS, DMSP and DMSO dynamics in Antarctic spring ice. *Elementa: Science of the Anthropocene* **4**, 000135.

Comiso JC, Cavalieri DJ and Markus T (2003) Sea ice concentration, ice temperature and snow depth using AMSR-E data. *IEEE Geoscience and Remote Sensing Letters* **41**(2), 243–252.

DeJong HB and 5 others (2017) Net community production and carbon export during the late summer in the Ross Sea, Antarctica. *Global Biogeochemical Cycles* **31**(3), 473–491.

DeJong HB, Dunbar RB and Lyons EA (2018) Late summer frazil ice-associated algal blooms around Antarctica. *Geophysical Research Letters* **45**(2), 826–833.

Delille B and 12 others (2014) Southern Ocean CO_2 sink: the contribution of the sea ice. *Journal of Geophysical Research: Oceans* **119** (9), 6340–6355.

Dieckmann GS and Hellmer HH (2010) The importance of sea ice: an overview. In Thomas DN and Dieckmann GS (eds), *Sea Ice*. Oxford, UK: Blackwell Publishing Ltd, p. 621.

Eicken H, Grenfell TC, Perovich DK, Richter-Menge JA and Frey K (2004) Hydraulic controls of summer Arctic pack ice albedo. *Journal of Geophysical Research* **109**(C08007). doi: 10.1029/2003JC001989.2004.

Flores H and 29 others (2012) Impact of climate change on Antarctic krill. *Marine Ecology Progress Series* **458**, 1–19.

Freitag J (1999) Untersuchungen zur hydrologie des arktischen Meereises-Konsequenzen für den kleinskaligen Stofftransport. *Polar Bear Temporal Range: Pleistocene-Recent* **325**, 150 pp.

Garrison DL and 6 others (2005) Sea-ice microbial communities in the Ross Sea: autumn and summer biota. *Marine Ecology Progress Series* **300**, 39–52.

Golden KM, Ackley SF and Lytle V (1998) The percolation phase transition in sea ice. *Science (New York, N.Y.)* **282**, 2238–2240.

Greene C, Gwyther D and Blankenship D (2017) Antarctic mapping tools for MATLAB. *Computers & Geosciences* **104**, 151–157.

Griewank PJ and Notz D (2013) Insights into brine dynamics and sea ice desalination from a 1-D model study of gravity drainage. *Journal of Geophysical Research: Oceans* **118**, 3370–3386.

Hunke EC, Notz D, Turner AK and Vancoppenolle M (2011) The multiphase physics of sea ice: a review for model developers. *The Cryosphere* **5** (4), 989–1009. doi: http://dx.doi.org/10.5194/tc-5-989-2011.

IPCC (2019) Summary for policymakers. In Po¨rtner H-O, Roberts DC, Masson-Delmotte V, Zhai P, Tignor M, Poloczanska E, Mintenbeck K, Alegri´a A, Nicolai M, Okem A, Petzold J, Rama B and Weyer NM (eds), *IPCC Special Report on the Ocean and Cryosphere in a Changing Climate*. Switzerland.

IPCC TF and 10 others (2013) *Climate Change 2013: The Physical Science Basis. Contribution of Working Group I to the Fifth Assessment Report of the Intergovernmental Panel on Climate Change*. Cambridge and New York, Cambridge University Press.

Jeffries MO, Krouse HR, Hurst-Cushing B and Maksym T (2001) Snow-ice accretion and snow-cover depletion on Antarctic first-year sea-ice floes. *Annals of Glaciology* **33**, 51–60.

Kauko HM and 9 others (2018) Algal colonization of Young Arctic Sea Ice in Spring. *Frontiers in Marine Science* **5**, 199.

Kimura N (2004) Sea ice motion in response to surface wind and ocean current in the Southern Ocean. *Journal of the Meteorological Society of Japan* **82**(4), 1223–1231.

Krembs C, Eicken H and Deming JW (2011) Exopolymer alteration of physical properties of sea ice and implications for ice habitability and biogeochemistry in a warmer Arctic. *Proceedings of the National Academy of Sciences of the USA* **108**, 3653–3658.

Langway CCJ (1958) Ice fabrics and the Universal stage. CRREL Technical Report, 62.

Lannuzel D and 5 others (2006) Development of a sampling and flow injection analysis technique for iron determination in the sea ice environment. *Analytica Chimica Acta* **556**(2), 476–483.

Leu E, Søreide JE, Hessen DO, Falk-Petersen S and Berge J (2011) Consequences of changing sea-ice cover for primary and secondary producers in the European Arctic shelf seas: timing, quantity, and quality. *Progress in Oceanography* **90**(1–4), 18–32.

Marion G, Mironenko M and Roberts M (2010) FREZCHEM: a geochemical model for cold aqueous solutions. *Computers & Geosciences* **36**, 10–15.

Matsuoka K, Skoglund A and von Deschwanden A (2013) Quantarctica: a free GIS package for research, education and operation in Antarctica. *Norwegian Polar Institute Seminar*, Tromso, Norway.

Mock T and Gradinger RR (1999) Determination of Arctic ice algal production with a new in situ incubation technique. *Marine Ecology Progress Series* **177**, 15–26. doi: 10.3354/meps177015.

Mock T, Meiners KM and Giesenhagen HC (1997) Bacteria in sea ice and underlying brackish water at 54°26′50″N (Baltic Sea, Kiel, Bight). *Marine Ecology Progress Series* **158**, 23–40.

Mouginot J, Scheuchl B and Rignot E (2017) MEaSUREs Antarctic Boundaries for IPY 2007–2009 from Satellite Radar, Version 2 [Grounding line and coastline]. NASA National Snow and Ice Data Center Distributed Active Archive Center.

Notz D and Worster MG (2008) In situ measurements of the evolution of young sea ice. *Journal of Geophysical Research* **113**(C3). doi: 10.1029/2007JC004333.

Notz D and Worster MG (2009) Desalination processes of sea ice revisited. *Journal of Geophysical Research-Oceans* **114**. doi: 10.1029/2008JC004885/2009.

Oshima KI and 12 others (2013) Antarctic bottom water production by intense sea-ice formation in the Cape Darnley polynya. *Nature Geoscience* **6**, 235–240.

Parkinson CL (2019) A 40-year record reveals gradual Antarctic sea ice increases followed by decreases at rates far exceeding the rates seen in the Arctic. *PNAS* **116**(29), 14414–14423.

Perovich D (1996) The optical properties of sea ice. *Cold Region Research and Engineering Laboratory* (CRREL)

Pringle D and Ingham M (2009) Measuring sea ice thermal, electric and hydraulic properties and processes. In Eicken H (ed.), *Field Techniques for sea ice Research*. Faibanks: University of Alaska Press, p. 592.

Rees Jones DW and Worster MG (2014) A physically based parameterization of gravity drainage for sea-ice. *Journal of Geophysical Research-Oceans* **119**, 5599–5621.

Rignot E, Jacobs S, Mouginot J and Scheuchl B (2013) Ice-shelf melting around Antarctica. *Science (New York, N.Y.)* **341**(6143), 266–270.

Rysgaard S and 9 others (2011) Sea ice contribution to the air–sea CO_2 exchange in the Arctic and Southern Oceans. *Tellus B* **63**(5), 823–830.

Schoemann V, Becquevort S, Stefels J, Rousseau V and Lancelot C (2005) Phaeocystis blooms in the global ocean and their controlling mechanisms: a review. *The Journal of Sea Research* **53**, 43–66.

Scott FJ and Marchant HJ (2005) *Antarctic Marine Protists*. Camberra: Goanna Print.

Spreen G, Kaleschke L and Heygster G (2008) Sea ice remote sensing using AMSR-E 89-GHz channels. *Journal of Geophysical Research-Oceans* **113**(C2).

Stammerjohn SE, Martinson DG, Smith RC, Yuan X and Rind D (2008) Trends in Antarctic annual sea ice retreat and advance and their relation to El Niño-Southern Oscillation and Southern Annular Mode variability. *Journal of Geophysical Research* **113**(C3). doi: 10.1029/2007JC004269.

Thomas CR (1997) *Identifying Marine Phytoplankton*. San Diego: Academic Press.

Thomas M and 6 others (2020). Tracer measurements in growing sea ice support convective gravity drainage parameterizations. *Journal of Geophysical Research: Oceans* **125**, e2019JC015791. https://doi.org/10.1029/2019JC015791.

Tison J-L and 17 others (2017*b*) Biogeochemical impact of snow cover and cyclonic intrusions on the winter Weddell Sea ice pack. *Journal of Geophysical Research: Oceans* **122**, 9548–9571.

Tison J-L, Delille B and Papadimitriou S (2017*a*) Gases in sea ice. In Thomas DN (ed.), *Sea Ice*. Chichester, UK: John Wiley and Sons, pp. 433–471.

Turner J and 6 others (2017) Unprecedented springtime retreat of Antarctic sea ice in 2016. *Geophysical Research Letters* **44**(13). doi: 10.1002/2017GL073656.

Universität Bremen (2018) Sea ice concentration. (May, 15).

Vancoppenolle M, Madec G, Thomas M and McDougall TJ (2018) Thermodynamics of sea ice phase composition revisited. *Journal of Geophysical Research: Oceans* **124**. doi: 10.1029/2018JC014611.

Wells A, Wettlaufer JS and Orszag SA (2011) Brine fluxes from growing sea ice. *Geophysical Research Letters* **38**(L04501). doi: 10.1029/2010GL046288.

Williams GD, Bindoff NL, Marsland SJ and Rintoul SR (2008) Formation and export of dense shelf water from the Adélie depression. East Antarctica. *Journal of Geophysical Research: Oceans* **113**, 4039.

Worby AP, Massom RA, Allison I, Lytle VI and Heil P (1998) East Antarctic sea ice: a review of structure, properties and drift. In Jeffries MO (ed.), *Antarctic Sea Ice: Physical Properties, Interactions and Variability*. Washington, DC: American Geophysical Union, pp. 41–67. (Antarctic Research Series 74).

Zhou J and 9 others (2013) Physical and biogeochemical properties in landfast sea ice (Barrow, Alaska): insights on brine and gas dynamics across seasons. *Journal of Geophysical Research: Oceans* **118**(6), 3172–3189.

Zhou J and 14 others (2014) Physical and bacterial controls on inorganic nutrients and dissolved organic carbon during a sea ice growth and decay experiment. *Marine Chemistry* **166**, 59–69.

Appendix C: The future of Arctic sea-ice biogeochemistry and ice-associated ecosystems

nature climate change

PERSPECTIVE

https://doi.org/10.1038/s41558-020-00940-4

The future of Arctic sea-ice biogeochemistry and ice-associated ecosystems

Delphine Lannuzel[1]✉, Letizia Tedesco[2], Maria van Leeuwe[3], Karley Campbell[4], Hauke Flores[5], Bruno Delille[6], Lisa Miller[7], Jacqueline Stefels[3], Philipp Assmy[8], Jeff Bowman[9], Kristina Brown[7], Giulia Castellani[5], Melissa Chierici[10,11], Odile Crabeck[12], Ellen Damm[5], Brent Else[13], Agneta Fransson[8], François Fripiat[14], Nicolas-Xavier Geilfus[15], Caroline Jacques[16], Elizabeth Jones[10], Hermanni Kaartokallio[2], Marie Kotovitch[6,16], Klaus Meiners[17], Sébastien Moreau[8], Daiki Nomura[18], Ilka Peeken[5], Janne-Markus Rintala[19], Nadja Steiner[7], Jean-Louis Tison[16], Martin Vancoppenolle[20], Fanny Van der Linden[6,16], Marcello Vichi[21] and Pat Wongpan[22]

The Arctic sea-ice-scape is rapidly transforming. Increasing light penetration will initiate earlier seasonal primary production. This earlier growing season may be accompanied by an increase in ice algae and phytoplankton biomass, augmenting the emission of dimethylsulfide and capture of carbon dioxide. Secondary production may also increase on the shelves, although the loss of sea ice exacerbates the demise of sea-ice fauna, endemic fish and megafauna. Sea-ice loss may also deliver more methane to the atmosphere, but warmer ice may release fewer halogens, resulting in fewer ozone depletion events. The net changes in carbon drawdown are still highly uncertain. Despite large uncertainties in these assessments, we expect disruptive changes that warrant intensified long-term observations and modelling efforts.

The reduction in Arctic sea ice is one of the most prominent manifestations of global climate change, with implications for the planetary albedo and ocean stratification, accelerating global warming and possibly affecting the global overturning circulation and northern hemisphere weather patterns. At the interface between the ocean and atmosphere, sea ice is a thin, ephemeral and active environment through which heat, momentum and mass (for example, fluid, gas and solutes) are regulated. These fluxes contribute to physical and biogeochemical processes (Fig. 1) that influence the climate system, provide food and support businesses.

Primary producers within the ice (ice algae, sympagic) and in the underlying ocean (phytoplankton, pelagic) rely on light and nutrients to grow. When conditions are optimal, sea ice harbours dense communities of algae, with sea-ice chlorophyll *a* concentrations among the highest ever recorded for any aquatic environment[1]. Ice algae and phytoplankton form the base of the food web, supporting key foraging species such as Arctic cod (*Boreogadus saida*), which sustain subsistence species like ringed seals and beluga whales[2,3]. Primary producers also control the production and export of particulate organic carbon (POC) to the deep ocean, the so-called 'biological carbon pump'[4,5]. This biological pump can be particularly efficient in sea-ice-covered areas because ice algae often form fast-sinking aggregates[4,5].

The sea-ice zone is also chemically active. The distribution, timing and properties of the sea-ice cover control the air–sea exchange of carbon dioxide (CO_2), and the Arctic Ocean is currently a sink for atmospheric CO_2 (refs. [6,7]). Sea ice also regulates the uptake and emission of other climate-relevant gases such as methane (CH_4) and dimethylsulfide (DMS), providing positive and negative climate feedbacks, respectively (Fig. 1). The ecosystem services provided by sea ice are however under threat in the Arctic due to its rapid retreat (Fig. 2) at a pace dictated by cumulative CO_2 emissions[8] as well as other anthropogenic stressors (Box 1).

The decrease in Arctic sea-ice extent spans all seasons and culminates in summer[9]. Arctic sea ice has also thinned over the last four decades[10] in response to warming. Older ice that has survived multiple summers (multi-year ice (MYI)) is rapidly shrinking and being replaced by first-year ice (FYI) that melts completely during the spring and summer each year[9,11]. Freeze-up also starts later and melt onset is earlier than in the recent past, leading to a longer ice-free period[12]. The snow cover is becoming thinner[13], while the extent of highly biologically productive marginal ice zones (MIZ) is

---

[1]Institute for Marine and Antarctic Studies, University of Tasmania, Hobart, Tasmania, Australia. [2]Finnish Environment Institute, Marine Research Centre, Helsinki, Finland. [3]Groningen Institute for Evolutionary Life Sciences, University of Groningen, Groningen, The Netherlands. [4]Department of Arctic and Marine Biology, The Arctic University of Norway, Tromsø, Norway. [5]Helmholtz Centre for Polar and Marine Research, Alfred Wegener Institute, Bremerhaven, Germany. [6]Unité d'océanographie chimique, FOCUS, Université de Liège, Liège, Belgium. [7]Institute of Ocean Sciences, Fisheries and Oceans Canada, Sidney, British Columbia, Canada. [8]Norwegian Polar Institute, Fram Centre, Tromsø, Norway. [9]Scripps Institution of Oceanography, University of California, San Diego, CA, USA. [10]Institute of Marine Research, Fram Centre, Tromsø, Norway. [11]University Centre in Svalbard, Longyearbyen, Svalbard, Norway. [12]Centre for Ocean and Atmospheric Sciences, University of East Anglia, Norwich, UK. [13]Department of Geography, University of Calgary, Calgary, Alberta, Canada. [14]Department of Geosciences, Environment and Society, Université Libre de Bruxelles, Brussels, Belgium. [15]Centre for Earth Observation Science, University of Manitoba, Winnipeg, Manitoba, Canada. [16]Laboratoire de Glaciologie, DGES, Université Libre de Bruxelles, Brussels, Belgium. [17]Australian Antarctic Division, Hobart, Tasmania, Australia. [18]Hokkaido University, Hakodate, Hokkaido, Japan. [19]Institute for Atmospheric and Earth System Research (INAR), Faculty of Science, University of Helsinki, Helsinki, Finland. [20]Laboratoire d'Océanographie et du Climat, Institut Pierre-Simon Laplace, Paris, France. [21]Department of Oceanography, University of Cape Town, Cape Town, South Africa. [22]Australian Antarctic Program Partnership, Institute for Marine and Antarctic Studies, University of Tasmania, Hobart, Tasmania, Australia. ✉e-mail: delphine.lannuzel@utas.edu.au

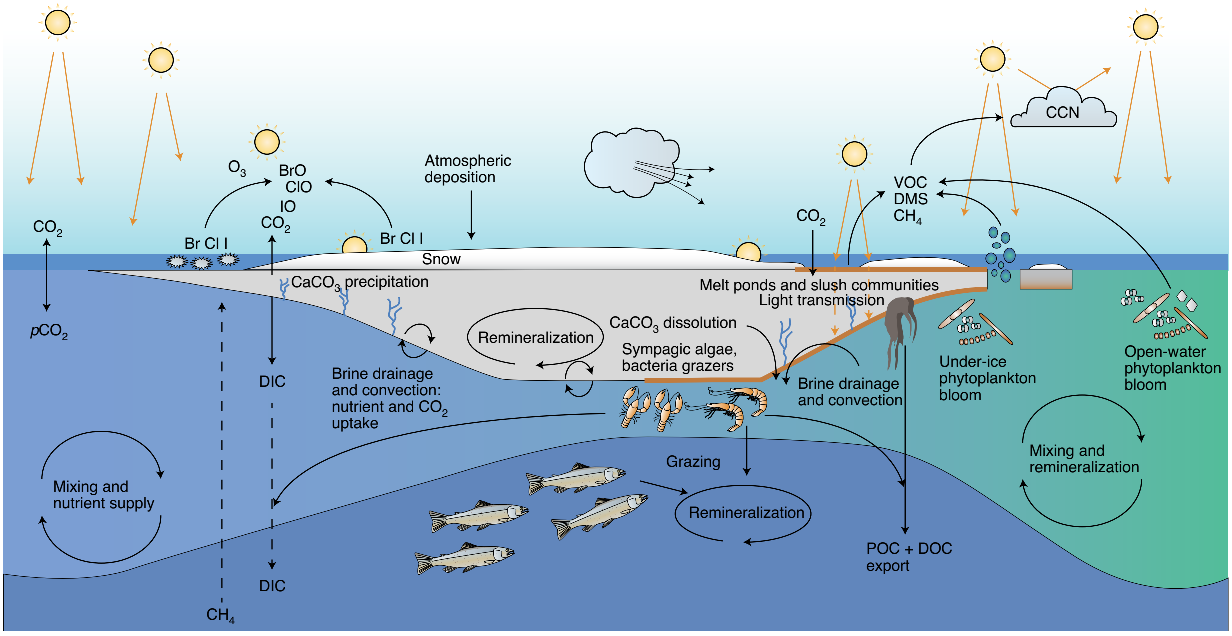

Fig. 1 | Schematic of seasonal sea-ice biogeochemical processes in the Arctic Ocean. Black arrows represent the directionality of biogeochemical exchanges; for example, across an interface (such as CO$_2$ efflux from the ocean to the atmosphere and release of reactive halogen species from the ice surface) or throughout an interval (such as brine drainage and convection along the ice–water interface, and heterotrophic remineralization of organic material throughout the brine network). Dashed lines illustrate diffusive gradients, such as that of dissolved inorganic carbon (DIC). Yellow arrows indicate solar radiation. Ice-associated and pelagic microalgal communities and their grazers are represented by orange shading and symbols. The biological carbon pump links carbon exchange processes in the surface to sequestration at depth through POC and dissolved organic carbon (DOC) export, illustrated by arrows penetrating below the mixed layer (darker shading). Surface processes further impact climate active gases, such as DMS and CH$_4$ as well as volatile organic compounds (VOC), which can contribute to the formation of cloud condensation nuclei (CCN). Figure adapted from ref. [109].

on the rise in summer, mostly advancing poleward towards regions where sea ice is increasingly younger and thinner[14]. These trends are projected to continue (Fig. 2), with their amplitude depending on the carbon emission scenario considered[15]. Several models predict a nearly ice-free summer Arctic Ocean by the end of the century or earlier under the Representative Concentration Pathway 8.5 (RCP8.5) 'worst-case' emission scenario[16] (Fig. 2c). Rain, rather than snow, may become the dominant form of precipitation by the end of the century[17], and ocean stratification is projected to increase[18].

As a consequence of these changes, sea ice is expected to generally become thinner, younger and more ephemeral than before (Fig. 2). This Perspective assesses potential changes for key sea-ice climatic, biogeochemical and biological properties as well as processes in response to environmental changes, and highlights crucial uncertainties in the understanding of the Arctic sea-ice system. With this assessment, we aim to motivate future scientific efforts, raise public awareness and facilitate policy making.

Framework

We consider the following aspects of change in the region.

Arctic sea-ice regions. The interplay between ocean circulation, continental influences, riverine input and complex bathymetry lead to vastly different sea-ice conditions across the Arctic. For example, the Canadian Arctic Archipelago (CAA) exhibits a large fraction of perennial land-fast sea ice. The Central Basin contains both seasonal and perennial pack ice, whereas the Eastern Arctic sector is mostly covered by seasonal drift ice[9] (Fig. 3). This contrast across icescapes leads to regional differences in biogeochemical processes and associated ecosystems. Ice-covered regions located north of the Arctic circle are discussed in this paper, and, when possible, our future expectations reflect regional differences.

Forcing categories. The near-future (that is, middle of this century) expectations address the potential response of key variables in two categories of physical forcings:

(1) Changes in sea-ice coverage (that is, horizontal changes): reduced overall sea-ice concentrations and reduced duration of the sea-ice season (later freeze-up and earlier break-up).
(2) Changes in sea-ice properties (that is, vertical changes): younger and thinner sea ice, and decreasing snow accumulation (and increasing rain).

Changes in environmental conditions

Changes in the properties and coverage of sea ice directly impact the light, nutrients and space available for primary producers to grow, with cascading effects on the entire Arctic marine ecosystem.

Light. Light is a primary driver of algal growth in the sea-ice zone. At high latitudes, a strong seasonality in light cycle[19] dictates the timing and magnitude of ice algal and phytoplankton blooms[20,21]. Downwelling solar radiation is largely reflected back to space due to much higher albedos for sea ice and snow than for seawater. Albedo is higher for deep snow-covered and thick ice, and lower when moisture is present within the snow, accumulated at the surface as melt ponds or as open water between ice floes[22]. The fraction of light available within sea ice decreases exponentially with depth; absorption is larger for snow than for sea ice and scattering depends on the presence of brine pockets, air bubbles

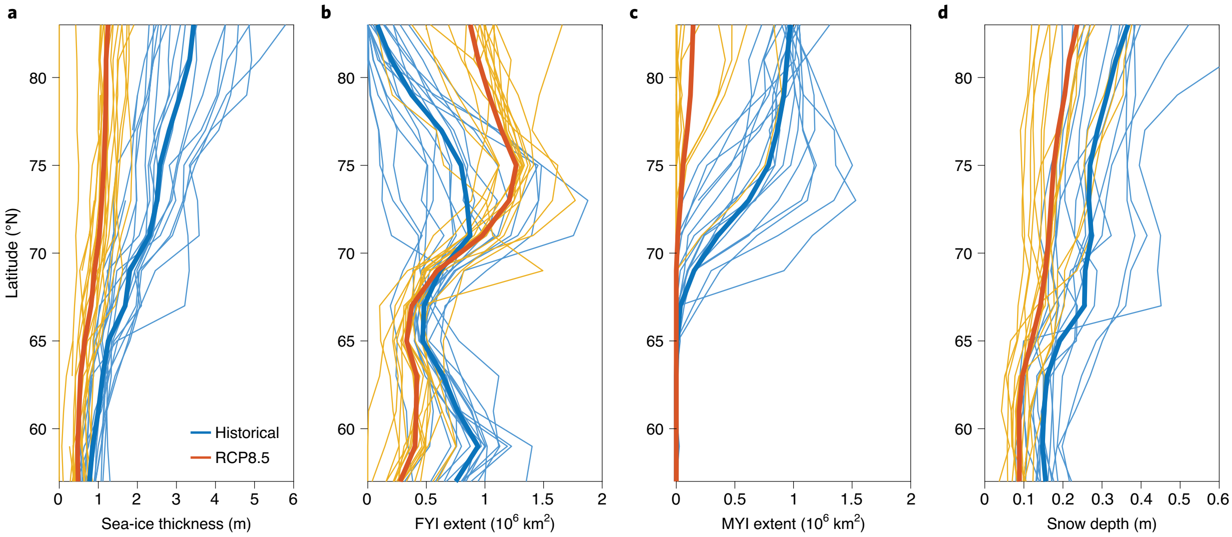

Fig. 2 | Past and predicted changes in sea-ice physical characteristics along latitudes. Comparison between the historical (1961–2005, blue lines) and the 'worst-case' RCP8.5 scenario (2061–2100, orange lines). Medians of the empirical probability density functions from each of 18 CMIP5 climate models[42] (thin lines) and their ensemble mean (thick lines) for sea-ice thickness (**a**), first-year ice extent (**b**), multi-year ice extent (**c**) and snow depth (**d**).

and impurities. Thus, depending on sea-ice and snow conditions, anywhere from less than 1% to ~20% of the incoming sunlight is transmitted to the ocean underneath[23]. Ice algae and phytoplankton directly respond to changes in available light stemming from variations in ice thickness, snow depth[20], lead opening[21] and/or melt pond formation[24].

Box 1 | Other anthropogenic stressors

Reduced sea-ice extent will result in an increase in human pressure on wildlife in the Arctic through shipping, oil and gas exploration, fisheries and tourism. In addition to direct pressure on stocks by fishing activities, general disturbance by an increasing human presence will have negative effects on the life cycles of many megafauna species. Smaller species seem to be more sensitive to pollution due to their higher surface area-to-volume ratios[110]. Concentrations of microplastics in sea ice are several orders of magnitude higher than in the underlying water[111], with potential to affect both sea-ice properties (for example, salinity and albedo) and marine life[112]. Given the small size of the particles (<50 µm), which are in the same range as sea-ice algae, it is likely that they are incorporated into the food web with yet unknown consequences.

Models suggest sea-ice retreat will promote ocean acidification due to increased air–sea exchange and meltwater input[113]. However, these models do not account for the rejection of CO$_2$-rich brines that further promote ocean acidification[114], nor for the dissolution of calcium carbonate in sea ice during melt, which can act to potentially decrease the effect of ocean acidification at the most critical time of the year in ice-covered areas[115] or remove alkalinity from the Arctic Basin via sea-ice drift and exit through the Fram Strait[116]. Mortenson[84] found that summer calcium carbonate saturation states are overestimated when the sea-ice carbon pump is excluded from models. Nonetheless, while the impact of changes in sea-ice properties is uncertain, changes in sea-ice coverage will probably promote ocean acidification overall.

Changes in both sea-ice coverage and sea-ice properties have similar effects on light availability. There is little doubt that because of snow and ice thinning, as well as longer surface melt and open-water seasons, the Arctic planetary albedo has decreased by 4–6% between 1979 and 2011 (ref. [25]). Thus, the light supply to ice algae and phytoplankton has likely increased over the same period, as indicated by model simulations[26]. Increased transmission of light includes greater exposure to potentially damaging ultraviolet (UV) radiation[27]. However, sympagic algae have shown capacity for UV photoprotection[28] and the positioning of a majority of cells beneath UV-absorbing materials (for example, snow, ice and other algae) likely makes UV impact minimal[29]. More light at the ocean surface contributes to initial increases in overall pelagic Arctic primary production, which has been captured by ocean colour[30]. Earth system model simulations reproduce this increase as long as nutrients are sufficient[18].

Future expectations. Likely increase in light availability (Fig. 4).

Nutrients. Nutrients are also key for algal growth. Both in sea ice[20,31] and in the water column[32], nutrients are thought to regulate the bloom magnitude and termination. However, compared to light, large uncertainties remain in the understanding of nutrient dynamics in sea ice. The ultimate source of nutrients in sea ice is seawater, with a possible atmospheric contribution[33] depending on the season. Nutrient concentrations in sea ice are controlled by brine circulation and exchange with underlying seawater as well as biogeochemical processes such as assimilation and remineralization[34]. Adsorption to brine channel walls and biofilm processes likely affect sea-ice nutrient availability and mobility[35]. Nutrients in the underlying seawater are controlled by stratification and the origin of water masses (that is, nutrient-rich Pacific versus nutrient-poor Atlantic waters), river and glacial runoff, and advection[36].

Sea-ice coverage. Increased meltwater and riverine input[37,38] enhance surface-water stratification, whereas thinner ice with larger open-water fraction increases exposure of the surface ocean to wind and waves[39], promoting mixing. These processes have competing and uncertain effects on the supply of sub-surface, nutrient-rich

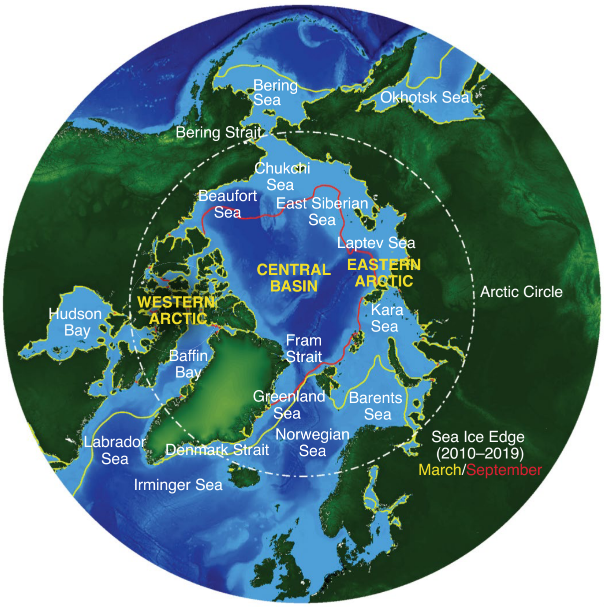

Fig. 3 | Map of the Arctic Ocean. The Western Arctic, Central Basin and Eastern Arctic regions discussed in the text are indicated in yellow, with bathymetry (blue shading) and land elevation (green shading) shown. Red and yellow lines represent the 2010–2019 averaged minimum (September) and maximum (March) sea-ice extents, respectively.

waters to phytoplankton and ice algae, and therefore on primary production. Earth system model simulations and theoretical arguments suggest that increasing stratification and decreasing nutrients will dominate in the pelagic environment[18]. Other models predict an increase in atmospheric deposition, which may overcome the nutrient limitation induced by the increasing stratification[40].

Sea-ice properties. Changes in nutrient concentrations in sea ice are mainly affected by vertical processes (for example, brine dynamics and ice–ocean fluxes), and future brine dynamics depend on ice temperature and salinity. Ice temperatures may increase because of a warmer atmosphere but could also decrease due to less snow accumulation. Sea-ice salinity is expected to increase in autumn and winter—because FYI is more saline than MYI—but would become lower in summer, due to increased flushing associated with earlier melt onset[41]. If seawater nutrient concentrations remain unchanged, more saline brine in winter would imply higher nutrients in sea ice in spring and possibly increase sympagic productivity. However, the nutrients gained from dynamics within sea ice would be counterbalanced if seawater nutrient concentrations decrease[18].

Future expectations. High uncertainties on future nutrient stocks in open waters and on nutrient dynamics in sea ice (Fig. 4).

Habitat. Sympagic algae depend on sea ice as a substrate to grow. Since a large fraction of Arctic sea ice is FYI, and more FYI is projected to replace MYI in the future (Fig. 2), sea ice may be considered a limiting resource and controlling factor of algal growth.

Sea-ice-algal biomass flourishes in brines mostly close to the underlying seawater (Fig. 1), where nutrients are easily accessible, and extends as far upwards as brine permeability allows fluid transport and nutrient supply[34]. The permeable space within sea ice therefore sets a boundary for algal biomass accumulation. Sea-ice permeability is determined by brine temperature and salinity: that is, the colder and saltier the ice, the lower the brine volume and permeability. We anticipate that ongoing climate warming will result in two possible categories of change in terms of sea-ice permeability and, consequently, space for colonization inside the ice.

Sea-ice coverage. In the most extreme case, the total disappearance of sea ice in some regions will have the obvious consequence of a disruption of sea-ice sympagic productivity in these areas. The delayed formation and earlier melt onset of seasonal sea ice will further reduce the space available for colonization. The loss of sea ice as a physical habitat for organisms may become a primary factor limiting ice-associated organisms and biodiversity in some Arctic regions[42].

Sea-ice properties. During the melting period, the current and future increase in temperatures at the interface between the lower atmosphere and the surface snow, ice or ocean (the so-called 'skin temperature') would lead to warmer and more permeable sea ice, thus to more habitable space. In winter, however, snow insulation, sea-ice temperature and permeability would decrease with thinner snow (Fig. 2d), contracting brine volume and reducing the space available for colonization.

Future expectations. Overall, the sea-ice habitat will likely decrease as sea ice continues to shrink (Fig. 4). Within the remaining sea ice, the space available for colonization may increase with warmer ice temperatures in spring–summer, allowing for higher local biomass build-up in ice, while in autumn–winter, the reverse will occur.

Changes in biota

Changes in the light, nutrient and habitat conditions discussed above affect the timing, composition and abundance of primary producers and, more specifically, the relative contribution of ice algae versus phytoplankton. Changes in primary production may then subsequently impact secondary production (microbial and metazoan consumers), higher trophic levels and ocean carbon sequestration.

Microalgal communities. Shifts in ice algae and phytoplankton communities will have cascading consequences for the Arctic marine ecosystem. For example, the efficiency of carbon export and role of organisms in the food web are dependent on the size and shape of algal cells. Furthermore, production of secondary aerosol precursors (that is, volatile organics, including DMS) varies between algae species.

Sea-ice coverage. The transition from MYI to FYI will reduce the availability of overwintering habitat and will possibly result in a decrease in diversity of the ice algae community[43,44]. Intrusion of sub-Arctic phytoplankton species like *Phaeocystis* into the high Arctic[21] will result in a more uniform latitudinal distribution of species. In particular, the abiotic changes described above will favour phytoplankton with greater capacity for growth under higher light conditions, and possibly lower nutrients and salinities compared to present communities[45]. This may include a greater presence of flagellate species within communities that at present are overwhelmingly dominated by diatoms[46]. We also anticipate a decrease in abundance of sea-ice specialists, such as *Nitzschia frigida*, in favour of cryo-pelagic species, like *Fragilariopsis cylindrus*. Melt ponds might become an increasingly dominant feature of spring sea ice, and they may favour the development of dense algal colonies like the centric diatom *Melosira arctica*[47], which presently drives episodic pulses of carbon export to the benthos[4]. Under-ice pelagic diatom species (*Chaetoceros*, *Thalassiosira* and *Fragilariopsis*) are also likely to increase in prevalence with melt pond coverage[1].

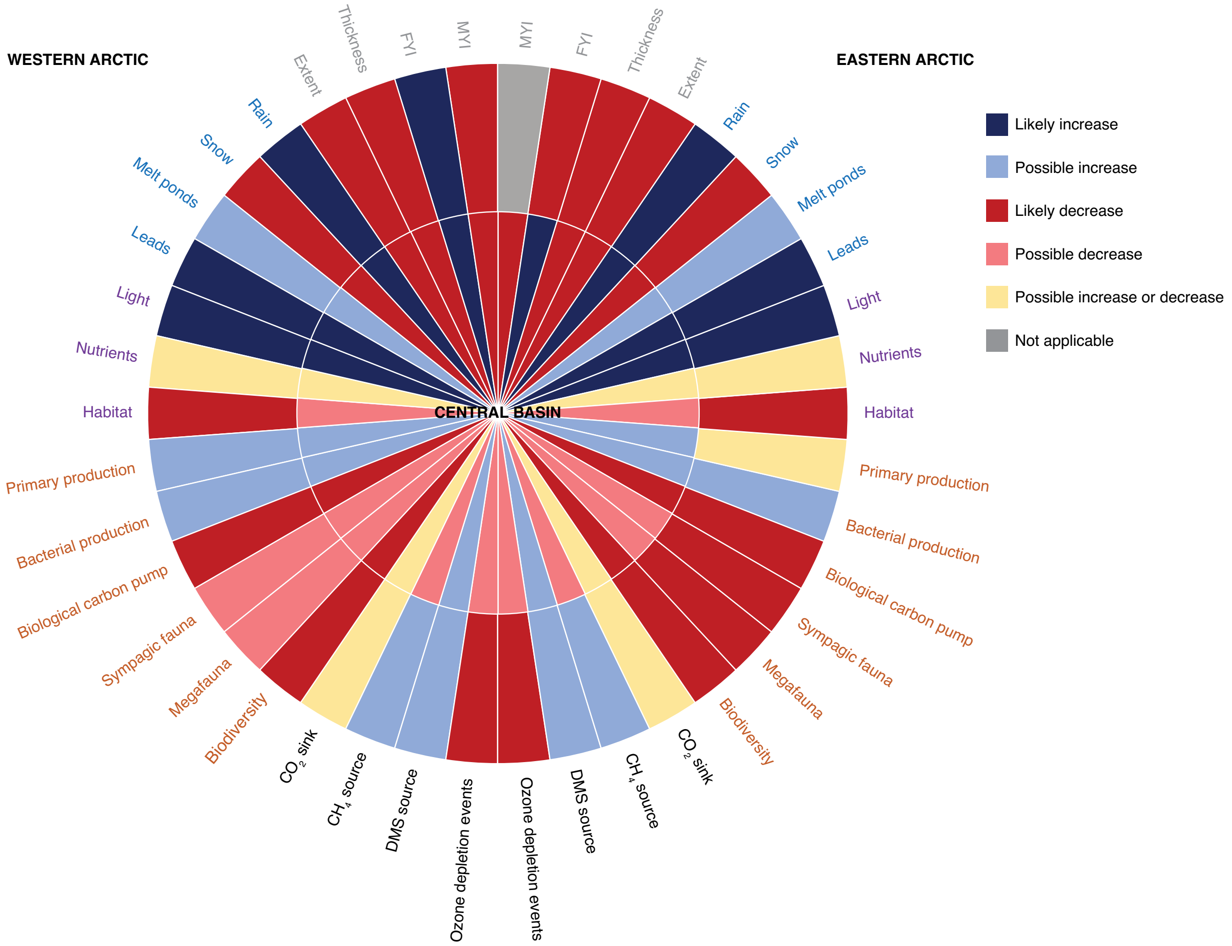

Fig. 4 | Future expectations of changes in the sea-ice biogeochemical system in the Arctic. The Western Arctic includes the Chukchi, Beaufort and Canadian Archipelago shelves, and the Eastern Arctic includes the shelves from the Barents to East Siberian Seas (as in Fig. 3). The categories of changes are repeated opposite to each other in the schematic hemispheres of the Western Arctic Ocean and the Eastern Arctic Ocean of the circular diagram. Their colours indicate sea-ice changes (grey), icescape changes (blue), abiotic drivers (purple), biological changes (brown) and changing gas fluxes (black). For further details, see Box 2.

Both open-ocean and under-ice phytoplankton production are expected to increase in magnitude and aerial extent as well as commence earlier in the spring due to earlier melt onset and increased light availability. However, the overall increase in phytoplankton production will be constrained by the finite availability of nutrients in the water column. Autumn phytoplankton blooms are likely to become a regular feature as a result of later freeze-up, particularly at the periphery of the Arctic Ocean[48].

Sea-ice properties. The predicted increase in light availability from a thinning ice and snow cover will increase the potential for ice-algal primary production across the Arctic. The substantial thinning of the snow cover is expected to have the greatest effect south of 66 °N, where light availability will significantly extend the length of the sympagic growing season[42]. From 66 to 74 °N, the decrease in duration of ice cover into spring and summer will set an upper limit to the total accumulation of ice-algal biomass[42]. In the Eurasian shelf areas and the CAA, the bloom of sea-ice bottom micro-algal communities may start and end earlier in the spring[49]. We expect the largest relative increase in algal primary production in the high Arctic due to the more productive FYI largely replacing the less productive MYI[42]. Whereas an increase in stratification of the upper water column would decrease the availability of surface water nutrients for bottom-ice communities, some regions will experience enhanced vertical mixing due to new open-water areas exposed to winds and storms[39], enhanced tidal currents[50] or increased upwelling[51], which would benefit ice-algal production.

The presence of under-ice phytoplankton blooms will become more frequent as the Arctic ice cover becomes thinner and more transparent, with possibly greater coverage of melt ponds[52] and leads[21] that act as windows into the underlying ocean. However, the blooms may also become smaller in magnitude and shorter in duration if nutrients become more limited.

Future expectations. Overall, increasing open-ocean conditions are expected to favour phytoplankton growth and an overall shift towards cryo-pelagic and pelagic species. As light availability and surface stratification increase, nutrients will become increasingly

Box 2 | Uncertainties in these prognoses

Our group of sea-ice experts has generated future expectations of how the changing sea-ice environment is likely to impact biogeochemical systems, based on the current knowledge of the Arctic (Fig. 4). These attempts are not quantitative. New and sustained field data and improved models are crucially needed to improve predictive capabilities. The most pertinent knowledge gaps include: sustained snow observations; the relative importance of freshwater inputs and storm events on Arctic Ocean stratification and nutrient budgets; contributions of the Pacific and Atlantic water masses to the nutrient reservoirs in the Arctic Ocean; the effect of shorter but more intense sea-ice algal blooms on biogases, consumers and carbon export; the composition of current sympagic algal communities and the potential shifts in speciation as a consequence of environmental changes; long-term trends in under-ice phytoplankton blooms; the life cycles of sympagic flora and fauna, and their resilience to habitat change or loss; the diversity, distribution and standing stocks of pelagic macrofauna, especially fish, in the Central Basin; partitioning between pathways of carbon transmission and nutrient cycling in the ecosystem, and their effect on the biological carbon pump; air–ice–water gas fluxes over the annual cycle, particularly in winter; the impact of shifts in phytoplankton phenology on pelagic DMS production; and the impact of ocean acidification on ice-associated species.

limiting for both sympagic and pelagic production. The sign and magnitude of changes in primary production will vary regionally, with the largest relative increase expected in the Central Basin (Fig. 4). In the Western Arctic, where FYI is expected to largely replace MYI, a general increase in primary productivity is expected (Fig. 4) alongside a likely loss in ice-algal biodiversity. In the Eastern Arctic, where a large fraction of FYI is shrinking, the potential increase in primary productivity will be constrained not only by uncertain future nutrient inventories, but also by the potential loss of habitat (Fig. 4).

Microbial loop. Although growth temperatures in sea ice are well below optimal, bacterial production in sea ice can exceed rates measured in the productive waters of temperate regions[53]. Carbon used to support this heterotrophic production is largely sourced from primary producers[54]. As a result, primary and secondary microbial production in the sympagic realm are expected to exhibit similar changes with climate warming.

Sea-ice coverage. As MYI has a low brine volume fraction compared to FYI, a shift from MYI to FYI will promote heterotrophic activity.

Sea-ice properties. The thinner and warmer sea ice in summer will support a greater degree of heterotrophic activity[55]. Because the brine channels in warmer ice are more connected—with larger pore spaces that may facilitate the grazing of bacteria by bacterivorous protists—there is the potential for a strengthened carbon transfer from microbial compartments to upper trophic levels. Following the trends in primary productivity, pelagic microbial heterotrophic activity is most likely to increase following spatial and seasonal changes in primary production.

Future expectations. Changes in the Arctic will result in increased heterotrophic activity (Fig. 4). The heterotrophic microbial community will directly benefit from increases in primary productivity. Secondly, heterotrophic activity will increase with warmer sea-ice temperatures.

Metazoan consumers. The continuing transformation of sea-ice habitats will profoundly change the biodiversity of Arctic metazoan consumer communities that depend significantly on ice algae as a carbon source[56]. On the Arctic shelves, a warmer ocean with a shorter seasonal ice coverage will promote the replacement of polar communities by sub-polar communities, causing a retreat of cold-adapted and sympagic species towards the Central Basin[2,57].

Sea-ice coverage. Changes in the areal coverage and timing of sea ice may disrupt the life cycles of sympagic consumers, especially those not adapted to survive in the water column[58]. Shorter ice-algae bloom seasons in the Eastern Arctic[59] will reduce sympagic food availability for ecologically important species, such as *Calanus*[58], ice amphipods and polar cod. Emerging mismatches of the timing of ice algae and phytoplankton blooms with grazer reproductive cycles could reduce reproductive success[44,58]. In some regions, an increase in total production of the Arctic Ocean, with a shift from sympagic to pelagic producers, would promote growth of herbivorous consumers[59]. Omnivores and predators (*Themisto* spp., euphausiids, jellyfish) may regionally increase in biomass too[59].

Sea-ice properties. The change to thinner, younger and more dynamic sea ice will alter the distribution patterns of sympagic consumers, including under-ice amphipods, in-ice meiofauna and forage fish. Species-specific habitat requirements cause variations in consumer community structure in response to variations in sea-ice properties[60]. On the shelves, the anticipated replacement of polar sympagic consumers by sub-polar pelagic consumers will predominantly result in a replacement of large, lipid-rich zooplankton by more numerous but smaller, and comparatively lipid-poor, species; for example, *Pseudocalanus* spp., *Metridia* spp. and *Cyanea* spp. Furthermore, these changes will negatively affect higher levels of the food chain; for instance, the replacement of polar cod with capelin and sand lance species of lower energetic contents[2]. In the future seasonally ice-covered Central Basin, a potential relative increase in primary production is unlikely to support large stocks of consumers if they cannot adapt their life cycles to the altered algal phenology[46,52]. Furthermore, declining taxonomic diversity[61] could cause a decline of functional diversity, reducing resilience to environmental stress.

Future expectations. We expect an overall decrease in biomass and diversity of sympagic consumers (Fig. 4) due to altered algal phenology and lower algal food quality. On the shelves, pelagic secondary productivity will mostly increase, but a shift to small and gelatinous zooplankton will profoundly affect food web structure. In the Central Basin, secondary productivity will remain low but loss of biodiversity will negatively affect the resilience of the ecosystem to environmental perturbations and anthropogenic stress.

Higher trophic levels and marine living resources. As sub-polar and Atlantic fish expand their ranges north, the biomass of polar cod and other cold-adapted fish resident to the Arctic Ocean[2,57] will continue to decline across many of the Arctic shelf regions[59,62]. These species have shifted their distribution range towards the northern shelf slope[57]. Benthic secondary production will generally decline due to reduced sympago-benthic coupling and a lack of ice-algae downfalls in spite of locally enhanced food availability due to increasing pelagic productivity[63]. In shallow regions, increased light and ice-scouring due to sea-ice retreat might positively impact macroalgal growth (for example, kelp[64]), and through increased planktonic primary production may also locally favour benthic animal communities including sponges[65]. Continued declines in key prey fish, such as polar cod, will likely intensify the loss of sympagic predators, including ringed seals, beluga whales and polar bears[2,66,67], which is already being observed. Consequently, these mammals may face local- to regional-scale extinctions in the Arctic shelf domains. In contrast, the presence of generalist predators like baleen whales, orcas and certain seabird species is expected to increasingly expand into Arctic shelf seas[68].

Future expectations. The abundance of species endemic or common to the Arctic like beluga whales, polar bears and polar cod will decline (Fig. 4) as sub-polar species become increasingly abundant in Arctic waters. Iconic Arctic fauna face the risk of local to regional extinction.

Biological carbon pump. A small fraction of the POC produced at the surface of the Arctic Ocean by sea-ice algae and under-ice phytoplankton can be directly exported to the seafloor. More specifically, events of massive downward flux of *Melosira* can cause episodic maxima of carbon export[4] in the Central Basin. The export of this POC can be significantly enhanced by minerals released by sea ice that ballast sinking algae aggregates and by zooplankton[69,70]. Primary producers also serve as a vital source of food for sympagic and (meso-)pelagic consumers. Through respiration, feeding and excretion during vertical migrations[71], as well as through faecal pellet production[72], (meso-)pelagic and sympagic consumers play an important role in the POC export and carbon burial at the seafloor.

Changing sea-ice habitats and nutrient limitation will promote a more heterotrophic food web[73]. The predicted shifts in food web structure will result in greater recycling and retention of carbon in the pelagic food web[63], which will directly compete with the intensifying biological carbon pump to determine the net flux of carbon in the Arctic Ocean. The most abundant sympagic and cryo-pelagic consumers (ice amphipods and *Calanus* spp. copepods) produce large and fast sinking faecal pellets[74]. As a result, the shift towards organisms that produce smaller faecal pellets (for example, *Pseudocalanus* spp.) will decrease the contribution of consumers to POC export on the Arctic shelves. In the Central Basin, future POC export by consumers is expected to remain low[75], but it has the potential to further decrease when populations of sympagic fauna decline.

Future expectations. The expected increase in primary productivity, shift towards smaller algae and warmer ice will lead to more grazing by smaller zooplankton and higher microbial remineralization. So, except for potentially periodic *Melosira* blooms and subsequent export pulses, all processes point towards a less efficient biological carbon pump (Fig. 4), as we expect a shift from an export system to a retention system.

Changes in climate-active gases

Gas dynamics and fluxes in sea ice strongly depend on ice temperature, salinity and texture. In addition, most climatically active gases (for example, CO_2, CH_4 and DMS) are produced and/or consumed by organisms living in or under the ice, and are taken up or released during the natural cycle of sea-ice formation and melt. The cycles of these 'biogases' are therefore closely linked to biological processes. Ice algae, phytoplankton and bacterial communities will adapt to changes in sea ice, with direct consequences for the uptake and release of climate active gases.

CO_2. During autumn and winter, sea ice acts as a source of CO_2 (ref. [76]) due to high brine partial pressure of CO_2 (pCO_2) and precipitation of calcium carbonate (Fig. 1)[77]. However, during spring and summer, sea ice acts as a sink of CO_2 due to brine dilution, calcium carbonate dissolution and the biological carbon pump, driven by algal productivity[78]. The balance may be a net sink due to the net export of brine to underlying waters.

Sea-ice coverage. In the Central Basin, the formation of more new ice will result in an increased CO_2 efflux to the atmosphere in winter[79]. However, sea-ice formation will also increase the rejection of CO_2-rich brines to the ocean[80]. Model simulations indicate that this rejection to the ocean and export to depth of CO_2-rich brines combined with precipitation and transport of calcium carbonate during sea-ice growth and melt processes (sea-ice carbon pump) has a minor effect on the global oceanic carbon uptake but can have larger regional effects[81,82].

The increase in ice-free ocean area and consequent carbon drawdown may have enhanced the CO_2 sink by as much as 1.4 TgC yr^{-1} between 1996 and 2007 (ref. [83]), and including the ice algal system may have added another 2% per decade to the pan-Arctic Ocean carbon uptake[84]. In winter, storms and openings in the ice cover, such as leads and cracks, will allow for increased ocean CO_2 uptake in undersaturated areas[85]. Outgassing will increase in open waters that become supersaturated (from excess respiration over photosynthesis), particularly in upwelling areas and coastal regions influenced by large rivers[86,87]. Model results indicate that enhanced fluxes due to continuing sea-ice retreat extend the maximum uptake in fall and reduce the uptake in summer[88], and the projected increase in ocean stratification will further limit the ocean's capacity to absorb CO_2 and possibly lead to widespread outgassing in summer[36,89,90].

Sea-ice properties. The shift from MYI to FYI will promote the formation of frost flowers and upwards brine rejection, which mediates ice-to-atmosphere CO_2 transfer in winter[91,92]. The general increase in ice temperature and permeability will favour air–sea ice gas exchange. However, with warmer and more rainy conditions, snow will tend to melt and refreeze (superimposed ice formation), decreasing air–sea-ice gas exchange[79]. In spring, precipitation (snow and rain) may promote melt pond formation, leading to greater CO_2 uptake from the atmosphere. The prediction of higher primary production at the bottom of Arctic FYI should enhance CO_2 uptake from the water[93] in spring and summer. A change from MYI to FYI will increase brine drainage and, therefore, increase brine CO_2 export from the ice to underlying water.

Future expectations. Increased air–sea fluxes, due to more open-ocean area and more leads over undersaturated waters, and increases in CO_2-rich brine export may lead to an increase in the Arctic Ocean CO_2 sink. This additional sink would be offset by increased stratification (capping CO_2 uptake) and outgassing in some regions due to enhanced vertical mixing with deep CO_2-rich waters, and to our prognosis that the Arctic Ocean will transfer from a carbon export system to a carbon retention system.

CH_4. The impact of sea ice on ocean–atmosphere fluxes of CH_4 is still unclear. Recent studies highlighted a CH_4 super-saturation in sea-ice-influenced waters of the Central Basin[94] and an enhanced CH_4 efflux to the atmosphere above areas with fractional sea-ice cover[95]. An impermeable sea-ice cover likely enhances CH_4 exposure to microbial oxidation[96]. This process would have the potential to reduce CH_4 sea–air fluxes, particularly above continental shelves whose sediments represent the main source of CH_4 to the Arctic Ocean[97].

Sea-ice coverage. More open water will facilitate the efflux of excess CH_4 to the atmosphere. Shorter sea-ice seasons and warmer temperatures will also result in an increase of sea-ice permeability, allowing CH_4 in under-ice seawater or in the sea ice itself to escape more readily. Indeed, seasonality directly influences ice permeability, which is one of the major physical processes controlling CH_4 storage in sea ice[98].

Sea-ice properties. The shift from MYI to FYI will accelerate CH_4 cycling and likely increase the transfer of CH_4 from sea ice to the atmosphere.

Future expectations. Significant uncertainties are still associated with the current and future CH_4 cycle in the Arctic Ocean. Nevertheless, sources of CH_4 are expected to increase. A decreasing sea-ice cover, enhanced sea-ice permeability and a shift from MYI to FYI will facilitate the CH_4 flux from the seawater to the atmosphere, likely resulting in an overall increase of the oceanic source of CH_4 in the Arctic (Fig. 4).

DMS. DMS is a precursor of sulfate aerosols in the atmosphere, limiting the exchange of both short- and long-wave radiation between Earth's atmosphere and space. Mainly derived from dimethylsulfoniopropionate (DMSP) produced by macro- and microalgae in response to stress (freezing, high salinity), DMS occurs at high concentrations in sea ice[99]. DMSP is either converted to DMS in the ice by bacterial activity and then released to the atmosphere or released to the underlying water where it is partly converted to DMS. The fraction of DMSP resulting in DMS emissions is strongly related to the abundance and taxonomy of microalgae, bacterial activity and environmental conditions. Model simulations highlight that the sea-ice sulfur cycle particularly affects DMS emissions in spring, when the accumulation of DMS under ice can sporadically escape and cause spikes in atmospheric concentrations high enough to initiate cloud nucleation[100,101] (Fig. 1).

Sea-ice coverage. Given that sea ice acts as a source of DMS to the atmosphere, sea-ice loss should weaken this source. However, an anticipated increase in under-ice and pelagic blooms—especially when consisting of *Phaeocystis* sp.—may increase the pelagic DMS source. Reduced ice extent may therefore have an insignificant impact on net, basin-scale DMS fluxes. However, regional changes in total primary production, microplankton assemblages and gas transfer velocity may result in very large regional variations in DMS fluxes.

Sea-ice properties. The shift from MYI to FYI, in association with less snow accumulation and ensuing shifts towards more *Phaeocystis* sp. and increased primary production, will promote DMS release to the atmosphere. The impact of increasing sea-ice mobility and related turbulence can potentially increase the fluxes, while increasing rain would promote flushing and release of DMS into the water column[102].

Future expectations. Since DMS pulses are associated with ice types of the MIZ, an increased aerial coverage of the MIZ is anticipated to result in increased DMS production (Fig. 4).

Halogens and ozone interactions. Reactive halogen species are responsible for atmospheric cleansing and ozone depletion events (ODEs) as well as associated mercury deposition in the polar tropospheric boundary layer[103]. Young sea ice is strongly associated with ODEs[104], which have been ascribed to the release of reactive halogen species (bromine and iodine compounds)[105] (Fig. 1). Sea ice, frost flowers and saline snow are potential sources of atmospheric halogens[105], and blowing snow above sea ice has been confirmed as a halogen source in the Southern Ocean[106].

Sea-ice coverage. A shift from sea-ice-covered seas to open waters will decrease ODEs.

Sea-ice properties. Younger and more permeable ice will likely promote salty ice and snow surfaces by brine wicking and related halogen activation. However, warmer sea-ice conditions may impede active bromine species release and ODEs requiring low surface temperatures[107]. In parallel, more rain and less snow accumulation are likely to reduce the specific surface area for halogen activation as well as the blowing-snow vector of halogen mobilization.

Future expectations. Decrease in ODEs (Fig. 4).

Challenges and future directions

The Intergovernmental Panel on Climate Change (IPCC) specifically calls for improvement in the fundamental understanding of sea ice to advance its representation in global climate models. Reducing uncertainties is currently the main challenge (Box 2). Ice algae production and biogeochemical exchange processes are now included in some Arctic ocean modelling efforts, but model intercomparisons reveal significant differences between models. Particularly important gaps include understanding and parameterizations of: (i) light transmission through snow and ice; (ii) controls on primary production and diversities in sea ice, as well as ice algal incorporation and release; and (iii) fluxes, deposition and emission of climatically active gases and aerosols.

In the short term, primary productivity is predicted to generally increase in both sea ice and seawater in the Arctic, as long as nutrients are plentiful[18,42]. The timing of the blooms is, however, likely to change, with negative downstream effects on ice-dependant consumers[58,108]. A number of studies[2,66,67] are reporting declines in condition, health and population sizes of high-Arctic top predators, which must be seen as a warning sign that ecosystem changes could be more disruptive than expected. Understanding the consequences of ecological changes in sea-ice habitats for resource conservation and management is fundamental to the development of marine governance schemes that consider both socio-economic and ecological changes.

There is an urgent need for the establishment of long-term observing platforms in climate-sensitive sea-ice regions (for example, the CAA, East Siberian Shelf and Central Basin) to collect benchmark data and to record seasonal and decadal trends, as well as to anticipate thresholds and tipping points for the full suite of variables discussed in this Perspective. Sea ice is still considered biogeochemically inert in most large-scale Arctic models and, in particular, Earth system models. As computer resources continue to become more affordable and available, we advocate for new modelling studies that can address the role of sea-ice biogeochemistry in the Earth system. This holistic approach will allow the science community to deliver firmer predictions on how the Arctic system is (and we, as a community, are) responding to the Great Arctic Thaw.

Received: 7 March 2019; Accepted: 24 September 2020;

References

1. Arrigo, K. R. in *Sea Ice* (Ed. Thomas, D. N.) 352–369 (John Wiley & Sons, Ltd, 2017).
2. Steiner, N. S. et al. Impacts of the changing ocean-sea ice system on the key forage fish Arctic cod (*Boreogadus saida*) and subsistence fisheries in the western Canadian Arctic—evaluating linked climate, ecosystem and economic (CEE) models. *Front. Mar. Sci.* **6**, 179 (2019).
3. Kohlbach, D. et al. The importance of ice algae-produced carbon in the central Arctic Ocean ecosystem: food web relationships revealed by lipid and stable isotope analyses. *Limnol. Oceanogr.* **61**, 2027–2044 (2016).
4. Boetius, A. et al. Export of algal biomass from the melting Arctic sea ice. *Science* **339**, 1430–1432 (2013).
5. Riebesell, U., Schloss, I. & Smetacek, V. Aggregation of algae released from melting sea ice: implications for seeding and sedimentation. *Polar Biol.* **11**, 239–248 (1991).
6. MacGilchrist, G. A. et al. The Arctic Ocean carbon sink. *Deep. Res. Part I Oceanogr. Res. Pap.* **86**, 39–55 (2014).
7. Bates, N. R. & Mathis, J. T. The Arctic Ocean marine carbon cycle: evaluation of air-sea CO_2 exchanges, ocean acidification impacts and potential feedbacks. *Biogeosciences* **6**, 2433–2459 (2009).
8. Notz, D. & Stroeve, J. Observed Arctic sea-ice loss directly follows anthropogenic CO_2 emission. *Science* **354**, 747–750 (2016).
9. Meier, W. N. et al. Arctic sea ice in transformation: a review of recent observed changes and impacts on biology and human activity. *Rev. Geophys.* **52**, 185–217 (2014).

10. Kwok, R. Arctic sea ice thickness, volume, and multiyear ice coverage: losses and coupled variability (1958–2018). *Environ. Res. Lett.* **13**, 105005 (2018).
11. Maslanik, J., Stroeve, J., Fowler, C. & Emery, W. Distribution and trends in Arctic sea ice age through spring 2011. *Geophys. Res. Lett.* **38**, L13502 (2011).
12. Stroeve, J. C., Crawford, A. D. & Stammerjohn, S. Using timing of ice retreat to predict timing of fall freeze-up in the Arctic. *Geophys. Res. Lett.* **43**, 6332–6340 (2016).
13. Webster, M. A. et al. Interdecadal changes in snow depth on Arctic sea ice. *J. Geophys. Res. Ocean.* **119**, 5395–5406 (2014).
14. Strong, C. & Rigor, I. G. Arctic marginal ice zone trending wider in summer and narrower in winter. *Geophys. Res. Lett.* **40**, 4864–4868 (2013).
15. IPCC *Climate Change 2013: The Physical Science Basis* (eds Stocker, T. F. et al.) 1029–1136 (Cambridge Univ. Press, 2013).
16. Overland, J. E. & Wang, M. When will the summer Arctic be nearly sea ice free? *Geophys. Res. Lett.* **40**, 2097–2101 (2013).
17. Bintanja, R. & Andry, O. Towards a rain-dominated Arctic. *Nat. Clim. Change* **7**, 263–267 (2017).
18. Vancoppenolle, M. et al. Role of sea ice in global biogeochemical cycles: emerging views and challenges. *Quat. Sci. Rev.* **79**, 207–230 (2013).
19. Berge, J. et al. In the dark: a review of ecosystem processes during the Arctic polar night. *Prog. Oceanogr.* **139**, 258–271 (2015).
20. Leu, E. et al. Arctic spring awakening — steering principles behind the phenology of vernal ice algal blooms. *Prog. Oceanogr.* **139**, 151–170 (2015).
21. Assmy, P. et al. Leads in Arctic pack ice enable early phytoplankton blooms below snow-covered sea ice. *Sci. Rep.* **7**, 40850 (2017).
22. Perovich, D. K. *Sea Ice* (Ed. Thomas, D. N.) 110–137 (John Wiley & Sons, Ltd, 2017).
23. Nicolaus, M., Katlein, C., Maslanik, J. A. & Hendricks, S. *Solar Radiation Over and Under Sea Ice During the POLARSTERN Cruise ARK-XXVI/3 (TransArc) in Summer 2011* (PANGAEA, 2011); https://doi.pangaea.de/10.1594/PANGAEA.786717
24. Arrigo, K. R. et al. Massive phytoplankton blooms under Arctic sea ice. *Science* **336**, 1408 (2012).
25. Pistone, K., Eisenman, I. & Ramanathan, V. Observational determination of albedo decrease caused by vanishing Arctic sea ice. *Proc. Natl Acad. Sci. USA* **111**, 3322–3326 (2014).
26. Horvat, C. et al. The frequency and extent of sub-ice phytoplankton blooms in the Arctic Ocean. *Sci. Adv.* **3**, e1601191 (2017).
27. El-Sayed, S. Z., Van Dijken, G. L. & Gonzalez-Rodas, G. Effects of ultraviolet radiation on marine ecosystems. *Int. J. Environ. Stud.* **51**, 199–216 (1996).
28. Elliott, A. et al. Spring production of mycosporine-like amino acids and other UV-absorbing compounds in sea ice-associated algae communities in the Canadian Arctic. *Mar. Ecol. Prog. Ser.* **541**, 91–104 (2015).
29. Ryan, K. G., Mcminn, A., Hegseth, E. N. & Davy, S. K. The effects of ultraviolet-b radiation on antarctic sea-ice algae. *J. Phycol.* **48**, 74–84 (2012).
30. Arrigo, K. R. & van Dijken, G. L. Continued increases in Arctic Ocean primary production. *Prog. Oceanogr.* **136**, 60–70 (2015).
31. Gradinger, R. Sea-ice algae: major contributors to primary production and algal biomass in the Chukchi and Beaufort Seas during May/June 2002. *Deep. Res. Part II Top. Stud. Oceanogr.* **56**, 1201–1212 (2009).
32. Tremblay, J.-E. & Gagnon, J. in *Influence of Climate Change on the Changing Arctic and Sub-Arctic Conditions* (eds Nihoul, J. C. J. & Kostianoy, A. G.) 73–93 (Springer, 2009).
33. Nomura, D. et al. Nutrient distributions associated with snow and sediment-laden layers in sea ice of the southern Sea of Okhotsk. *Mar. Chem.* **119**, 1–8 (2010).
34. Meiners, K. M. & Michel, C. in *Sea Ice* (Ed. Thomas, D. N.) 415–432 (John Wiley & Sons, Ltd, 2017).
35. Fripiat, F. et al. Macro-nutrient concentrations in Antarctic pack ice: overall patterns and overlooked processes. *Elem. Sci. Anth.* **5**, p13 (2017).
36. Tremblay, J. É. et al. Global and regional drivers of nutrient supply, primary production and CO$_2$ drawdown in the changing Arctic Ocean. *Prog. Oceanogr.* **139**, 171–196 (2015).
37. Miller, J. R. & Russell, G. L. Projected impact of climate change on the freshwater and salt budgets of the Arctic Ocean by a global climate model. *Geophys. Res. Lett.* **27**, 1183–1186 (2000).
38. Peterson, B. J. et al. Increasing river discharge to the Arctic Ocean. *Science* **298**, 2171–2173 (2002).
39. Rainville, L., M. Lee, C. & Woodgate, A. R. Impact of wind-driven mixing in the Arctic Ocean. *Oceanography* **24**, 136–145 (2011).
40. Lamarque, J. F. et al. Multi-model mean nitrogen and sulfur deposition from the atmospheric chemistry and climate model intercomparison project (ACCMIP): evaluation of historical and projected future changes. *Atmos. Chem. Phys.* **13**, 7997–8018 (2013).
41. Stroeve, J. C., Markus, T., Boisvert, L., Miller, J. & Barrett, A. Changes in Arctic melt season and implications for sea ice loss. *Geophys. Res. Lett.* **41**, 1216–1225 (2014).
42. Tedesco, L., Vichi, M. & Scoccimarro, E. Sea-ice algal phenology in a warmer Arctic. *Sci. Adv.* **5**, eaav4830 (2019).
43. van Leeuwe, M. A. et al. Microalgal community structure and primary production in Arctic and Antarctic sea ice: a synthesis. *Elem. Sci. Anth.* https://doi.org/10.1525/elementa.267 (2018).
44. Hardge, K. et al. Sea ice origin and sea ice retreat as possible drivers of variability in Arctic marine protist composition. *Mar. Ecol. Prog. Ser.* **571**, 43–57 (2017).
45. Campbell, K., Mundy, C. J., Belzile, C., Delaforge, A. & Rysgaard, S. Seasonal dynamics of algal and bacterial communities in Arctic sea ice under variable snow cover. *Polar Biol.* **41**, 41–58 (2018).
46. Leu, E., Søreide, J. E., Hessen, D. O., Falk-Petersen, S. & Berge, J. Consequences of changing sea-ice cover for primary and secondary producers in the European Arctic shelf seas: timing, quantity, and quality. *Prog. Oceanogr.* **90**, 18–32 (2011).
47. Fernández-Méndez, M. et al. Composition, buoyancy regulation and fate of ice algal aggregates in the Central Arctic Ocean. *PLoS ONE* **9**, e107452 (2014).
48. Ardyna, M. et al. Recent Arctic Ocean sea ice loss triggers novel fall phytoplankton blooms. *Geophys. Res. Lett.* **41**, 6207–6212 (2014).
49. Wassmann, P. & Reigstad, M. Future Arctic Ocean seasonal ice zones and implications for pelagic-benthic coupling. *Oceanography* **24**, 220–231 (2011).
50. Dalman, L. et al. Enhanced bottom-ice algal biomass across a tidal strait in the Kitikmeot Sea of the Canadian Arctic. *Elem. Sci. Anth.* **7**, p22 (2019).
51. Williams, W. et al. Joint effects of wind and ice motion in forcing upwelling in Mackenzie Trough, Beaufort Sea. *Cont. Shelf Res.* **26**, 2352–2366 (2006).
52. Ardyna, M. et al. Environmental drivers of under-ice phytoplankton bloom dynamics in the Arctic Ocean. *Elem. Sci. Anth.* **8**, 30 (2020).
53. Eronen-Rasimus, E. et al. Ice formation and growth shape bacterial community structure in Baltic Sea drift ice. *FEMS Microbiol. Ecol.* **91**, 1–13 (2015).
54. Bowman, J. S. The relationship between sea ice bacterial community structure and biogeochemistry: a synthesis of current knowledge and known unknowns. *Elem. Sci. Anthr.* **3**, 000072 (2015).
55. Eronen-Rasimus, E. et al. An active bacterial community linked to high chl-a concentrations in Antarctic winter-pack ice and evidence for the development of an anaerobic sea-ice bacterial community. *ISME J.* **11**, 2345–2355 (2017).
56. Kohlbach, D. et al. The importance of ice algae-produced carbon in the central Arctic Ocean ecosystem: food web relationships revealed by lipid and stable isotope analyses. *Limnol. Oceanogr.* **61**, 2027–2044 (2016).
57. Fossheim, M. et al. Recent warming leads to a rapid borealization of fish communities in the Arctic. *Nat. Clim. Change* **5**, 673–677 (2015).
58. Søreide, J. E., Leu, E. V. A., Berge, J., Graeve, M. & Falk-Petersen, S. Timing of blooms, algal food quality and *Calanus glacialis* reproduction and growth in a changing Arctic. *Glob. Chang. Biol.* **16**, 3154–3163 (2010).
59. Eriksen, E., Skjoldal, H. R., Gjøsæter, H. & Primicerio, R. Spatial and temporal changes in the Barents Sea pelagic compartment during the recent warming. *Prog. Oceanogr.* **151**, 206–226 (2017).
60. David, C., Lange, B., Rabe, B. & Flores, H. Community structure of under-ice fauna in the Eurasian central Arctic Ocean in relation to environmental properties of sea-ice habitats. *Mar. Ecol. Prog. Ser.* **522**, 15–32 (2015).
61. Melnikov, I. Recent Arctic sea-ice ecosystem: dynamics and forecast. *Dokl. Earth Sci.* **423**, 1516–1519 (2008).
62. Haug, T. et al. Future harvest of living resources in the Arctic Ocean north of the Nordic and Barents Seas: a review of possibilities and constraints. *Fish. Res.* **188**, 38–57 (2017).
63. Kędra, M. et al. Status and trends in the structure of Arctic benthic food webs. *Polar Res.* **34**, 23775 (2015).
64. Filbee-Dexter, K., Wernberg, T., Fredriksen, S., Norderhaug, K. M. & Pedersen, M. F. Arctic kelp forests: diversity, resilience and future. *Glob. Planet. Change* **172**, 1–14 (2019).
65. Murillo, F. J. et al. Sponge assemblages and predicted archetypes in the eastern Canadian Arctic. *Mar. Ecol. Prog. Ser.* **597**, 115–135 (2018).
66. Hamilton, C. D., Lydersen, C., Ims, R. A. & Kovacs, K. M. Predictions replaced by facts: a keystone species' behavioural responses to declining arctic sea-ice. *Biol. Lett.* **11**, 20150803 (2015).
67. O'Corry-Crowe, G. et al. Genetic profiling links changing sea-ice to shifting beluga whale migration patterns. *Biol. Lett.* **12**, 20160404 (2016).
68. Descamps, S. et al. Climate change impacts on wildlife in a High Arctic archipelago — Svalbard, Norway. *Glob. Chang. Biol.* **23**, 490–502 (2017).
69. Wollenburg, J. E. et al. Ballasting by cryogenic gypsum enhances carbon export in a *Phaeocystis* under-ice bloom. *Sci. Rep.* **8**, 7703 (2018).
70. Darnis, G. & Fortier, L. Zooplankton respiration and the export of carbon at depth in the Amundsen Gulf (Arctic Ocean). *J. Geophys. Res.* **117**, C04013 (2012).

71. Darnis, G. et al. From polar night to midnight sun: diel vertical migration, metabolism and biogeochemical role of zooplankton in a high Arctic fjord (Kongsfjorden, Svalbard). *Limnol. Oceanogr.* **62**, 1586–1605 (2017).
72. Wiedmann, I., Reigstad, M., Sundfjord, A. & Basedow, S. Potential drivers of sinking particle's size spectra and vertical flux of particulate organic carbon (POC): turbulence, phytoplankton, and zooplankton. *J. Geophys. Res. Ocean.* **119**, 6900–6917 (2014).
73. Flores, H. et al. Sea-ice properties and nutrient concentration as drivers of the taxonomic and trophic structure of high-Arctic protist and metazoan communities. *Polar Biol.* **42**, 1377–1395 (2019).
74. Belcher, A. et al. The potential role of Antarctic krill faecal pellets in efficient carbon export at the marginal ice zone of the South Orkney Islands in spring. *Polar Biol.* **40**, 2001–2013 (2017).
75. Lalande, C. et al. Variability in under-ice export fluxes of biogenic matter in the Arctic Ocean. *Global Biogeochem. Cycles* **28**, 571–583 (2014).
76. Miller, L. A., Carnat, G., Else, B. G. T., Sutherland, N. & Papakyriakou, T. N. Carbonate system evolution at the Arctic Ocean surface during autumn freeze-up. *J. Geophys. Res. Ocean.* **116**, C00G04 (2011).
77. Dieckmann, G. S. et al. Brief Communication: ikaite ($CaCO_3{\cdot}6H_2O$) discovered in Arctic sea ice. *Cryosphere* **4**, 227–230 (2010).
78. Rysgaard, S. et al. Ikaite crystals in melting sea ice — implications for pCO_2 and pH levels in Arctic surface waters. *Cryosphere* **6**, 901–908 (2012).
79. Nomura, D. et al. CO_2 flux over young and snow-covered Arctic pack ice in winter and spring. *Biogeosciences* **15**, 3331–3343 (2018).
80. König, D., Miller, L. A., Simpson, K. G. & Vagle, S. Carbon dynamics during the formation of sea ice at different growth rates. *Front. Earth Sci.* **6**, 234 (2018).
81. Grimm, R., Notz, D., Glud, R. N., Rysgaard, S. & Six, K. D. Assessment of the sea-ice carbon pump: insights from a three-dimensional ocean-sea-ice-biogeochemical model (MPIOM/HAMOCC). *Elem. Sci. Anthr.* **4**, 000136 (2016).
82. Rysgaard, S., Glud, R. N., Sejr, M. K., Bendtsen, J. & Christensen, P. B. Inorganic carbon transport during sea ice growth and decay: a carbon pump in polar seas. *J. Geophys. Res.* **112**, C03016 (2007).
83. Manizza, M. et al. Changes in the Arctic Ocean CO_2 sink (1996–2007): a regional model analysis. *Global Biogeochem. Cycles* **27**, 1108–1118 (2013).
84. Mortenson, E. *Modelling carbon exchange in the air, sea, and ice of the Arctic Ocean*. PhD thesis, Univ. of Victoria (2019).
85. Fransson, A. et al. Effects of sea-ice and biogeochemical processes and storms on under-ice water fCO_2 during the winter-spring transition in the high Arctic Ocean: implications for sea-air CO_2 fluxes. *J. Geophys. Res. Ocean.* **122**, 5566–5587 (2017).
86. Mathis, J. T. et al. Storm-induced upwelling of high pCO_2 waters onto the continental shelf of the western Arctic Ocean and implications for carbonate mineral saturation states. *Geophys. Res. Lett.* **39**, L07606 (2012).
87. Pipko, I. I., Semiletov, I. P., Pugach, S. P., Wählstrãm, I. & Anderson, L. G. Interannual variability of air-sea CO_2 fluxes and carbon system in the East Siberian Sea. *Biogeosciences* **8**, 1987–2007 (2011).
88. Steiner, N. et al. What sea-ice biogeochemical modellers need from observers. *Elementa* **4**, 000084 (2016).
89. Cai, W.-J. et al. Decrease in the CO_2 uptake capacity in an ice-free Arctic Ocean Basin. *Science* **329**, 556–559 (2010).
90. Else, B. et al. Further observations of a decreasing atmospheric CO_2 uptake capacity in the Canada Basin (Arctic Ocean) due to sea ice loss. *Geophys. Res. Lett.* **40**, 1132–1137 (2013).
91. Fransson, A. et al. CO_2-system development in young sea ice and CO_2 gas exchange at the ice/air interface mediated by brine and frost flowers in Kongsfjorden, Spitsbergen. *Ann. Glaciol.* **56**, 245–257 (2015).
92. Geilfus, N. X. et al. First estimates of the contribution of $CaCO_3$ precipitation to the release of CO_2 to the atmosphere during young sea ice growth. *J. Geophys. Res. Ocean.* **118**, 244–255 (2013).
93. Brown, K. A. et al. Inorganic carbon system dynamics in landfast Arctic sea ice during the early-melt period. *J. Geophys. Res. Ocean.* **120**, 3542–3566 (2015).
94. Damm, E., Rudels, B., Schauer, U., Mau, S. & Dieckmann, G. Methane excess in Arctic surface water- triggered by sea ice formation and melting. *Sci. Rep.* **5**, 16179 (2015).
95. Kort, E. A. et al. Atmospheric observations of Arctic Ocean methane emissions up to 82° north. *Nat. Geosci.* **5**, 318–321 (2012).
96. Tison, J.-L. Biogeochemical impact of snow cover and cyclonic intrusions on the winter weddell sea ice pack. *J. Geophys. Res. Ocean.* **122**, 7291–7311 (2017).
97. *AMAP Assessment 2015: Methane as an Arctic Climate Forcer* (AMAP, 2015).
98. Zhou, J. et al. Physical and biogeochemical properties in landfast sea ice (Barrow, Alaska): insights on brine and gas dynamics across seasons. *J. Geophys. Res. Ocean.* **118**, 3172–3189 (2013).
99. Levasseur, M. Impact of Arctic meltdown on the microbial cycling of sulphur. *Nat. Geosci.* **6**, 691–700 (2013).
100. Hayashida, H. et al. Implications of sea-ice biogeochemistry for oceanic production and emissions of dimethyl sulfide in the Arctic. *Biogeosciences* **14**, 3129–3155 (2017).
101. Abbatt, J. P. D. et al. Overview paper: new insights into aerosol and climate in the Arctic. *Atmos. Chem. Phys.* **19**, 2527–2560 (2019).
102. Galindo, V. et al. Biological and physical processes influencing sea ice, under-ice algae, and dimethylsulfoniopropionate during spring in the Canadian Arctic Archipelago. *J. Geophys. Res. Ocean.* **119**, 3746–3766 (2014).
103. Simpson, W. R. et al. Halogens and their role in polar boundary-layer ozone depletion. *Atmos. Chem. Phys.* **7**, 4375–4418 (2007).
104. Jacobi, H.-W., Morin, S. & Bottenheim, J. W. Observation of widespread depletion of ozone in the springtime boundary layer of the central Arctic linked to mesoscale synoptic conditions. *J. Geophys. Res. Atmos.* **115**, 17302 (2010).
105. Abbatt, J. P. D. et al. Halogen activation via interactions with environmental ice and snow in the polar lower troposphere and other regions. *Atmos. Chem. Phys.* **12**, 6237–6271 (2012).
106. Frey, M. M. et al. First direct observation of sea salt aerosol production from blowing snow above sea ice. *Atmos. Chem. Phys.* **20**, 2549–2578 (2020).
107. Tarasick, D. W. & Bottenheim, J. W. Surface ozone depletion episodes in the Arctic and Antarctic from historical ozonesonde records. *Atmos. Chem. Phys.* **2**, 197–205 (2002).
108. Kiko, R., Kern, S., Kramer, M. & Mütze, H. Colonization of newly forming Arctic sea ice by meiofauna: a case study for the future Arctic? *Polar Biol.* **40**, 1277–1288 (2017).
109. Steiner, N. & Stefels, J. Commentary on the outputs and future of Biogeochemical Exchange Processes at Sea-Ice Interfaces (BEPSII). *Elem. Sci. Anth.* **5**, 81 (2017).
110. Echeveste, P., Agustí, S. & Dachs, J. Cell size dependent toxicity thresholds of polycyclic aromatic hydrocarbons to natural and cultured phytoplankton populations. *Environ. Pollut.* **158**, 299–307 (2010).
111. Peeken, I. et al. Arctic sea ice is an important temporal sink and means of transport for microplastic. *Nat. Commun.* **9**, 1505 (2018).
112. Obbard, R. W. et al. Global warming releases microplastic legacy frozen in Arctic Sea ice. *Earth's Futur.* **2**, 315–320 (2014).
113. Steiner, N. S., Christian, J. R., Six, K. D., Yamamoto, A. & Yamamoto-Kawai, M. Future ocean acidification in the Canada Basin and surrounding Arctic Ocean from CMIP5 earth system models. *J. Geophys. Res. Ocean.* **119**, 332–347 (2014).
114. Fransson, A. et al. Impact of sea-ice processes on the carbonate system and ocean acidification at the ice-water interface of the Amundsen Gulf, Arctic Ocean. *J. Geophys. Res. Ocean.* **118**, 7001–7023 (2013).
115. Geilfus, N.-X. et al. Estimates of ikaite export from sea ice to the underlying seawater in a sea ice–seawater mesocosm. *Cryosphere* **10**, 2173–2189 (2016).
116. Moreau, S. et al. Assessment of the sea-ice carbon pump: Insights from a three-dimensional ocean-sea-ice biogeochemical model (NEMO-LIM-PISCES). *Elementa* **4**, 000122 (2016).

Acknowledgements

This Perspective is a product of the Biogeochemical Exchange Processes at Sea-Ice Interfaces (BEPSII) research community. This manuscript was first conceived at the Arctic Sea-Ice Change foresight workshop held in Davos, Switzerland, in June 2018 and is supported by the Euromarine Network.

Author contributions

D.L., L.T., M. v.L., K.C., H.F., B.D., L.M. and J.S. led the design and the writing of the paper. G.C., F.F., N.S., M.V. and M.V. significantly contributed to the 'Environmental conditions' section. P.A., J.B., H.K., K.M., I.P., J.-M.R. and P.W. significantly contributed to the 'Biota' section. K.B., M.C., O.C., E.D., B.E., A.F., N.-X.G., C.J., E.J., M.K., S.M., D.N., N.S., J.-L.T. and F.v.d.L. significantly contributed to the 'Gases' section.

Competing interests

The authors declare no competing interests.

Additional information

Supplementary information is available for this paper at https://doi.org/10.1038/s41558-020-00940-4.

Correspondence should be addressed to D.L.

Peer review information *Nature Climate Change* thanks Jørgen Berge, Suhas Shetye and the other, anonymous, reviewer(s) for their contribution to the peer review of this work.